Miha Založnik

Modeling of Macrosegregation in Direct Chill Casting

Doctoral Dissertation

Mentor: Prof. Dr. Božidar Šarler

Graduate School
University of Nova Gorica

2006

CIP - Kataložni zapis o publikaciji
Narodna in univerzitetna knjižnica, Ljubljana

621.74.047(043.3)

ZALOŽNIK, Miha
Modeling of macrosegregation in direct chill casting : doctoral dissertation / Miha Založnik. - Nova Gorica : M. Založnik, 2006

229974528

Miha Založnik

Modeling of Macrosegregation in Direct Chill Casting

Doctoral Dissertation

Mentor: Prof. Dr. Božidar Šarler

Graduate School
University of Nova Gorica

2006

We can be knowledgeable with other men's knowledge, but we cannot be wise with other men's wisdom.

Michel de Montaigne

Acknowledgements

My research life started when Professor Božidar Šarler established the Laboratory for Multiphase Processes. There I articulated my scientific curiosity, began to gain autonomy in conducting research, and learned to swim when thrown into water. I thank Professor Šarler for being my doctoral advisor, for his initiative, perseverance, guidance and appreciation of my work.

Further I thank the committee members, Dr. Dominique Gobin, Professor Matjaž Hriberšek, and Professor Boris Štok for their time, flexibility and rapid evaluation of the manuscript.

Special thanks go to Dominique Gobin for providing an invaluable working refuge at the FAST laboratory in Orsay, for his continuing encouragement, guidance, and inspiring suggestions. Further thanks to Benoît Goyeau for the several profound discussions, which clarified the model development. My thanks also go to Shihe Xin who provided the data of his natural convection computations used for comparison.

The working atmosphere was brightened up by Igor (always up for a discussion and always helping me to get a more lucid viewpoint), Janez, Robert, Jure, Marko, Simo, Henrik, Stanislav, Miran, and Gregor. Thank you for all the stimulating discussions of our work, for sharing enthusiasm and the (occasionally too good) pinch of sarcasm that was sometimes needed to overcome temporary frustrations.

I would also like to thank everybody at Impol Aluminium Industry for their friendliness and encouragement. Especially Edvard Slaček and Rajko Šafhalter for supporting the project, and Marina Jelen, Vili Strnad and Vukašin Dragojević for all discussions and their efforts in the attempts of providing reliable experimental macrosegregation data.

The least direct but the most valuable way of support and stimulation came from my family and friends who kept me sane in moments of deep immersion into curiosity by leading me onto other warm and exciting paths.

This work was carried out during 2001-2006 at the Laboratory of Multiphase Processes of the University of Nova Gorica. The research was funded by the Slovenian Government through the Young Researchers program and by Impol Aluminium Industry.

Modeling of Macrosegregation in Direct Chill Casting
Miha Založnik

Abstract

In the dissertation a numerical model for simulation of macrosegregation in direct chill (DC) casting is developed and applied to study the behavior of the process. The model development encompasses the derivation of a single-domain mixture model to describe the solidification of binary metal alloys, the implementation of the numerical solution method, and the verification of the numerical code. The single-domain model accounts for two distinct flow regimes in the solidification region—the mushy zone. In the slurry regime the solid phase is in the form of free-floating grains and behaves rheologically as a slurry. Above a threshold solid volume fraction—the consolidation limit—the solid forms a porous medium. Initiation and growth of the free-floating grains are modeled by a simplified treatment, based on the free-growth model of grain initiation on inoculant particles. The momentum equation of the slurry-porous dual-flow-regime mixture model is formulated as a single-domain equation for the first time. This is done by penalization of terms, which are distinct for slurry and porous flow. The numerical solution scheme is based on the finite volume method, using stable second-order accurate discretization schemes for advection. Numerical verification for the flow of molten metal in the liquid pool of the DC casting, driven by thermosolutal natural convection, is conducted on simplified cases of thermal, solutal, and thermosolutal natural convection in rectangular differential cavities. The code is tested and the discretization errors are analyzed in the pertinent range of dimensionless parameters (Prandtl, Schmidt, and thermal and solutal Rayleigh numbers estimated for the flow in the liquid pool of the DC casting), where numerical reference solutions do not exist. In the investigation of the DC casting process behavior emphasis is placed on the thermosolutal natural convection of the binary metal in the liquid pool of the casting. The characteristics of the thermosolutal flow in the pertinent range of dimensionless parameters are studied on simplified prototypal cases of thermal, solutal, and thermosolutal natural convection in rectangular differential cavities. Thermosolutal natural convection is studied for the first time in the pertinent parameter range. The numerical model is used to simulate the dependence of macrosegregation on casting velocity, casting temperature, mold cooling, and casting size for industrial Al-5.25 %Cu billets. The model predicts a significant dependence of the natural-convection flow structure in the liquid pool on the casting parameters and their impact on macrosegregation through the altered solute transport by the flow. The interaction of trans-

port phenomena leading to macrosegregation in DC cast billets and ingots is studied by simulating the effects of shrinkage flow, natural convection and grain transport. It is found that the thermosolutal flow affects macrosegregation both, through the impact on melt flow in the porous mushy zone and through transport of solute in the bulk liquid pool. Both thermosolutal flow and shrinkage are found to significantly affect the macrosegregation pattern. The impact of grain transport is studied by a simplified thermal model and qualitative observations of dependence of the negative centerline segregation zone on grain size and consolidation solid fraction are made.

Key words

Direct chill casting, macrosegregation, solidification, thermosolutal natural convection, aluminum alloys

Modeliranje makroizcejanja pri polkontinuirnem ulivanju
Miha Založnik

Povzetek

V disertaciji je razvit numerični model za simulacijo makroizcejanja v procesu polkontinuirnega ulivanja. Model je uporabljen za študij procesa. Razvoj modela obsega izpeljavo enoobmočnega modela mešanice, ki popisuje strjevanje binarne kovinske zlitine, implementacijo numerične metode za rešitev modelskih enačb ter verifikacijo numeričnega modela. Enoobmočni model upošteva prisotnost dveh tokovnih režimov v območju strjevanja. V brozgastem režimu je trdna faza v obliki prosto plavajočih zrn in je reološko popisana kot trdno-kapljevinasta suspenzija. Nad mejnim deležem trdne faze (meja konsolidacije) je trdna faza zrasčena v tog porozen medij. Nukleacija in rast prosto plavajočih zrn sta modelirana na poenostavljen način, temelječ na modelu proste rasti, ki popisuje aktivacijo in rast zrn na delcih modifikatorja. Gibalna enačba mešanice za brozgasti in porozni tokovni režim je prvič formulirana kot enovita enoobmočna enačba. To je doseženo s penalizacijo členov enačbe, ki se razlikujejo med tokovnima režimoma. Numerično reševanje modelskih enačb temelji na metodi kontrolnih prostornin, ob uporabi stabilnih diskretizacijskih shem, najmanj drugega reda natančnosti. Numerična verifikacija za izračun toka dvojno difuzivne naravne konvekcije v kapljevinastem območju ulitka je izvedena na geometrijsko poenostavljenih primerih termične, sestavinske in dvojno difuzivne naravne konvekcije v pravokotnih kotanjah. Preizkusi in ocene diskretizacijskih napak so izvedeni za relevantno območje brezdimenzijskih parametrov (Prandtlovo, Schmidtovo, ter termično in sestavinsko Rayleighovo število, ocenjena za tok v kapljevinastem območju ulitka), v katerem ni na voljo referenčnih numeričnih rešitev. Pri raziskavi odziva procesa je poudarjen vpliv dvojno difuzivne naravne konvekcije v kapljevinastem območju ulitka. Značilnosti dvojno difuzivne konvekcije v ustreznem območju brezdimenzijskih števil so študirane na poenostavljenih prototipnih primerih termične, sestavinske in dvojno difuzivne naravne konvekcije v pravokotnih kotanjah. Pri tem je prvič študirana dvojno difuzivna naravna konvekcija v ustreznem območju parametrov. Nadalje je z numeričnim modelom simulirana odvisnost makroizcejanja od hitrosti ulivanja, temperature ulivanja, hlajenja kokile in velikosti ulitka v primeru industrijskih ulitkov—drogov iz zlitine Al-5.25 %Cu. Napovedan je pomemben vpliv omenjenih procesnih parametrov na strukturo dvojno difuzivnega toka v kapljevinastem območju in posledičen vpliv na transport sestavin ter s tem na makroizcejno polje. Študirane so interakcije transportnih pojavov, ki povzročajo makroizcejanje: toka vsled krčenja, naravne konvek-

cije in transporta prosto plavajočih zrn. Ugotovljeno je, da tok vsled dvojno difuzivne naravne konvekcije vpliva na makroizcejanje preko vpliva na tok taline v poroznem območju strjevanja in preko transporta sestavin v kapljevinastem območju. Oba pojava, naravna konvekcija in krčenje, bistveno vplivata na makroizcejno polje. Vpliv transporta prosto plavajočih zrn je študiran s poenostavljenim termičnim modelom. Podane so ugotovitve o kvalitativnem vplivu velikosti zrn in meje konsolidacije na negativno izcejno cono v središču ulitka.

Ključne besede

polkontinuirno ulivanje, makroizcejanje, strjevanje, dvojno difuzivna naravna konvekcija, aluminijeve zlitine

Contents

List of Figures

List of Tables

List of Symbols

Latin symbols

A	cavity aspect ratio (H/L), CV face area
A_k	phase interface area in phase k
$\boldsymbol{A}$	FVM coefficient matrix
$\tilde{\boldsymbol{A}}$	ADI-TDMA/PDMA transformed coefficient matrix
A_in	DC casting mold inlet area
$\vec{b}$	buoyancy force per unit volume
c_p	specific heat
$c_\mathcal{R}$	slope parameter for the flow regime function $\mathcal{R}$
$c_\mathcal{D}$	slope parameter for the Darcy function $\mathcal{D}$
C	concentration
C_0	reference concentration in the buoyancy term
C_ref	thermodynamic reference concentration
ΔC	characteristic concentration difference for natural convection
d_g	grain diameter
D	diffusion coefficient
$\mathcal{D}$	Darcy function
f_exact	exact solution
f_i	numerical solution on grid with grid distance h_i
f_k	mass fraction of phase k
f_s^c	consolidation solid mass fraction
F	mass flux across CV face
$\vec{F}$	general vector field
$\boldsymbol{F}$	Forchheimer inertia tensor
F_s	GCI safety factor
$\vec{g}$, g	gravity acceleration
g_k	volume fraction of phase k
g_s^c	consolidation solid volume fraction
g_s^D	Darcy function threshold solid volume fraction
GCI	grid convergence index

h	specific enthalpy, heat transfer coefficient, grid distance
Δh_{mix}	mixing enthalpy
H	cavity height
I	coefficient for linear interpolation of CV face values
$\boldsymbol{I}$	identity matrix
j_{k}^{Γ}	solute transport due to the movement of the phase interface
j_{k}^{j}	diffusive solute flux across the interface
$\vec{j}_{\mathrm{k}}^{\mathrm{d}}$	dispersion solute flux
$\vec{j}_{\mathrm{k}}^{\mathrm{t}}$	tortuosity solute flux
k	thermal conductivity, interpolation coefficient for ULTRA-QUICK interpolation of CV face values
k_{p}	equilibrium partition coefficient
K	permeability
$\boldsymbol{K}$	permeability tensor
K_0	permeability constant
L	cavity width, macroscopic system scale
L_ε	length scale of porosity variation
L_v	length scale of velocity variation
l_{l}	length scale of liquid microscopic structures
l_{s}	length scale of solid microscopic structures
m	mass
m_{L}	liquidus slope
m_{S}	solidus slope
$\boldsymbol{M}$	second-order tensor used to represent $\hat{\vec{v}}_{\mathrm{l}}$
$\vec{M}_{\mathrm{i}}$	interfacial momentum source due to surface tension
$\vec{M}_{\mathrm{k}}^{\Gamma}$	momentum exchange due to phase change
$\vec{M}_{\mathrm{k}}^{\tau}$	momentum exchange due to interface stress
$\vec{M}_{\mathrm{k}}^{d}$	momentum exchange due to interface drag
$\vec{M}_{\mathrm{k}}^{p}$	momentum exchange due to interface pressure
$\vec{n}_{\mathrm{k}}$	normal vector of the interface pointing into phase k
n_{s}	number of grains per unit volume
N	buoyancy ratio ($N = (\beta_{\mathrm{l}}^{T}\Delta T)/(\beta_{\mathrm{l}}^{C}\Delta C)$)
Nu	Nusselt number
$O(\quad)$	order of leading error term of the discrete approximation
p	pressure, order of convergence
P	reduced pressure
P^*	dimensionless reduced pressure
Pe	Peclet number
Pr	Prandtl number
Q	volumetric source term

Q	interpolation coefficient for quadratic interpolation of CV face values
Q_w	chill water volume flow rate
Q_k^Γ	energy exchange due to the movement of the phase interface
Q_k^q	diffusive heat flux across the interface
$\vec{q}_\mathrm{k}^\mathrm{d}$	dispersion heat flux
$\vec{q}_\mathrm{k}^\mathrm{t}$	tortuosity heat flux
r	grain radius, grid refinement ratio, radial coordinate
$\vec{r}$	position vector of a phase interface point
r_0	scale of representative elementary volume (REV)
Ra_C	solutal Rayleigh number
Ra_T	thermal Rayleigh number
RDE	relative discretization error
RDE^band	RDE-based error band
$\mathcal{R}$	regime function
$\vec{S}$	control volume surface
ΔS_V	entropy of formation
Sc	Schmidt number
Sh	Sherwood number
t	time
t^*	dimensionless time
T	temperature
T_0	reference temperature in the buoyancy term
T_cast	casting temperature
T_L	liquidus temperature
T_ref	reference temperature
T_S	solidus temperature
T_w	cooling water temperature
Δt	discrete timestep
ΔT	characteristic temperature difference for natural convection
ΔT_fg	free-growth barrier
u	horizontal velocity component
u^*	dimensionless horizontal velocity component
U	horizontal velocity scale
v	vertical velocity component
$\vec{v}$	velocity
v^*	dimensionless vertical velocity component
$\vec{v}^*$	dimensionless velocity
v_cast	casting velocity
$\overline{\vec{v}}_\mathrm{il}$	average velocity of liquid at the phase interface

v_{in}	melt velocity at mold inlet
$\vec{v}_{\mathrm{sys}}$	system velocity
V	vertical velocity scale
V_0	averaging volume
V_{k}	volume of phase k
$\vec{w}_{\mathrm{i}}$	velocity of the phase interface
$\vec{x}$	position vector of the REV centroid
x	horizontal cartesian coordinate
x^*	dimensionless horizontal cartesian coordinate
Δx	discretization (grid) distance
X_{k}	phase function
y	vertical cartesian coordinate
y^*	dimensionless horizontal cartesian coordinate
Δy	discretization (grid) distance
$\vec{z}$	position vector
$\vec{z}_0$	reference level position vector

Greek symbols

β_{k}	relative solidification shrinkage
β_{k}^T	volumetric thermal expansion coefficient of phase k
β_{k}^C	volumetric solutal expansion coefficient of phase k
Γ	general diffusion coefficient in the general transport equation
Γ_{ik}	mass flux into phase k due to phase change
δ_C	width of vertical concentration boundary layer
δ_T	width of vertical thermal boundary layer
δ_v	width of vertical velocity boundary layer
ζ	interface curvature
$\overline{\zeta}$	average interface curvature
θ	dimensionless temperature
κ	thermal diffusivity
λ_2	secondary dendrite arm spacing
λ_{s}	grain growth parameter
μ	dynamic viscosity
ν	kinematic viscosity
ρ	density
ρ_0	reference density
$\rho_{\mathrm{k}}^{\mathrm{ref}}$	reference density of phase k
σ	interface energy
σ_{ii}	normal stress

τ	time scale based on thermal boundary layer growth time
$\boldsymbol{\tau}$	tangential stress tensor
τ_{ij}	tangential stress
Φ	factor in the LSRE
ϕ	general variable, dimensionless concentration
$\tilde{\phi}$	normalized variable (NVD)
Ψ	macrosegregation parameter (criterion)
ψ	general variable, streamfunction
ψ^*	dimensionless streamfunction
Ω	control volume volume

Subscripts

AESex	approximate error spline extrapolation
C	central node in FVM interpolation
D	downstream node in FVM interpolation
E	east node in FVM discretization stencil
e	east CV face
EE	second east node in FVM discretization stencil
i	interface
k	phase k
l	liquid phase
m	solid phase
N	north node in FVM discretization stencil
n	north CV face
nb	neighboring nodes in FVM discretization stencil
NE	northeast node in FVM discretization stencil
nee	north CV face of CV 'E'
NN	second north node in FVM discretization stencil
nn	north CV face of CV 'N'
nne	east CV face of CV 'N'
nnw	west CV face of CV 'N'
NW	northwest node in FVM discretization stencil
P	central node in FVM discretization stencil
ref	reference state
Rex	Richardson extrapolation
s	solid phase
S	south node in FVM discretization stencil
s	south CV face
SE	southeast node in FVM discretization stencil
see	south CV face of CV 'E'

SS	second south node in FVM discretization stencil
ss	south CV face of CV 'S'
SW	southwest node in FVM discretization stencil
U	upstream node in FVM interpolation
W	west node in FVM discretization stencil
w	west CV face
WW	second west node in FVM discretization stencil
α	primary solid phase

Superscripts

*	thermodynamic equilibrium state
*	dimensionless quantity, dimensionless operator

Other supplementary symbols

$\langle\ \rangle$	volume average
$\langle\ \rangle^k$	intrinsic volume average in phase k
$\hat{}$	deviation from intrinsic volume average

Acronyms

AES	approximate error spline
AESex	approximate error spline method extrapolated solution
CV	control volume
DC	direst chill
DSC	discrete singular convolution method
FVM	finite volume method
LSRE	local solute redistribution equation
OES	optical emission spectrometry
OOC	observed order of convergence
Rex	Richardson extrapolated solution
SM	spectral method

1 Introduction

1.1 Background and Rationale

The use of aluminum and its alloys has been rapidly expanding in the last few decades. The annual world production of primary aluminum grew from around 10 million tons in the 1970s to 15 million tons in 1994, reaching 23 million tons in 2005 [IAI, 2006]. The main applications of aluminum products are found in transport (aerospace, rail, automotive, marine), building, packaging (foil, cans) and electrical power transmission. New applications (e.g. the increasing use of aluminum in the automotive industry), more stringent demands as regards quality, as well as growing demands relating to process yield, energy efficiency and recycling in production are posing new challenges to production processes and require their further development and optimization.

Rolled and extruded aluminum products constitute the majority of all aluminum alloys in use. In the production chain of rolled and extruded products the starting stock is a direct chill (DC) cast sheet ingot or an extrusion billet, which gives a fine-grained material suitable for forming. In vertical DC casting, shown in Figs. 1.1 and 1.2, molten metal is poured from the furnace through a troughing system onto a mold table containing molds with the cross-section of the casting. At the beginning of the batch process, a starting head mounted to a hydraulic ram keeps the mold closed. When the metal fills the water-cooled mold, the starting head is lowered at a controlled rate. As it lowers, water jets below the mold spray water onto the casting (direct chill) and complete the solidification. During DC casting many defects can occur which are a direct consequence of the transport phenomena taking place in the process. Severe defects can range from cracks, hot tears and warping as a consequence of the residual stresses that build up due to uneven contractions during solidification through to shrinkage-induced porosity.

A less serious but inevitable defect that occurs in solidifying alloys is macrosegregation, an inhomogeneous macroscopic distribution of alloy components in the solidified casting. Chemical inhomogeneity can significantly

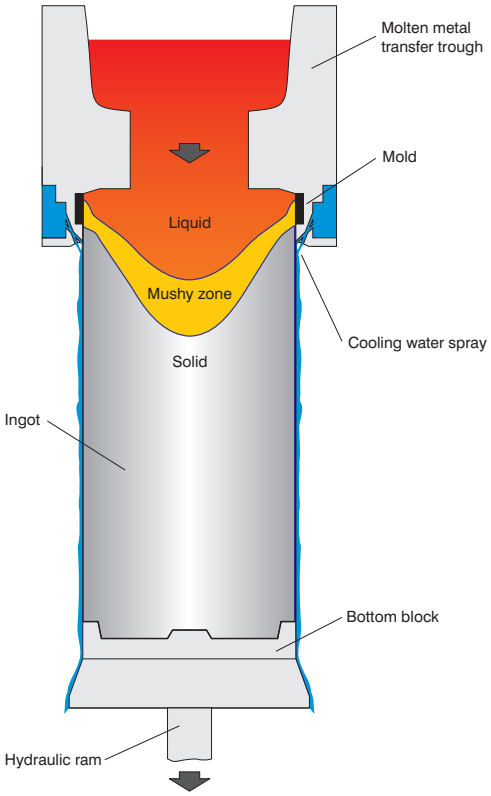

Figure 1.1: The DC casting process.

Figure 1.2: A DC billet casting machine in the Impol casthouse. Photo by Božidar Šarler.

deteriorate the mechanical properties, corrosion resistance, fatigue resistance and processing characteristics of the material. While macrosegregation can usually be kept within acceptable margins, it is desired to be able to control and minimize it in order to improve and optimize the product quality and process efficiency.

In the processing of materials, as in many other engineering fields, modeling and simulation are key tools for gaining an understanding of the process and the underlying physical phenomena. The complexity of the physics of alloy solidification and its still limited understanding make it indispensable to use modeling as a complement to experimentation to deepen our understanding. In addition, the development should finally result in predictive models to be used in connection with the models of other processes in the aluminum production chain. This linkage is envisioned to enable optimization of the whole production process from the base material to the final product [VIR[*], 2004].

1.2 Macrosegregation: The Underlying Physical Phenomena

1.2.1 Microsegregation

During the solidification of a mixture the liquid phase is transformed into one or more solid phases. The solubility of the mixture components in the solid phases is usually not the same as in the liquid. In the case of a hypoeutectic alloy, which is typical of most alloying elements used in wrought Al-alloys cast by the DC process, the primary solid phase forms with a composition lower than that of the liquid. This is shown in the equilibrium phase diagram in Fig. 1.3, depicting equilibrium compositions of coexisting phases (denoted by *) as a function of temperature. As the alloy of initial composition $C_1 = C_{2\mathrm{L}}$ begins to solidify, the first primary solid particle forms with composition $C^*_{2\mathrm{S}}$. Upon the formation of the low-concentration solid the excess solute must be rejected into the liquid. We can assume that, during the course of solidification, the interface of the growing solid particle is at thermodynamic equilibrium [Kurz and Fisher, 1998], thus determining the local phase compositions from the equilibrium phase diagram. From the phase diagram we can see that due to the gradual enrichment of the liquid with decreasing temperature the subsequently forming layers of solid have to have an increasing solute concentration (shown in Fig. 1.4 on a simplified 1D model). As a consequence, the average phase concentrations are lower than the equilibrium concentrations at the interface. In addition, a certain, although very small,

temperature gradient has to exist across the phase-change system to drive the heat flow required for the phase change. These two effects are depicted in Fig. 1.3 with the points without an asterisk. During the course of solidification the diffusion processes in both phases drive the solute away from the interface, somewhat equilibrating the concentration gradients (Fig. 1.4).

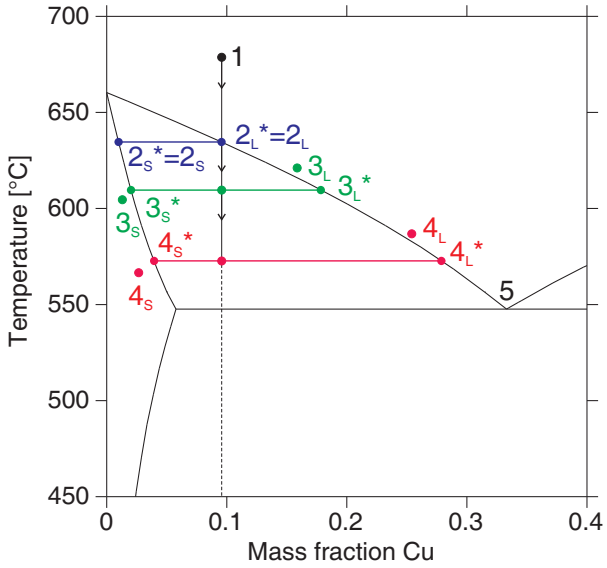

Figure 1.3: Solidification in the binary equilibrium phase diagram.

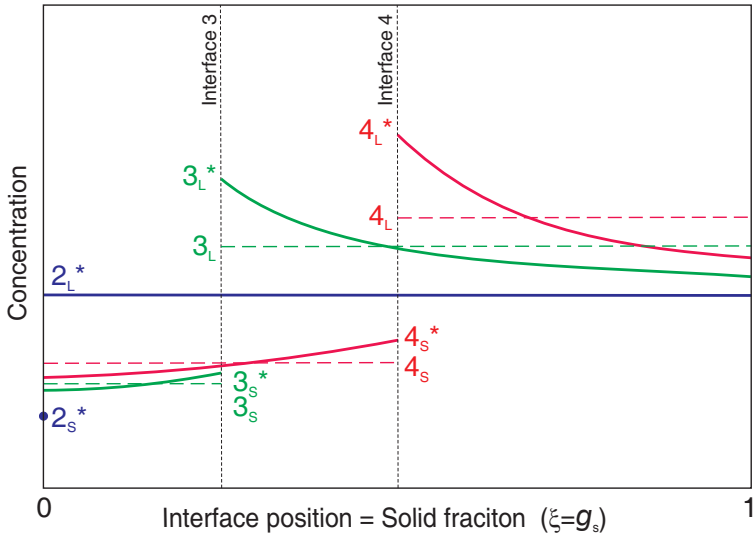

Figure 1.4: Evolution of the concentration profiles at the secondary dendrite arm scale.

The described processes of solute rejection take place on the scale of the

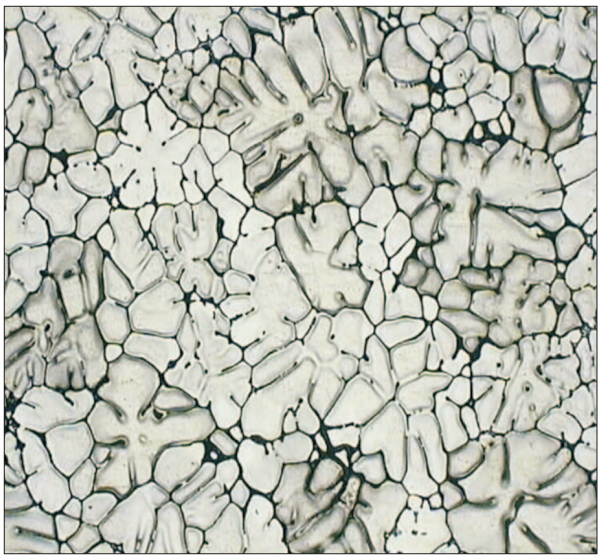

Figure 1.5: Coarse dendritic structure in a DC cast 2024 alloy billet. Courtesy of Impol d.d.

smallest structures of the growing solid. In an alloy the crystalline solid grows in the form of dendritic grains, usually comprising two levels of branching dendrites (Fig. 1.5). The representative structures for processes of local solute partitioning are thus secondary dendrite arms with a typical spacing of the order of $\sim 10\,\mu$m.

1.2.2 Relative Motion of Solid and Liquid Phases

Due to the solute rejection into the liquid on the scale of the growing grains any macroscopically significant relative motion of the solute-rich liquid and the solute-lean solid grains causes the macroscopic transport of the solute and thus macrosegregation in the solidified material.

Unlike pure materials which freeze at a fixed melting temperature, alloys solidify over a range of temperatures and phase compositions. In a solidifying system with moderate temperature gradients we can thus expect a solidification region of a substantial size where the growing solid grains and the surrounding liquid coexist—the 'mushy zone'. If the solid grains in such a region are grown together they form a porous solid skeleton (Fig. 1.6). Given a sufficient pressure head the liquid can flow through the porous solid structure.

If the solid grains are not coalesced they can freely move with the flow of liquid. Such a mushy zone behaves as a slurry of dispersed free-floating grains (Fig. 1.7). Such grains can form through the fragmentation of den-

Figure 1.6: Columnar mushy zone in a solidifying ammonium chloride solution [Huppert and Worster, 1985]. Photo by Mark Hallworth, courtesy of M. Grae Worster, University of Cambridge.

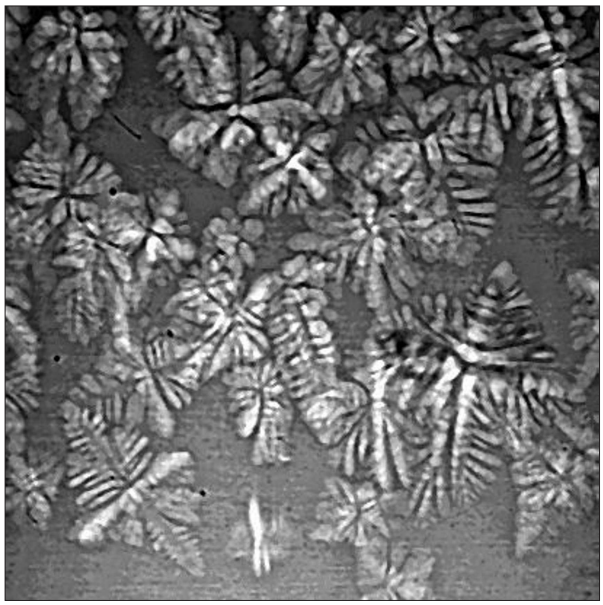

Figure 1.7: Equiaxed mushy zone in solidifying Al-20 wt%Cu, synchrotron X-ray radiography image [Mathiesen and Arnberg, 2006]. Courtesy of Ragnvald H. Mathiesen, SINTEF Materials and Chemistry.

drite branches from the porous skeleton or by heterogeneous nucleation on impurity particles in the subcooled bulk melt. The latter is common in the DC casting of aluminum alloys where grain-refiner particles, acting as potent nucleation sites for the growth of equiaxed grains, are added to refine the cast macrostructure.

Given these two possible structures of the mushy zone, macrosegregation by the relative motion of solid and liquid can be caused by the following phenomena.

Shrinkage flow The density of the solid phases is generally larger than that of the liquid. The volume change upon solidification (shrinkage) drives the inflow of liquid to feed the contraction. This mode of flow is important in the high-solid-fraction part of the porous mushy zone, where the other flow effects become negligible due to the strong drag forces and where the liquid is highly enriched and thus even small liquid velocities can result in significant solute redistribution.

Forced flow In casting processes the flow is also influenced by pouring, stirring, magnetic fields, vibrations etc.

Natural convection Temperature and composition gradients in the liquid give rise to density variations resulting in thermal and solutal buoyancy forces, which drive natural convection. The flow as well as the heat and mass transfer in natural convection are governed by the interaction of advection-diffusion heat, mass and momentum transport and by the thermal and solutal buoyancy forces. These interactions can become particularly complex in liquid metals due to their peculiar thermophysical properties. Liquid metals generally have a low viscosity and a high thermal diffusivity, their ratio, expressed by the Prandtl number ($Pr = \mu/\kappa$, where μ is the dynamic viscosity and κ is the thermal diffusivity) being of the order of 10^{-2}. This causes an important disparity in the diffusion lengths for momentum and heat transfer. The quick diffusion of heat beyond the range of the effect of viscous forces results in the presence of regions governed by a balance between buoyancy (the driving force) and inertia resulting in a relatively unstable flow structures. The effect of solutal buoyancy by itself is quite well behaved as the ratio of solute and momentum diffusivity, the Schmidt number ($Sc = \mu/D$, where D is the diffusion coefficient), is large and of the order of 10^2. This confines the solutal-buoyancy effect to a layer of balanced viscous and buoyancy forces resulting in stable flows. Now, the situation becomes highly complex when the solutal convection is combined with the unstable thermal convection. The unstable flow can

transport the very slowly diffusing solute (i.e. by advection) into thermally unstable regions and cause sharp, fine-scaled solutal structures (due to the low diffusivity) and complex interactions of the thermal and solutal buoyancy forces [Hyun *et al.*, 1995, Bergman and Hyun, 1996].

Motion of solid grains Free-floating grains in the slurry part of the mushy zone move due to the density differences between the solid and liquid (settling or flotation), due to drag forces exerted by the flowing liquid, and due to interactions with other grains.

Deformation of the solid skeleton The deformation of the solid skeleton causes the motion of the solid and the expulsion or suction of the enriched interdendritic liquid. It can be caused by thermal stresses, metalostatic head or external forces (as in compression from rolls in a continuous steel slab caster)

1.2.3 Macrosegregation in DC Casting

In a DC cast billet or ingot the solidification region has a characteristic shape resulting from the cooling. The molten metal, enriched with grain-refiner particles, enters the mold at the top through a distributor determining the initial path of the melt flow. The first grains start to grow on the grain-refiner seeds in an only slightly subcooled melt. They can move with the flow and, due to their larger density, they tend to settle at the bottom of the liquid pool, forming a slurry zone. In the zone close to the chill, where heat extraction is strong, and at high solid fractions of the mush (higher than the consolidation limit f_{s}^{c}) the grains coalesce to form a porous mushy zone. The flow in the bulk liquid region is driven by thermosolutal natural convection caused by the cooling and by the transport of enriched liquid from the solidification region. The natural-convection induced flow competes with the settling tendency of the grains in the slurry zone and drives the flow of liquid in the low-solid-fraction part of the porous zone. In the high-solid-fraction part of the mushy zone, a shrinkage-induced flow directed parallel to the solid-fraction gradient dominates the solute transport. Despite its small velocities, it can significantly affect macrosegregation by driving highly enriched liquid in the direction from the centerline towards the shell. In the subsurface region a shrinkage flow causes an inverse segregation—a narrow band of positive segregation due to a pileup of enriched liquid at the impermeable surface. In a water-cooled mold the thin forming solid shell may contract and detach from the mold before the impingement point of the direct-chill jet. The air gap between the mold and the casting causes a local termination of heat

extraction allowing the solid shell to reheat and partially remelt. In these conditions the metalostatic head can force highly enriched liquid through the permeable remelted shell and result in a thin layer of enriched metal at the casting surface (exudation).

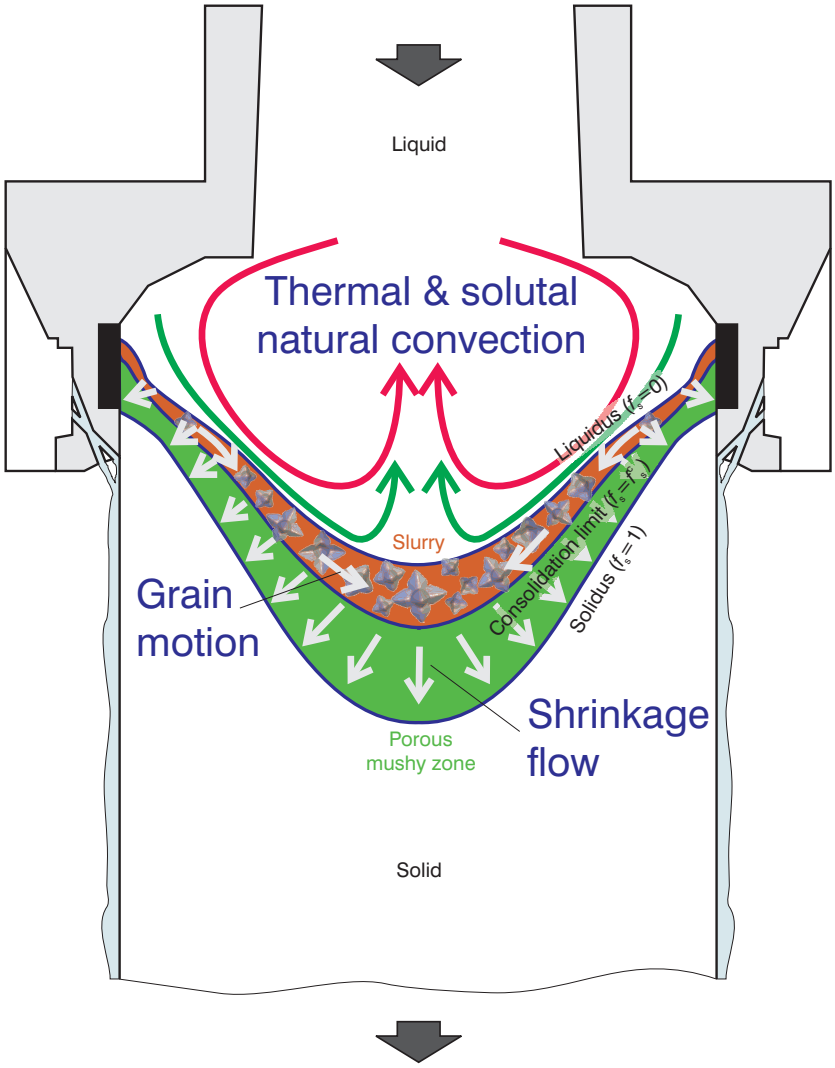

Figure 1.8: Transport mechanisms causing macrosegregation in DC casting.

A typical solute distribution pattern in a DC casting is a symmetric composition profile across the casting cross-section, as shown in Fig. 1.9. A solute-depleted region is present in the billet center, adjoined by a positive segregation zone spreading into the outward radial direction, an adjacent thin negative segregation zone and another positive segregation layer at the surface. The positive subsurface segregation is caused by the inverse segregation

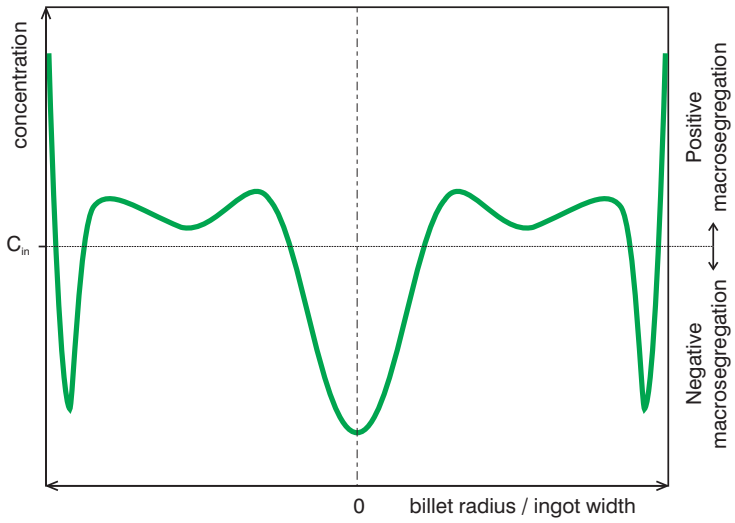

Figure 1.9: Typical macrosegregation profile in a DC casting.

as a result of the shrinkage flow towards the surface during shell formation. The adjacent negative zone is a consequence of depletion due to the shrinkage flow towards the surface and rapid cooling from the direct chill. The mechanisms of the formation of other patterns are still not entirely clear. The primary effect leading to negative centerline segregation is believed to be the settling of solute-lean free-floating grains accumulating at the bottom of the sump; however, natural convection flow and shrinkage may also have some influence on the degree of centerline segregation. The zone between the surface and center is most probably influenced by several competing phenomena. The exact mechanism of macrosegregation formation in DC casting is still not completely understood as will become evident from the literature review in Chapter 2.

1.2.4 Numerical Modeling of Macrosegregation

The diversity of the physical phenomena involved in the creation of macrosegregation and the complexity of their interactions makes numerical modeling very challenging.

Multiple scales The transport phenomena leading to macrosegregation occur on different length and time scales. The most basic solute redistribution occurs on the length scale of dendritic structures ($\sim 10\,\mu$m) and the time scale roughly identical with the solidification time, with the solute partitioning originating in phase equilibrium relations valid at the solid-liquid interface ($\sim 1\,$nm [Kurz and Fisher, 1998]). The inter-

facial drag forces in the mushy zone originate in the fluid dynamics at the scale of the solid structures. Macroscopic heat, momentum and solute transport are all related to the length scale of the casting ($\sim 1\,\mathrm{m}$) with the important observation that the largest gradients are found in the mushy zone ($\sim 1\,\mathrm{cm}$). Another scale disparity is found in diffusive transport where the length scales of solute and momentum diffusion are much smaller than for heat diffusion.

Different flow regimes Fluid flow occurs in the bulk liquid, the slurry, and the porous regions. Regarding the system on the macroscopic continuum scale, different kinds of drag and viscous forces act on the liquid in the different flow regimes.

Coupling of transport equations The transport equations are strongly coupled via the buoyancy forces. The solidification dynamics are governed by all: heat, solute transport, and the fluid flow.

Accuracy of numerical solution The accuracy of a solution is an important and difficult issue when solving predominantly advective transport equations, which is the case for momentum and species transport in metal alloys. More generally, accuracy is critical whenever steep gradients occur in an otherwise smooth field. This occurs in the mushy zone in a narrow region close to the liquidus, in the boundary layers, and across the bulk liquid in the flow and species redistribution patterns arising from the unstable thermosolutal convection in liquid metal mixtures.

The following techniques are used to cope with these challenges.

Volume averaging Due to the scale disparities of microscopic and macroscopic transport and the complex interface morphology of the dendritic structure it is impossible to solve the exact conservation equations on the microscopic scale for a macroscopic problem. To overcome this problem we take advantage of the large-scale disparities. To model the solidification region, averaged macroscopic equations are obtained by averaging the microscopic equations over an averaging volume (representative elementary volume—REV) that is large compared to the dendritic structure (i.e. large enough to make the average quantities representative) and small compared to the scale of the system (i.e. small enough to enable a continuum description of the average quantities). In other words, $l_\mathrm{l}, l_\mathrm{s} \ll r_0 \ll L$, where l_l, l_s, r_0, and L are the characteristic scales of the liquid and solid phase structures, the REV, and the

macroscopic system, respectively. By averaging, microscopic phenomena (microscopic solute transport, drag forces) are no longer accounted for. They have to be modeled using phenomenological models linked to the averaged transport equations.

Single-domain momentum equation The equations describing the flow in the bulk liquid, the slurry and the porous flow regime are different and turn out to be not easily compatible. As it is advantageous to use a single-domain model, i.e. a model capable of describing the whole domain with the same equations, we attempt to recast the averaged transport equations into a form capable of describing all flow regimes.

Iterative solution techniques Iterative solution schemes are used to solve the coupled transport equations. They are usually based on extended standard techniques for the coupling of pressure, velocity and scalar transport. However, due to the strong coupling the iterative stability of the system becomes very sensitive.

Use of accurate discretization methods and error analysis In the past, inaccurate discretization methods were often used in the numerical modeling of macrosegregation to avoid stability problems in species and momentum transport. Accuracy is crucial when modeling the influence of advective transport on macrosegregation. We therefore seek to implement more accurate but stable discretization methods and to rigorously analyze the accuracy of the numerical solution.

2 Literature Review

Be careful about reading health books. You may die of a misprint.

Mark Twain

2.1 Modeling of Alloy Solidification

The first studies that modeled the development of macrosegregation during the solidification of alloys were published in the 1960s by Merton C. Flemings and his coworkers [Flemings and Nereo, 1967a,Flemings *et al.*, 1967,Flemings and Nereo, 1967b] who laid the foundations of the modern macrosegregation theory. Flemings and Nereo [Flemings and Nereo, 1967a] developed a local solute redistribution equation; an ordinary differential equation based on mass continuity, solute conservation, and the Scheil equation for local solute partitioning. This equation models the solute redistribution in a mushy zone caused by shrinkage-driven flow at a prescribed cooling velocity (velocity of isotherms) in unidirectional solidification. The model was solved analytically and gave general expressions for macrosegregation as a function of the shrinkage flow velocity, the thermal gradient in the mush and the cooling rate. This enabled them to model the effects of changing heat flow conditions and casting cross-sections and to thereby propose qualitative explanations for macrosegregation patterns found in castings [Flemings *et al.*, 1967, Flemings and Nereo, 1967b]. The next big step forward was the model developed in 1981 by Ridder, Kou and Mehrabian [Ridder *et al.*, 1981], the first to account for the coupling of the flow between the bulk liquid and mushy regions. Ridder et al. solved the coupled set of equations, describing the motion of liquid due to thermal convection and shrinkage, the heat transfer and the solute redistribution by Darcy's law, the energy equation and Flemings' local solute redistribution equation in the mushy zone and by the momentum and energy equations in the bulk liquid region. They coupled the two regions by boundary conditions at the fixed liquid-mush boundary of the quasi-steady system. The macrosegregation predictions of the model compared favorably

to their experimental measurements.

Substantial progress in solidification modeling started in the mid-1980s with the advent of so-called single-domain models. In contrast to the multidomain models, like the one by Ridder et al., where liquid, mushy and solid regions are modeled by separate equations and the regions are coupled via boundary conditions, single-domain models are based on equations that are valid in all regions. This reduces the need to track the region boundaries and enforce internal boundary conditions and thus facilitates implementation.

Single-domain models were developed on two different tracks. The first group includes models based on the multiphase mixture theory (also called continuum mixture models). The dependent variables in the governing equations are mixture quantities, defined in terms of phase (solid and liquid) quantities, weighted by mass or volume phase fractions. The first mixture model accounting for the advection-diffusion transport of momentum, energy and species was developed by Bennon, Incropera and Prescott [Bennon and Incropera, 1987, Bennon and Incropera, 1988, Prescott *et al.*, 1991]. They cast the transport equations in a form that made it easier to solve them using existing popular methods of computational fluid dynamics (CFD). Following the parallel development of two-phase models (they will be reviewed later on), which seem to offer the advantage of more elegantly modeling microscopic phenomena through the inclusion of constitutive models of interfacial transfer, Ni and Incropera [Ni and Incropera, 1995a, Ni and Incropera, 1995b] extended the continuum mixture model to account for many important microscopic phenomena. However, apparently the complex full model has not been implemented and applied to date. Vreeman, Krane and Incropera [Vreeman *et al.*, 2000] extended the mixture continuum model to account for the motion of free-floating grains and the consequent effect on macrosegregation in a grain-refined casting. They ended up with separate and distinct momentum equations for the slurry (dispersed solid phase) and porous (consolidated solid phase) regions of the mushy zone and modeled the transition between the regions by switching between the equations at a solid packing fraction. Krane [Krane *et al.*, 1997, Krane, 2004] later also adapted this model for ternary alloys. Šarler and coworkers [Šarler *et al.*, 2003, Šarler and Pepper, 2004] tried to avoid switching between different momentum equations for the slurry and porous mushy regions and proposed modeling this kind of flow by the penalization of the distinct terms, an idea also followed in the present work.

The second group of single-domain models includes two-phase and multiphase models. Two-phase models consist of separate conservation equations for each phase, valid in all regions, and additional constitutive models that describe the interphase interactions at the phase interfaces and which are

needed to close the model. The first of such models were developed by Beckermann and coworkers [Beckermann, 1987, Beckermann and Viskanta, 1988, Ni and Beckermann, 1991, Beckermann and Viskanta, 1993] and by Ganesan and Poirier [Ganesan and Poirier, 1990]. Their derivations are based on averaging the usual conservation equations for mass, momentum and solute, which are valid locally (on the microscopic scale of the phase structures) in each phase, along with appropriate interface boundary conditions, over the continuum scale of the macroscopic system. This is done by a formal volume averaging procedure [Drew, 1983]. This results in separate conservation equations for each phase that have to be supplemented by constitutive models of the interface interactions to close the model. The main advantage of the volume-averaged two-phase models seems to be the more natural incorporation of microscopic interphase phenomena and the clear connection of all equation terms with the original local continuum equations. Many extended variants of the aforementioned two-phase models were subsequently developed. Probably the most prominent is the multiphase model by Wang and Beckermann [Wang and Beckermann, 1993, Wang and Beckermann, 1996a, Wang and Beckermann, 1996b, Wang and Beckermann, 1996c]. It models the interdendritic liquid as a separate phase, which enables the accounting of different solute-diffusion length scales in the solid, liquid and interdendritic liquid phases in order to more rigorously model the effect of the dendritic grain structure. Recently, Wu and coworkers [Ludwig and Wu, 2002, Wu *et al.*, 2003] developed a version of the two-phase model that is simpler than the model by Wang and Beckermann, but which includes a stochastic nucleation model to account for the appearance of free-floating globular grains.

In the development of two-phase models many interfacial phase interactions, effective properties and other contributions (dispersion and tortuosity) were modeled semi-empirically. Some of these simplifications in the momentum equation were clarified in a rigorous manner by Goyeau et al. [Goyeau *et al.*, 1997] and Bousquet-Melou et al. [Bousquet-Melou *et al.*, 2002a]. They rederived the equations using volume averaging, estimated the magnitudes of individual terms by scaling analysis, and defined a local closure problem for the fluctuating variables (the difference between the average and the local value of the variable). The solution of the closure problem enables the determination of effective transport properties (permeability, inertia tensor etc.). A similar task was performed by Neculae et al. [Neculae *et al.*, 2002] and Bousquet-Melou et al. [Bousquet-Melou *et al.*, 2002b] for species transport.

2.2 Macrosegregation in DC Casting

2.2.1 Experimental Investigations

One of the first attempts to explain the mechanisms of the formation of typical macrosegregation patterns in DC cast ingots was the work by Yu and Granger in 1986 [Yu and Granger, 1986]. They examined the typical positive segregation at the ingot subsurface and negative segregation in the ingot center. Deriving a specialized version of Flemings' local solute redistribution equation for the subsurface zone they could show the formation of the positive subsurface segregation due to shrinkage flow. Examining the grain structure in the center of the ingot they found a duplex structure of small dendritic grains and coarse nondendritic (cellular) grains. The dendrite cell size depends on the cooling rate and suggests that the coarse grains must have grown at a much smaller cooling rate. In addition, microprobe measurements of grain composition profiles showed that the coarse grains must have grown isothermally at an approximately constant melt composition, close to the liquidus, while the fine dendrites exhibit a normal microsegregation profile. Both suggests that the two types of grains have different origins. The accumulation of coarse grains at the centerline and the finding that they have to grow isothermally, together with temperature measurements in the liquid pool, suggest when combined that the coarse grains form close to the solid shell and are swept in the thermal boundary layer where they grow isothermally at a low melt concentration, along the liquidus front to the bottom of the liquid pool, where they accumulate. The formation of coarse free-floating grains thus decisively contributes to the negative centerline segregation. The hypotheses of Yu and Granger seemed to be supported by the findings of Gariepy and Caron [Gariepy and Caron, 1991], who found a strong dependence of the severity of macrosegregation on the grain refiner additions and the metal feeding system. Dorward and Beerntsen [Dorward and Beerntsen, 1990] related the severity of macrosegregation to the sump depth and thermal gradients in the sump. They found that a deep sump (higher casting speed) promotes overall macrosegregation and suggested that this provides favorable conditions for the collection of the observed coarse isothermal grains at the centerline, for which they presumed that they cause a negative centerline segregation. A shallow sump results in less macrosegregation and, in combination with an increased casting temperature attenuating the accumulation of isothermal grains at the centerline, this can result in a positive centerline macrosegregation. In contrast to these interpretations, Chu and Jacoby [Chu and Jacoby, 1990], who also attributed the negative centerline segregation to grain transport, contended with a somewhat loose justification that the fine

dendritic grains are those that were detached in a high cooling rate region, suspended growth during transport to the bottom of the liquid pool and continued to grow in situ. They hypothesized that the coarse grains in the center grew in situ and coarsened due to the lower cooling rate.

In more recent investigations of the European EMPACT project, Joly et al. [Joly *et al.*, 2000], Lesoult et al. [Lesoult *et al.*, 2001], and Daloz et al. [Daloz *et al.*, 2002] investigated macrosegregation and macrostructure in grain refined and non-grain refined ingots using two different melt distributor systems. They found that macrosegregation generally increases with grain refinement and linked this to the increased transport of free-floating coarse (slowly growing) grains, formed either by the fragmentation of dendrites or by nucleation on grain refiner particles. In addition, they showed the strong dependence of macrosegregation on the entry melt flow (distributor system). This led them to contend from a detailed analysis of the macrosegregation field that, in addition to the effect of grain transport, there should be a significant impact of the interdendritic flow on the macrosegregation pattern, possibly also affected by the influence of the grain structure on the local permeability of the porous mush [Daloz *et al.*, 2002].

Eskin and coworkers [Eskin *et al.*, 2004, Suyitno *et al.*, 2004, Eskin *et al.*, 2005] very recently investigated the effects of alloy composition and different casting parameters on the macrosegregation, structure, and casting defects in DC cast billets in an attempt to complement their experimental investigations with somewhat simplified numerical simulations. They again confirmed that casting speed increases macrosegregation in all regions across the casting cross section [Eskin *et al.*, 2005]. The effect of casting temperature was shown to affect macrosegregation only in the region close to the surface [Eskin *et al.*, 2005], while the water flow rate did not exhibit a notable effect on macrosegregation [Eskin *et al.*, 2004]. Concerning the origin of negative centerline segregation, they show, quite convincingly, that the structure of coarse grains in the billet center can only be explained with their longer solidification trajectory in the presence of a slurry flow. However, they did not find a clear correlation between the fraction of coarse grains and the segregation intensity [Eskin *et al.*, 2004, Eskin *et al.*, 2005], which suggests that the effect of the settling of solute-lean grains must be complemented by a competing effect of the flow of the enriched melt.

2.2.2 Model Investigations

The first to study macrosegregation in DC cast billets using a computational model were Flood, Katgerman and Voller [Flood *et al.*, 1991] in 1991. Their model assumed a rigid mushy zone moving at the casting speed and

neglected solidification shrinkage. Their results for a 420 mm Al-4.5 wt%Cu billet indicated a positively segregated centerline segregation as a result of heavy enriched liquid settling at the sump bottom and emphasized the importance of solutal convection. Many other attempts using similar models then followed. The first to attempt to include the influence of free-floating grains was made by Reddy and Beckermann [Reddy and Beckermann, 1995]. The free-floating grains were modeled by employing a constant grain density in the domain (i.e. no grain generation or annihilation) solving a grain transport equation to calculate the local grain density, and calculating the grain size from the number of grains and the solid volume fraction. They simulated the casting of Al-4.5 wt%Cu billets of 533 mm diameter with and without free-floating dendrites and compared their preliminary results to the measurements. Although neither of the cases showed consistent agreement with experimental data, the case with free-floating grains succeeded to predict negative centerline segregation for the first time. Later, Reddy and Beckermann [Reddy and Beckermann, 1997] simulated macrosegregation in a billet with a consolidated porous mush and studied the effects of mushy zone permeability, thermosolutal convection and shrinkage flow. They found that centerline segregation can depend on the permeability and can be either positive (at high permeability) or negative (at low permeability) as a result of the competing effects of thermosolutal flow penetrating the mushy zone (transporting enriched liquid in the mushy zone), and the shrinkage flow that transports solute away from the centerline.

In their later investigation, Vreeman and Incropera [Vreeman and Incropera, 2000] used their own simplified version [Vreeman *et al.*, 2000] of the model [Ni and Incropera, 1995a,Ni and Incropera, 1995b] to calculate macrosegregation distributions in DC cast billets, assuming the presence of slurry and porous flows in the mushy zone. They set a constant characteristic grain diameter and did not explicitly calculate the grain density since the relative solid velocity was obtained directly from the grain diameter and the solid volume fraction. A parametric study was performed for Al-4.5 wt%Cu and Al-6 wt%Mg billets with a diameter of 400 mm. It evaluated the effect of two key model parameters, the packing fraction (the solid volume fraction at which solid grains are supposed to coalesce and form a connected rigid matrix) and the characteristic grain diameter on the macrosegregation profile. The results were qualitatively consistent with commonly observed trends. The parametric study revealed a large degree of dependence on both the packing fraction and grain diameter. Both parameters are hard to define since the mechanisms of grain coalescence and grain growth in the presence of convection are poorly known. In addition, it has to be noted that the characteristic grain diameter has to represent an actual grain size dis-

tribution and that the packing fraction might not be uniform throughout the two-phase region. This reveals a large source of uncertainty in an otherwise plausible model. Vreeman's DC casting model was again later used by Vreeman, Schloz and Krane [Vreeman *et al.*, 2002]. They compared model predictions to measurements on industrial-scale (450 mm diameter) DC cast billets of an Al–6 wt%Cu alloy trying to determine the value of the packing fraction. While finding some agreement between the experimental and model results they restated the problem concerning the uniform grain diameter and packing fraction used in the model.

Jalanti [Jalanti, 2000, Jalanti *et al.*, 2001] studied macrosegregation in small (5 cm thick) and industrial-size (27.5 cm thick) Al-Mg ingots. Studying the effects of thermal and solutal buoyancy and shrinkage flow, he contended that the effect of shrinkage dominates and should be responsible for the almost whole macrosegregation effect in both small- and industrial-size ingots; for the latter the results were compared to the EMPACT measurements [Joly *et al.*, 2000], showing good agreement. These conclusions should be treated with some caution. In one case they were based on results obtained for small geometries, where the flow induced by thermosolutal convection is relatively weak and thus cannot penetrate the mushy zone and can indeed be outweighed by the shrinkage-induced flow. In the industrial-size case, the flow was modeled using a viscosity increased by a factor of 100 (trying to mimic turbulent flow) which importantly changes the fundamental flow characteristics (recall the discussion of natural convection in Section 1.2.2).

Very recently Du, Eskin and Katgerman [Du *et al.*, 2006] again investigated the effects of buoyancy forces and shrinkage on macrosegregation in a 200 mm Al-4.5 wt%Cu billet, using a porous-mush model. Their results suggest that both the thermal and solutal components of the natural convection flow have a significant impact on the segregation profile, but the effect of shrinkage flow competes with it and decisively alters the segregation in the billet center (producing the negative segregation) and close to the surface (inverse segregation in the subsurface region).

Gruber-Pretzler et al. [Gruber-Pretzler *et al.*, 2006] made a very systematic investigation of the impacts of feeding flow, thermal and solutal convection, and shrinkage flow as well as of mushy zone permeability on macrosegregation in a DC cast bronze (Cu–6 wt%Sn) billet, studying each effect separately and in combination. Their results indicate that the shrinkage flow decisively determines the macrosegregation pattern at low permeabilities of the mush, when the convection flow cannot significantly penetrate the mushy zone; whereas at higher permeabilities it is combined in a more complex manner with forced and natural convection flows.

2.2.3 Summary

The mechanisms of the formation of macrosegregation in DC cast ingots and billets have been investigated for many years but a full understanding is still lacking. Due to the complexity of the phenomena involved, a merely experimental approach cannot provide sufficient clarity. Recent efforts at complementing experimentation with numerical model studies [Vreeman *et al.*, 2002, Jalanti, 2000, Eskin *et al.*, 2004, Suyitno *et al.*, 2004, Eskin *et al.*, 2005] seem the most promising. Since the physical mechanisms involved in the species transport are difficult to model and are coupled in a complex way, the final objective has still not been achieved. The most prominent macrosegregation patterns in commercial ingots are the positive subsurface segregation, the negative centerline segregation and smaller, sometimes alternating, deviations in between. While it is agreed that the former is well explained by the inverse segregation caused by shrinkage flow, the mechanisms of the formation of other patterns are still a source of much controversy. The transport of free-floating coarse grains is widely accepted to be an important effect, especially in the formation of the negative centerline segregation. The reviewed studies also indicate that shrinkage flow, thermosolutal convection, mush permeability, and feeding flow do play an important role and can interact in a complex way. Assuming the correctness of all the reviewed studies, we can also conclude that a general explanation of the importance of the different macrosegregation formation mechanisms in DC castings is unlikely and may strongly depend on the casting size, geometry, composition, structure, casting parameters, and melt feeding system.

2.3 Flow in Liquid Metals

Thermal natural convection flow in low-Prandtl-number[1] fluids (as are liquid metals) is prone to instability, as was explained in the Introduction. Experimental investigations are difficult since a visualization of the flow is impossible in opaque metals. In numerical studies the physical complexity is complemented with high requirements on the accuracy and stability of numerical methods to obtain accurate solutions of the governing equations. These may be the reasons that not many studies exist and their results are not easily interpreted. Some information and basic ideas about the flow structures can be extracted from the early numerical work on natural convection in low-Pr fluids by Mohamad and Viskanta [Mohamad and Viskanta, 1991] and

[1] Refer to Section 6.3.1 for the definitions and explanation of dimensionless parameters Pr, Sc, Ra_T and Ra_C.

later by Cless and Prescott [Cless and Prescott, 1996a, Cless and Prescott, 1996b]. These works study natural convection in differentially heated enclosures mostly at relatively low Rayleigh numbers (with one exception of $Ra = 10^5$ in [Mohamad and Viskanta, 1991]) and very low Prandtl numbers (down to $Pr = 10^{-3}$) and they also put a lot of emphasis on the impact of numerical methods on the results. Kamakura and Ozoe [Kamakura and Ozoe, 1996] later moved to higher Rayleigh numbers (up to $Ra = 10^6$ at $Pr = 10^{-2}$) and observed oscillatory and rotating multicellular flow structures.

Thermosolutal natural convection in the range of Pr and Sc found in liquid metal alloys ($Pr \sim 10^{-2}$, $Sc \sim 10^2$) is not well explored. Numerical investigations are scarce, in fact the only published numerical studies are those of Hyun, Bergman and coworkers [Hyun *et al.*, 1995, Bergman and Hyun, 1996] and Shyy and Chen [Shyy and Chen, 1991]. While Hyun and coworkers worked with liquid Al-Cu and Pb-Sn alloys, i.e. relevant Pr and Sc, their studies are limited to low Rayleigh numbers of only up to $Ra_T = 5000$. The study of Shyy and Chen, on the other hand, reaches the interesting range of Rayleigh numbers $Ra_T \sim 2{\cdot}10^6$, however it keeps a relatively low Schmidt ($Sc \sim 10$) and a relatively high Prandtl number ($Pr \sim 10^{-1}$ in most cases). In summary, there is no known investigation of thermosolutal flow in the parameter range relevant for solidification during casting.

Our understanding of thermosolutal flow in high-Pr fluids is much more profound. The work by Bennacer and Gobin [Bennacer and Gobin, 1996, Gobin and Bennacer, 1996] investigates a range of parameters and studies the effect on the flow structure and heat and mass transfer. It explains the mechanism of thermal destabilization of solutally stratified layers and the generation of multicellular thermosolutal flow structures. These studies can be used as a basis for studying thermosolutal convection in low-Pr fluids, although we have to keep in mind the fundamentally different relations in thermal convection.

2.4 Numerical Modeling Issues

The principal issues related to numerical solution methods, which require special attention in DC casting simulation are

- Accurate solution of the thermosolutal flow in the bulk liquid region.
- Resolution at the liquid-mush interface.

The numerical simulation of natural convection in metals (low-Pr fluids) is challenging due to the high requirements of numerical methods. These emanate primarily from the predominance of advective over viscous momentum

transport. The consequences are high local velocity gradients and thus potential numerical instability. In addition, the physical instability of the flow can create unsteady flows, requiring relatively fine time discretization for a proper resolution of the flow structure and its temporal evolution. All this was already shown in the early work on thermal natural convection in liquid metals by Mohamad and Viskanta [Mohamad and Viskanta, 1991] and Cless and Prescott [Cless and Prescott, 1996a, Cless and Prescott, 1996b]. They found the simulation results to be very sensitive to the accuracy of the space (advection) and time discretization schemes employed, even affecting the prediction of the qualitative flow structure (multicellular flow) and oscillatory flow. Although these findings are not very recent it sometimes seems that, in the context of casting simulations, they cannot be overemphasized even today. The problem is accentuated by the lack of reference benchmark solutions in the pertinent physical parameter range of natural convection. Some recent activity on this topic [Bertrand *et al.*, 1999, Hannoun *et al.*, 2003] seems set to raise awareness of the problems and hopefully boost the development of a wider spectrum of relevant benchmark solutions. In their development as well as in "standalone" testing of specific codes and solutions, stringent verification and estimation of discretization errors is required using well developed verification techniques and concepts [Roache, 1998b, Roy, 2005, Oberkampf *et al.*, 2003].

The most critical regions in any simulation are those with steep slopes and fast changes of gradients. In solidification problems these typically occur in the solidification region. At the transition from the fully liquid melt to the mushy zone the velocities and concentrations experience fast changes. In simulations of DC casting a common [Reddy and Beckermann, 1997, Vreeman and Incropera, 2000, Venneker and Katgerman, 2002, Vreeman *et al.*, 2002] and characteristic problem is an oscillatory concentration profile in regions where the transitions of liquid-fraction are fast, i.e. close to the surface. This numerical effect was explained by Venneker et al. [Venneker and Katgerman, 2000, Venneker, 2001]. A remedy was sought through the use of high-resolution discretization schemes [Venneker, 2001], local mesh refinement [Jalanti, 2000, Kaempfer, 2002] or mesh alignment with the liquid-mush interface [Venneker and Katgerman, 2000], and recently both refinement and alignment [Du *et al.*, 2006, Gruber-Pretzler *et al.*, 2006], mostly using commercial CFD software [Jalanti, 2000, Venneker and Katgerman, 2000, Du *et al.*, 2006, Gruber-Pretzler *et al.*, 2006]. Fully automated self-adaptive grid refinement has not yet been applied for macrosegregation simulations in DC casting. Nevertheless, the method developed in a preceding project [Mencinger, 2001] would seem feasible since it combines local grid refinement in a relatively limited region with grid alignment to the steep

gradients of the mushy zone.

3 Objectives

3.1 Purpose of the Research

The purpose of the dissertation is to further develop a solidification model and implement it in a numerical code for the simulation of macrosegregation in the DC casting of aluminum alloys. The code was to be based on a previously existing finite-volume code for the simulation of heat transfer and fluid flow in DC casting [Mencinger, 2002]. The old code assumes a rigid mushy zone and had been extended by a model of species transport and microsegregation [Založnik *et al.*, 2004] by the author. The first step towards further extension of the model had been outlined in [Šarler *et al.*, 2003] by proposing a mixture model which accounts for the motion of free-floating grains. A lack of understanding of the thermosolutal flow in the liquid pool and deficiencies in the numerical approach had been identified in [Založnik *et al.*, 2004].

More precisely, findings from my previous research and the literature review presented in the preceding chapter suggest:

- the need to understand the thermosolutal flow in the liquid pool and its interaction with the solidification zone in the formation of macrosegregation
- the need to extend the current DC casting model with a model which accounts for the transport of solid grains
- the need to estimate and reduce numerical inaccuracies in casting simulations

3.2 Objectives and Methods

The objectives of the research are

- To extend the single-domain mixture model [Bennon and Incropera, 1987, Prescott *et al.*, 1991] of the solidification of binary alloys to accommodate the phenomena of initiation (nucleation) and transport of

free-floating grains. To implement the model in a numerical code for the simulation of DC casting.

- To gain an understanding of flow patterns and heat and mass transfer in thermosolutal natural convection in the liquid pool of DC castings.
- To determine the accuracy of numerical solutions of flow and solute transport relevant for the simulation of macrosegregation in industrial-size DC castings.
- To investigate the influence of the main DC casting parameters on the resulting macrosegregation pattern. Here, the model's predictive capabilities are to be considered.

These objectives were addressed as follows

- The physical model was derived through the volume averaging of local conservation equations. The volume averaged equations, distinct for each phase, were combined to obtain a mixture model. Special considerations had to be adhered to in the derivation of the single-domain mixture momentum equation as the volume-averaged equations turn out to have different forms in the porous and slurry flow regimes in the mushy zone and cannot be easily combined. Further, models of grain initiation on grain refiner particles and grain transport with appropriate solution procedures were included in the model. The model was partly implemented in the DC casting simulation code.
- The flow patterns and heat and mass transfer in thermosolutal natural convection were studied by conducting numerical experiments on simplified cases of thermal, solutal and thermosolutal natural convection at parameter (Pr, Sc, Ra_T, Ra_C) values relevant for the flow in the liquid pool of DC castings.
- The accuracy of the flow resolution in the liquid region of the casting was verified and quantified using systematic convergence studies and error analysis. The verification was performed on prototypal cases of natural convection in enclosures and was proposed as a generalized verification procedure for the (Pr, Sc, Ra_T, Ra_C) parameter range.
- The system behavior was studied through the DC casting simulations. Simulations at varying casting velocity, temperature, and cooling were performed. The impact of these parameters on the flow in the liquid pool and the effect of the flow on macrosegregation were studied. Further, the interaction of natural convection flow and shrinkage flow in

the mushy zone and their impact on macrosegregation were investigated. The effect of the presence of free-floating grains was qualitatively estimated by a parameter study of the implemented simplified grain transport model.

4 Physical Model

Science may be described as the art of systematic over-simplification.

Karl R. Popper

4.1 Introduction

This chapter is dedicated to formulating the physical model and deriving the corresponding governing model equations. The objective is to define a one-phase one-domain model capable of describing binary solidification during DC casting. The model shall account for two distinct flow regimes in the solidification zone of the casting, shown in Fig. 4.1. In the slurry regime the solid is in the form of dispersed grains, which can move with the flow. The flow behaves as a solid-liquid suspension—a slurry. In the porous regime the solid phase is grown into a rigid matrix, moving with the system velocity (e.g. the casting velocity in DC casting). There, the flow is regarded as a one-phase liquid flow through a saturated porous medium. The purpose of this modeling is to properly capture the effect the presence of a slurry zone has on macrosegregation via the transport of solute-lean free-floating grains.

The model is constructed from the continuum description of the transport of mass, momentum, heat and species in the solidifying system and of constitutive laws, which provide additional information on the diffusion transport, stresses, buoyancy forces, interfacial forces, thermodynamical interface conditions, species rejection, interphase heat and species transfer etc. The constitutive laws are needed to provide the information that is needed but not provided by the continuum equations themselves. Mathematically, they are required to close the model.

Several alternative approaches can be used to derive a continuum model of a multiphase flow. The mixture theory [Bennon and Incropera, 1987, Ni and Incropera, 1995a], volume averaging [Drew, 1983, Ganesan and Poirier, 1990, Ni and Beckermann, 1991, Wang and Beckermann, 1993, Wang and Beckermann, 1996a] and ensemble averaging [Furmański, 1992, Banaszek and

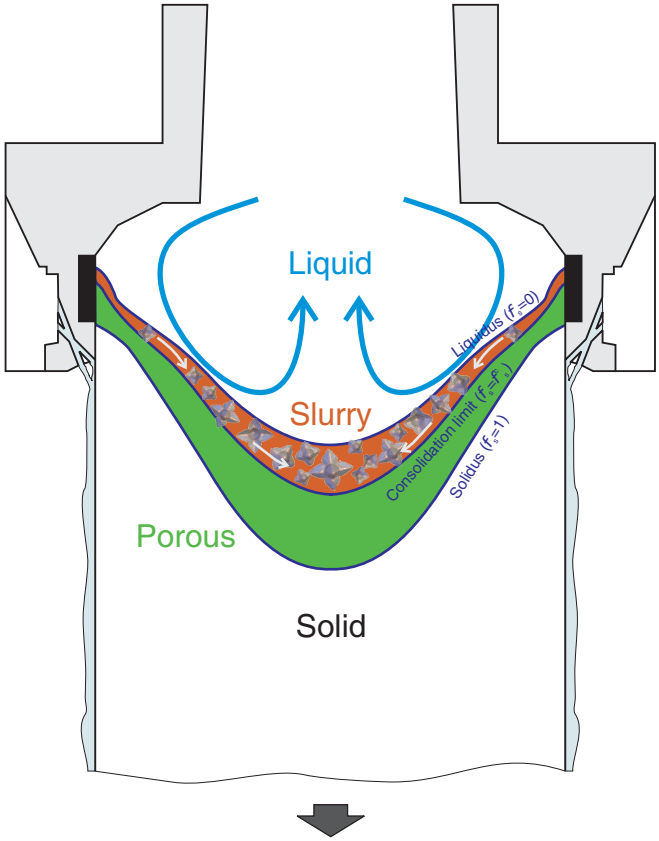

Figure 4.1: Slurry and porous flow regimes in a solidifying DC casting

Furmański, 2005] were all used in the past to define solidification models. In this work the volume-averaging procedure was used because it provides, from the author's viewpoint, a clearer relation between the original local equations and the volume-averaged macroscopic equations. The rigorous procedure also elucidates the phase interactions and the introduction of constitutive models. To derive the continuum transport equations in the two-phase system, the volume-averaging methodology is used for each of the interspersed solid and liquid phases, resulting in a two-phase model. However, the fact that at the start of its development the model implementation was based on the thermal model code developed by Mencinger [Mencinger, 2002] presents "historical" reasons for using a one-phase model. Hence, the objective of this work is to define a one-phase model and so the two-phase model is finally reshaped into a one-phase model, defined in terms of mixture quantities. In the course of this reformulation the interphase balances are taken into account and supplementary phenomenological (constitutive) models are formulated, accounting for the interphase interactions.

The development of the model essentially relates to the previous work by Ni and Beckermann [Ni and Beckermann, 1991] on the derivation of a volume-averaged model of solidification, to the modeling of porous media flows by Whitaker [Whitaker, 1996], and to the modeling of porous media formed by dendritic mushy zones by Goyeau et al. [Goyeau *et al.*, 1997], and Bousquet-Melou et al. [Bousquet-Melou *et al.*, 2002a]. The volume-averaging procedures used in the derivation are explained in Appendix A.

4.2 Local Transport Equations

The local continuum conservation equations for phase mass (continuum equation), heat (energy equation), momentum, and species are valid internally in each phase. They are formulated on a scale that is large enough to accommodate the continuum concept, but is smaller than the scale of the phase structures. Inside each phase these equations are identical with the classical transport equations for one continuous phase, which is modeled as a (pseudo)fluid.

The local continuum, momentum, energy, and species conservation equations, respectively, are

$$\frac{\partial \rho}{\partial t} + \nabla \cdot (\rho \vec{v}) = 0 \tag{4.1}$$

$$\frac{\partial}{\partial t}(\rho \vec{v}) + \nabla \cdot (\rho \vec{v} \vec{v}) = -\nabla p + \nabla \cdot \boldsymbol{\tau} + \vec{b} \tag{4.2}$$

$$\frac{\partial}{\partial t}(\rho h) + \nabla \cdot (\rho \vec{v} h) = \nabla \cdot (k \nabla T) \tag{4.3}$$

$$\frac{\partial}{\partial t}(\rho C) + \nabla \cdot (\rho \vec{v} C) = \nabla \cdot (\rho D \nabla C)\,, \tag{4.4}$$

where ρ is the density, $\vec{v}$ the velocity, p the pressure, $\boldsymbol{\tau}$ the tangential stress tensor, $\vec{b}$ the body force, h the specific enthalpy, k the thermal conductivity, T the temperature, C the concentration (mass fraction of solute), and D the diffusion coefficient.

The local heat and mass diffusion fluxes in both phases are modeled using the Fourier and Fick laws, respectively. The tangential stress tensor $\boldsymbol{\tau}$ requires different approaches for the solid and liquid phases and therefore remains in general notation here. All other assumptions about the constitutive laws are left to be taken and justified during the course of derivation.

4.3 Derivation of Volume-Averaged Macroscopic Conservation Equations (Two-phase Model)

In this section the volume-averaging procedure, explained in detail in Appendix A, is performed on all governing local continuum equations to obtain separate volume-averaged conservation equations for each phase, i.e. a two-phase model. Supplementary constitutive models are introduced and, where possible, the resulting governing equations are simplified based on an estimation of the scale relationships between different equation terms. Two separate momentum equations are developed to account for the two different flow regimes in the mushy zone, the slurry and porous regimes. The flow in the bulk liquid (Navier-Stokes flow) and the motion of the bulk solid (uniform casting velocity) are shown to be described by the slurry and porous regime equations, respectively. The slurry-regime momentum equation reduces to the Navier-Stokes equation at a zero solid fraction and the porous-regime equation reduces to $\vec{v} = \vec{v}_{\text{cast}}$ at a solid fraction of unity. In this sense, the four distinct flow regimes (liquid, slurry, porous and solid) are reduced to two (slurry and porous). The other transport equations remain identical for both regimes. Special care is taken with the two-phase equations, especially with the momentum equations, to develop them in a form best adaptable to the objective of combining them into a one-phase one-domain model, which is done in Section 4.4.

4.3.1 Mass Conservation

The local continuity equation is constrained to phase k using the phase function X_{k}.

$$X_{\text{k}}(\vec{x},t) = \begin{cases} 1 & \text{where } \vec{x} \text{ is in phase } k \text{ at time } t \\ 0 & \text{elsewhere} \end{cases} \tag{A.9}$$

$$X_{\text{k}}\frac{\partial \rho}{\partial t} + X_{\text{k}}\nabla\cdot(\rho\vec{v}) = 0 \tag{4.5}$$

Volume-averaging of the equation is simply performed by using the summation rule of averaging (Eq. (A.4)) and applying the rules of volume-averaging (Appendix A) on each term. $\langle\phi\rangle^{\text{k}}$ denotes the intrinsic average of quantity ϕ in phase k, V_0 is the averaging volume, A_{k} the interface area of phase k, $\vec{w}_{\text{i}}$ the phase interface velocity, $\vec{n}_{\text{k}}$ the normal of the interface pointing into phase k, g_{k} the volume fraction of phase k, $\hat{\phi}$ the local deviation of quantity

ϕ from the average $\langle\phi\rangle^{\mathrm{k}}$, and subscript k generally denotes phase k.

$$\left\langle X_{\mathrm{k}} \frac{\partial \rho}{\partial t} \right\rangle = \frac{\partial}{\partial t}\left(g_{\mathrm{k}} \langle \rho_{\mathrm{k}} \rangle^{\mathrm{k}}\right) + \frac{1}{V_0} \int\limits_{A_{\mathrm{k}}} \rho_{\mathrm{k}}\, \vec{w}_{\mathrm{i}} \cdot \vec{n}_{\mathrm{k}}\, dA \tag{4.6}$$

$$\begin{aligned} \langle X_{\mathrm{k}} \nabla \cdot (\rho \vec{v}) \rangle &= \nabla \cdot \left(g_{\mathrm{k}} \langle \rho_{\mathrm{k}} \vec{v}_{\mathrm{k}} \rangle^{\mathrm{k}}\right) - \frac{1}{V_0} \int\limits_{A_{\mathrm{k}}} \rho_{\mathrm{k}}\, \vec{v}_{\mathrm{k}} \cdot \vec{n}_{\mathrm{k}}\, dA \\ &= \nabla \cdot \left(g_{\mathrm{k}} \langle \rho_{\mathrm{k}} \rangle^{\mathrm{k}} \langle \vec{v}_{\mathrm{k}} \rangle^{\mathrm{k}}\right) + \nabla \cdot \left(g_{\mathrm{k}} \left\langle \hat{\rho}_{\mathrm{k}} \hat{\vec{v}}_{\mathrm{k}} \right\rangle^{\mathrm{k}}\right) \\ &\quad - \frac{1}{V_0} \int\limits_{A_{\mathrm{k}}} \rho_{\mathrm{k}}\, \vec{v}_{\mathrm{k}} \cdot \vec{n}_{\mathrm{k}}\, dA \end{aligned} \tag{4.7}$$

Generally, it can be assumed that the contribution of the density fluctuations on the averaged product of density and any quantity is small,

$$\langle \hat{\rho}_{\mathrm{k}} \phi_{\mathrm{k}} \rangle \approx 0 \qquad \left\langle \hat{\rho}_{\mathrm{k}} \hat{\phi}_{\mathrm{k}} \right\rangle \approx 0, \tag{4.8}$$

and thus the respective term in Eq. (4.7) is dropped. The last terms in Eqs. (4.6) and (4.7) can be combined to give

$$-\frac{1}{V_0} \int\limits_{A_{\mathrm{k}}} \rho_{\mathrm{k}} (\vec{v}_{\mathrm{k}} - \vec{w}_{\mathrm{i}}) \cdot \vec{n}_{\mathrm{k}}\, dA = -\Gamma_{\mathrm{ik}}, \tag{4.9}$$

where Γ_{ik} is the mass flux of phase k across the phase interface due to a difference in velocities of the interface and the phase at the interface. In solidification this is the mass flux due to the phase change.

The volume-averaged continuity equation for phase k is thus

$$\frac{\partial}{\partial t}\left(g_{\mathrm{k}} \langle \rho_{\mathrm{k}} \rangle^{\mathrm{k}}\right) + \nabla \cdot \left(g_{\mathrm{k}} \langle \rho_{\mathrm{k}} \rangle^{\mathrm{k}} \langle \vec{v}_{\mathrm{k}} \rangle^{\mathrm{k}}\right) = \Gamma_{\mathrm{ik}} \tag{4.10}$$

$$\Gamma_{\mathrm{ik}} = \frac{1}{V_0} \int\limits_{A_{\mathrm{k}}} \left(\rho_{\mathrm{k}} (\vec{v}_{\mathrm{k}} - \vec{w}_{\mathrm{i}}) \cdot \vec{n}_{\mathrm{k}}\right)\, dA.$$

4.3.2 Momentum Conservation

As already mentioned in the introduction, two flow regimes are modeled, the slurry and the porous regime. The volume-averaged momentum equation developed in this section is in a general form that is valid for both regimes and all phases. Specific constitutive laws for the two regimes are then introduced in the following Section 4.3.3.

The local momentum equation for phase k is written using the phase function X_k.

$$X_\mathrm{k}\frac{\partial}{\partial t}(\rho\vec{v}) + X_\mathrm{k}\nabla\cdot(\rho\vec{v}\vec{v}) = -X_\mathrm{k}\nabla p + X_\mathrm{k}\nabla\cdot\boldsymbol{\tau} + X_\mathrm{k}\vec{b} \tag{4.11}$$

The unsteady term is averaged as

$$\begin{aligned}
\left\langle X_\mathrm{k}\frac{\partial}{\partial t}(\rho\vec{v})\right\rangle &= \frac{\partial}{\partial t}\left(g_\mathrm{k}\left\langle\rho_\mathrm{k}\vec{v}_\mathrm{k}\right\rangle^\mathrm{k}\right) + \frac{1}{V_0}\int\limits_{A_\mathrm{k}}\rho_\mathrm{k}\vec{v}_\mathrm{k}\vec{w}_\mathrm{i}\cdot\vec{n}_\mathrm{k}\,dA \\
&= \frac{\partial}{\partial t}\left(g_\mathrm{k}\left\langle\rho\right\rangle_\mathrm{k}^\mathrm{k}\left\langle\vec{v}\right\rangle_\mathrm{k}^\mathrm{k}\right) + \frac{\partial}{\partial t}\left(g_\mathrm{k}\cancelto{\approx\,0\,\text{(Eq. (4.8))}}{\left\langle\hat{\rho}_\mathrm{k}\hat{\vec{v}}_\mathrm{k}\right\rangle^\mathrm{k}}\right) \\
&\quad + \frac{1}{V_0}\int\limits_{A_\mathrm{k}}\rho_\mathrm{k}\vec{v}_\mathrm{k}\vec{w}_\mathrm{i}\cdot\vec{n}_\mathrm{k}\,dA \\
&= \frac{\partial}{\partial t}\left(g_\mathrm{k}\left\langle\rho_\mathrm{k}\right\rangle^\mathrm{k}\left\langle\vec{v}_\mathrm{k}\right\rangle^\mathrm{k}\right) + \frac{1}{V_0}\int\limits_{A_\mathrm{k}}\rho_\mathrm{k}\vec{v}_\mathrm{k}\vec{w}_\mathrm{i}\cdot\vec{n}_\mathrm{k}\,dA.
\end{aligned} \tag{4.12}$$

The advective term is averaged as

$$\begin{aligned}
\left\langle X_\mathrm{k}\nabla\cdot(\rho\vec{v}\vec{v})\right\rangle &= \nabla\cdot\left(g_\mathrm{k}\left\langle\rho_\mathrm{k}\vec{v}_\mathrm{k}\vec{v}_\mathrm{k}\right\rangle^\mathrm{k}\right) - \frac{1}{V_0}\int\limits_{A_\mathrm{k}}\rho_\mathrm{k}\vec{v}_\mathrm{k}\vec{v}_\mathrm{k}\cdot\vec{n}_\mathrm{k}\,dA \\
&= \nabla\cdot\left(g_\mathrm{k}\left\langle\left\langle\rho_\mathrm{k}\right\rangle^\mathrm{k}\left\langle\vec{v}_\mathrm{k}\vec{v}_\mathrm{k}\right\rangle^\mathrm{k} + \hat{\rho}_\mathrm{k}\widehat{\vec{v}_\mathrm{k}\vec{v}_\mathrm{k}}\right\rangle^\mathrm{k}\right) \\
&\quad - \frac{1}{V_0}\int\limits_{A_\mathrm{k}}\rho_\mathrm{k}\vec{v}_\mathrm{k}\vec{v}_\mathrm{k}\cdot\vec{n}_\mathrm{k}\,dA \\
&= \nabla\cdot\left(g_\mathrm{k}\left\langle\rho_\mathrm{k}\right\rangle^\mathrm{k}\left\langle\vec{v}_\mathrm{k}\right\rangle^\mathrm{k}\left\langle\vec{v}_\mathrm{k}\right\rangle^\mathrm{k}\right) + \nabla\cdot\left(g_\mathrm{k}\left\langle\rho_\mathrm{k}\right\rangle^\mathrm{k}\left\langle\hat{\vec{v}}_\mathrm{k}\hat{\vec{v}}_\mathrm{k}\right\rangle^\mathrm{k}\right) \\
&\quad + \nabla\cdot\left(g_\mathrm{k}\cancelto{\approx\,0\,\text{(Eq. (4.8))}}{\left\langle\hat{\rho}_\mathrm{k}\widehat{\vec{v}_\mathrm{k}\vec{v}_\mathrm{k}}\right\rangle^\mathrm{k}}\right) - \frac{1}{V_0}\int\limits_{A_\mathrm{k}}\rho_\mathrm{k}\vec{v}_\mathrm{k}\vec{v}_\mathrm{k}\cdot\vec{n}_\mathrm{k}\,dA \\
&= \nabla\cdot\left(g_\mathrm{k}\left\langle\rho_\mathrm{k}\right\rangle^\mathrm{k}\left\langle\vec{v}_\mathrm{k}\right\rangle^\mathrm{k}\left\langle\vec{v}_\mathrm{k}\right\rangle^\mathrm{k}\right) + \nabla\cdot\left(g_\mathrm{k}\left\langle\rho_\mathrm{k}\right\rangle^\mathrm{k}\left\langle\hat{\vec{v}}_\mathrm{k}\hat{\vec{v}}_\mathrm{k}\right\rangle^\mathrm{k}\right) \\
&\quad - \frac{1}{V_0}\int\limits_{A_\mathrm{k}}\rho_\mathrm{k}\vec{v}_\mathrm{k}\vec{v}_\mathrm{k}\cdot\vec{n}_\mathrm{k}\,dA.
\end{aligned} \tag{4.13}$$

The pressure term is averaged as

$$-\left\langle X_{\mathrm{k}} \nabla p \right\rangle = -\nabla \left(g_{\mathrm{k}} \left\langle p_{\mathrm{k}} \right\rangle^{\mathrm{k}} \right) + \frac{1}{V_0} \int\limits_{A_{\mathrm{k}}} p_{\mathrm{k}} \vec{n}_{\mathrm{k}} \, dA. \tag{4.14}$$

The tangential stress term is averaged as

$$\left\langle X_{\mathrm{k}} \nabla \cdot \boldsymbol{\tau} \right\rangle = \nabla \cdot \left(g_{\mathrm{k}} \left\langle \boldsymbol{\tau}_{\mathrm{k}} \right\rangle^{\mathrm{k}} \right) - \frac{1}{V_0} \int\limits_{A_{\mathrm{k}}} \boldsymbol{\tau}_{\mathrm{k}} \cdot \vec{n}_{\mathrm{k}} \, dA. \tag{4.15}$$

The body force (buoyancy) term is averaged as

$$\left\langle X_{\mathrm{k}} \vec{b} \right\rangle = g_{\mathrm{k}} \left\langle b_{\mathrm{k}} \right\rangle^{\mathrm{k}}. \tag{4.16}$$

The surface integral terms arising in Eqs. (4.12)-(4.15) are interpreted as interphase momentum exchange at the solid-liquid phase interface. The interface terms from Eqs. (4.12) and (4.13) are combined to give the momentum flux across the interface due to the phase change (mass and consequently momentum transfer from one phase to the other).

$$\frac{1}{V_0} \int\limits_{A_{\mathrm{k}}} \rho_{\mathrm{k}} \vec{v}_{\mathrm{k}} \vec{w}_{\mathrm{i}} \cdot \vec{n}_{\mathrm{k}} \, dA - \frac{1}{V_0} \int\limits_{A_{\mathrm{k}}} \rho_{\mathrm{k}} \vec{v}_{\mathrm{k}} \vec{v}_{\mathrm{k}} \cdot \vec{n}_{\mathrm{k}} \, dA = \frac{1}{V_0} \int\limits_{A_{\mathrm{k}}} \rho_{\mathrm{k}} \vec{v}_{\mathrm{k}} (\vec{w}_{\mathrm{i}} - \vec{v}_{\mathrm{k}}) \cdot \vec{n}_{\mathrm{k}} \, dA = \vec{M}_{\mathrm{k}}^{\Gamma} \tag{4.17}$$

The interphase momentum transfer due to interfacial stress $\vec{M}_{\mathrm{k}}^{\tau}$ is described by the interfacial terms in Eqs. (4.14) and (4.15), the interfacial pressure force $\vec{M}_{\mathrm{k}}^{\mathrm{p}}$

$$\frac{1}{V_0} \int\limits_{A_{\mathrm{k}}} p_{\mathrm{k}} \vec{n}_{\mathrm{k}} \, dA = \vec{M}_{\mathrm{k}}^{\mathrm{p}} \tag{4.18}$$

and the interfacial drag force $\vec{M}_{\mathrm{k}}^{\mathrm{d}}$

$$-\frac{1}{V_0} \int\limits_{A_{\mathrm{k}}} \boldsymbol{\tau}_{\mathrm{k}} \cdot \vec{n}_{\mathrm{k}} \, dA = \vec{M}_{\mathrm{k}}^{\mathrm{d}}. \tag{4.19}$$

$$\frac{1}{V_0} \int\limits_{A_{\mathrm{k}}} p_{\mathrm{k}} \vec{n}_{\mathrm{k}} \, dA - \frac{1}{V_0} \int\limits_{A_{\mathrm{k}}} \boldsymbol{\tau}_{\mathrm{k}} \cdot \vec{n}_{\mathrm{k}} \, dA = \frac{1}{V_0} \int\limits_{A_{\mathrm{k}}} (p_{\mathrm{k}} \cdot \boldsymbol{I} - \boldsymbol{\tau}_{\mathrm{k}}) \cdot \vec{n}_{\mathrm{k}} \, dA = \vec{M}_{\mathrm{k}}^{\mathrm{p}} + \vec{M}_{\mathrm{k}}^{\mathrm{d}} = \vec{M}_{\mathrm{k}}^{\tau} \tag{4.20}$$

The additional dispersion term arising from the averaging of the velocity fluctuations is mathematically the variance of the velocity. The modeling of

the term is omitted for now and shall be discussed later. To compact the notation it is customary to write it as a stress $\boldsymbol{\tau}_{\mathrm{k}}^{\mathrm{t}}$ [Ni and Beckermann, 1991], in analogy with the Reynolds turbulent stress in the modeling of turbulent flow.

$$-\nabla \cdot \left(g_{\mathrm{k}} \left\langle \rho_{\mathrm{k}} \right\rangle^{\mathrm{k}} \left\langle \hat{\vec{v}}_{\mathrm{k}} \hat{\vec{v}}_{\mathrm{k}} \right\rangle^{\mathrm{k}} \right) = \nabla \cdot \left(g_{\mathrm{k}} \left\langle \boldsymbol{\tau}_{\mathrm{k}}^{\mathrm{t}} \right\rangle^{\mathrm{k}} \right) \tag{4.21}$$

The final general volume-averaged momentum equation for phase k is thus

$$\begin{aligned} \frac{\partial}{\partial t} \left(g_{\mathrm{k}} \left\langle \rho_{\mathrm{k}} \right\rangle^{\mathrm{k}} \left\langle \vec{v}_{\mathrm{k}} \right\rangle^{\mathrm{k}} \right) + \nabla \cdot \left(g_{\mathrm{k}} \left\langle \rho_{\mathrm{k}} \right\rangle^{\mathrm{k}} \left\langle \vec{v}_{\mathrm{k}} \right\rangle^{\mathrm{k}} \left\langle \vec{v}_{\mathrm{k}} \right\rangle^{\mathrm{k}} \right) &= -\nabla \left(g_{\mathrm{k}} \left\langle p_{\mathrm{k}} \right\rangle^{\mathrm{k}} \right) \\ + \nabla \cdot \left(g_{\mathrm{k}} \left\langle \boldsymbol{\tau}_{\mathrm{k}} \right\rangle^{\mathrm{k}} \right) + g_{\mathrm{k}} \left\langle \vec{b}_{\mathrm{k}} \right\rangle^{\mathrm{k}} + \vec{M}_{\mathrm{k}}^{\Gamma} + \vec{M}_{\mathrm{k}}^{\tau} + \nabla \cdot \left(g_{\mathrm{k}} \left\langle \boldsymbol{\tau}_{\mathrm{k}}^{\mathrm{t}} \right\rangle^{\mathrm{k}} \right) & \end{aligned} \tag{4.22}$$

$$\vec{M}_{\mathrm{k}}^{\Gamma} = \frac{1}{V_0} \int_{A_{\mathrm{k}}} \rho_{\mathrm{k}} \vec{v}_{\mathrm{k}} (\vec{w}_{\mathrm{i}} - \vec{v}_{\mathrm{k}}) \cdot \vec{n}_{\mathrm{k}} \, dA$$

$$\vec{M}_{\mathrm{k}}^{\tau} = \vec{M}_{\mathrm{k}}^{\mathrm{p}} + \vec{M}_{\mathrm{k}}^{\mathrm{d}} = \frac{1}{V_0} \int_{A_{\mathrm{k}}} (p_{\mathrm{k}} \cdot \boldsymbol{I} - \boldsymbol{\tau}_{\mathrm{k}}) \cdot \vec{n}_{\mathrm{k}} \, dA$$

$$\left\langle \boldsymbol{\tau}_{\mathbf{k}}^{\mathbf{t}} \right\rangle^{\mathrm{k}} = - \left\langle \rho_{\mathrm{k}} \right\rangle^{\mathrm{k}} \left\langle \hat{\vec{v}}_{\mathrm{k}} \hat{\vec{v}}_{\mathrm{k}} \right\rangle^{\mathrm{k}} \approx - \left\langle \rho_{\mathrm{k}} \hat{\vec{v}}_{\mathrm{k}} \hat{\vec{v}}_{\mathrm{k}} \right\rangle^{\mathrm{k}}.$$

4.3.3 Constitutive Models for Momentum Transport

When developing constitutive models for momentum transport we have to distinguish two different flow regimes that have to be described by the final one-phase model. In the slurry regime the solid phase is in the form of dispersed particles. This regime is modeled as a slurry flow. The one-phase model for this regime can be developed by adding the solid and liquid phase equations of the two-phase model. Via a balance of interfacial forces this also eliminates the interfacial momentum transfer terms and thus the need to model them explicitly. The second flow regime is the porous regime, where the solid phase is modeled as a consolidated, rigid porous structure. As will be explained later, it turns out that the most convenient way of developing the one-phase model in the porous regime is to construct it from the liquid phase equation of the two-phase model, using approaches for the introduction of constitutive models known from the modeling of porous media. For these reasons, the constitutive models for the two regimes will be developed separately. The slurry-regime equations of the two-phase model are not explicitly given since the terms describing the interfacial momentum exchange cancel out due to a force balance at the interface. They thus disappear in the one-phase formulation and therefore do not have to be modeled here.

Slurry Regime

In general, normal and tangential stresses are transferred "inside" the dispersed solid phase and stress gradients can exist. The stress state is described by a stress tensor $\boldsymbol{\tau}$.

$$\boldsymbol{\tau} = \begin{pmatrix} \sigma_{xx} & \tau_{xy} & \tau_{xz} \\ \tau_{yx} & \sigma_{yy} & \tau_{yz} \\ \tau_{zx} & \tau_{zy} & \sigma_{zz} \end{pmatrix} \tag{4.23}$$

The average pressure in the solid phase $\langle p_\mathrm{s} \rangle^\mathrm{s}$ can be defined as part of this tensor.

$$\boldsymbol{\tau} = \begin{pmatrix} \sigma_{xx} - \langle p_\mathrm{s} \rangle^\mathrm{s} & \tau_{xy} & \tau_{xz} \\ \tau_{yx} & \sigma_{yy} - \langle p_\mathrm{s} \rangle^\mathrm{s} & \tau_{yz} \\ \tau_{zx} & \tau_{zy} & \sigma_{zz} - \langle p_\mathrm{s} \rangle^\mathrm{s} \end{pmatrix} + \begin{pmatrix} \langle p_\mathrm{s} \rangle^\mathrm{s} & 0 & 0 \\ 0 & \langle p_\mathrm{s} \rangle^\mathrm{s} & 0 \\ 0 & 0 & \langle p_\mathrm{s} \rangle^\mathrm{s} \end{pmatrix} \tag{4.24}$$

The suspended solid particles in the slurry regime can be regarded as a pseudo-fluid (not a fluid, but modeled as a fluid). Normal forces inside the suspended solid phase can be transferred via the pressure $\langle p_s \rangle^\mathrm{s}$ and the normal stresses σ_{ii} via collisions, i.e. with direct contact of the particles. We can assume that the collisions and the related momentum transfer in the direction normal to the direction of the motion of solid particles (the pressure gradient "in" the solid phase) is not important for the motion of the mixture and thus assume $\sigma_{ii} = 0$. Thus the normal stress components are all equal to the pressure in the solid $\langle p \rangle_\mathrm{s}^\mathrm{k}$. In principle, the local pressure inside the solid particles p_s is different from the liquid pressure p_l due to the interface tension σ_i and the interface curvature ζ.

$$p_\mathrm{s} = p_\mathrm{l} + \sigma_\mathrm{i} \zeta \tag{4.25}$$

For simplification a mean curvature $\bar{\zeta}$ is defined; and if in addition the surface tension is assumed to be isotropic and constant ($\sigma_\mathrm{i} = \text{const.}$) the averaged pressure in the solid and liquid phases is related by

$$\langle p \rangle_\mathrm{s}^\mathrm{s} = \langle p \rangle_\mathrm{l}^\mathrm{l} + \langle \sigma_\mathrm{i} \zeta \rangle = \langle p \rangle_\mathrm{l}^\mathrm{l} + \sigma_\mathrm{i} \bar{\zeta}. \tag{4.26}$$

To comply with the common notation a reduced pressure $P = p + \rho_\mathrm{l}^\mathrm{ref} \vec{g} \cdot (\vec{z^\mathrm{ref}} - \vec{z})$ is introduced and we write

$$\langle P \rangle_\mathrm{s}^\mathrm{s} = \langle P \rangle_\mathrm{l}^\mathrm{l} + \sigma_\mathrm{i} \bar{\zeta} \tag{4.27}$$

In the liquid phase on the microscopic scale the general constitutive relation for the viscous stress tensor in a Newtonian fluid is valid

$$\boldsymbol{\tau}_\mathrm{l} = \mu_\mathrm{l} \left(\nabla \vec{v}_\mathrm{l} + (\nabla \vec{v}_\mathrm{l})^T \right) - \frac{2}{3} \mu_\mathrm{l} (\nabla \cdot \vec{v}_\mathrm{l}) \cdot \boldsymbol{I}, \tag{4.28}$$

where μ_l is the dynamic viscosity of liquid and $\boldsymbol{I}$ is the identity tensor. The solid phase could be, as mentioned before and as attempted by other researchers [Ni and Beckermann, 1991, Vreeman *et al.*, 2000, Ludwig and Wu, 2002], modeled as a pseudo-fluid and the tangential stress in the solid due to collisions of the particles could be described as a pseudo-viscous stress. In this case, an expression analogous to Eq. (4.28) would be used for the solid tangential stress. The problem with this approach is that it is not entirely consistent with the usual treatment of solid-liquid suspensions and slurries. Rheological experimental data and constitutional laws are usually given for the effective viscosity of the suspension, i.e. for the mixture of liquid and suspended solid phase [Barnes *et al.*, 1998, Larson, 1998]. A compact review of constitutional laws for the viscosity of slurries is given by Kitanovski et al. [Kitanovski *et al.*, 2005]. Because of this and since a one-phase mixture model is developed here anyway, it is more feasible to retain the mixture formulation of the viscosity and viscous tangential stress in the slurry regime. For a Newtonian slurry the pertinent law is

$$g_\mathrm{s} \left\langle \boldsymbol{\tau}_\mathrm{s} \right\rangle^\mathrm{s} + g_\mathrm{l} \left\langle \boldsymbol{\tau}_\mathrm{l} \right\rangle^\mathrm{l} = \boldsymbol{\tau}_\mathrm{m} = \mu_\mathrm{m} \left(\nabla \vec{v}_\mathrm{m} + (\nabla \vec{v}_\mathrm{m})^T \right) - \frac{2}{3} \mu_\mathrm{m} (\nabla \cdot \vec{v}_\mathrm{m}) \cdot \boldsymbol{I}, \quad (4.29)$$

where subscript m denotes the continuum mixture of solid particles and liquid, μ_m is the dynamic viscosity of the slurry, and $\vec{v}_\mathrm{m}$ is the velocity of the slurry mixture. The viscosity of the slurry depends on the volume fraction of solid according to Thomas' law, which is valid for $g_\mathrm{s} \leq 0.625$ and for particle sizes of $0.1 - 435\,\mu$m [Kitanovski *et al.*, 2005, Dhodapkar *et al.*, 2006].

$$\mu_\mathrm{m} = \mu_\mathrm{l} \left[1 + 2.5 g_\mathrm{s} + 10.05 g_\mathrm{s}^2 + 0.00273 \exp(16.6 g_\mathrm{s}) \right] \quad (4.30)$$

Thomas' law dependence of the mixture viscosity on the solid volume fraction is shown in Fig. 4.2.

The body force term consists of the buoyancy force. The liquid buoyancy force is

$$\left\langle \vec{b}_\mathrm{l} \right\rangle^\mathrm{l} = \vec{g} \rho_\mathrm{l}^\mathrm{ref} \left[1 - \beta_\mathrm{l}^T \left(\langle T_\mathrm{l} \rangle^\mathrm{l} - T^\mathrm{ref} \right) - \beta_\mathrm{l}^C \left(\langle C_\mathrm{l} \rangle^\mathrm{l} - C^\mathrm{ref} \right) \right], \quad (4.31)$$

where $\vec{g}$ is the gravity acceleration, $\rho_\mathrm{l}^\mathrm{ref}$ the reference density of liquid, T^ref and C^ref the reference temperature and concentration, and β_l^T the thermal and β_l^C the solutal expansion coefficients of liquid. The solid buoyancy force is

$$\begin{aligned} \left\langle \vec{b}_\mathrm{s} \right\rangle^\mathrm{s} &= \vec{g} \rho_\mathrm{s}^\mathrm{ref} \left[1 - \beta_\mathrm{s}^T \left(\langle T_\mathrm{s} \rangle^\mathrm{s} - T^\mathrm{ref} \right) - \beta_\mathrm{s}^C \left(\langle C_\mathrm{s} \rangle^\mathrm{s} - C^\mathrm{ref} \right) \right] \quad (4.32) \\ &= \vec{g} \rho_\mathrm{l}^\mathrm{ref} + \vec{g} \left(\rho_\mathrm{s}^\mathrm{ref} - \rho_\mathrm{l}^\mathrm{ref} \right) - \vec{g} \rho_\mathrm{s}^\mathrm{ref} \left[\beta_\mathrm{s}^T \left(\langle T_\mathrm{s} \rangle^\mathrm{s} - T^\mathrm{ref} \right) + \beta_\mathrm{s}^C \left(\langle C_\mathrm{s} \rangle^\mathrm{s} - C^\mathrm{ref} \right) \right], \end{aligned}$$

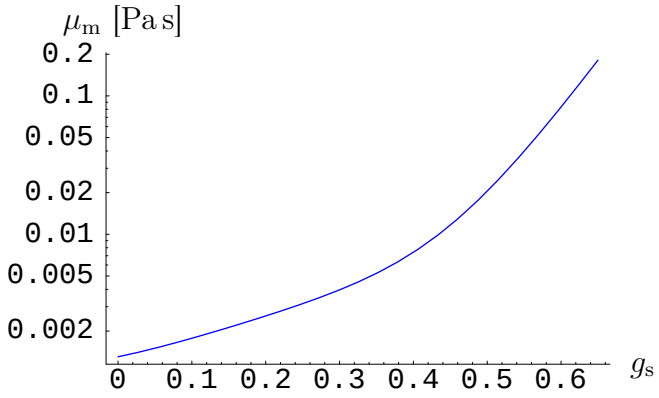

Figure 4.2: Mixture viscosity as a function of solid fraction according to Thomas' law for liquid viscosity of aluminum $\mu_l = 1.3 \cdot 10^{-3}$ Pa s.

where ρ_s^{ref} is the reference density of solid, and β_l^T and β_l^C the thermal and solutal expansion coefficients of solid, respectively. The momentum is transferred between the phases via interfacial forces due to phase change ($\vec{M}_k^\Gamma$), interfacial drag ($\vec{M}_k^d$), and pressure ($\vec{M}_k^p$). The force balance at the solid-liquid interface requires that

$$\vec{M}_s^\Gamma + \vec{M}_l^\Gamma + \vec{M}_s^d + \vec{M}_l^d + \vec{M}_s^p + \vec{M}_l^p + \vec{M}_i = 0 \tag{4.33}$$

where $\vec{M}_i$ is the interfacial momentum source due to surface tension and may be modeled [Ishii, 1975].

$$\vec{M}_i = -\frac{1}{V_0} \int_{A_s} \sigma_i \zeta \vec{n}_s \, dA = -\sigma_i \bar{\zeta} \nabla g_s \,, \tag{4.34}$$

again using the mean interface curvature $\bar{\zeta}$. Thus the interface balance gives

$$\vec{M}_s^\Gamma + \vec{M}_l^\Gamma + \vec{M}_s^d + \vec{M}_l^d + \vec{M}_s^p + \vec{M}_l^p = \sigma_i \bar{\zeta} \nabla g_s \,, \tag{4.35}$$

a result that will be used in the one-phase momentum equation for the slurry regime.

The velocity of the solid phase that will be needed in the final governing equation system can be modeled in different ways, taking into account collisions of particles and other effects. For the initial model a simple approach that was shown by Ni and Incropera [Ni and Incropera, 1995b] is chosen. In their grain-velocity model they assumed that the predominant effect is that of the buoyancy forces and interfacial momentum transfer (drag), and neglected inertia effects, viscous effects and interfacial momentum transfer

due to phase change. By additionally assuming equal pressure in the solid and liquid phases they combined the solid and liquid phase equations and finally obtained an expression for the relative velocity of a solid particle of diameter d_g.

$$\vec{v}_s - \vec{v}_l = \frac{(1 - g_s)(\rho_l - \rho_s) d_g^2 \vec{g}}{18 \mu_m} \tag{4.36}$$

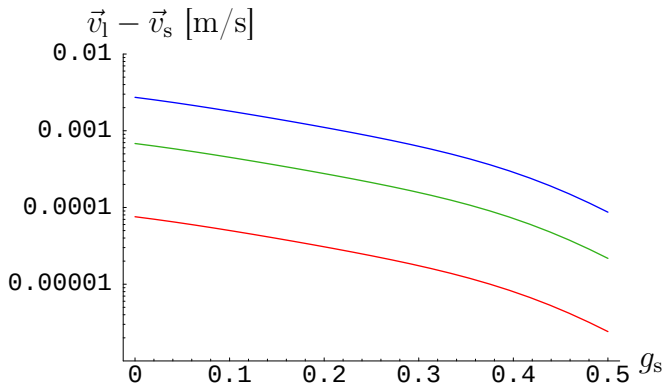

Figure 4.3: Difference of velocities of solid grains and liquid according to Eq. (4.36) for grain diameters of 150 μm, 75 μm, and 25 μm (lines from top to bottom).

The grain size is modeled by a grain growth model that takes into account the onset and growth of grains in aluminum melts in the presence of a grain refiner and is developed in Section 4.4.6.

Porous Regime

in the porous regime the solid phase forms a rigid and connected porous matrix which moves with a specified system velocity $\vec{v}_{syst}$ (casting velocity $\vec{v}_{cast}$ in the case of DC casting). To model the porous flow regime in the solidification region, theoretically the same approach of adding the solid and liquid momentum equations to a one-phase model could be used. In this case, it would not be possible to model stress terms in the solid ($-\nabla(g_s \langle p_s \rangle^s) + \nabla \cdot (g_s \langle \boldsymbol{\tau}_s \rangle^s)$) as a pseudo-fluid. Instead, it would be necessary to use appropriate solid-mechanics models to model the stresses. An alternative is to use only the liquid-phase momentum equation and to model the interfacial forces using principles used in the modeling of porous media [Bousquet-Melou *et al.*, 2002a]. In accordance with the assumption of a rigid solid matrix the solid-phase momentum equation is at the same time simply reduced to

$$\langle \vec{v}_s \rangle^s = \vec{v}_{syst} = \text{const.} \tag{4.37}$$

To obtain the one-phase model equation, the liquid momentum equation is then rearranged and reformulated in terms of the mixture velocity $\vec{v}_\mathrm{m}$.

The pressure term is split into two parts and the reduced pressure $P = p + \rho_\mathrm{l}^\mathrm{ref}\vec{g}\cdot(\vec{z^\mathrm{ref}} - \vec{z})$ is introduced again.

$$-\nabla\left(g_\mathrm{l}\left\langle p_\mathrm{l}\right\rangle^\mathrm{l}\right) = -g_\mathrm{l}\nabla\left\langle P_\mathrm{l}\right\rangle^\mathrm{l} - \nabla g_\mathrm{l}\left\langle P_\mathrm{l}\right\rangle^\mathrm{l} - g_\mathrm{l}\rho_\mathrm{l}^\mathrm{ref}\vec{g} \tag{4.38}$$

The volume-averaged viscous stress term in Equation (4.22) can be expanded using the volume-averaging rules.

$$\begin{aligned}
\nabla\cdot\left(g_\mathrm{l}\left\langle\boldsymbol{\tau}_\mathrm{l}\right\rangle^\mathrm{l}\right) &= \nabla\cdot\left\langle\boldsymbol{\tau}_\mathrm{l}\right\rangle = \nabla\cdot\left\langle X_\mathrm{l}\boldsymbol{\tau}\right\rangle \\
&= \nabla\cdot\Big(\mu_\mathrm{l}\Big[\left\langle\nabla(X_\mathrm{l}\vec{v})\right\rangle + \left\langle\nabla(X_\mathrm{l}\vec{v})^T\right\rangle - \left\langle\vec{v}(\nabla X_\mathrm{l})\right\rangle - \left\langle(\nabla X_\mathrm{l})\vec{v}\right\rangle \\
&\qquad -\frac{2}{3}\boldsymbol{I}\left(\left\langle\nabla\cdot(X_\mathrm{l}\vec{v})\right\rangle - \left\langle\vec{v}\cdot\nabla X_\mathrm{l}\right\rangle\right)\Big]\Big) \\
&= \nabla\cdot\left(\mu_\mathrm{l}\left[\nabla(g_\mathrm{l}\left\langle\vec{v}_\mathrm{l}\right\rangle^\mathrm{l}) + \left[\nabla(g_\mathrm{l}\left\langle\vec{v}_\mathrm{l}\right\rangle^\mathrm{l})\right]^T - \frac{2}{3}\boldsymbol{I}\nabla\cdot(g_\mathrm{l}\left\langle\vec{v}_\mathrm{l}\right\rangle^\mathrm{l})\right]\right) \\
-\nabla\cdot\left(\mu_\mathrm{l}\left[\frac{1}{V_0}\int\limits_{A_\mathrm{l}}\vec{v}_\mathrm{l}\vec{n}_\mathrm{l}\,dA + \frac{1}{V_0}\int\limits_{A_\mathrm{l}}\vec{n}_\mathrm{l}\vec{v}_\mathrm{l}\,dA - \frac{2}{3}\boldsymbol{I}\frac{1}{V_0}\int\limits_{A_\mathrm{l}}\vec{v}_\mathrm{l}\vec{n}_\mathrm{l}\,dA\right]\right)
\end{aligned} \tag{4.39}$$

To develop the interface integrals in the second divergence term in Eq. (4.39) the velocity at the interface is expressed using Gray's decomposition. For position $\vec{r}$ at the interface it is defined $\vec{v}_\mathrm{l}|_{\vec{r}} = \left\langle\vec{v}_\mathrm{l}\right\rangle^\mathrm{l}|_{\vec{r}} + \hat{\vec{v}}_\mathrm{l}|_{\vec{r}}$. Here we are confronted with the problem that the average quantities $\left\langle\vec{v}_\mathrm{l}\right\rangle^\mathrm{l}|_{\vec{r}}$ in the surface integrals are evaluated for an averaging volume centered in $\vec{r}$ instead of $\vec{x}$ like other averaged quantities. This can be overcome using a Taylor series expansion of the quantity around the averaging volume centroid $\vec{x}$ [Goyeau *et al.*, 1997]. Goyeau et al. [Goyeau *et al.*, 1997] showed that the higher order geometrical moments in the integrated Taylor expansion are very small for dendritic structures and can therefore be ignored. This means that

$$\frac{1}{V_0}\int\limits_{A_\mathrm{l}}\left\langle\vec{v}_\mathrm{l}\right\rangle^\mathrm{l}|_{\vec{r}}\,\vec{n}_\mathrm{l}\,dA \approx \left\langle\vec{v}_\mathrm{l}\right\rangle^\mathrm{l}|_{\vec{x}}\left(\frac{1}{V_0}\int\limits_{A_\mathrm{l}}\vec{n}_\mathrm{l}\,dA\right) = \left\langle\vec{v}_\mathrm{l}\right\rangle^\mathrm{l}|_{\vec{x}}\nabla g_\mathrm{l}. \tag{4.40}$$

Thus the interface integral term in Eq. (4.39) is developed to get

$$\frac{1}{V_0}\int\limits_{A_\mathrm{l}} \vec{v}_\mathrm{l}\vec{n}_\mathrm{l}\,dA + \frac{1}{V_0}\int\limits_{A_\mathrm{l}} \vec{n}_\mathrm{l}\vec{v}_\mathrm{l}\,dA - \frac{2}{3}\boldsymbol{I}\frac{1}{V_0}\int\limits_{A_\mathrm{l}} \vec{v}_\mathrm{l}\vec{n}_\mathrm{l}\,dA = \langle\vec{v}_\mathrm{l}\rangle^\mathrm{l}\nabla g_\mathrm{l} + \nabla g_\mathrm{l}\langle\vec{v}_\mathrm{l}\rangle^\mathrm{l} - \frac{2}{3}\boldsymbol{I}\langle\vec{v}_\mathrm{l}\rangle^\mathrm{l}\cdot\nabla g_\mathrm{l} + \frac{1}{V_0}\int\limits_{A_\mathrm{l}}\left[\hat{\vec{v}}_\mathrm{l}\vec{n}_\mathrm{l} + \vec{n}_\mathrm{l}\hat{\vec{v}}_\mathrm{l} - \frac{2}{3}\boldsymbol{I}\left(\hat{\vec{v}}_\mathrm{l}\cdot\vec{n}_\mathrm{l}\right)\right]dA. \quad (4.41)$$

Expression (4.41) is substituted into Eq. (4.39). The whole viscous term is thus

$$\nabla\cdot\left(g_\mathrm{l}\langle\boldsymbol{\tau}_\mathrm{l}\rangle^\mathrm{l}\right) = \nabla\cdot\left(\mu_\mathrm{l}\left[\nabla(g_\mathrm{l}\langle\vec{v}_\mathrm{l}\rangle) + [\nabla(g_\mathrm{l}\langle\vec{v}_\mathrm{l}\rangle)]^T - \frac{2}{3}\boldsymbol{I}\nabla\cdot\left(g_\mathrm{l}\langle\vec{v}_\mathrm{l}\rangle^\mathrm{k}\right)\right]\right) - \nabla\cdot\left(\mu_\mathrm{l}\left[+\langle\vec{v}_\mathrm{l}\rangle^\mathrm{l}\nabla g_\mathrm{l} + \nabla g_\mathrm{l}\langle\vec{v}_\mathrm{l}\rangle^\mathrm{l} - \frac{2}{3}\boldsymbol{I}\langle\vec{v}_\mathrm{l}\rangle^\mathrm{l}\cdot\nabla g_\mathrm{l}\right]\right) - \nabla\cdot\left(\mu_\mathrm{l}\left[\frac{1}{V_0}\int\limits_{A_\mathrm{l}}\left[\hat{\vec{v}}_\mathrm{l}\vec{n}_\mathrm{l} + \vec{n}_\mathrm{l}\hat{\vec{v}}_\mathrm{l} - \frac{2}{3}\boldsymbol{I}\left(\hat{\vec{v}}_\mathrm{l}\cdot\vec{n}_\mathrm{l}\right)\right]dA\right]\right). \quad (4.42)$$

The interfacial tangential stress term is developed.

$$\vec{M}_\mathrm{l}^\mathrm{d} = -\frac{1}{V_0}\int\limits_{A_\mathrm{l}}\boldsymbol{\tau}_\mathrm{l}\cdot\vec{n}_\mathrm{l}\,dA = -\frac{1}{V_0}\int\limits_{A_\mathrm{l}}\left[\mu_\mathrm{l}\left(\nabla\vec{v}_\mathrm{l} + (\nabla\vec{v}_\mathrm{l})^T\right) - \frac{2}{3}\mu_\mathrm{l}(\nabla\cdot\vec{v}_\mathrm{l})\cdot\boldsymbol{I}\right]\cdot\vec{n}_\mathrm{l}\,dA \quad (4.43)$$

Using Gray's decomposition and a Taylor expansion for the interfacial velocities, as before, and again employing the justified approximation in Eq. (4.40) after some manipulation we obtain

$$\vec{M}_\mathrm{l}^\mathrm{d} = -\mu_\mathrm{l}\left[\nabla\langle\vec{v}_\mathrm{l}\rangle^\mathrm{l}\cdot\nabla g_\mathrm{l} + \nabla g_\mathrm{l}\cdot\nabla\langle\vec{v}_\mathrm{l}\rangle^\mathrm{l} - \frac{2}{3}(\nabla\cdot\langle\vec{v}_\mathrm{l}\rangle^\mathrm{l})\nabla g_\mathrm{l}\right] - \mu_\mathrm{l}\frac{1}{V_0}\int\limits_{A_\mathrm{l}}\left[\nabla\hat{\vec{v}}_\mathrm{l}\cdot\vec{n}_\mathrm{l} + \vec{n}_\mathrm{l}\cdot\nabla\hat{\vec{v}}_\mathrm{l} - \frac{2}{3}\boldsymbol{I}(\nabla\cdot\hat{\vec{v}}_\mathrm{l})\cdot\vec{n}_\mathrm{l}\right]dA. \quad (4.44)$$

Adding the bulk and interfacial viscous stress terms (Eqs. (4.42) and (4.44))

after some arithmetical manipulation we obtain

$$\begin{aligned}\nabla \cdot (g_\mathrm{l} \langle \boldsymbol{\tau}_\mathrm{l} \rangle^\mathrm{l}) + \vec{M}_\mathrm{l}^\mathrm{d} = g_\mathrm{l}\mu_\mathrm{l} &\left[\nabla^2 \langle \vec{v}_\mathrm{l} \rangle^\mathrm{l} + \frac{1}{3} \nabla (\nabla \cdot \langle \vec{v}_\mathrm{l} \rangle^\mathrm{l}) \right] \\ &+ g_\mathrm{l} \left[\left(\nabla \langle \vec{v}_\mathrm{l} \rangle^\mathrm{l} + (\nabla \langle \vec{v}_\mathrm{l} \rangle^\mathrm{l})^T \right) - \frac{2}{3} \mu_\mathrm{l} (\nabla \cdot \langle \vec{v}_\mathrm{l} \rangle^\mathrm{l}) \cdot \boldsymbol{I} \right] \cdot (\nabla \mu_\mathrm{l}) \\ &- \nabla \cdot \left(\mu_\mathrm{l} \left[\frac{1}{V_0} \int\limits_{A_\mathrm{l}} \left[\hat{\vec{v}}_\mathrm{l} \vec{n}_\mathrm{l} + \vec{n}_\mathrm{l} \hat{\vec{v}}_\mathrm{l} - \frac{2}{3} \boldsymbol{I} \left(\hat{\vec{v}}_\mathrm{l} \cdot \vec{n}_\mathrm{l} \right) \right] dA \right] \right) \\ &- \mu_\mathrm{l} \frac{1}{V_0} \int\limits_{A_\mathrm{l}} \left[\nabla \hat{\vec{v}}_\mathrm{l} \cdot \vec{n}_\mathrm{l} + \vec{n}_\mathrm{l} \cdot \nabla \hat{\vec{v}}_\mathrm{l} - \frac{2}{3} \boldsymbol{I} (\nabla \cdot \hat{\vec{v}}_\mathrm{l}) \cdot \vec{n}_\mathrm{l} \right] dA. \end{aligned} \tag{4.45}$$

The interfacial pressure term for the liquid phase is

$$\vec{M}_\mathrm{l}^\mathrm{p} = \frac{1}{V_0} \int\limits_{A_\mathrm{l}} P_\mathrm{l} \boldsymbol{I} \cdot \vec{n}_\mathrm{l} \, dA. \tag{4.46}$$

Applying Gray's decomposition, a Taylor expansion of the average interfacial pressure, and again employing the approximation of Eq. (4.40) we obtain

$$\vec{M}_\mathrm{l}^\mathrm{p} = \frac{1}{V_0} \int\limits_{A_\mathrm{l}} \langle P_\mathrm{l} \rangle^\mathrm{l} \boldsymbol{I} \cdot \vec{n}_\mathrm{l} \, dA + \frac{1}{V_0} \int\limits_{A_\mathrm{l}} \hat{P}_\mathrm{l} \boldsymbol{I} \cdot \vec{n}_\mathrm{l} \, dA = \langle P_\mathrm{l} \rangle^\mathrm{l} \nabla g_\mathrm{l} + \frac{1}{V_0} \int\limits_{A_\mathrm{l}} \hat{P}_\mathrm{l} \boldsymbol{I} \cdot \vec{n}_\mathrm{l} \, dA. \tag{4.47}$$

The liquid buoyancy force was given in equation (4.31).

$$\left\langle \vec{b}_\mathrm{l} \right\rangle^\mathrm{l} = \vec{g} \rho_\mathrm{l}^\mathrm{ref} \left[1 - \beta_\mathrm{l}^T \left(\langle T_\mathrm{l} \rangle^\mathrm{l} - T^\mathrm{ref} \right) - \beta_\mathrm{l}^C \left(\langle C_\mathrm{l} \rangle^\mathrm{l} - C^\mathrm{ref} \right) \right] \tag{4.31}$$

The interfacial force originating in the mass transfer due to the phase change is

$$\vec{M}_\mathrm{l}^\Gamma = \frac{1}{V_0} \int\limits_{A_\mathrm{l}} \rho_\mathrm{l} \vec{v}_\mathrm{l} (\vec{w}_\mathrm{i} - \vec{v}_\mathrm{l}) \cdot \vec{n}_\mathrm{l} \, dA. \tag{4.48}$$

The expressions developed for the individual terms of the momentum conservation equation, Eqs. (4.31), (4.38), (4.45), (4.47), and (4.48) are now substituted into the liquid phase momentum equation (4.22) (for $\mathrm{k} \equiv \mathrm{l}$).

$$
\begin{aligned}
\frac{\partial}{\partial t}\left(g_\mathrm{l}\left\langle\rho_\mathrm{l}\right\rangle^\mathrm{l}\left\langle\vec{v}_\mathrm{l}\right\rangle^\mathrm{l}\right)+\nabla\cdot\left(g_\mathrm{l}\left\langle\rho_\mathrm{l}\right\rangle^\mathrm{l}\left\langle\vec{v}_\mathrm{l}\right\rangle^\mathrm{l}\left\langle\vec{v}_\mathrm{l}\right\rangle^\mathrm{l}\right) &= -g_\mathrm{l}\nabla\left\langle P_\mathrm{l}\right\rangle^\mathrm{l}-\cancel{g_\mathrm{l}\rho_\mathrm{l}^\mathrm{ref}\vec{g}}\\
&\quad-\cancel{\left\langle P_\mathrm{l}\right\rangle^\mathrm{l}\nabla g_\mathrm{l}}+g_\mathrm{l}\mu_\mathrm{l}\left[\nabla^2\left\langle\vec{v}_\mathrm{l}\right\rangle^\mathrm{l}+\frac{1}{3}\nabla(\nabla\cdot\left\langle\vec{v}_\mathrm{l}\right\rangle^\mathrm{l})\right]\\
&\quad+g_\mathrm{l}\left[\left(\nabla\left\langle\vec{v}_\mathrm{l}\right\rangle^\mathrm{l}+(\nabla\left\langle\vec{v}_\mathrm{l}\right\rangle^\mathrm{l})^T\right)-\frac{2}{3}(\nabla\cdot\left\langle\vec{v}_\mathrm{l}\right\rangle^\mathrm{l})\cdot\boldsymbol{I}\right]\cdot(\nabla\mu_\mathrm{l})\\
&\quad+g_\mathrm{l}\rho_\mathrm{l}^\mathrm{ref}\vec{g}\left[\cancel{1}-\beta_\mathrm{l}^T\left(\left\langle T_\mathrm{l}\right\rangle^\mathrm{l}-T^\mathrm{ref}\right)-\beta_\mathrm{l}^C\left(\left\langle C_\mathrm{l}\right\rangle^\mathrm{l}-C^\mathrm{ref}\right)\right]+\cancel{\left\langle P_\mathrm{l}\right\rangle^\mathrm{l}\nabla g_\mathrm{l}}\\
&\quad+\frac{1}{V_0}\int\limits_{A_\mathrm{l}}\hat{P}_\mathrm{l}\boldsymbol{I}\cdot\vec{n}_\mathrm{l}\,dA-\nabla\cdot\left(\mu_\mathrm{l}\frac{1}{V_0}\int\limits_{A_\mathrm{l}}\left[\hat{\vec{v}}_\mathrm{l}\vec{n}_\mathrm{l}+\vec{n}_\mathrm{l}\hat{\vec{v}}_\mathrm{l}-\frac{2}{3}\boldsymbol{I}\left(\hat{\vec{v}}_\mathrm{l}\cdot\vec{n}_\mathrm{l}\right)\right]\,dA\right)\\
&\quad-\mu_\mathrm{l}\frac{1}{V_0}\int\limits_{A_\mathrm{l}}\left[\nabla\hat{\vec{v}}_\mathrm{l}\cdot\vec{n}_\mathrm{l}+\vec{n}_\mathrm{l}\cdot\nabla\hat{\vec{v}}_\mathrm{l}-\frac{2}{3}\boldsymbol{I}(\nabla\cdot\hat{\vec{v}}_\mathrm{l})\cdot\vec{n}_\mathrm{l}\right]\,dA\\
&\quad+\frac{1}{V_0}\int\limits_{A_\mathrm{l}}\rho_\mathrm{l}\vec{v}_\mathrm{l}(\vec{w}_\mathrm{i}-\vec{v}_\mathrm{l})\cdot\vec{n}_\mathrm{l}\,dA-\nabla\cdot\left(g_\mathrm{l}\left\langle\rho_\mathrm{l}\right\rangle^\mathrm{l}\left\langle\hat{\vec{v}}_\mathrm{l}\hat{\vec{v}}_\mathrm{l}\right\rangle^\mathrm{l}\right)
\end{aligned}
\tag{4.49}
$$

The above equation is the general volume-averaged momentum equation for the solidifying liquid phase in the porous regime, subject only to the marginal assumption (4.8) and the assumption of negligible local variations of viscosity. In the above equation the surface integral terms involving deviations of velocities and velocity gradients at the interface are left to be determined. In derivations of porous media flow models this was done by the definition of an appropriate closure problem [Whitaker, 1986, Whitaker, 1996, Goyeau *et al.*, 1997, Bousquet-Melou *et al.*, 2002a]. The solution of the closure problem then gave expressions for the surface integral terms in terms of the averaged pressure $\left\langle P_\mathrm{l}\right\rangle^\mathrm{l}$ and velocity $\left\langle\vec{v}_\mathrm{l}\right\rangle^\mathrm{l}$ and characteristics of the porous medium—the permeability tensor $\boldsymbol{K}$, the Forchheimer correction tensor $\boldsymbol{F}$, and a dispersion tensor $\boldsymbol{M}$ [Bousquet-Melou *et al.*, 2002a]. The definition and solution of such a closure problem is clearly beyond the scope of this work. The derivations are performed only to clearly show the origin of the terms in the final model. Instead we can, by making a few further justifiable and common assumptions, reduce Eq. (4.49) to the equation obtained by Bousquet-Melou et al. [Bousquet-Melou *et al.*, 2002a] and apply their findings and closure model solution. To do this we have to take some further acceptable simplifying assumptions. We assume the local density variations to be generally negligible ($\hat{\rho}_\mathrm{k}\approx 0\Rightarrow\rho_\mathrm{k}\approx\left\langle\rho_\mathrm{k}\right\rangle^\mathrm{k}$), neglect the effect of variable viscosity ($\nabla\mu_\mathrm{l}\approx 0$) and assume a divergence-free velocity field ($\nabla\cdot\vec{v}_\mathrm{l}\approx 0$) in the

viscous stress terms, which is consistent with the usual Boussinesq assumption used in buoyancy-driven flows. The following equation, identical to the equation derived in [Bousquet-Melou *et al.*, 2002a], as already mentioned, is obtained in this way.

$$\begin{aligned}\frac{\partial}{\partial t}\left(g_\mathrm{l}\rho_\mathrm{l}\left\langle\vec{v}_\mathrm{l}\right\rangle^\mathrm{l}\right)+\nabla\cdot\left(g_\mathrm{l}\rho_\mathrm{l}\left\langle\vec{v}_\mathrm{l}\right\rangle^\mathrm{l}\left\langle\vec{v}_\mathrm{l}\right\rangle^\mathrm{l}\right)&=-g_\mathrm{l}\nabla\left\langle P_\mathrm{l}\right\rangle^\mathrm{l}+g_\mathrm{l}\mu_\mathrm{l}\nabla^2\left\langle\vec{v}_\mathrm{l}\right\rangle^\mathrm{l}\\&-g_\mathrm{l}\rho_\mathrm{l}^\mathrm{ref}\vec{g}\left[\beta_\mathrm{l}^T\left(\left\langle T_\mathrm{l}\right\rangle^\mathrm{l}-T^\mathrm{ref}\right)+\beta_\mathrm{l}^C\left(\left\langle C_\mathrm{l}\right\rangle^\mathrm{l}-C^\mathrm{ref}\right)\right]\\&+\frac{1}{V_0}\int\limits_{A_\mathrm{l}}\rho_\mathrm{l}\vec{v}_\mathrm{l}(\vec{w}_\mathrm{i}-\vec{v}_\mathrm{l})\cdot\vec{n}_\mathrm{l}\,dA+\underbrace{\frac{1}{V_0}\int\limits_{A_\mathrm{l}}\left[\hat{P}_\mathrm{l}\boldsymbol{I}-\mu_\mathrm{l}\nabla\hat{\vec{v}}_\mathrm{l}\right]\cdot\vec{n}_\mathrm{l}\,dA}_{\text{Darcy-Forchheimer term}}\\&\underbrace{-\mu_\mathrm{l}\nabla\cdot\left[\frac{1}{V_0}\int\limits_{A_\mathrm{l}}\hat{\vec{v}}_\mathrm{l}\vec{n}_\mathrm{l}\,dA\right]}_{\text{2nd and 3rd Brinkman correction terms}}\underbrace{-\nabla\cdot\left[g_\mathrm{l}\rho_\mathrm{l}\left\langle\hat{\vec{v}}_\mathrm{l}\hat{\vec{v}}_\mathrm{l}\right\rangle^\mathrm{l}\right]}_{\text{Dispersion term}}\end{aligned}\tag{4.50}$$

After the solution of the closure model the interface integral terms result in the Darcy term with the Forchheimer correction, the 2nd and 3rd Brinkman correction terms, and the dispersion term, all known from porous media flow models. In the equation below we take into account that the solid porous matrix moves with a uniform nonzero velocity $\left\langle\vec{v}_\mathrm{s}\right\rangle^\mathrm{s}$.

$$\begin{aligned}\frac{\partial}{\partial t}\left(g_\mathrm{l}\rho_\mathrm{l}\left\langle\vec{v}_\mathrm{l}\right\rangle^\mathrm{l}\right)+\nabla\cdot\left(g_\mathrm{l}\rho_\mathrm{l}\left\langle\vec{v}_\mathrm{l}\right\rangle^\mathrm{l}\left\langle\vec{v}_\mathrm{l}\right\rangle^\mathrm{l}\right)&=-g_\mathrm{l}\nabla\left\langle P_\mathrm{l}\right\rangle^\mathrm{l}+g_\mathrm{l}\mu_\mathrm{l}\nabla^2\left\langle\vec{v}_\mathrm{l}\right\rangle^\mathrm{l}\\&-\vec{g}\rho_\mathrm{l}^\mathrm{ref}\left[\beta_\mathrm{l}^T\left(\left\langle T_\mathrm{l}\right\rangle^\mathrm{l}-T^\mathrm{ref}\right)+\beta_\mathrm{l}^C\left(\left\langle C_\mathrm{l}\right\rangle^\mathrm{l}-C^\mathrm{ref}\right)\right]\\&+\frac{1}{V_0}\int\limits_{A_\mathrm{l}}\rho_\mathrm{l}\vec{v}_\mathrm{l}(\vec{w}_\mathrm{i}-\vec{v}_\mathrm{l})\cdot\vec{n}_\mathrm{l}\,dA+\underbrace{g_\mathrm{l}^2\mu_\mathrm{l}\boldsymbol{K}^{-1}\cdot(\boldsymbol{I}+\boldsymbol{F})\cdot\left(\left\langle\vec{v}_\mathrm{l}\right\rangle^\mathrm{l}-\left\langle\vec{v}_\mathrm{s}\right\rangle^\mathrm{s}\right)}_{\text{Darcy-Forchheimer term}}\\&\underbrace{+\mu_\mathrm{l}\nabla\left(\left\langle\vec{v}_\mathrm{s}\right\rangle^\mathrm{s}-\left\langle\vec{v}_\mathrm{l}\right\rangle^\mathrm{l}\right)\cdot\nabla g_\mathrm{l}+\mu_\mathrm{l}\nabla^2 g_\mathrm{l}\left(\left\langle\vec{v}_\mathrm{s}\right\rangle^\mathrm{s}-\left\langle\vec{v}_\mathrm{l}\right\rangle^\mathrm{l}\right)}_{\text{2nd and 3rd Brinkman correction terms}}\\&\underbrace{-\nabla\cdot\left[g_\mathrm{l}\rho_\mathrm{l}\left(\left\langle\vec{v}_\mathrm{l}\right\rangle^\mathrm{l}-\left\langle\vec{v}_\mathrm{s}\right\rangle^\mathrm{s}\right)\cdot\left\langle\boldsymbol{M}^T\boldsymbol{M}\right\rangle^\mathrm{l}\cdot\left(\left\langle\vec{v}_\mathrm{l}\right\rangle^\mathrm{l}-\left\langle\vec{v}_\mathrm{s}\right\rangle^\mathrm{s}\right)\right]}_{\text{Dispersion term}}\end{aligned}\tag{4.51}$$

Bousquet-Melou et al. [Bousquet-Melou *et al.*, 2002a] estimated the scales of the individual terms in Eq. (4.51). They concluded that the 2nd and 3rd Brinkman correction terms can be important in porous media formed by a dendritic mushy zone, presenting moderate evolving heterogeneities, if the

length scale of porosity L_ε and length scale of velocity L_v are similar. Based on numerical results we can say that this is not the case in the high-f_l region of the mushy zone, where the velocity gradients are large (or $L_\varepsilon \gg L_v$ in the language of the scale estimates). In any case, this situation is not of much interest in the two-regime model since the porous zone starts with lower f_l. In the lower-f_l regions, on the other hand, where $L_\varepsilon \sim L_v$, the pressure and Darcy terms will dominate by far. Thus the Brinkman terms are not expected to have a notable influence and will be neglected. The Forchheimer correction term can be, as shown above, modeled as a modification of the permeability tensor. Bousquet-Melou et al. [Bousquet-Melou *et al.*, 2002a] show that the Forchheimer term is the dominant inertia term for moderate and small porosity. However, from a rough estimation of the relative scales of $\boldsymbol{K}$ and $\boldsymbol{F}$, based on formulae, found in [Whitaker, 1996] and [Dong and Dullen, 2006], we get estimates of the order of magnitude $\|\boldsymbol{F}\|/\|\boldsymbol{K}\| \sim 10^{-4}$. Thus, the Forchheimer correction can clearly be neglected. Further, Bousquet-Melou et al. [Bousquet-Melou *et al.*, 2002a] also show that the dispersion term and the influence of interfacial momentum transfer due to phase change can be neglected. Although the porous mushy zone is clearly not an isotropic porous medium, at this stage of development and due to lack of detailed data, we will model the mushy zone as an isotropic porous medium and simplify the permeability tensor $\boldsymbol{K}$ to a scalar permeability K. Finally, we obtain the simplified liquid momentum equation for the porous regime.

$$\begin{aligned}\frac{\partial}{\partial t}\left(g_\mathrm{l}\rho_\mathrm{l}\left\langle\vec{v}_\mathrm{l}\right\rangle^\mathrm{l}\right)+\nabla\cdot\left(g_\mathrm{l}\rho_\mathrm{l}\left\langle\vec{v}_\mathrm{l}\right\rangle^\mathrm{l}\left\langle\vec{v}_\mathrm{l}\right\rangle^\mathrm{l}\right)&=-g_\mathrm{l}\nabla\left\langle P_\mathrm{l}\right\rangle^\mathrm{l}+g_\mathrm{l}\mu_\mathrm{l}\nabla\cdot\left(\nabla\left\langle\vec{v}_\mathrm{l}\right\rangle^\mathrm{l}\right)\\&+g_\mathrm{l}^2\frac{\mu_\mathrm{l}}{K}\left(\left\langle\vec{v}_\mathrm{l}\right\rangle^\mathrm{l}-\left\langle\vec{v}_\mathrm{s}\right\rangle^\mathrm{s}\right)-\vec{g}\rho_\mathrm{l}^\mathrm{ref}\left[\beta_\mathrm{l}^T\left(\left\langle T_\mathrm{l}\right\rangle^\mathrm{l}-T^\mathrm{ref}\right)+\beta_\mathrm{l}^C\left(\left\langle C_\mathrm{l}\right\rangle^\mathrm{l}-C^\mathrm{ref}\right)\right]\end{aligned} \tag{4.52}$$

4.3.4 Energy Conservation

The transient term is averaged.

$$\begin{aligned}
\left\langle X_\mathrm{k} \frac{\partial}{\partial t}(\rho h) \right\rangle &= \frac{\partial}{\partial t}\left(g_\mathrm{k} \left\langle \rho_\mathrm{k} h_\mathrm{k} \right\rangle^\mathrm{k} \right) + \frac{1}{V_0} \int\limits_{A_\mathrm{k}} \rho h_\mathrm{k} \vec{w}_\mathrm{i} \cdot \vec{n}_\mathrm{k} \, dA \\
&= \frac{\partial}{\partial t}\left(g_\mathrm{k} \left\langle \rho_\mathrm{k} \right\rangle^\mathrm{k} \left\langle h_\mathrm{k} \right\rangle^\mathrm{k} \right) + \frac{\partial}{\partial t}\left(g_\mathrm{k} \cancelto{\approx 0}{\left\langle \hat{\rho}_\mathrm{k} \hat{h}_\mathrm{k} \right\rangle^\mathrm{k}} \right)^{\text{(Eq. (4.8))}} \\
&\quad + \frac{1}{V_0} \int\limits_{A_\mathrm{k}} \rho h_\mathrm{k} \vec{w}_\mathrm{i} \cdot \vec{n}_\mathrm{k} \, dA \\
&= \frac{\partial}{\partial t}\left(g_\mathrm{k} \left\langle \rho_\mathrm{k} \right\rangle^\mathrm{k} \left\langle h_\mathrm{k} \right\rangle^\mathrm{k} \right) + \frac{1}{V_0} \int\limits_{A_\mathrm{k}} \rho h_\mathrm{k} \vec{w}_\mathrm{i} \cdot \vec{n}_\mathrm{k} \, dA
\end{aligned} \tag{4.53}$$

The advective term is averaged.

$$\begin{aligned}
\left\langle X_\mathrm{k} \nabla \cdot (\rho h \vec{v}) \right\rangle &= \nabla \cdot \left(g_\mathrm{k} \left\langle \rho_\mathrm{k} h_\mathrm{k} \vec{v}_\mathrm{k} \right\rangle^\mathrm{k} \right) - \frac{1}{V_0} \int\limits_{A_\mathrm{k}} \rho_\mathrm{k} h_\mathrm{k} \vec{v}_\mathrm{k} \cdot \vec{n}_\mathrm{k} \, dA \\
&= \nabla \cdot \left(g_\mathrm{k} \left\langle \left\langle \rho_\mathrm{k} \right\rangle^\mathrm{k} \left\langle h_\mathrm{k} \vec{v}_\mathrm{k} \right\rangle^\mathrm{k} \right\rangle^\mathrm{k} \right) + \nabla \cdot \left(g_\mathrm{k} \cancelto{\approx 0}{\left\langle \hat{\rho}_\mathrm{k} \widehat{h_\mathrm{k} \vec{v}_\mathrm{k}} \right\rangle^\mathrm{k}} \right)^{\text{(Eq. (4.8))}} \\
&\quad - \frac{1}{V_0} \int\limits_{A_\mathrm{k}} \rho_\mathrm{k} h_\mathrm{k} \vec{v}_\mathrm{k} \cdot \vec{n}_\mathrm{k} \, dA \\
&= \nabla \cdot \left(g_\mathrm{k} \left\langle \rho_\mathrm{k} \right\rangle^\mathrm{k} \left\langle h_\mathrm{k} \right\rangle^\mathrm{k} \left\langle \vec{v}_\mathrm{k} \right\rangle^\mathrm{k} \right) + \nabla \cdot \left(g_\mathrm{k} \left\langle \rho_\mathrm{k} \right\rangle^\mathrm{k} \left\langle \hat{h}_\mathrm{k} \hat{\vec{v}}_\mathrm{k} \right\rangle^\mathrm{k} \right) \\
&\quad - \frac{1}{V_0} \int\limits_{A_\mathrm{k}} \rho_\mathrm{k} h_\mathrm{k} \vec{v}_\mathrm{k} \cdot \vec{n}_\mathrm{k} \, dA
\end{aligned} \tag{4.54}$$

The diffusive term is averaged.

$$\begin{aligned}
\langle X_\mathrm{k} \nabla \cdot (k \nabla T) \rangle &= \nabla \cdot \left(g_\mathrm{k} \langle k_\mathrm{k} \nabla T_\mathrm{k} \rangle^\mathrm{k} \right) - \frac{1}{V_0} \int\limits_{A_\mathrm{k}} k_\mathrm{k} \nabla T_\mathrm{k} \vec{n}_\mathrm{k} \, dA \\
&= \nabla \cdot \left(g_\mathrm{k} \langle k_\mathrm{k} \rangle^\mathrm{k} \langle \nabla T_\mathrm{k} \rangle^\mathrm{k} \right) + \nabla \cdot \left(g_\mathrm{k} \cancel{\left\langle \hat{k}_\mathrm{k} \widehat{\nabla T}_\mathrm{k} \right\rangle^\mathrm{k}} \right) \approx 0 \,^{(\text{Eq. (4.8)})} \\
&\quad - \frac{1}{V_0} \int\limits_{A_\mathrm{k}} k_\mathrm{k} \nabla T_\mathrm{k} \vec{n}_\mathrm{k} \, dA \\
&= \nabla \cdot \left(g_\mathrm{k} \langle k_\mathrm{k} \rangle^\mathrm{k} \nabla \langle T_\mathrm{k} \rangle^\mathrm{k} \right) - \nabla \cdot \left(\langle k_\mathrm{k} \rangle^\mathrm{k} \frac{1}{V_0} \int\limits_{A_\mathrm{k}} \hat{T}_\mathrm{k} \vec{n}_\mathrm{k} \, dA \right) \\
&\quad - \frac{1}{V_0} \int\limits_{A_\mathrm{k}} k_\mathrm{k} \nabla T_\mathrm{k} \vec{n}_\mathrm{k} \, dA
\end{aligned} \tag{4.55}$$

The final volume-averaged energy equation for phase k is thus

$$\begin{aligned}
\frac{\partial}{\partial t} \left(g_\mathrm{k} \langle \rho_\mathrm{k} \rangle^\mathrm{k} \langle h_\mathrm{k} \rangle^\mathrm{k} \right) + \nabla \cdot \left(g_\mathrm{k} \langle \rho_\mathrm{k} \rangle^\mathrm{k} \langle h_\mathrm{k} \rangle^\mathrm{k} \langle \vec{v}_\mathrm{k} \rangle^\mathrm{k} \right) &= \nabla \cdot \left(g_\mathrm{k} \langle k_\mathrm{k} \rangle^\mathrm{k} \langle \nabla T_\mathrm{k} \rangle^\mathrm{k} \right) \\
&\quad + Q_\mathrm{k}^\Gamma + Q_\mathrm{k}^q + \nabla \cdot \vec{q}_\mathrm{k}^\mathrm{t} + \nabla \cdot \left(g_\mathrm{k} \left\langle \vec{q}_\mathrm{k}^\mathrm{d} \right\rangle^\mathrm{k} \right)
\end{aligned} \tag{4.56}$$

$$\begin{aligned}
Q_\mathrm{k}^\Gamma &= \frac{1}{V_0} \int\limits_{A_\mathrm{k}} \rho_\mathrm{k} h_\mathrm{k} (\vec{w}_\mathrm{i} - \vec{v}_\mathrm{k}) \cdot \vec{n}_\mathrm{k} \, dA \\
Q_\mathrm{k}^q &= -\frac{1}{V_0} \int\limits_{A_\mathrm{k}} k_\mathrm{k} \nabla T_\mathrm{k} \vec{n}_\mathrm{k} \, dA \\
\vec{q}_\mathrm{k}^\mathrm{t} &= - \langle k_\mathrm{k} \rangle^\mathrm{k} \frac{1}{V_0} \int\limits_{A_\mathrm{k}} \hat{T}_\mathrm{k} \vec{n}_\mathrm{k} \, dA \\
\left\langle \vec{q}_\mathrm{k}^\mathrm{d} \right\rangle^\mathrm{k} &= - \langle \rho_\mathrm{k} \rangle^\mathrm{k} \left\langle \hat{h}_\mathrm{k} \hat{\vec{v}}_\mathrm{k} \right\rangle^\mathrm{k} \approx - \left\langle \rho_\mathrm{k} \hat{h}_\mathrm{k} \hat{\vec{v}}_\mathrm{k} \right\rangle^\mathrm{k} .
\end{aligned}$$

Q_k^Γ is the energy exchange due to the movement of the phase interface, Q_k^q is the diffusive heat flux across the interface, $\vec{q}_\mathrm{k}^\mathrm{t}$ is the tortuosity flux, and $\left\langle \vec{q}_\mathrm{k}^\mathrm{d} \right\rangle^\mathrm{k}$ is the dispersion flux.

4.3.5 Constitutive Models for Heat Transport

Transport terms

The two least obvious terms to model in Eq. (4.56) are the terms involving temperature, enthalpy and velocity fluctuations; the tortuosity vector $\vec{q}_{\mathrm{k}}^{\,\mathrm{t}}$ and the dispersion flux $\vec{q}_{\mathrm{k}}^{\,\mathrm{d}}$. An insight into these terms is provided by the studies of Neculae et al. [Neculae *et al.*, 2002] and Bousquet-Melou et al. [Bousquet-Melou *et al.*, 2002b]. There, the terms were investigated for solute transport but the governing equation has the same mathematical form so the results can also be used for the energy equation. They formulated a closure problem which enables us to formulate the dispersion and tortuosity terms in terms of the averaged macroscopic variable and a modification of the diffusion tensor. The numerical solution of the closure problem on schematic and real dendritic structures then gave them the values of the modified diffusion tensor. Using their results it can be shown that for low Péclet numbers

$$Pe = \frac{\ell_\alpha \left| \langle \vec{v}_{\mathrm{l}} \rangle^{\mathrm{l}} \right|}{\kappa} \tag{4.57}$$

(based on the characteristic size of the dendritic structure ℓ_α and thermal diffusivity κ), as they occur in heat transfer, the modification of the diffusion tensor is negligible and thus the dispersion and tortuosity terms in the energy equation can be neglected.

$$\nabla \cdot \vec{q}_{\mathrm{k}}^{\,\mathrm{t}} + \nabla \cdot \left(g_{\mathrm{k}} \left\langle \vec{q}_{\mathrm{k}}^{\,\mathrm{d}} \right\rangle^{\mathrm{k}} \right) \approx 0 \tag{4.58}$$

Thermal equilibrium

Due to the large thermal diffusivity and small solutal diffusivity on metal alloys (large Schmidt number $Sc = \kappa / D \sim 10^2$) the phase change at the microscopic scale and at solidification rates encountered in normal casting processes is controlled by solute diffusion. The thermal fields are quickly equilibrated and it can be assumed that the temperatures of both phases are equal.

$$\langle T_{\mathrm{s}} \rangle^{\mathrm{s}} = \langle T_{\mathrm{l}} \rangle^{\mathrm{l}} = T \tag{4.59}$$

Thermodynamic state relations

The main variable in the energy equation is the enthalpy. However, the diffusive flux is modeled by the Fourier relation in terms of the temperature

gradient. Moreover, the temperature is needed for the determination of possibly temperature-dependent thermophysical properties. Thus, a thermodynamic state model has to be provided which relates the temperature and the enthalpy. In general, the enthalpy in a multiphase multicomponent system is a function of the phase, temperature and the concentrations of the mixture components. If the thermodynamic reference state is defined to be the primary solid phase α at temperature T_{ref} and concentration $C_{\mathrm{ref}} = 0$ (pure solvent) the enthalpy of the primary solid phase α at temperature T and concentration C in a binary system is

$$h_\alpha(T,C) = (1-C)h_{\mathrm{ref}} + Ch_\alpha(T_{\mathrm{ref}}, C=1) + \Delta h_{\mathrm{mix}}(T_{\mathrm{ref}}, C) + \int_{T_{\mathrm{ref}}}^{T} c_{p\alpha}(T,C)dT, \tag{4.60}$$

where $h_{\mathrm{ref}} = h_\alpha(T_{\mathrm{ref}}, C_{\mathrm{ref}})$ is the reference enthalpy, $c_{p\alpha}$ is the specific heat of phase α, and Δh_{mix} is the mixing enthalpy. The enthalpy of the liquid phase is

$$\begin{aligned} h_{\mathrm{l}}(T,C) = (1-C)\left[h_{\mathrm{ref}} + \int_{T_{\mathrm{ref}}}^{T_{\mathrm{f}}} c_{p\alpha}(T,C=0)dT + L_{\mathrm{f}} + \int_{T_{\mathrm{f}}}^{T} c_{p\mathrm{l}}(T,C=0)dT\right] \\ + Ch_{\mathrm{l}}(T,C=1) + \Delta h_{\mathrm{mix}}(T_{\mathrm{ref}}, C), \end{aligned} \tag{4.61}$$

where T_{f} is the melting temperature of pure solvent and L_{f} the heat of fusion of pure solvent. A common simplification can be applied, where the concentration dependence of the enthalpy is neglected. Thus the following simplified relations for the enthalpies of solid and liquid phases are obtained.

$$h_{\mathrm{s}}(T) = h_{\mathrm{ref}} + \int_{T_{\mathrm{ref}}}^{T} c_{p\mathrm{s}}(T)dT \tag{4.62}$$

$$h_{\mathrm{l}}(T) = h_{\mathrm{ref}} + \int_{T_{\mathrm{ref}}}^{T_{\mathrm{m}}} c_{p\mathrm{s}}(T)dT + L_{\mathrm{f}} + \int_{T_{\mathrm{m}}}^{T} c_{p\mathrm{l}}(T)dT \tag{4.63}$$

To be able to use the exact thermodynamic relations (4.60) and (4.61) it would be most feasible to connect the model to data from a CALPHAD thermodynamic database (e.g. Thermocalc, JMatPro). Such data recently became available and with an effective implementation of the thermodynamic data in the model the need for complex analytical expressions for the properties becomes obsolete.

4.3.6 Species Conservation

All terms in the species conservation equation are analogous to the terms in the energy equation.

$$\left\langle X_\mathrm{k} \frac{\partial}{\partial t}(\rho C) \right\rangle = \frac{\partial}{\partial t}\left(g_\mathrm{k} \left\langle \rho_\mathrm{k} \right\rangle^\mathrm{k} \left\langle C_\mathrm{k} \right\rangle^\mathrm{k} \right) + \frac{1}{V_0} \int\limits_{A_\mathrm{k}} \rho C_\mathrm{k} \vec{w}_\mathrm{i} \cdot \vec{n}_\mathrm{k} \, dA \tag{4.64}$$

The advective term is averaged.

$$\begin{aligned} \left\langle X_\mathrm{k} \nabla \cdot (\rho C \vec{v}) \right\rangle = {} & \nabla \cdot \left(g_\mathrm{k} \left\langle \rho_\mathrm{k} \right\rangle^\mathrm{k} \left\langle C_\mathrm{k} \right\rangle^\mathrm{k} \left\langle \vec{v}_\mathrm{k} \right\rangle^\mathrm{k} \right) + \nabla \cdot \left(g_\mathrm{k} \left\langle \rho_\mathrm{k} \right\rangle^\mathrm{k} \left\langle \hat{C}_\mathrm{k} \hat{\vec{v}}_\mathrm{k} \right\rangle^\mathrm{k} \right) \\ & - \frac{1}{V_0} \int\limits_{A_\mathrm{k}} \rho_\mathrm{k} C_\mathrm{k} \vec{v}_\mathrm{k} \cdot \vec{n}_\mathrm{k} \, dA \end{aligned} \tag{4.65}$$

The diffusive term is averaged.

$$\begin{aligned} \left\langle X_\mathrm{k} \nabla \cdot (\rho D \nabla C) \right\rangle = {} & \nabla \cdot \left(g_\mathrm{k} \left\langle \rho_\mathrm{k} \right\rangle^\mathrm{k} \left\langle D_\mathrm{k} \right\rangle^\mathrm{k} \nabla \left\langle C_\mathrm{k} \right\rangle^\mathrm{k} \right) \\ & - \nabla \cdot \left(\left\langle \rho_\mathrm{k} \right\rangle^\mathrm{k} \left\langle D_\mathrm{k} \right\rangle^\mathrm{k} \frac{1}{V_0} \int\limits_{A_\mathrm{k}} \hat{C}_\mathrm{k} \vec{n}_\mathrm{k} \, dA \right) \\ & - \frac{1}{V_0} \int\limits_{A_\mathrm{k}} \rho_\mathrm{k} D_\mathrm{k} \nabla C_\mathrm{k} \vec{n}_\mathrm{k} \, dA \end{aligned} \tag{4.66}$$

The final volume-averaged energy equation for phase k is thus

$$\begin{aligned} & \frac{\partial}{\partial t}\left(g_\mathrm{k} \left\langle \rho_\mathrm{k} \right\rangle^\mathrm{k} \left\langle C_\mathrm{k} \right\rangle^\mathrm{k} \right) + \nabla \cdot \left(g_\mathrm{k} \left\langle \rho_\mathrm{k} \right\rangle^\mathrm{k} \left\langle C_\mathrm{k} \right\rangle^\mathrm{k} \left\langle \vec{v}_\mathrm{k} \right\rangle^\mathrm{k} \right) = \\ & \nabla \cdot \left(g_\mathrm{k} \left\langle \rho_\mathrm{k} \right\rangle^\mathrm{k} \left\langle D_\mathrm{k} \right\rangle^\mathrm{k} \nabla \left\langle C_\mathrm{k} \right\rangle^\mathrm{k} \right) + j_\mathrm{k}^\Gamma + j_\mathrm{k}^j + \nabla \cdot \vec{j}_\mathrm{k}^\mathrm{t} + \nabla \cdot \left(g_\mathrm{k} \left\langle \vec{j}_\mathrm{k}^\mathrm{d} \right\rangle^\mathrm{k} \right) \end{aligned} \tag{4.67}$$

$$
\begin{aligned}
j_{\mathrm{k}}^{\Gamma} &= \frac{1}{V_0} \int\limits_{A_{\mathrm{k}}} \rho_{\mathrm{k}} C_{\mathrm{k}} (\vec{w}_{\mathrm{i}} - \vec{v}_{\mathrm{k}}) \cdot \vec{n}_{\mathrm{k}} \, dA \\
j_{\mathrm{k}}^{j} &= -\frac{1}{V_0} \int\limits_{A_{\mathrm{k}}} \rho_{\mathrm{k}} D_{\mathrm{k}} \nabla C_{\mathrm{k}} \vec{n}_{\mathrm{k}} \, dA \\
\vec{j}_{\mathrm{k}}^{\mathrm{t}} &= - \left\langle \rho_{\mathrm{k}} \right\rangle^{\mathrm{k}} \left\langle D_{\mathrm{k}} \right\rangle^{\mathrm{k}} \frac{1}{V_0} \int\limits_{A_{\mathrm{k}}} \hat{C}_{\mathrm{k}} \vec{n}_{\mathrm{k}} \, dA \\
\left\langle \vec{j}_{\mathrm{k}}^{\mathrm{d}} \right\rangle^{\mathrm{k}} &= - \left\langle \rho_{\mathrm{k}} \right\rangle^{\mathrm{k}} \left\langle \hat{C}_{\mathrm{k}} \hat{\vec{v}}_{\mathrm{k}} \right\rangle^{\mathrm{k}} \approx - \left\langle \rho_{\mathrm{k}} \hat{C}_{\mathrm{k}} \hat{\vec{v}}_{\mathrm{k}} \right\rangle^{\mathrm{k}} .
\end{aligned}
$$

j_{k}^{Γ} is the solute transport due to the movement of the phase interface, j_{k}^{j} is the diffusive solute flux across the interface, $\vec{j}_{\mathrm{k}}^{\mathrm{t}}$ is the tortuosity flux, and $\langle \vec{j}_{\mathrm{k}}^{\mathrm{d}} \rangle^{k}$ is the dispersion flux.

4.3.7 Constitutive Models for Species Transport

Macroscopic Transport terms

To model the tortuosity vector $\vec{j}_{\mathrm{k}}^{\mathrm{t}}$ and the dispersion flux $\vec{j}_{\mathrm{k}}^{\mathrm{d}}$ we again refer to the studies of Neculae et al. [Neculae *et al.*, 2002] and Bousquet-Melou et al. [Bousquet-Melou *et al.*, 2002b], which were already mentioned in Section 4.3.5. Regarding the tortuosity vector, Bousquet-Melou et al. [Bousquet-Melou *et al.*, 2002b] show that it is negligible in active dispersion (dispersion in a porous medium in the presence of interfacial species transfer as it occurs during phase change). The dispersion flux becomes important at high cell Péclet numbers (based on the characteristic size of the dendritic structure ℓ_{α} and diffusion coefficient in the liquid D_{l}), when

$$
Pe = \frac{|\left\langle \vec{v}_{\mathrm{l}} \right\rangle^{\mathrm{l}}| \ell_{\alpha}}{D_{\mathrm{l}}} \gtrapprox 100. \tag{4.68}
$$

In DC casting the Péclet numbers can be estimated based on velocities in the mushy zone that were obtained in computations. The relevant quantities are estimated as

$$
\begin{aligned}
\left\langle \vec{v}_{\mathrm{l}} \right\rangle^{\mathrm{l}} &\sim 10^{-3} \, \mathrm{m/s} \\
\ell_{\alpha} &\sim 10^{-5} \ldots 10^{-4} \, \mathrm{m} \\
D_{\mathrm{l}} &\sim 5 \cdot 10^{-9} \, \mathrm{m^2/s}.
\end{aligned} \tag{4.69}
$$

We obtain an estimate of $Pe \sim 20$. Looking at the calculations by Bousquet-Melou et al. [Bousquet-Melou *et al.*, 2002b] it is clear that the effect of dispersion will be very weak. When looking at the results in ref. [Bousquet-Melou

et al., 2002b] we also have to note that the dispersion is modeled as a pseudo-diffusive flux via an augmentation of the macroscopic diffusion coefficient to get an effective diffusion-dispersion coefficient. The effect of dispersion is assessed from the ratio of the augmented diffusion-dispersion coefficient and the original diffusion coefficient. However, even with a strong augmentation of the diffusion-dispersion flux, i.e. more prominent dispersion at higher Pe, the impact of dispersion on the macroscopic species transport can still be insignificant compared to the undoubtedly dominant advection. The conclusion of this discussion is that both dispersion and tortuosity can be neglected

$$\nabla \cdot \vec{j}_{\mathrm{k}}^{\,\mathrm{t}} + \nabla \cdot \left(g_{\mathrm{k}} \left\langle \vec{j}_{\mathrm{k}}^{\,\mathrm{d}} \right\rangle^{\mathrm{k}} \right) \approx 0 \tag{4.70}$$

Microscopic Species Transport

To describe the relations of the local concentrations of individual phases on the REV scale, which is needed in the macroscopic model, the species transport at the scale of phase structures (ℓ_α) has to be modeled to capture the pertinent transport processes. The structures relevant for microscopic species redistribution are secondary dendrite arms. Diffusion is the transport mechanism responsible for species transport at this scale. To characterize the microscopic species transport in dendritic microsegregation it is usually analyzed on a small volume element, a control volume perpendicular to the periodic dendrite arms [Kurz and Fisher, 1998], shown in Fig. 4.4. Based on the geometry and scale of the control volume the following common assumptions are made:

- The control volume is small enough to be in thermal equilibrium (see thermal equilibrium assumption, Section 4.3.5)
- The control volume is narrow; the concentration field is assumed to be one-dimensional
- The geometry of the secondary dendrite arms is periodic and symmetry, i.e. zero solute flux, is assumed at both ends of the control volume of length $\lambda_2/2$, where λ_2 is the secondary dendrite arm spacing
- The phase interface is in thermodynamic equilibrium at solidification rates encountered in normal casting and welding processes [Kurz and Fisher, 1998][1]

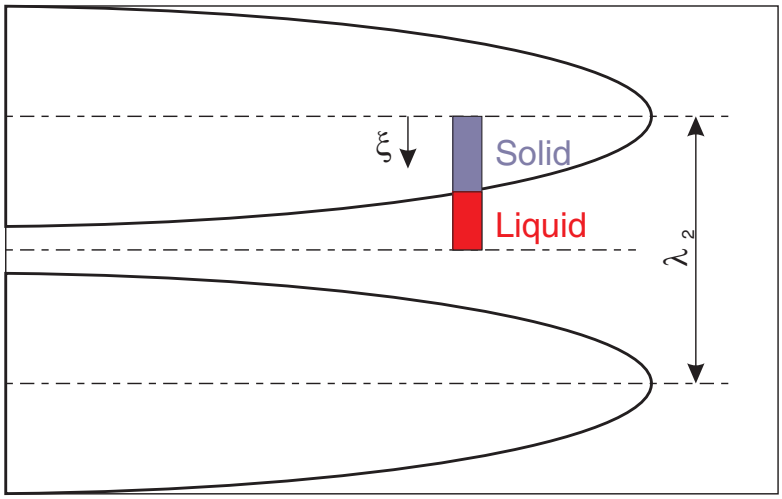

Figure 4.4: Control volume for microscopic species transport. λ_2 is the secondary dendrite arm spacing.

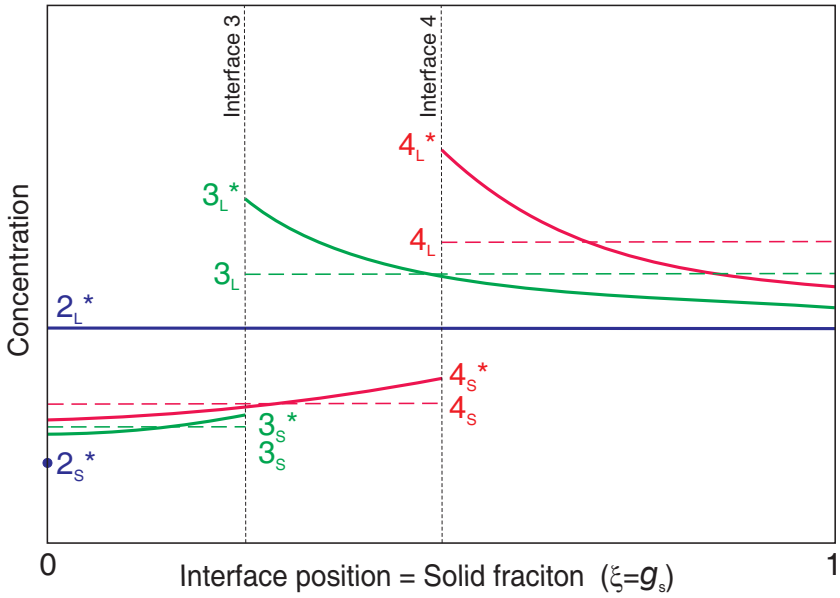

Figure 4.5: Evolution of the concentration profiles at the secondary dendrite arm scale.

Mathematically the problem is formulated as a Stefan problem. The diffusion in the solid and liquid phases is modeled according to Fick's law of diffusion.

$$\frac{\partial C_\mathrm{k}}{\partial t} = D_\mathrm{k} \nabla^2 C_\mathrm{k} \tag{4.71}$$

At both ends of the control volume, i.e. the dendrite arm symmetry axes, Neumann boundary conditions apply in either phase.

$$\left.\frac{\partial C}{\partial x}\right|_{x=0} = 0 \tag{4.72}$$

$$\left.\frac{\partial C}{\partial x}\right|_{x=\frac{\lambda_2}{2}} = 0 \tag{4.73}$$

Initially, the control volume is liquid, i.e. the initial position of the interface is $x_\mathrm{i}(t=0) = 0$ and the initial concentration of the liquid is uniform $C(t=0) = C_0$. The equilibrium of both phases at the interface is described by the condition

$$C_\mathrm{ik} = C_\mathrm{k}(x_\mathrm{i}) = C_\mathrm{k}^*(T), \tag{4.74}$$

where $C_\mathrm{k}^*(T)$ is the equilibrium concentration of phase k at the local temperature T, $*$ denotes the thermodynamic equilibrium state, and subscript i the solid-liquid interface. As the interface is advancing during solidification, the velocity of the moving interface ($v_\mathrm{i} = dx_\mathrm{i}/dt$) is defined by the solute mass balance at the interface

$$(C_\mathrm{l}(x_\mathrm{i}) - C_\mathrm{s}(x_\mathrm{i}))\frac{dx_\mathrm{i}}{dt} = (C_\mathrm{l}^*(T) - C_\mathrm{s}^*(T))\frac{dx_\mathrm{i}}{dt} = D_\mathrm{s}\left.\frac{\partial C_\mathrm{s}}{\partial x}\right|_{x=x_\mathrm{i}} - D_\mathrm{l}\left.\frac{\partial C_\mathrm{l}}{\partial x}\right|_{x=x_\mathrm{i}}, \tag{4.75}$$

which is often called the Stefan condition.

The microsegregation problem becomes more complex when eutectic reactions occur during solidification. Then the eutectic, a mixture of fine lamellar primary and secondary phases, can be modeled as a pseudophase and equilibrium boundary conditions can be prescribed at all phase (and pseudophase) interfaces. Such a complete description would thus model diffusion in the liquid, growth of the eutectic at the liquid-eutectic interface and the dissolution of the eutectic and back diffusion in the primary phase at the eutectic-primary interface. To the author's knowledge, a complete model like this has not been developed yet as part of a coupled micro-macro solidification model. Instead,

[1] In contrast to rapid solidification processes, where the interface is not in equilibrium and solute trapping occurs. The range of validity of the equilibrium interface assumption with respect to the solidification rate is analyzed in [Kurz and Fisher, 1998].

additional simplifying assumptions of the moving boundary problem (4.71)-(4.75) are commonly taken to facilitate the consideration of the problem. These assumptions include

- The liquid diffusivity is large enough (3-4 orders of magnitude larger than that of the solid phases) to be able to assume a homogeneous concentration in the liquid phase at normal solidification rates.

$$\langle C_\mathrm{l}\rangle^\mathrm{l} = C_\mathrm{il} = C_\mathrm{l}^*(T) \tag{4.76}$$

- The back diffusion in the primary solid phase after the onset of the eutectic reaction, which causes dissolution of the eutectic, is not considered.

In the context of macroscopic solidification, where macroscopic relative motion of solid and liquid phases is present, the additional effect of macrosegregation has to be taken into account. During the course of solidification the interdendritic liquid is mixed with liquid flowing from other regions of the casting, which might be richer or leaner in solute. This causes an alteration of the relation between the averaged phase concentrations, compared to solidification in the absence of macrosegregation. In terms of macroscopic averaged variables this means a modified evolution of $\langle C_\mathrm{s}\rangle^\mathrm{l}$ and T as a function of g_s. If the rate of change of the overall concentration in the microscopic control volume due to macrosegregation is dC_m/dt, the general equation of dendritic microsegregation is written [Založnik and Šarler, 2003]

$$dC_\mathrm{m} = \underbrace{(1-f_\mathrm{s})\, d\langle C_\mathrm{l}\rangle^\mathrm{l}}_{\substack{\text{change of solute}\\ \text{mass in the liquid}}} + \underbrace{(k_\mathrm{p}-1)\,\langle C_\mathrm{l}\rangle^\mathrm{l}\, df_\mathrm{s}}_{\substack{\text{change of solute mass}\\ \text{in the solid due to}\\ \text{phase change}}} + \underbrace{\frac{1}{g_\mathrm{s}}\frac{2D_\mathrm{s}}{\lambda_2}\left.\frac{\partial C_\mathrm{s}}{\partial x}\right|_{x=x_\mathrm{i}} dt}_{\substack{\text{change of solute mass}\\ \text{in the solid due to}\\ \text{back diffusion}}}, \tag{4.77}$$

where $k_\mathrm{p} = C_\mathrm{s}/C_\mathrm{l}$ is the solute partition ratio, f_s the solid mass fraction, and g_s the solid volume fraction. This equation attributes the whole solute mass change in the control volume due to macrosegregation (dC_m), which appears as a consequence of relative motion of segregated solid and liquid, to the liquid phase. The solute content in the solid changes only due to its growth from the liquid at the solid-liquid interface (phase change) and due to diffusion of solute from the interface, where the solid concentration is highest, into the solid phase (back diffusion). This means that the influence of a moving solid phase, as it is modeled in the slurry flow regime of the model developed here, is not accounted for. Equation 4.77, exact in the case

of a rigid and stationary solid phase, is thus unsuitable to model microscopic solute transport in a solidifying slurry. The two possible alternatives are to develop a model that will take into account the motion of solid particles or take further simplifications to omit the inconsistency that has arisen.

Scheil Model The two most popular further assumptions of the microscopic diffusion model, leading to significant simplifications, concern the treatment of diffusion in the solid phase. If the diffusivity in the solid is assumed to be small enough to be neglected at the space and time scale of the dendritic solidification structures, which is usually a good approximation, the Scheil [Scheil, 1942] limit of the model is obtained. It is often written neglecting macrosegregation

$$(1 - f_\mathrm{s})\, d\langle C_\mathrm{l}\rangle^\mathrm{l} + (k_\mathrm{p} - 1)\, \langle C_\mathrm{l}\rangle^\mathrm{l}\, df_\mathrm{s} = 0\,, \tag{4.78}$$

and integrated

$$\frac{1}{(1 - k_\mathrm{p})} \int_{C_0}^{\langle C_\mathrm{l}\rangle^\mathrm{l}} \frac{d\,\langle C_\mathrm{l}\rangle^\mathrm{l}}{\langle C_\mathrm{l}\rangle^\mathrm{l}} = \int_0^{f_\mathrm{s}} \frac{df_\mathrm{s}}{(1 - f_\mathrm{s})}\,, \tag{4.79}$$

to give

$$\begin{aligned} \langle C_\mathrm{l}\rangle^\mathrm{l} &= C_0 (1 - f_\mathrm{s})^{(k_\mathrm{p}-1)} \\ \langle C_\mathrm{s}\rangle^\mathrm{s} &= \frac{C_0 - (1 - f_\mathrm{s})\, \langle C_\mathrm{l}\rangle^\mathrm{l}}{f_\mathrm{s}}\,. \end{aligned} \tag{4.80}$$

To mimic an open system it is also possible to attribute the concentration change due to macrosegregation only to the liquid phase at the beginning of each discrete timestep Δt, to get the initial liquid concentration at timestep $t + \Delta t$ [Založnik and Šarler, 2003]

$$\left[\langle C_\mathrm{l}\rangle^\mathrm{l}\right]_0^{t+\Delta t} = \left[\langle C_\mathrm{l}\rangle^\mathrm{l}\right]^t + \frac{[C_\mathrm{m}]^{t+\Delta t} - [C_\mathrm{m}]^t}{1 - [f_\mathrm{s}]^t}\,, \tag{4.81}$$

to then integrate the Scheil equation over the timestep

$$\left[\langle C_\mathrm{l}\rangle^\mathrm{l}\right]^{t+\Delta t} = \left[\langle C_\mathrm{l}\rangle^\mathrm{l}\right]_0^{t+\Delta t} \left(\frac{1 - [f_\mathrm{s}]^{t+\Delta t}}{1 - [f_\mathrm{s}]^t}\right)^{(k_\mathrm{p}-1)}\,. \tag{4.82}$$

Local Equilibrium—Lever rule Another common, rather grave simplification is to assume local thermodynamic equilibrium of the solid and liquid phases (equivalent to infinitely fast diffusion in both phases). This eliminates the need of modeling microscopic solute transport and requires only thermodynamic equilibrium data.

$$\begin{aligned} \langle C_\mathrm{s} \rangle^\mathrm{s} &= C_\mathrm{s}^*(T) \\ \langle C_\mathrm{l} \rangle^\mathrm{l} &= C_\mathrm{l}^*(T) \end{aligned} \tag{4.83}$$

The model study by Vušanović [Vušanović, 2001] claims that the effect of the equilibrium assumption, if compared to the Scheil assumption, on the macrosegregation prediction is not significant. It thus presents a justification for the equilibrium approach. However, the effect may be different for different alloys (a larger partition ratio will increase the differences) or applications and should thus be further investigated to affirm the evidence and its general applicability.

In the present model the equilibrium assumption is employed for the sake of simplicity. In the presence of moving solid grains, a model that can handle the tracking of the solid phase should be included if a more detailed microsegregation model (with finite or zero diffusion in the solid) is used. The present model is, however, implemented in the macroscopic model in a way that enables a simple replacement with more complex microsegregation models later on.

Thermodynamic state relations

The relations between state variables of a multiphase system in thermodynamic equilibrium are described by the equilibrium phase diagram. In the modeling of macrosegregation this information is needed to describe the conditions at the phase interface, which is in thermodynamic equilibrium, as shown before. A binary eutectic phase diagram, which is an adequate model, suitable for all Al-rich binary aluminum alloys of interest (Cu, Mg, Si, Zn, Mn, Fe and Ni), is shown in Fig. 4.6(a). The equilibrium (interface) and average phase concentrations at a temperature are shown schematically. The same situation is shown in Fig. 4.6(b) on an enthalpy phase diagram, which makes it easier to understand the enthalpy-concentration coupling used in the model developed here. In most binary phase diagrams of binary aluminum alloys the liquidus and solidus curves are close to straight lines. Therefore, the common linearization of the phase diagram can be used and the solidus and liquidus lines are given by

$$T_\mathrm{S} = T_\mathrm{f} - m_\mathrm{S} C_\mathrm{s}^* \tag{4.84}$$

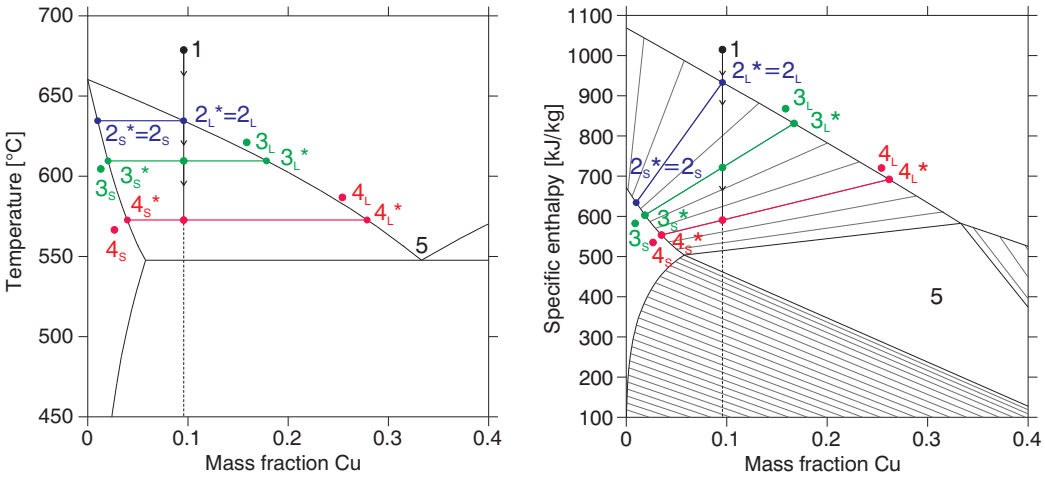

(a) Temperature-concentration.

(b) Enthalpy-concentration.

Figure 4.6: Solidification in the binary equilibrium phase diagram.

$$T_{\mathrm{L}} = T_{\mathrm{f}} - m_{\mathrm{L}} C_{\mathrm{l}}^{*}, \tag{4.85}$$

where T_{S} and T_{L} are the solidus and liquidus temperatures, m_{S} is the solidus line slope and m_{L} the liquidus line slope. Thus in conjunction with Eq. 4.83

$$C_{\mathrm{s}}^{*} = k_{\mathrm{p}} C_{\mathrm{l}}^{*}, \qquad k_{\mathrm{p}} = \frac{m_{\mathrm{L}}}{m_{\mathrm{S}}}. \tag{4.86}$$

Combeau and Mo [Combeau and Mo, 1997] have demonstrated that the linearization of the solidus and liquidus lines can have a noticeable effect on the resulting solidification path. However, compared to the effect of the much more crude assumption of local equilibrium, which is used in the present model, the effect of the simplification of the phase diagram will be minor. In any case, these days the most feasible way to model phase equilibria, especially in multicomponent mixtures, is to use CALPHAD thermodynamic models [Kattner, 1997], which is left for the future extension of the model developed here.

4.4 Formulation of the One-Phase Model

The one-phase model is to be developed from the two-phase model and the supplementary constitutional laws. It is formulated in terms of mixture quantities and properties, which are defined in terms of phase quantities and phase

fractions

$$\begin{aligned} \rho_{\mathrm{m}} &= g_{\mathrm{s}}\rho_{\mathrm{s}} + g_{\mathrm{l}}\rho_{\mathrm{l}} \qquad & \vec{v}_{\mathrm{m}} &= f_{\mathrm{s}}\vec{v}_{\mathrm{s}} + f_{\mathrm{l}}\vec{v}_{\mathrm{l}} \\ h_{\mathrm{m}} &= f_{\mathrm{s}}h_{\mathrm{s}} + f_{\mathrm{l}}h_{\mathrm{l}} \qquad & C_{\mathrm{m}} &= f_{\mathrm{s}}C_{\mathrm{s}} + f_{\mathrm{l}}C_{\mathrm{l}} \\ k_{\mathrm{m}} &= g_{\mathrm{s}}k_{\mathrm{s}} + g_{\mathrm{l}}k_{\mathrm{l}} \qquad & D_{\mathrm{m}} &= f_{\mathrm{s}}D_{\mathrm{s}} + f_{\mathrm{l}}D_{\mathrm{l}}, \end{aligned} \tag{4.87}$$

where subscript m generally denotes the solid-liquid mixture. The phase mass and volume fractions (f_{k} and g_{k} respectively) are defined

$$f_{\mathrm{k}} = \frac{m_{\mathrm{k}}}{\sum_k m_{\mathrm{k}}} \qquad g_{\mathrm{k}} = \frac{V_{\mathrm{k}}}{\sum_k V_{\mathrm{k}}} \qquad g_{\mathrm{k}} = \frac{\rho_{\mathrm{m}}}{\rho_{\mathrm{k}}} f_{\mathrm{k}} \tag{4.88}$$

and the sum of phase fractions is unity.

$$f_{\mathrm{s}} + f_{\mathrm{l}} = 1 \qquad g_{\mathrm{s}} + g_{\mathrm{l}} = 1 \tag{4.89}$$

4.4.1 Mass Conservation

The continuity equation of the one-phase model is obtained by adding the continuity equations for the liquid and solid phases (Eq. (4.10)). Taking into account the mass balance at the solid-liquid interface

$$\Gamma_{\mathrm{il}} + \Gamma_{\mathrm{is}} = 0, \tag{4.90}$$

we obtain

$$\frac{\partial \rho_{\mathrm{m}}}{\partial t} + \nabla \cdot (\rho_{\mathrm{m}} \vec{v}_{\mathrm{m}}) = 0. \tag{4.91}$$

4.4.2 Momentum Conservation

Slurry Regime

The most convenient way of deriving the one phase- momentum equation in the slurry regime appears to be the addition of the phase equations, Eq. (4.22). In this way the rheological considerations are included in the most natural way, as already mentioned in Section 4.3.3, and the need for modeling of interfacial transfer terms is partly omitted. The interfacial force balance, as already given in Section 4.3.3, is

$$\vec{M}_{\mathrm{s}}^{\Gamma} + \vec{M}_{\mathrm{l}}^{\Gamma} + \vec{M}_{\mathrm{s}}^{\mathrm{d}} + \vec{M}_{\mathrm{l}}^{\mathrm{d}} + \vec{M}_{\mathrm{s}}^{\mathrm{p}} + \vec{M}_{\mathrm{l}}^{\mathrm{p}} = \sigma_{\mathrm{i}} \bar{\zeta} \nabla g_{\mathrm{s}}. \tag{4.35}$$

Further, phase pressure relations (Eq. (4.27)), the mixture viscous stress term (Eq. (4.29)), and the Boussinesq buoyancy forces (Eqs. (4.31) and (4.32)) are

incorporated. The one-phase equation is thus

$$\begin{aligned}\frac{\partial}{\partial t}(\rho_{\mathrm{m}}\vec{v}_{\mathrm{m}}) + \nabla\cdot\left(g_{\mathrm{s}}\left\langle\rho_{\mathrm{s}}\right\rangle^{\mathrm{s}}\left\langle\vec{v}_{\mathrm{s}}\right\rangle^{\mathrm{s}}\left\langle\vec{v}_{\mathrm{s}}\right\rangle^{\mathrm{s}} + g_{\mathrm{l}}\left\langle\rho_{\mathrm{l}}\right\rangle^{\mathrm{l}}\left\langle\vec{v}_{\mathrm{l}}\right\rangle^{\mathrm{l}}\left\langle\vec{v}_{\mathrm{l}}\right\rangle^{\mathrm{l}}\right) &= -\nabla\left\langle P_{\mathrm{l}}\right\rangle^{\mathrm{l}} - g_{\mathrm{s}}\sigma_{\mathrm{i}}\nabla\bar{\zeta} \\ + \nabla\cdot\left[\mu_{\mathrm{m}}\left(\nabla\vec{v}_{\mathrm{m}} + (\nabla\vec{v}_{\mathrm{m}})^{T}\right) - \frac{2}{3}\mu_{\mathrm{m}}(\nabla\cdot\vec{v}_{\mathrm{m}})\cdot\boldsymbol{I}\right] + g_{\mathrm{s}}\vec{g}\left(\rho_{\mathrm{s}}^{\mathrm{ref}} - \rho_{\mathrm{l}}^{\mathrm{ref}}\right) \\ - g_{\mathrm{l}}\vec{g}\rho_{\mathrm{l}}^{\mathrm{ref}}\left[\beta_{\mathrm{l}}^{T}\left(T - T^{\mathrm{ref}}\right) + \beta_{\mathrm{l}}^{C}\left(\left\langle C_{\mathrm{l}}\right\rangle^{\mathrm{l}} - C^{\mathrm{ref}}\right)\right] \\ - g_{\mathrm{s}}\vec{g}\rho_{\mathrm{s}}^{\mathrm{ref}}\left[\beta_{\mathrm{s}}^{T}\left(T - T^{\mathrm{ref}}\right) + \beta_{\mathrm{s}}^{C}\left(\left\langle C_{\mathrm{s}}\right\rangle^{\mathrm{s}} - C^{\mathrm{ref}}\right)\right] \\ - \nabla\cdot\left(g_{\mathrm{s}}\left\langle\rho_{\mathrm{s}}\right\rangle^{\mathrm{s}}\left\langle\hat{\vec{v}}_{\mathrm{s}}\hat{\vec{v}}_{\mathrm{s}}\right\rangle^{\mathrm{s}}\right) - \nabla\cdot\left(g_{\mathrm{l}}\left\langle\rho_{\mathrm{l}}\right\rangle^{\mathrm{l}}\left\langle\hat{\vec{v}}_{\mathrm{l}}\hat{\vec{v}}_{\mathrm{l}}\right\rangle^{\mathrm{l}}\right). \quad (4.92)\end{aligned}$$

The advective term is reformulated in terms of mixture quantities $\vec{v}_{\mathrm{m}}$ and ρ_{m}, but this does not add up to a simple formulation. The difference is placed to the RHS of the equation as a correction source term. The interface tension term ($\sigma_{\mathrm{i}}\nabla\bar{\zeta} \approx 0$) can be neglected. A new closure problem would have to be solved to estimate the scale of the dispersion terms in the slurry regime, but they are neglected for now ($g_{\mathrm{s}}\left\langle\boldsymbol{\tau}_{\mathrm{s}}^{\mathrm{t}}\right\rangle^{\mathrm{s}} + g_{\mathrm{l}}\left\langle\boldsymbol{\tau}_{\mathrm{l}}^{\mathrm{t}}\right\rangle^{\mathrm{l}} \approx 0$). Also, as before in the modeling of the porous regime, the assumption of a divergence-free velocity field is taken in the expression for the viscous stress in the mixture ($\nabla\cdot\vec{v}_{\mathrm{m}} \approx 0$). However, due to the possibility of large macroscopic variations of the mixture viscosity in the slurry zone, which is a function of the solid fraction, the viscosity μ_{m} is retained inside the divergence operator, which keeps the velocity-gradient transpose term $(\nabla\vec{v}_{\mathrm{m}})^{T}$.

$$\begin{aligned}\frac{\partial}{\partial t}(\rho_{\mathrm{m}}\vec{v}_{\mathrm{m}}) + \nabla\cdot(\rho_{\mathrm{m}}\vec{v}_{\mathrm{m}}\vec{v}_{\mathrm{m}}) &= -\nabla\left\langle P_{\mathrm{l}}\right\rangle^{\mathrm{l}} + \nabla\cdot\left[\mu_{\mathrm{m}}\left(\nabla\vec{v}_{\mathrm{m}} + (\nabla\vec{v}_{\mathrm{m}})^{T}\right)\right] \\ + g_{\mathrm{s}}\vec{g}\left(\rho_{\mathrm{s}}^{\mathrm{ref}} - \rho_{\mathrm{l}}^{\mathrm{ref}}\right) - g_{\mathrm{l}}\vec{g}\rho_{\mathrm{l}}^{\mathrm{ref}}\left[\beta_{\mathrm{l}}^{T}\left(T - T^{\mathrm{ref}}\right) + \beta_{\mathrm{l}}^{C}\left(\left\langle C_{\mathrm{l}}\right\rangle^{\mathrm{l}} - C^{\mathrm{ref}}\right)\right] \\ - g_{\mathrm{s}}\vec{g}\rho_{\mathrm{s}}^{\mathrm{ref}}\left[\beta_{\mathrm{s}}^{T}\left(T - T^{\mathrm{ref}}\right) + \beta_{\mathrm{s}}^{C}\left(\left\langle C_{\mathrm{s}}\right\rangle^{\mathrm{s}} - C^{\mathrm{ref}}\right)\right] \\ + \left[\nabla\cdot(\rho_{\mathrm{m}}\vec{v}_{\mathrm{m}}\vec{v}_{\mathrm{m}}) - \nabla\cdot(g_{\mathrm{s}}\left\langle\rho_{\mathrm{s}}\right\rangle^{\mathrm{s}}\left\langle\vec{v}_{\mathrm{s}}\right\rangle^{\mathrm{s}}\left\langle\vec{v}_{\mathrm{s}}\right\rangle^{\mathrm{s}}) - \nabla\cdot\left(g_{\mathrm{l}}\left\langle\rho_{\mathrm{l}}\right\rangle^{\mathrm{l}}\left\langle\vec{v}_{\mathrm{l}}\right\rangle^{\mathrm{l}}\left\langle\vec{v}_{\mathrm{l}}\right\rangle^{\mathrm{l}}\right)\right] \quad (4.93)\end{aligned}$$

Porous Regime

The volume-averaged momentum equation for the liquid phase in the porous mushy zone is reformulated in terms of the mixture velocity to fit the one-phase model. The mixture velocity in the porous regime is defined as

$$\vec{v}_{\mathrm{m}} = f_{\mathrm{l}}\vec{v}_{\mathrm{l}} + (1 - f_{\mathrm{l}})\vec{v}_{\mathrm{cast}}, \quad (4.94)$$

where $\vec{v}_{\mathrm{cast}}$ is the system velocity with which the connected rigid solid phase moves. In the DC casting process this is the casting velocity. The development

of all terms is quite straightforward, with the exception of the viscous term, for which we obtain

$$\begin{aligned} g_\mathrm{l}\mu_\mathrm{l}\nabla\cdot\left(\nabla\left\langle\vec{v}_\mathrm{l}\right\rangle^\mathrm{l}\right) =& \mu_\mathrm{l}\frac{\rho_\mathrm{m}}{\rho_\mathrm{l}}\nabla\cdot(\nabla\vec{v}_\mathrm{m}) - 2\frac{\mu_\mathrm{l}}{f_\mathrm{l}}\frac{\rho_\mathrm{m}}{\rho_\mathrm{l}}(\nabla\vec{v}_\mathrm{m})\cdot(\nabla f_\mathrm{l}) \\ &+ \frac{\mu_\mathrm{l}}{f_\mathrm{l}^2}\frac{\rho_\mathrm{m}}{\rho_\mathrm{l}}(\vec{v}_\mathrm{cast}-\vec{v}_\mathrm{m})(\nabla^2 f_\mathrm{l} - 2\nabla f_\mathrm{l}\cdot\nabla f_\mathrm{l}). \end{aligned} \tag{4.95}$$

The scales of the three terms can be estimated using characteristic length scales for velocity and porosity variation, L_v and L_ε, respectively.

$$\mu_\mathrm{l}\frac{\rho_\mathrm{m}}{\rho_\mathrm{l}}\nabla\cdot(\nabla\vec{v}_\mathrm{m}) \sim \mu_\mathrm{l}\frac{v_\mathrm{m}}{L_v^2} \tag{4.96}$$

$$-2\frac{\mu_\mathrm{l}}{f_\mathrm{l}}\frac{\rho_\mathrm{m}}{\rho_\mathrm{l}}(\nabla\vec{v}_\mathrm{m})\cdot(\nabla f_\mathrm{l}) \sim \left(\mu_\mathrm{l}\frac{v_\mathrm{m}}{L_v^2}\right)\frac{2L_v}{f_\mathrm{l}L_\varepsilon} \tag{4.97}$$

$$\frac{\mu_\mathrm{l}}{f_\mathrm{l}^2}\frac{\rho_\mathrm{m}}{\rho_\mathrm{l}}(\vec{v}_\mathrm{cast}-\vec{v}_\mathrm{m})(\nabla^2 f_\mathrm{l} - 2\nabla f_\mathrm{l}\cdot\nabla f_\mathrm{l}) \sim \left(\mu_\mathrm{l}\frac{v_\mathrm{m}}{L_v^2}\right)\frac{L_v^2}{f_\mathrm{l}^2 L_\varepsilon^2}\left(1-\frac{\vec{v}_\mathrm{cast}}{v_\mathrm{m}}\right) \tag{4.98}$$

If $L_v < L_\varepsilon$ and $f_\mathrm{l} \sim 1$, which is true at the dendrite tips, the two latter ((4.97) and (4.98)) will be smaller than the first term and can be neglected. Deeper in the mushy zone, however, the scales can be different ($L_v \sim L_\varepsilon$, $f_\mathrm{l} \ll 1$) and these terms can be important in relation to the first viscous term. However, the scales of these terms should be compared to the scales of all other terms in the equation and we can say, that in the low-f_l regions of the mushy zone, the pressure, buoyancy and Darcy terms clearly dominate. Using the Kozeny-Carman model for the permeability of the porous mush [Dong and Dullen, 2006]

$$K = K_0\frac{g_\mathrm{l}^3}{(1-g_\mathrm{l})^2}\,, \tag{4.99}$$

they scale as

$$\left.\begin{array}{l} g_\mathrm{l}\nabla\left\langle P_\mathrm{l}\right\rangle^\mathrm{l} \\ g_\mathrm{l}\vec{g}\rho_\mathrm{l}^\mathrm{ref}\left[\beta_\mathrm{l}^T\left(T-T^\mathrm{ref}\right)+\beta_\mathrm{l}^C\left(\left\langle C_\mathrm{l}\right\rangle^\mathrm{l}-C^\mathrm{ref}\right)\right] \\ g_\mathrm{l}\left(\frac{\rho_\mathrm{m}}{\rho_\mathrm{l}}\right)\frac{\mu_\mathrm{l}}{K}\cdot(\vec{v}_\mathrm{m}-\vec{v}_\mathrm{cast}) \end{array}\right) \sim \left(\frac{1-g_\mathrm{l}}{g_\mathrm{l}}\right)^2\frac{\mu_\mathrm{l}}{K_0}(v_\mathrm{m}-v_\mathrm{cast}), \tag{4.100}$$

where the permeability constant K_0 scales as $K_0 \sim 10^{-10}$. The terms (4.97) and (4.98) will therefore be negligible in comparison with the viscous term in the high-f_l region and in comparison with the Darcy term in the low-f_l region of the mushy zone.

Keeping in mind the objective of combining momentum equations of both regimes into a one-domain equation, the viscous term is reshaped to comply

with the form of the slurry-regime equation. There, the viscosity had to be kept inside the divergence operator to account for viscosity variations which occur with varying solid fraction. Keeping only the first term on the RHS of Eq. (4.95) as justified by the foregoing discussion, we reshape Eq. (4.95).

$$\mu_\mathrm{l}\frac{\rho_\mathrm{m}}{\rho_\mathrm{l}}\nabla\cdot(\nabla\vec{v}_\mathrm{m}) = \nabla\cdot\left(\frac{\rho_\mathrm{m}}{\rho_\mathrm{l}}\mu_\mathrm{l}\nabla\vec{v}_\mathrm{m}\right) - \mu_\mathrm{l}\left(1-\frac{\rho_\mathrm{s}}{\rho_\mathrm{l}}\right)(\nabla\vec{v}_\mathrm{m})\cdot(\nabla f_\mathrm{l}) \quad (4.101)$$

The two terms on the RHS of Eq. (4.101) are scaled as

$$\nabla\cdot\left(\frac{\rho_\mathrm{m}}{\rho_\mathrm{l}}\mu_\mathrm{l}\nabla\vec{v}_\mathrm{m}\right) \sim \mu_\mathrm{l}\frac{v_\mathrm{m}}{L_v^2} \quad (4.102)$$

$$\mu_\mathrm{l}\left(1-\frac{\rho_\mathrm{s}}{\rho_\mathrm{l}}\right)(\nabla\vec{v}_\mathrm{m})\cdot(\nabla f_\mathrm{l}) \sim \mu_\mathrm{l}\frac{v_\mathrm{m}}{L_v^2}\left(\frac{L_v}{10L_\varepsilon}\right). \quad (4.103)$$

Based on the difference of length scales ($L_v < L_\varepsilon$) for $f_\mathrm{l} \sim 1$ and on the scale comparison with the pressure, buoyancy and Darcy terms for $f_\mathrm{l} \ll 1$, as before, the second term in Eq. (4.101) can be neglected.

After these considerations the following momentum equation is obtained for the porous regime.

$$\begin{aligned}\frac{\partial}{\partial t}(\rho_\mathrm{m}\vec{v}_\mathrm{m}) + \nabla\cdot(\rho_\mathrm{m}\vec{v}_\mathrm{m}\vec{v}_\mathrm{m}) &= -g_\mathrm{l}\nabla\langle P_\mathrm{l}\rangle^\mathrm{l} + \nabla\cdot\left(\frac{\rho_\mathrm{m}}{\rho_\mathrm{l}}\mu_\mathrm{l}\nabla\vec{v}_\mathrm{m}\right)\\ + g_\mathrm{l}\left(\frac{\rho_\mathrm{m}}{\rho_\mathrm{l}}\right)\frac{\mu_\mathrm{l}}{K}\cdot(\vec{v}_\mathrm{m}-\vec{v}_\mathrm{cast}) - \vec{g}\rho_\mathrm{l}^\mathrm{ref}&\left[\beta_\mathrm{l}^T\left(T-T^\mathrm{ref}\right)+\beta_\mathrm{l}^C\left(\langle C_\mathrm{l}\rangle^\mathrm{l}-C^\mathrm{ref}\right)\right]\\ + [\nabla\cdot(\rho_\mathrm{m}\vec{v}_\mathrm{m}\vec{v}_\mathrm{m}) - \nabla\cdot(g_\mathrm{s}\langle\rho_\mathrm{s}\rangle^\mathrm{s}\langle\vec{v}_\mathrm{s}\rangle^\mathrm{s}\langle\vec{v}_\mathrm{s}\rangle^\mathrm{s}) &-\nabla\cdot\left(g_\mathrm{l}\langle\rho_\mathrm{l}\rangle^\mathrm{l}\langle\vec{v}_\mathrm{l}\rangle^\mathrm{l}\langle\vec{v}_\mathrm{l}\rangle^\mathrm{l}\right)]\\ &+\frac{D}{Dt}(\rho_\mathrm{m}f_\mathrm{s}\vec{v}_\mathrm{cast}) \quad (4.104)\end{aligned}$$

Comparing it to the solid-phase continuity equation, Eq. (4.10), and general momentum equation (4.22) we can see that the last term on the right-hand side of Eq. (4.104) is equivalent to the solid-phase interfacial transport due to the phase change.

$$\frac{D}{Dt}(\rho_\mathrm{m}f_\mathrm{s}\vec{v}_\mathrm{cast}) = \vec{v}_\mathrm{cast}\frac{\partial}{\partial t}(g_\mathrm{s}\rho_\mathrm{s}) + \vec{v}_\mathrm{cast}\nabla\cdot(g_\mathrm{s}\rho_\mathrm{s}\vec{v}_\mathrm{s}) = \vec{v}_\mathrm{cast}\Gamma_\mathrm{is} = \vec{M}_\mathrm{s}^\Gamma \quad (4.105)$$

It is convenient if the liquid-phase interfacial transport term due to phase change $\vec{M}_\mathrm{l}^\Gamma$, which was already estimated as negligible in the derivation of the porous-regime momentum equation in Section 4.3.3, is recovered again. An approximation of $\vec{M}_\mathrm{l}^\Gamma = \overline{\vec{v}}_\mathrm{il}\Gamma_\mathrm{il}$ [Ni and Beckermann, 1991] and addition to $\vec{M}_\mathrm{s}^\Gamma$ yields

$$\vec{M}_\mathrm{s}^\Gamma + \vec{M}_\mathrm{l}^\Gamma = \left(\vec{v}_\mathrm{cast} - \overline{\vec{v}}_\mathrm{il}\right)\Gamma_\mathrm{is}. \quad (4.106)$$

This can be neglected using the same scaling argument as used previously for $\vec{M}_{\mathrm{l}}^{\Gamma}$. The final simplified one-phase equation for the porous regime is then

$$\begin{aligned}\frac{\partial}{\partial t}\left(\rho_{\mathrm{m}}\vec{v}_{\mathrm{m}}\right)+\nabla\cdot\left(\rho_{\mathrm{m}}\vec{v}_{\mathrm{m}}\vec{v}_{\mathrm{m}}\right)&=-g_{\mathrm{l}}\nabla\left\langle P_{\mathrm{l}}\right\rangle^{\mathrm{l}}+\nabla\cdot\left(\frac{\rho_{\mathrm{m}}}{\rho_{\mathrm{l}}}\mu_{\mathrm{l}}\nabla\vec{v}_{\mathrm{m}}\right)\\&+g_{\mathrm{l}}\left(\frac{\rho_{\mathrm{m}}}{\rho_{\mathrm{l}}}\right)\frac{\mu_{\mathrm{l}}}{K}\cdot\left(\vec{v}_{\mathrm{m}}-\vec{v}_{\mathrm{cast}}\right)-\vec{g}\rho_{\mathrm{l}}^{\mathrm{ref}}\left[\beta_{\mathrm{l}}^{T}\left(T-T^{\mathrm{ref}}\right)+\beta_{\mathrm{l}}^{C}\left(\left\langle C_{\mathrm{l}}\right\rangle^{\mathrm{l}}-C^{\mathrm{ref}}\right)\right]\\&+\left[\nabla\cdot\left(\rho_{\mathrm{m}}\vec{v}_{\mathrm{m}}\vec{v}_{\mathrm{m}}\right)-\nabla\cdot\left(g_{\mathrm{s}}\left\langle\rho_{\mathrm{s}}\right\rangle^{\mathrm{s}}\left\langle\vec{v}_{\mathrm{s}}\right\rangle^{\mathrm{s}}\left\langle\vec{v}_{\mathrm{s}}\right\rangle^{\mathrm{s}}\right)-\nabla\cdot\left(g_{\mathrm{l}}\left\langle\rho_{\mathrm{l}}\right\rangle^{\mathrm{l}}\left\langle\vec{v}_{\mathrm{l}}\right\rangle^{\mathrm{l}}\left\langle\vec{v}_{\mathrm{l}}\right\rangle^{\mathrm{l}}\right)\right].\end{aligned}\tag{4.107}$$

One-domain equation

To obtain a one-domain momentum equation, valid in the liquid, slurry and porous flow regimes, the momentum equations for the slurry and porous regimes are cast into one equation valid all over the domain by the penalization of the differing terms, an idea previously proposed by Šarler et al. [Šarler *et al.*, 2003, Šarler and Pepper, 2004]. For this purpose, the flow regime function is introduced

$$\mathcal{R}(\vec{x},t)=\begin{cases}1 & g_{\mathrm{s}}(\vec{x},t)>g_{\mathrm{s}}^{\mathrm{c}}\\ 0 & g_{\mathrm{s}}(\vec{x},t)\leq g_{\mathrm{s}}^{\mathrm{c}}\end{cases},\tag{4.108}$$

where $g_{\mathrm{s}}^{\mathrm{c}}$ is the consolidation solid volume fraction, defining the transition between slurry and porous flow regimes. In implementation of the numerical model the zone function has to be represented by some smooth function, which will be discussed in Chapter 5. The one-domain momentum equation is then

$$\begin{aligned}\frac{\partial}{\partial t}\left(\rho_{\mathrm{m}}\vec{v}_{\mathrm{m}}\right)+\nabla\cdot\left(\rho_{\mathrm{m}}\vec{v}_{\mathrm{m}}\vec{v}_{\mathrm{m}}\right)&=-\nabla\left\langle P_{\mathrm{l}}\right\rangle^{\mathrm{l}}+\nabla\cdot\left(\mu_{\mathrm{eff}}\nabla\vec{v}_{\mathrm{m}}\right)\\&-\vec{g}\rho_{\mathrm{l}}^{\mathrm{ref}}\left[\beta_{\mathrm{l}}^{T}\left(T-T^{\mathrm{ref}}\right)+\beta_{\mathrm{l}}^{C}\left(\left\langle C_{\mathrm{l}}\right\rangle^{\mathrm{l}}-C^{\mathrm{ref}}\right)\right]\\&+\left[\nabla\cdot\left(\rho_{\mathrm{m}}\vec{v}_{\mathrm{m}}\vec{v}_{\mathrm{m}}\right)-\nabla\cdot\left(g_{\mathrm{s}}\left\langle\rho_{\mathrm{s}}\right\rangle^{\mathrm{s}}\left\langle\vec{v}_{\mathrm{s}}\right\rangle^{\mathrm{s}}\left\langle\vec{v}_{\mathrm{s}}\right\rangle^{\mathrm{s}}\right)-\nabla\cdot\left(g_{\mathrm{l}}\left\langle\rho_{\mathrm{l}}\right\rangle^{\mathrm{l}}\left\langle\vec{v}_{\mathrm{l}}\right\rangle^{\mathrm{l}}\left\langle\vec{v}_{\mathrm{l}}\right\rangle^{\mathrm{l}}\right)\right]\\&+\mathcal{R}\left[g_{\mathrm{s}}\nabla\left\langle P_{\mathrm{l}}\right\rangle^{\mathrm{l}}+g_{\mathrm{l}}\left(\frac{\rho_{\mathrm{m}}}{\rho_{\mathrm{l}}}\right)\frac{\mu_{\mathrm{l}}}{K}\cdot\left(\vec{v}_{\mathrm{m}}-\vec{v}_{\mathrm{cast}}\right)\right]\\&+\left(1-\mathcal{R}\right)\left[\nabla\cdot\left(\mu_{\mathrm{m}}(\nabla\vec{v}_{\mathrm{m}})^{T}\right)+g_{\mathrm{s}}\vec{g}\left(\rho_{\mathrm{s}}^{\mathrm{ref}}-\rho_{\mathrm{l}}^{\mathrm{ref}}\right)\right.\\&\left.-g_{\mathrm{s}}\vec{g}\rho_{\mathrm{s}}^{\mathrm{ref}}\left[\beta_{\mathrm{s}}^{T}\left(T-T^{\mathrm{ref}}\right)+\beta_{\mathrm{s}}^{C}\left(\left\langle C_{\mathrm{s}}\right\rangle^{\mathrm{s}}-C^{\mathrm{ref}}\right)\right]\right].\end{aligned}\tag{4.109}$$

The effective viscosity is defined

$$\mu_{\mathrm{eff}}=\mathcal{R}\frac{\rho_{\mathrm{m}}}{\rho_{\mathrm{l}}}\mu_{\mathrm{l}}+(1-\mathcal{R})\mu_{\mathrm{m}}.\tag{4.110}$$

4.4.3 Energy Conservation

The energy equation of the one-phase model is obtained by adding the solid and liquid phase equations and taking into account the interfacial heat balance.

$$Q_{\mathrm{s}}^{\Gamma} + Q_{\mathrm{l}}^{\Gamma} + Q_{\mathrm{s}}^{q} + Q_{\mathrm{l}}^{q} = 0 \tag{4.111}$$

To facilitate the numerical solution, the diffusive term is expressed in terms of the leading variable h_{m}. The correction needed in the solidification and liquid zones is expressed as a correction term on the rhs of the equation.

$$\nabla \cdot (k_{\mathrm{m}} \nabla T) = \nabla \cdot \left(\frac{k_{\mathrm{m}}}{c_{p\mathrm{s}}} \nabla h_{\mathrm{m}} \right) - \nabla \cdot \left(\frac{k_{\mathrm{m}}}{c_{p\mathrm{s}}} \nabla h_{\mathrm{m}} - k_{\mathrm{m}} \nabla T \right) \tag{4.112}$$

The final equation is

$$\begin{aligned} \frac{\partial}{\partial t} (\rho_{\mathrm{m}} h_{\mathrm{m}}) + \nabla \cdot (\rho_{\mathrm{m}} h_{\mathrm{m}} \vec{v}_{\mathrm{m}}) &= \nabla \cdot \left(\frac{k_{\mathrm{m}}}{c_{p\mathrm{s}}} \nabla h_{\mathrm{m}} \right) - \nabla \cdot \left(\frac{k_{\mathrm{m}}}{c_{p\mathrm{s}}} \nabla h_{\mathrm{m}} - k_{\mathrm{m}} \nabla T \right) \\ &+ \left[\nabla \cdot (\rho_{\mathrm{m}} h_{\mathrm{m}} \vec{v}_{\mathrm{m}}) - \nabla \cdot \left(g_{\mathrm{s}} \langle \rho_{\mathrm{s}} \rangle^{\mathrm{s}} \langle h_{\mathrm{s}} \rangle^{\mathrm{s}} \langle \vec{v}_{\mathrm{s}} \rangle^{\mathrm{s}} \right) - \nabla \cdot \left(g_{\mathrm{l}} \langle \rho_{\mathrm{l}} \rangle^{\mathrm{l}} \langle h_{\mathrm{l}} \rangle^{\mathrm{l}} \langle \vec{v}_{\mathrm{l}} \rangle^{\mathrm{l}} \right) \right]. \end{aligned} \tag{4.113}$$

4.4.4 Species Conservation

The species equation of the one-phase model is obtained by adding the solid and liquid phase equations and taking into account the interfacial solute mass balance.

$$j_{\mathrm{s}}^{\Gamma} + j_{\mathrm{l}}^{\Gamma} + j_{\mathrm{s}}^{j} + j_{\mathrm{l}}^{j} = 0 \tag{4.114}$$

$$\begin{aligned} \frac{\partial}{\partial t} (\rho_{\mathrm{m}} C_{\mathrm{m}}) + \nabla \cdot (\rho_{\mathrm{m}} C_{\mathrm{m}} \vec{v}_{\mathrm{m}}) &= \nabla \cdot (\rho_{\mathrm{m}} D_{\mathrm{m}} \nabla C_{\mathrm{m}}) \\ &+ \nabla \cdot \left[\rho_{\mathrm{m}} C_{\mathrm{m}} \vec{v}_{\mathrm{m}} - g_{\mathrm{s}} \langle \rho_{\mathrm{s}} \rangle^{\mathrm{s}} \langle C_{\mathrm{s}} \rangle^{\mathrm{s}} \langle \vec{v}_{\mathrm{s}} \rangle^{\mathrm{s}} - g_{\mathrm{l}} \langle \rho_{\mathrm{l}} \rangle^{\mathrm{l}} \langle C_{\mathrm{l}} \rangle^{\mathrm{l}} \langle \vec{v}_{\mathrm{l}} \rangle^{\mathrm{l}} \right] \\ &+ \nabla \cdot \left[\rho_{\mathrm{m}} D_{\mathrm{m}} \nabla C_{\mathrm{m}} - g_{\mathrm{s}} \langle \rho_{\mathrm{s}} \rangle^{\mathrm{s}} D_{\mathrm{s}} \nabla \langle C_{\mathrm{s}} \rangle^{\mathrm{s}} - g_{\mathrm{l}} \langle \rho_{\mathrm{l}} \rangle^{\mathrm{l}} D_{\mathrm{l}} \nabla \langle C_{\mathrm{l}} \rangle^{\mathrm{l}} \right] \end{aligned} \tag{4.115}$$

4.4.5 Microsegregation Model

The phase quantities (f_{s}, f_{l}, $\langle h_{\mathrm{s}} \rangle^{\mathrm{s}}$, $\langle h_{\mathrm{l}} \rangle^{\mathrm{l}}$, $\langle C_{\mathrm{s}} \rangle^{\mathrm{s}}$, $\langle C_{\mathrm{l}} \rangle^{\mathrm{l}}$) and the temperature T, which still appear in the mixture transport equations (4.91), (4.107), (4.113), and (4.115) are determined from the leading quantities (h_{m} and C_{m}) by the supplementary microsegregation model. The model consists of descriptions of phase equilibria at the solid-liquid interface, thermodynamic

state, and microscopic species transport, simplified by the local equilibrium assumption (inverse lever rule). The three unknowns f_l, $\langle C_\mathrm{l}\rangle^\mathrm{l}$, and T are calculated by solving a system of three equations: the definition of mixture enthalpy—Eq. (4.116), deduced from Eqs. (4.87), and (4.62-4.63), the inverse lever rule—Eq. (4.117), which is deduced from Eqs. (4.87) and (4.120), and an additional equation, describing the linearized liquidus line—Eq. (4.118).

$$h_\mathrm{m}(T, f_\mathrm{l}) = h_\mathrm{ref} + \int_{T_\mathrm{ref}}^{T} c_{ps}(T)dT + f_\mathrm{l}\left[L_\mathrm{f} + \int_{T_\mathrm{f}}^{T}(c_{pl}(T) - c_{ps}(T))dT\right] \tag{4.116}$$

$$\langle C_\mathrm{l}\rangle^\mathrm{l}(C_\mathrm{m}, f_\mathrm{l}) = \frac{C_\mathrm{m}}{k_\mathrm{p} + f_\mathrm{l}(1 - k_\mathrm{p})} \tag{4.117}$$

$$T_\mathrm{L}(\langle C_\mathrm{l}\rangle^\mathrm{l}) = T_\mathrm{f} + m_\mathrm{L}\langle C_\mathrm{l}\rangle^\mathrm{l} \tag{4.118}$$

If we assume that the specific heats c_{ps} and c_{pl} do not depend on temperature but are constant, a quadratic equation for f_l is obtained by substitution of variables in Eqs. (4.116)-(4.118)

$$Af_\mathrm{l}^2 + Bf_\mathrm{l} + C = 0 \tag{4.119}$$

$$\begin{aligned}
A &= (k_\mathrm{p} - 1)L_\mathrm{f}\\
B &= (1 - k_\mathrm{p})(h_\mathrm{m} - h_\mathrm{fS}) - k_\mathrm{p}L_\mathrm{f} + (c_{pl} - c_{ps})(T_\mathrm{f} - T_\mathrm{L})\\
C &= k_\mathrm{p}(h_\mathrm{m} - h_\mathrm{fS}) + c_{ps}(T_\mathrm{f} - T_\mathrm{L})\\
h_\mathrm{fS} &= h_\mathrm{ref} + c_{ps}(T_\mathrm{f} - T_\mathrm{ref}),
\end{aligned}$$

where h_fS is the enthalpy of the pure solid phase at the melting temperature T_f. This equation is solved analytically for f_l. Then the remaining unknowns f_s, $\langle h_\mathrm{s}\rangle^\mathrm{s}$, and $\langle h_\mathrm{l}\rangle^\mathrm{l}$ can be directly determined from f_l and T using Eqs. (4.89), (4.62), and (4.63). The solid concentration $\langle C_\mathrm{s}\rangle^\mathrm{s}$ is determined by the partitioning that follows from the inverse lever rule.

$$\langle C_\mathrm{s}\rangle^\mathrm{s} = k_\mathrm{p}\langle C_\mathrm{l}\rangle^\mathrm{l} \tag{4.120}$$

4.4.6 Onset and Growth of Grains

The Free-Growth Model

In the casting of aluminum and aluminum alloys grain refinement is commonly used to achieve a finer grain structure and thus better mechanical properties of the cast material. Grain refinement involves the addition of master alloys (Al-Ti-B, Al-Ti-C, Al-Mg-Si, or Al-B) introducing inoculant

particles (e.g. TiB_2 particles in Al-Ti-B refiners, which consist of TiB_2 and Al_3Ti phases) into the melt. These particles act as nucleation sites (seed crystals) for α-Al grains, resulting in a uniformly fine, equiaxed cast microstructure.

Formerly, the onset of grain growth on inoculant particles was understood as a stochastic nucleation process. The classical spherical-cap model of heterogeneous nucleation [Kurz and Fisher, 1998] was used. According to this model, nucleation of a grain occurs when the crystal cluster (embryo) that forms by *stochastic* atomic additions on the inoculant particle (which is an energetically favorable site) in the form of a spherical cap, exceeds the critical radius corresponding to the momentary undercooling. Once the *stochastically* formed embryo is larger than the critical radius of the momentary undercooling, further growth leads to a decrease of the overall Gibbs free energy and so the crystallite can freely grow. This kind of stochastic formation of embryos is modeled with different models [Hecht *et al.*, 2004].

A few years ago, Greer et al. [Greer *et al.*, 2000] showed that this growth onset model is not applicable for grain-refined melts. They developed the free-growth model, which assumes that the embryo is formed on an inoculant particle at very low undercooling. It can continue to grow as long as its radius of curvature exceeds the critical radius. Since during its growth on the inoculant particle the spherically growing crystal has to go through a radius minimum, equal to the particle radius, the critical condition for free growth of the crystal is then the size of the particle. This means that the free growth of a crystallite on the inoculant particle begins as soon as the undercooling is reached, where the corresponding critical radius is equal to the particle radius. For usual grain refiner particle sizes this happens much faster and at much smaller undercoolings than the stochastic process can form embryos large enough for further growth. The growth onset is thus *deterministic* and is not controlled by the probability of stochastic formation of sufficiently large nuclei, but by the free-growth barrier. The thermodynamics of this barrier was investigated by Quested [Quested, 2004] and was shown to be controlled mainly by the size of inoculant particles.

When modeling the growth of the initiated crystal grains, Greer et al. [Greer *et al.*, 2000] justified the simplifying assumption of a locally isothermal melt and showed that the growth is controlled by the solute diffusion field in front of the solid-liquid interface. The solute-diffusion controlled growth rate of the spherical grain of radius r is

$$\frac{dr}{dt} = \frac{\lambda_s^2 D_s}{2r}, \tag{4.121}$$

where λ_s is a parameter, dependent on the liquidus slope m_L, solute partition

coefficient k_p, melt concentration $\langle C_\mathrm{l}\rangle^1$, and the solutal undercooling ΔT_us, which is

$$\Delta T_\mathrm{us} = m_\mathrm{L}\left(\langle C_\mathrm{l}\rangle^1 - C_\mathrm{il}\right). \tag{4.122}$$

The relations in the solutal diffusion layer producing the undercooling and controlling the growth are shown in Figs. 4.5 and 4.6(a).

Using the free-growth model, Greer et al. [Greer *et al.*, 2000] modeled the performance of the grain refiner by using an experimentally determined distribution of inoculant TiB_2 particles. The smaller particles need a larger undercooling to initiate free growth. In their calculations they show that soon after the growth onset on the largest inoculant particles (with diameters of about $3-6\,\mu$m, representing around 1% of all TiB_2 particles), which starts at undercoolings of the order of magnitude

$$\Delta T_\mathrm{fg} = \frac{4\sigma_\mathrm{i}}{\Delta S_V d_\mathrm{g}} \sim 0.1\,\mathrm{K}, \tag{4.123}$$

the latent heat release causes a temperature increase (recalescence) and thus entirely blocks the activation of smaller particles. In Eq. (4.123) σ_i is the solid-liquid interfacial energy, ΔS_V is the entropy of fusion per unit volume, and d_g is the inoculant particle diameter.

A Simplified Treatment

From these findings a first approximation of a model of grain onset and growth can be developed, whose primary aim is to model the grain size needed in the solid-velocity model (Eq. (4.36)). Two simplifying assumptions are extracted from the discussion of the free-growth model.

- The range of inoculant particle size, which effectively initiates growth, is rather limited and therefore the corresponding undercoolings needed for free growth are in a relatively narrow range. As the order of magnitude of these undercoolings is small $\Delta T_\mathrm{fg} \sim 0.1\,\mathrm{K}$, they are thermally certainly negligible. However, if the curvature undercooling and thus the free-growth barrier are not modeled, we cannot model the activation of the particles using the inoculant particle size distribution as in Greer's model. Instead, I introduce a parameter of *active particle density*. This is the number of particles per unit volume that actually initiate growth. All active particles are assumed to initiate growth at the local equilibrium liquidus temperature. The active particle density can be determined experimentally from the grain density in the casting or by a simulation by Greer's model, using the expected cooling rate and inoculant particle size distribution of the grain refiner. The

downside of this simplification is that by using a single value of active particle density the variation of the cooling rate in the casting is not taken into account.

- As shown in Fig. 4.6(a), the local fraction of the solid phase during solute-diffusion controlled growth must follow from the composition relations

$$f_\mathrm{s} = \frac{C_\mathrm{m} - \langle C_\mathrm{s}\rangle^\mathrm{s}}{\langle C_\mathrm{l}\rangle^\mathrm{l} - \langle C_\mathrm{s}\rangle^\mathrm{s}}, \tag{4.124}$$

whereas the solid-liquid interface is in thermodynamic equilibrium.

$$C_\mathrm{is} = k_\mathrm{p} C_\mathrm{il} \tag{4.125}$$

This means that in the framework of the present one-phase model the grain growth could be modeled by a microsegregation model that includes a microscale solute transport model accounting for solute diffusion in both phases. If the model is kept in the present simplified form, adapted for the equilibrium assumption (Section 4.4.5), the solutal undercooling could also be modeled by modified solidus and liquidus lines in the binary phase diagram, resp. a corrected solute partition coefficient k'_p, such that

$$\langle C_\mathrm{s}\rangle^\mathrm{s} = k'_\mathrm{p} \langle C_\mathrm{l}\rangle^\mathrm{l}, \tag{4.126}$$

as proposed by Ni and Incropera [Ni and Incropera, 1995b]. Such a corrected phase diagram would then give the solid fraction from Eq. (4.124) corresponding to the grain growth rate given by Eq. (4.121). Although this is not entirely consistent with the grain growth mechanism, I do not take into account the solutal undercooling in this first version of the model, but rather keep the local equilibrium assumption (Eq. (4.83)). Later, this can be improved by a more intricate microsegregation model.

Following from these two simplifying assumptions, the local grain size d_g is simply determined from the local grain density n_s (local density of active particles), and the solid mass fraction f_s.

$$d_\mathrm{g} = \sqrt[3]{\frac{6\rho_\mathrm{m} f_\mathrm{s}}{\pi \rho_\mathrm{s} n_\mathrm{s}}} \tag{4.127}$$

The solid mass fraction f_s is determined by the microsegregation model, described in Section 4.4.5. The local grain density n_s is determined by the grain transport model which uses the active particle density as a parameter and is given in the following section.

4.4.7 Transport of Grains

The transport of grains is described by an advective transport equation

$$\frac{\partial n_\mathrm{s}}{\partial t} + \nabla \cdot (n_\mathrm{s} \vec{v}_\mathrm{s}) = 0, \tag{4.128}$$

where n_s is the grain density—the number of grains per unit volume. The grain velocity $\vec{v}_\mathrm{s}$ is deduced from Eqs. (4.36), (4.37) and (4.87)

$$\vec{v}_\mathrm{s} = \mathcal{R}\vec{v}_\mathrm{cast} + (1 - \mathcal{R}) \left(\vec{v}_\mathrm{m} - \frac{f_\mathrm{l}^2 \rho_\mathrm{m} (\rho_\mathrm{l} - \rho_\mathrm{s}) d_\mathrm{g}^2 \vec{g}}{18 \rho_\mathrm{l} \mu_\mathrm{m}}, \right) \tag{4.129}$$

where the viscosity of the slurry is as given before (Section 4.3.3).

$$\mu_\mathrm{m} = \mu_\mathrm{l} \left[1 + 2.5 g_\mathrm{s} + 10.05 g_\mathrm{s}^2 + 0.00273 \exp(16.6 g_\mathrm{s}) \right] \tag{4.30}$$

At the melt inlet the grain density is prescribed at the active particle density n_apd. There is no generation of grains, only activation, which proceeds via the solid fraction. Once f_s exceeds zero, the grain diameter defines the grain velocity, which is different for different grain diameters and thus different across the slurry zone. In the liquid region, on the other hand, the "virtual" grain density remains uniform as the solid velocity is equal to the liquid velocity at a zero grain diameter.

4.5 Summary

The system of equations of the one-phase model is summarized in Tables 4.1 and 4.2.

Table 4.1: Transport equations

$$\frac{\partial \rho_{\mathrm{m}}}{\partial t} + \nabla \cdot (\rho_{\mathrm{m}} \vec{v}_{\mathrm{m}}) = 0 \tag{4.91}$$

$$\begin{aligned}\frac{\partial}{\partial t}(\rho_{\mathrm{m}}\vec{v}_{\mathrm{m}}) + \nabla \cdot (\rho_{\mathrm{m}}\vec{v}_{\mathrm{m}}\vec{v}_{\mathrm{m}}) &= -\nabla \langle P_{\mathrm{l}} \rangle^{\mathrm{l}} + \nabla \cdot (\mu_{\mathrm{eff}} \nabla \vec{v}_{\mathrm{m}}) \\ &\quad - g_{\mathrm{l}}\vec{g}\rho_{\mathrm{l}}^{\mathrm{ref}} \left[\beta_{\mathrm{l}}^{T}\left(T - T^{\mathrm{ref}}\right) + \beta_{\mathrm{l}}^{C}\left(\langle C_{\mathrm{l}} \rangle^{\mathrm{l}} - C^{\mathrm{ref}}\right)\right] \\ &\quad + \left[\nabla \cdot (\rho_{\mathrm{m}}\vec{v}_{\mathrm{m}}\vec{v}_{\mathrm{m}}) - \nabla \cdot (g_{\mathrm{s}} \langle \rho_{\mathrm{s}} \rangle^{\mathrm{s}} \langle \vec{v}_{\mathrm{s}} \rangle^{\mathrm{s}} \langle \vec{v}_{\mathrm{s}} \rangle^{\mathrm{s}}) - \nabla \cdot \left(g_{\mathrm{l}} \langle \rho_{\mathrm{l}} \rangle^{\mathrm{l}} \langle \vec{v}_{\mathrm{l}} \rangle^{\mathrm{l}} \langle \vec{v}_{\mathrm{l}} \rangle^{\mathrm{l}}\right)\right] \\ &\quad + \mathcal{R}\left[g_{\mathrm{s}} \nabla \langle P_{\mathrm{l}} \rangle^{\mathrm{l}} + g_{\mathrm{l}} \left(\frac{\rho_{\mathrm{m}}}{\rho_{\mathrm{l}}}\right) \frac{\mu_{\mathrm{l}}}{K} \cdot (\vec{v}_{\mathrm{m}} - \vec{v}_{\mathrm{cast}})\right] + (1 - \mathcal{R})\left[\nabla \cdot \left(\mu_{\mathrm{m}} (\nabla \vec{v}_{\mathrm{m}})^{T}\right)\right. \\ &\quad \left. + g_{\mathrm{s}}\vec{g}\left(\rho_{\mathrm{s}}^{\mathrm{ref}} - \rho_{\mathrm{l}}^{\mathrm{ref}}\right) - g_{\mathrm{s}}\vec{g}\rho_{\mathrm{s}}^{\mathrm{ref}}\left[\beta_{\mathrm{s}}^{T}\left(T - T^{\mathrm{ref}}\right) + \beta_{\mathrm{s}}^{C}\left(\langle C_{\mathrm{s}} \rangle^{\mathrm{s}} - C^{\mathrm{ref}}\right)\right]\right]\end{aligned} \tag{4.109}$$

$$\begin{aligned}\frac{\partial}{\partial t}(\rho_{\mathrm{m}} h_{\mathrm{m}}) + \nabla \cdot (\rho_{\mathrm{m}} h_{\mathrm{m}} \vec{v}_{\mathrm{m}}) &= \nabla \cdot \left(\frac{k_{\mathrm{m}}}{c_{ps}} \nabla h_{\mathrm{m}}\right) - \nabla \cdot \left(\frac{k_{\mathrm{m}}}{c_{ps}} \nabla h_{\mathrm{m}} - k_{\mathrm{m}} \nabla T\right) \\ &\quad + \left[\nabla \cdot (\rho_{\mathrm{m}} h_{\mathrm{m}} \vec{v}_{\mathrm{m}}) - \nabla \cdot (g_{\mathrm{s}} \langle \rho_{\mathrm{s}} \rangle^{\mathrm{s}} \langle h_{\mathrm{s}} \rangle^{\mathrm{s}} \langle \vec{v}_{\mathrm{s}} \rangle^{\mathrm{s}}) - \nabla \cdot \left(g_{\mathrm{l}} \langle \rho_{\mathrm{l}} \rangle^{\mathrm{l}} \langle h_{\mathrm{l}} \rangle^{\mathrm{l}} \langle \vec{v}_{\mathrm{l}} \rangle^{\mathrm{l}}\right)\right]\end{aligned} \tag{4.113}$$

$$\begin{aligned}\frac{\partial}{\partial t}(\rho_{\mathrm{m}} C_{\mathrm{m}}) + \nabla \cdot (\rho_{\mathrm{m}} C_{\mathrm{m}} \vec{v}_{\mathrm{m}}) &= \nabla \cdot (\rho_{\mathrm{m}} D_{\mathrm{m}} \nabla C_{\mathrm{m}}) \\ &\quad + \nabla \cdot \left[\rho_{\mathrm{m}} C_{\mathrm{m}} \vec{v}_{\mathrm{m}} - g_{\mathrm{s}} \langle \rho_{\mathrm{s}} \rangle^{\mathrm{s}} \langle C_{\mathrm{s}} \rangle^{\mathrm{s}} \langle \vec{v}_{\mathrm{s}} \rangle^{\mathrm{s}} - g_{\mathrm{l}} \langle \rho_{\mathrm{l}} \rangle^{\mathrm{l}} \langle C_{\mathrm{l}} \rangle^{\mathrm{l}} \langle \vec{v}_{\mathrm{l}} \rangle^{\mathrm{l}}\right] \\ &\quad + \nabla \cdot \left[\rho_{\mathrm{m}} D_{\mathrm{m}} \nabla C_{\mathrm{m}} - g_{\mathrm{s}} \langle \rho_{\mathrm{s}} \rangle^{\mathrm{s}} D_{\mathrm{s}} \nabla \langle C_{\mathrm{s}} \rangle^{\mathrm{s}} - g_{\mathrm{l}} \langle \rho_{\mathrm{l}} \rangle^{\mathrm{l}} D_{\mathrm{l}} \nabla \langle C_{\mathrm{l}} \rangle^{\mathrm{l}}\right]\end{aligned} \tag{4.115}$$

$$\frac{\partial n_{\mathrm{s}}}{\partial t} + \nabla \cdot (n_{\mathrm{s}} \vec{v}_{\mathrm{s}}) = 0, \tag{4.128}$$

Table 4.2: Constitutional laws and mixture relations

$$\begin{aligned} \rho_\mathrm{m} &= g_\mathrm{s}\rho_\mathrm{s} + g_\mathrm{l}\rho_\mathrm{l} & \vec{v}_\mathrm{m} &= f_\mathrm{s}\vec{v}_\mathrm{s} + f_\mathrm{l}\vec{v}_\mathrm{l} \\ k_\mathrm{m} &= g_\mathrm{s}k_\mathrm{s} + g_\mathrm{l}k_\mathrm{l} & D_\mathrm{m} &= f_\mathrm{s}D_\mathrm{s} + f_\mathrm{l}D_\mathrm{l} \end{aligned} \tag{4.87}$$

$$g_\mathrm{k} = \frac{\rho_\mathrm{m}}{\rho_\mathrm{l}} f_\mathrm{k} \tag{4.88}$$

$$f_\mathrm{s} + f_\mathrm{l} = 1 \tag{4.89}$$

$$\mathcal{R}(\vec{x},t) = \begin{cases} 1 & g_\mathrm{s}(\vec{x},t) > g_\mathrm{s}^\mathrm{c} \\ 0 & g_\mathrm{s}(\vec{x},t) \leq g_\mathrm{s}^\mathrm{c} \end{cases} \tag{4.108}$$

$$\vec{v}_\mathrm{s} = \mathcal{R}\vec{v}_\mathrm{cast} + (1-\mathcal{R})\left(\vec{v}_\mathrm{m} - \frac{f_\mathrm{l}^2\rho_\mathrm{m}(\rho_\mathrm{l}-\rho_\mathrm{s})d_\mathrm{g}^2\vec{g}}{18\rho_\mathrm{l}\mu_\mathrm{m}}\right) \tag{4.129}$$

$$d_\mathrm{g} = \sqrt[3]{\frac{6\rho_\mathrm{m}f_\mathrm{s}}{\pi\rho_\mathrm{s}n_\mathrm{s}}} \tag{4.127}$$

$$\mu_\mathrm{m} = \mu_\mathrm{l}\left[1 + 2.5g_\mathrm{s} + 10.05g_\mathrm{s}^2 + 0.00273\exp(16.6g_\mathrm{s})\right] \tag{4.30}$$

$$\mu_\mathrm{eff} = \mathcal{R}\mu_\mathrm{l} + (1-\mathcal{R})\mu_\mathrm{m} \tag{4.110}$$

$$K = K_0\frac{g_\mathrm{l}^3}{(1-g_\mathrm{l})^2} \tag{4.99}$$

$$h_\mathrm{s}(T) = h_\mathrm{ref} + \int_{T_\mathrm{ref}}^{T} c_{p\mathrm{s}}(T)dT \tag{4.62}$$

$$h_\mathrm{l}(T) = h_\mathrm{ref} + \int_{T_\mathrm{ref}}^{T_\mathrm{m}} c_{p\mathrm{s}}(T)dT + L_\mathrm{f} + \int_{T_\mathrm{m}}^{T} c_{p\mathrm{l}}(T)dT \tag{4.63}$$

$$h_\mathrm{m}(T,f_\mathrm{l}) = h_\mathrm{ref} + \int_{T_\mathrm{ref}}^{T} c_{p\mathrm{s}}(T)dT + f_\mathrm{l}\left[L_\mathrm{f} + \int_{T_\mathrm{f}}^{T}(c_{p\mathrm{l}}(T) - c_{p\mathrm{s}}(T))dT\right] \tag{4.116}$$

$$C_\mathrm{l}(C_\mathrm{m},f_\mathrm{l}) = \frac{C_\mathrm{m}}{k_\mathrm{p} + f_\mathrm{l}(1-k_\mathrm{p})} \tag{4.117}$$

$$T(C_\mathrm{l}) = T_\mathrm{f} + m_\mathrm{L}C_\mathrm{l} \tag{4.118}$$

$$\langle C_\mathrm{s}\rangle^\mathrm{l} = k_\mathrm{p}\langle C_\mathrm{l}\rangle^\mathrm{s} \tag{4.120}$$

5 Numerical Method

> So far I have paid piece rates for the operation $\partial_x^2 + \partial_y^2$ of about $\frac{n}{18}$ pence per coordinate point, n being the number of digits. The chief trouble to the computers has been the intermixture of plus and minus signs. As to the rate of working, one of the quickest boys averaged 2000 operations $\partial_x^2 + \partial_y^2$ per week, for three digits, those done wrong discounted.
>
> Lewis F. Richardson

5.1 Introduction

In this chapter I describe the method of numerically solving the model equations developed in the previous chapter. To solve the continuum transport equations the well-established finite volume method was used. I will only explain the basic features of the method and focus primarily on the specifics of the implementation of the method in the DC casting model. After a general explanation of the method and the discretization technique, I discuss in detail the discretization of the advection and viscous terms, the computation of the phase velocities and phase mass fluxes, the implementation of the flow regime function, and the introduction of the Darcy function which enables the solution of the momentum equation in the porous regime at high g_s. Further, I comment on the specifics of the pressure-velocity coupling scheme with a collocated variable arrangement and a scaled pressure term and specify in detail the SIMPLE-based iterative solution scheme for the coupled model equations. Finally, I explain the approach to the solution of the linear equation system given by the discretized equations and give suggestions for its improvement.

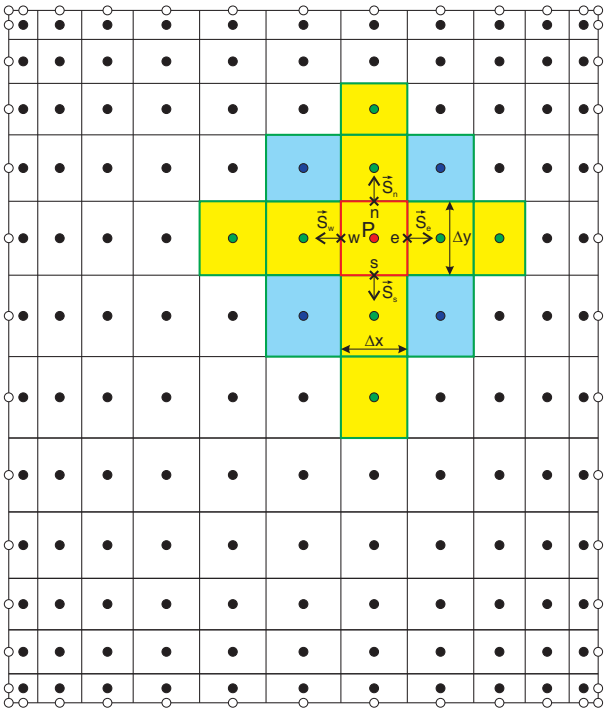

Figure 5.1: Finite volume grid. Control volumes, control volume nodes (•) and boundary nodes (∘), faces of the control volume P in compass notation ($\vec{S}_i$), grid distances (Δx, Δy) and interpolation stencil (yellow+blue).

5.2 Finite Volume Method

The main principle of the finite volume method is the subdivision of the problem domain into small polygonal *control volumes* (CVs) over which the equations are integrated (Fig. 5.1). The integrations over each CV are approximated by numerical integration formulae using field values represented in computational *nodes*. This finally gives the discretized linear equation system that is then solved by an appropriate linear system solver. The *volume integrals* of terms that contain a divergence term are converted to *surface integrals*, using the divergence theorem (Gauss's theorem). This means that these terms are evaluated as fluxes over the surfaces of each control volume. Because the flux entering a given volume is identical to that leaving the adjacent volume, the method is locally and globally conservative.

The method will only be described for orthogonal structured grids with rectangular CVs, which are used in the developed numerical model. Moreover, only specific approaches for the approximation of the integrations, gradients, function interpolation etc., that were used in the developed numerical code, are to be explained. The method can be extended to unstructured grids,

curved coordinate systems, general polyhedral CVs, higher-order approximation functions etc. More on these topics can be found in the literature (e.g. [Ferziger and Perić, 1996, Peyret, 2000, Fletcher *et al.*, 1991, Roache, 1998a]).

5.2.1 Discretization of the Macroscopic Equations

As already said, we develop the finite volume method by integrating the general transport equation for the scalar quantity ϕ over the fixed control volume Ω.

$$\underbrace{\frac{\partial(\rho\phi)}{\partial t}}_{\text{Transient term}} + \underbrace{\nabla\cdot(\rho\vec{v}\phi)}_{\text{Advection term}} = \underbrace{\nabla\cdot(\Gamma\nabla\phi)}_{\text{Diffusion term}} + \underbrace{Q_\Omega}_{\text{Source term}} \tag{5.1}$$

$$\int_\Omega \frac{\partial(\rho\phi)}{\partial t}d\Omega + \int_\Omega \nabla\cdot(\rho\vec{v}\phi)d\Omega = \int_\Omega \nabla\cdot(\Gamma\nabla\phi)\,d\Omega + \int_\Omega Q_\Omega d\Omega \tag{5.2}$$

Using the divergence theorem

$$\int_\Omega (\nabla\cdot\vec{F})d\Omega = \oint_{S\equiv\partial\Omega} \vec{F}\cdot d\vec{S}\,, \tag{5.3}$$

the diffusion and advection term are transformed into surface integrals over the surface of the integration volume and we obtain

$$\frac{\partial}{\partial t}\int_\Omega \rho\phi\,d\Omega + \oint_S \rho\vec{v}\phi\cdot d\vec{S} = \oint_S \Gamma\nabla\phi\cdot d\vec{S} + \int_\Omega Q_\Omega d\Omega. \tag{5.4}$$

The transient term is integrated over the control volume Ω using a second-order approximation of the mean value in the CV by the value at the CV center node. The time derivative can be approximated in different ways. We use the implicit first-order (implicit Euler) approximation with the time step Δt.

$$\overline{\frac{\partial}{\partial t}\int_\Omega \rho\phi\,d\Omega} = \frac{\Delta\Omega(\rho_\mathrm{P}\phi_\mathrm{P} - \rho_\mathrm{P}^\mathrm{old}\phi_\mathrm{P}^\mathrm{old})}{\Delta t} + O\left((\Delta x)^2\right) + O(\Delta t) \tag{5.5}$$

The overbar denotes the discrete approximation of the term for CV 'P', the superscript 'old' denotes values from the preceding timestep, $\Delta\Omega$ is the CV volume, Δx is the representative discretization length, and Δt is the timestep.

The advection term is integrated over the surface, i.e. the four faces of the rectangular CV, usually denoted in compass notation as north ('n'), south

('s'), east ('e') and west ('w') faces. To perform the integration we need to know the value of $(\rho\vec{v}\phi)$ everywhere on the CV face. Since this is not available we have to use some kind of approximation. The first level of approximation is to approximate the flux integral in terms of variable values along the CV face. The simplest for this purpose is the midpoint rule, where the integral is approximated as the product of the integrand at the face center and the face area, which is a second-order accurate approximation.

$$\begin{aligned}\overline{\oint_S \rho\vec{v}\phi \cdot d\vec{S}} &= \overline{(\rho\vec{v}\phi)}_{\mathrm{e}} \cdot \vec{A}_{\mathrm{e}} + \overline{(\rho\vec{v}\phi)}_{\mathrm{w}} \cdot \vec{A}_{\mathrm{w}} + \overline{(\rho\vec{v}\phi)}_{\mathrm{n}} \cdot \vec{A}_{\mathrm{n}} + \overline{(\rho\vec{v}\phi)}_{\mathrm{s}} \cdot \vec{A}_{\mathrm{s}} \\ &\quad + O\left((\Delta x)^2\right) \\ &= -\overline{(\rho u\phi)}_{\mathrm{e}} A_{\mathrm{e}} + \overline{(\rho u\phi)}_{\mathrm{w}} A_{\mathrm{w}} - \overline{(\rho v\phi)}_{\mathrm{n}} A_{\mathrm{n}} + \overline{(\rho v\phi)}_{\mathrm{s}} A_{\mathrm{s}} \\ &\quad + O\left((\Delta x)^2\right) \\ &= -(\rho u)_{\mathrm{e}} A_{\mathrm{e}} \phi_{\mathrm{e}} + (\rho u)_{\mathrm{w}} A_{\mathrm{w}} \phi_{\mathrm{w}} - (\rho v)_{\mathrm{n}} A_{\mathrm{n}} \phi_{\mathrm{n}} + (\rho v)_{\mathrm{s}} A_{\mathrm{s}} \phi_{\mathrm{s}} \\ &\quad + O\left((\Delta x)^2\right),\end{aligned} \tag{5.6}$$

where A is the area of the respective CV face. The mass fluxes across the CV surfaces are assumed to be known from the velocity field solution and we denote them

$$F_{\mathrm{w}} = (\rho u)_{\mathrm{w}} A_{\mathrm{w}} \tag{5.7a}$$
$$F_{\mathrm{e}} = (\rho u)_{\mathrm{e}} A_{\mathrm{e}} \tag{5.7b}$$
$$F_{\mathrm{s}} = (\rho v)_{\mathrm{s}} A_{\mathrm{s}} \tag{5.7c}$$
$$F_{\mathrm{n}} = (\rho v)_{\mathrm{n}} A_{\mathrm{n}}. \tag{5.7d}$$

Thus we write

$$\overline{\oint_S \rho\vec{v}\phi \cdot d\vec{S}} = F_{\mathrm{e}}\phi_{\mathrm{e}} - F_{\mathrm{w}}\phi_{\mathrm{w}} + F_{\mathrm{n}}\phi_{\mathrm{n}} - F_{\mathrm{s}}\phi_{\mathrm{s}} + O\left((\Delta x)^2\right). \tag{5.8}$$

Since the values of ϕ at the CV faces are not available, a second level of approximation has to be used to obtain them by interpolation of the node values. Numerous interpolation methods can be used. When the influence of advection in the transport problem is large compared to diffusion, the choice of the interpolation function has a key impact on the overall accuracy of the FVM approximation. This is a very important issue in the problems tackled with the model developed in this dissertation and will be explained in more detail later on. For now, we leave the advective term as it is at the first approximation level.

The diffusion term is approximated using the midpoint rule and the central difference scheme (CDS) approximation of the normal derivative.

$$\begin{aligned}\overline{\oint_S \Gamma\nabla\phi\cdot d\vec{S}} &= \left(\Gamma\frac{\partial\phi}{\partial x}\right)_{\mathrm{e}} A_{\mathrm{e}} - \left(\Gamma\frac{\partial\phi}{\partial x}\right)_{\mathrm{w}} A_{\mathrm{w}} + \left(\Gamma\frac{\partial\phi}{\partial y}\right)_{\mathrm{n}} A_{\mathrm{n}} \\ &\quad - \left(\Gamma\frac{\partial\phi}{\partial y}\right)_{\mathrm{s}} A_{\mathrm{s}} + O\left((\Delta x)^2\right) \\ &= \Gamma_{\mathrm{e}}\frac{\phi_{\mathrm{E}}-\phi_{\mathrm{P}}}{x_{\mathrm{E}}-x_{\mathrm{P}}}A_{\mathrm{e}} - \Gamma_{\mathrm{w}}\frac{\phi_{\mathrm{P}}-\phi_{\mathrm{W}}}{x_{\mathrm{P}}-x_{\mathrm{W}}}A_{\mathrm{w}} + \Gamma_{\mathrm{n}}\frac{\phi_{\mathrm{N}}-\phi_{\mathrm{P}}}{y_{\mathrm{N}}-y_{\mathrm{P}}}A_{\mathrm{n}} \\ &\quad - \Gamma_{\mathrm{s}}\frac{\phi_{\mathrm{P}}-\phi_{\mathrm{S}}}{y_{\mathrm{P}}-y_{\mathrm{S}}}A_{\mathrm{s}} + \underbrace{O\left(\Delta x(r-1)+(\Delta x)^2\right)}_{\approx O((\Delta x)^2)}\end{aligned} \tag{5.9}$$

The CDS approximation of the gradient is formally first-order accurate on nonuniform grids, but the first-order error term scales with $(r-1)$, where $r = (\Delta x^{i+1})/(\Delta x^i)$ is the grid refinement factor. r is usually only slightly different than unity and the approximation therefore approaches second-order accuracy on reasonably arranged grids.

The source term is split into a linear part $S_\phi\phi$ dependent on ϕ and a constant source S_C (which can depend on other variables). It is then integrated over the CV volume using an approximation for the mean values of $\overline{S}_\phi$ and $\overline{S}_C$ and the center-node approximation of the mean value of ϕ, which was already used for the transient term. The splitting of the source term is made to put the linear part to the LHS of the equation and the constant part on the RHS.

$$\overline{\int_\Omega Q_\Omega d\Omega} = \overline{\int_\Omega (Q_\phi\phi + S_C)d\Omega} = \overline{Q}_\phi\phi_{\mathrm{P}}\Delta\Omega + \overline{Q}_C\Delta\Omega + O\left((\Delta x)^2\right) \tag{5.10}$$

5.3 Specific Issues

5.3.1 Discretization Scheme for Advection

As mentioned before, we have to know the values of the field variable ϕ at the CV faces to evaluate the advective fluxes. Since the values of ϕ are only known at the CV nodes we have to get the face values by *interpolation* of the nodal values. Numerous interpolation schemes can be used for this. I show those used in the model implemented within the present work.

A proper choice of the discretization scheme is critical for the quality of the numerical solution of the model equations in the parameter range of interest in casting. Advection is the most important transport mode for species

Table 5.1: Terms of the transport equations

ϕ	Γ	Volumetric source term	Surface force	Correction Flux
u_m	μ_eff	$\mathcal{R}\left[g_\mathrm{l}\left(\frac{\rho_\mathrm{m}}{\rho_\mathrm{l}}\right)\frac{\mu_\mathrm{l}}{K}u_\mathrm{m}\right]$	$\frac{\partial p}{\partial x}$	$[\nabla\cdot(\rho_\mathrm{m}\vec{v}_\mathrm{m}\vec{v}_\mathrm{m})-\nabla\cdot(g_\mathrm{s}\rho_\mathrm{s}\vec{v}_\mathrm{s}\vec{v}_\mathrm{s})-\nabla\cdot(g_\mathrm{l}\rho_\mathrm{l}\vec{v}_\mathrm{l}\vec{v}_\mathrm{l})]$ $+(1-\mathcal{R})\nabla\cdot\left(\mu_\mathrm{m}(\nabla\vec{v}_\mathrm{m})^T\right)$
v_m	μ_eff	$-\vec{g}\rho_\mathrm{l}^\mathrm{ref}\left[\beta_\mathrm{l}^T\left(T-T_\mathrm{ref}\right)+\beta_\mathrm{l}^C\left(C_\mathrm{l}-C_\mathrm{ref}\right)\right]$ $+(1-\mathcal{R})\left[g_\mathrm{s}\vec{g}\left(\rho_\mathrm{s}^\mathrm{ref}-\rho_\mathrm{l}^\mathrm{ref}\right)\right.$ $\left.-g_\mathrm{s}\vec{g}\rho_\mathrm{s}^\mathrm{ref}\left[\beta_\mathrm{s}^T\left(T-T_\mathrm{ref}\right)+\beta_\mathrm{s}^C\left(C_\mathrm{s}-C_\mathrm{ref}\right)\right]\right]$ $+\mathcal{R}\left[g_\mathrm{l}\left(\frac{\rho_\mathrm{m}}{\rho_\mathrm{l}}\right)\frac{\mu_\mathrm{l}}{K}\left(v_\mathrm{m}-v_\mathrm{cast}\right)\right]$	$\frac{\partial p}{\partial y}$	$[\nabla\cdot(\rho_\mathrm{m}\vec{v}_\mathrm{m}\vec{v}_\mathrm{m})-\nabla\cdot(g_\mathrm{s}\rho_\mathrm{s}\vec{v}_\mathrm{s}\vec{v}_\mathrm{s})-\nabla\cdot(g_\mathrm{l}\rho_\mathrm{l}\vec{v}_\mathrm{l}\vec{v}_\mathrm{l})]$ $+(1-\mathcal{R})\nabla\cdot\left(\mu_\mathrm{m}(\nabla\vec{v}_\mathrm{m})^T\right)$
h_m	$\frac{\lambda_\mathrm{m}}{c_{ps}}$	0	0	$[\nabla\cdot(\rho_\mathrm{m}h_\mathrm{m}\vec{v}_\mathrm{m})-\nabla\cdot(g_\mathrm{s}\rho_\mathrm{s}h_\mathrm{s}\vec{v}_\mathrm{s})-\nabla\cdot(g_\mathrm{l}\rho_\mathrm{l}h_\mathrm{l}\vec{v}_\mathrm{l})]$ $-\nabla\cdot\left(\frac{\lambda_\mathrm{m}}{c_{ps}}\nabla h_\mathrm{m}-\lambda_\mathrm{m}\nabla T\right)$
C_m	$\rho_\mathrm{m}D_\mathrm{m}$	0	0	$\nabla\cdot[\rho_\mathrm{m}C_\mathrm{m}\vec{v}_\mathrm{m}-g_\mathrm{s}\rho_\mathrm{s}C_\mathrm{s}\vec{v}_\mathrm{s}-g_\mathrm{l}\rho_\mathrm{l}C_\mathrm{l}\vec{v}_\mathrm{l}]$ $+\nabla\cdot[\rho_\mathrm{m}D_\mathrm{m}\nabla C_\mathrm{m}-g_\mathrm{s}\rho_\mathrm{s}D_\mathrm{s}\nabla C_\mathrm{s}-g_\mathrm{l}\rho_\mathrm{l}D_\mathrm{l}\nabla C_\mathrm{l}]$
n_s	0	0	0	0

and momentum. Due to very low species diffusion coefficients and viscosities in liquid metals and relatively large flow velocities it strongly dominates over diffusion. To be able to obtain a reasonably accurate numerical result we therefore rely on sufficient accuracy of the advection term approximation. This is critical because the rate of grid convergence of the numerical result towards the exact solution depends on the order of accuracy of the discrete approximation. The numerical solution f_i of a p-th order method on grid spacing Δx_i relates to the exact solution f_{exact} by

$$f_i = f_{\text{exact}} + O\left((\Delta x_i)^p\right). \tag{5.11}$$

With grid refinement from grid spacing Δx_i to Δx_{i+1} and the corresponding solutions f_i and f_{i+1} the discretization error then evolves as

$$\frac{f_{i+1} - f_{\text{exact}}}{f_i - f_{\text{exact}}} = \left(\frac{\Delta x_{i+1}}{\Delta x_i}\right)^p. \tag{5.12}$$

Eq. (5.12) clearly shows why the order of accuracy of the discretization method is crucial for obtaining reasonable accuracy on reasonable grid sizes. Generally, at least second-order accuracy is desired. The problem with second- and higher-order discretizations of the advection term is that they are only conditionally stable. Godunov's monotonicity theorem [Murthy, 2002] proves that *linear* monotonicity-preserving (not prone to oscillations) discretization schemes are at best first-order accurate.

The interpolation is always shown for the east face 'e'. It is analogous for face 'n'.

Central Difference Scheme

The most straightforward way is to use the linear interpolation of two adjacent nodal values, which implies a locally linear variation of ϕ (Fig. 5.2(a))

$$\phi_{\text{e}} = I_{\text{e}}\phi_{\text{E}} + (1 - I_{\text{e}})\phi_{\text{P}} + O\left((\Delta x)^2\right) \tag{5.13}$$

$$I_{\text{e}} = \frac{x_{\text{e}} - x_{\text{P}}}{x_{\text{E}} - x_{\text{P}}}, \tag{5.14}$$

where I_{e} is the linear interpolation coefficient for CV face 'e'. This is termed the central difference scheme (CDS). The Taylor series expansion can show that its truncation error is $O((\Delta x)^2)$ (second-order accurate). The second-order accuracy means a good accuracy performance of the CDS scheme and makes it a good choice. The problem is that in the case of a strongly predominant advection the CDS scheme becomes numerically unstable and produces oscillations in the solution. We thus seek a remedy. In accordance with Godunov's monotonicity theorem the most robust solution to the problem of numerical instability is hence the use of a first-order scheme.

First-Order Upwind Scheme

The most commonly used remedy to the instability of higher-order discretization schemes is the first-order upwind scheme, which is unconditionally stable according to Godunov's theorem. The face value of ϕ is approximated by the upstream nodal value and thus depends on the direction of the mass flux across the CV face F_e (Fig. 5.2(b)).

$$\phi_\mathrm{e} = \max\left[\mathrm{sgn}(F_\mathrm{e}), 0\right]\phi_\mathrm{P} + \max\left[\mathrm{sgn}(-F_\mathrm{e}), 0\right]\phi_\mathrm{E} + O\left(\Delta x\right) \tag{5.15}$$

$$-\phi_\mathrm{e}F_\mathrm{e}A_\mathrm{e} = -\max[F_\mathrm{e}, 0]\phi_\mathrm{P}A_\mathrm{e} + \max[-F_\mathrm{e}, 0]\phi_\mathrm{E}A_\mathrm{e} + O\left(\Delta x\right) \tag{5.16}$$

The first-order method is not a legitimate remedy to the stability problem. The leading first-order error term is proportional to Δx, which means very slow grid convergence that often prevents the achieving of sufficiently accurate results on reasonably large computational grids. From a Taylor expansion of ϕ around face 'e' it can be easily shown that the leading error term of the approximation of ϕ_e is

$$\left(\frac{\partial\phi}{\partial x}\right)_\mathrm{e}\frac{\Delta x}{2}. \tag{5.17}$$

The leading discretization error term is thus proportional to the discretized diffusion term. This type of error leads to results that often appear to be physically sensible, as they would with stronger diffusion. This does not present a large problem so long as the diffusion term is dominant as the error in the advection term remains small in the overall transport. In any case, the use of UDS is not necessary in these cases as higher-order schemes are stable enough. The use of UDS becomes tempting as a cure to numerical instability at strong advection. As advection becomes more prominent, the impact of the quasi-diffusive discretization error (also termed numerical or false diffusion) on the solution becomes larger. The impact of the first-order discretization error is thus particularly unacceptable just in those situations where a stable scheme is most needed. However, with the development of various stabilized higher-order schemes there is actually no real justification for the use of first-order schemes any more [Leonard and Drummond, 1995].

QUICK

Seeking an alternative to overcome the problems with instability of the CDS and the large discretization errors of the UDS, we look for a discretization scheme that will be both accurate and stable for the problems of interest. During the development of the DC casting model it turned out that the QUICK (Quadratic Upwind Interpolation for Convective Kinematics) [Leonard, 1997]

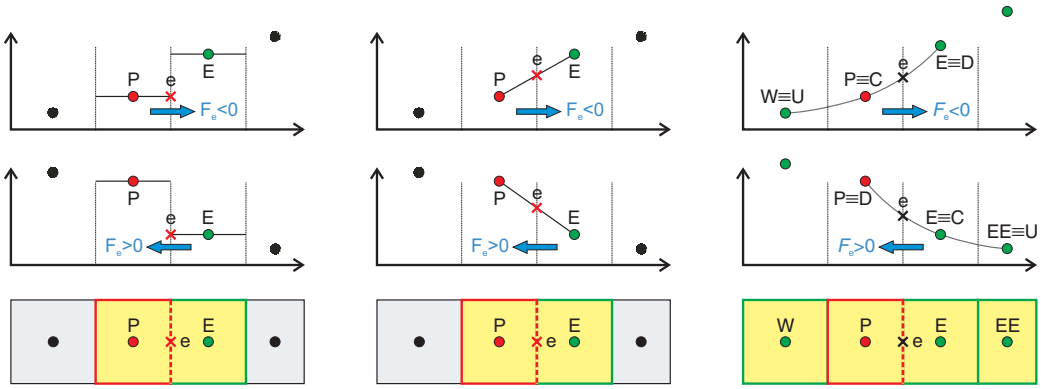

(a) 1st-order upwind (b) Central difference (c) QUICK

Figure 5.2: Interpolation of the CV 'e' face value in the advection term with different interpolation schemes.

scheme gives sufficient stability (preventing numerical oscillations) combined with excellent accuracy. The QUICK scheme approximates the local variation of ϕ by a one-dimensional second-order polynomial (parabola). To construct a parabola we need three interpolation nodes. In addition to the two nodes adjacent to the CV face ('P' and 'E') the third point is chosen in accordance with the flow direction across the CV face (upwinding). We then interpolate over the upstream ('U'), center ('C') and downstream ('D') nodes (Fig. 5.2(c)). The profile of ϕ between the 'C' and 'D' nodes is then defined by the interpolation parabola

$$\begin{aligned}\phi(x) = &\frac{(x-x_\mathrm{D})(x-x_\mathrm{C})}{(x_\mathrm{E}-x_\mathrm{U})(x_\mathrm{C}-x_\mathrm{U})}\,\phi_\mathrm{U} + \frac{(-x+x_\mathrm{D})(x-x_\mathrm{U})}{(x_\mathrm{E}-x_\mathrm{C})(x_\mathrm{C}-x_\mathrm{U})}\,\phi_\mathrm{C} \\ &+ \frac{(x-x_\mathrm{C})(x-x_\mathrm{U})}{(x_\mathrm{E}-x_\mathrm{C})(x_\mathrm{D}-x_\mathrm{U})}\,\phi_\mathrm{D}\end{aligned} \tag{5.18}$$

To implement the interpolation for face 'e' we choose the interpolation nodes according to the sign of F_e as shown in Fig. 5.2(c). If $F_\mathrm{e} > 0$, 'U'≡'W', 'C'≡'P', and 'D'≡'E'. If $F_\mathrm{e} < 0$, 'U'≡'EE', 'C'≡'E', and 'D'≡'P'. In general notation this formulates ϕ_e in terms of values in *four* adjacent nodes: ϕ_W, ϕ_P, ϕ_E, and ϕ_EE.

$$\begin{aligned}\phi_\mathrm{e} = &\left[\mathrm{sgn}(F_\mathrm{e}), 0\right]\left(Q_\mathrm{e}^{1\mathrm{u}}\phi_\mathrm{W} + Q_\mathrm{e}^{1\mathrm{c}}\phi_\mathrm{P} + Q_\mathrm{e}^{1\mathrm{d}}\phi_\mathrm{E}\right) \\ &+ \left[\mathrm{sgn}(-F_\mathrm{e}), 0\right]\left(Q_\mathrm{e}^{2\mathrm{u}}\phi_\mathrm{EE} + Q_\mathrm{e}^{2\mathrm{c}}\phi_\mathrm{E} + Q_\mathrm{e}^{2\mathrm{d}}\phi_\mathrm{P}\right)\end{aligned} \tag{5.19}$$

The convective flux of ϕ is then

$$\begin{aligned} -\phi_{\mathrm{e}} F_{\mathrm{e}} A_{\mathrm{e}} = &- \phi_{\mathrm{W}} Q_{\mathrm{e}}^{1\mathrm{u}} \max[F_{\mathrm{e}}, 0] A_{\mathrm{e}} \\ &+ \phi_{\mathrm{P}} \left(-Q_{\mathrm{e}}^{1\mathrm{c}} \max[F_{\mathrm{e}}, 0] + Q_{\mathrm{e}}^{2\mathrm{d}} \max[-F_{\mathrm{e}}, 0] \right) A_{\mathrm{e}} \\ &+ \phi_{\mathrm{E}} \left(-Q_{\mathrm{e}}^{1\mathrm{d}} \max[F_{\mathrm{e}}, 0] + Q_{\mathrm{e}}^{2\mathrm{c}} \max[-F_{\mathrm{e}}, 0] \right) A_{\mathrm{e}} \\ &+ \phi_{\mathrm{EE}} Q_{\mathrm{e}}^{2\mathrm{u}} \max[-F_{\mathrm{e}}, 0] A_{\mathrm{e}}, \end{aligned} \tag{5.20}$$

where the quadratic interpolation coefficients are

$$Q_{\mathrm{e}}^{1\mathrm{u}} = \frac{(x_{\mathrm{e}} - x_{\mathrm{E}})(x_{\mathrm{e}} - x_{\mathrm{P}})}{(x_{\mathrm{E}} - x_{\mathrm{W}})(x_{\mathrm{P}} - x_{\mathrm{W}})} \tag{5.21}$$

$$Q_{\mathrm{e}}^{1\mathrm{c}} = \frac{(-x_{\mathrm{e}} + x_{\mathrm{E}})(x_{\mathrm{e}} - x_{\mathrm{W}})}{(x_{\mathrm{E}} - x_{\mathrm{P}})(x_{\mathrm{P}} - x_{\mathrm{W}})} \tag{5.22}$$

$$Q_{\mathrm{e}}^{1\mathrm{d}} = \frac{(x_{\mathrm{e}} - x_{\mathrm{P}})(x_{\mathrm{e}} - x_{\mathrm{W}})}{(x_{\mathrm{E}} - x_{\mathrm{P}})(x_{\mathrm{E}} - x_{\mathrm{W}})} \tag{5.23}$$

$$(Q_{\mathrm{e}}^{1\mathrm{u}} + Q_{\mathrm{e}}^{1\mathrm{c}} + Q_{\mathrm{e}}^{1\mathrm{d}} = 1)$$

$$Q_{\mathrm{e}}^{2\mathrm{u}} = \frac{(-x_{\mathrm{e}} + x_{\mathrm{E}})(x_{\mathrm{e}} - x_{\mathrm{P}})}{(x_{\mathrm{E}} - x_{\mathrm{EE}})(x_{\mathrm{EE}} - x_{\mathrm{P}})} \tag{5.24}$$

$$Q_{\mathrm{e}}^{2\mathrm{c}} = \frac{(x_{\mathrm{e}} - x_{\mathrm{EE}})(x_{\mathrm{e}} - x_{\mathrm{P}})}{(x_{\mathrm{E}} - x_{\mathrm{EE}})(x_{\mathrm{E}} - x_{\mathrm{P}})} \tag{5.25}$$

$$Q_{\mathrm{e}}^{2\mathrm{d}} = \frac{(x_{\mathrm{e}} - x_{\mathrm{E}})(x_{\mathrm{e}} - x_{\mathrm{EE}})}{(x_{\mathrm{E}} - x_{\mathrm{P}})(x_{\mathrm{EE}} - x_{\mathrm{P}})} \tag{5.26}$$

$$(Q_{\mathrm{e}}^{2\mathrm{u}} + Q_{\mathrm{e}}^{2\mathrm{c}} + Q_{\mathrm{e}}^{2\mathrm{d}} = 1)$$

The analogous discretization of CV faces 'n', 'w', and 's' results in a general discretization stencil of nine cells, shown in Fig. 5.3.

Leonard [Leonard, 1997] shows using Taylor expansion that the leading error term of QUICK is $O(\Delta x^3)$ on an equidistant grid. Moreover, if the diffusive term is discretized by the standard CDS approximation it is consistent with the slope of the QUICK parabola on an equidistant grid and thus the discretization of the advection-diffusion equation is formally third-order accurate overall.

On the right hand side of the transport equations additional correction flux terms show up (Table 5.1), which are actually solid and liquid phase convection and diffusion terms. These terms appear due to the difference of

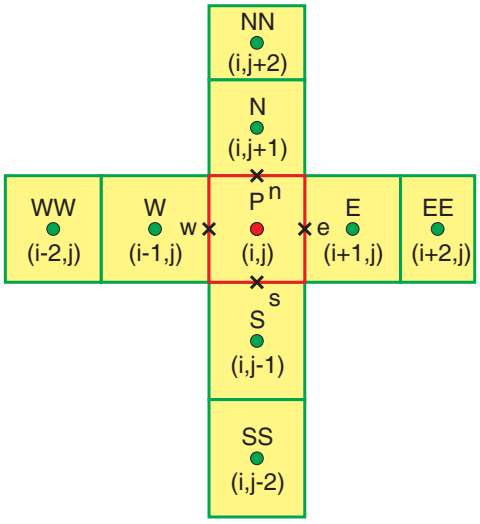

Figure 5.3: Discretization stencil of the QUICK advection interpolation scheme in compass and index notation.

the convective flux on the LHS of the equation, which is expressed in terms of the mixture variables and the sum of the actual phase convective fluxes. All convection and diffusion correction flux terms are discretized in the same way as the mixture fluxes. The only difference is that they are evaluated from known variable values (from the previous iteration) and combined with the source terms.

ULTRA-QUICK

Looking at the grain transport equation (Eq. (4.128)) we note that it is fundamentally different from the other transport equations by the absence of diffusion and source terms. It represents a hyperbolic partial differential equation. As already discussed, the notorious problem with numerically solving predominantly advective or even hyperbolic transport is apparently the restriction of having to choose between unstable linear high-order accurate discretization schemes or stable but inaccurate first-order schemes. Since we know from Godunov's theorem that unconditionally stable *linear* discretization schemes are limited to first-order accuracy, the quest for stable higher-order accurate schemes has to move to nonlinear schemes. Nonlinear schemes are those where the coefficients of the interpolant function depend on the field values. Many different approaches to the design of such methods (often termed bounded high-order or high-resolution methods) exist [Drikakis and Rider, 2005]. The philosophies on which the different methods are based are different. As the *necessary* criterion for high-order stability has not yet

been defined, different methods rely upon different *sufficient* criteria. One such philosophy is expressed by the ULTRA-SHARP flux limiter [Leonard and Mokhtari, 1990]. This limiter function is used in conjunction with higher order (usually polynomial) interpolation schemes with the objective of preserving the monotonicity of the original interpolation function, which may cause overshoots. ULTRA-SHARP is an extension of the convective boundedness criterion (CBC) on which the well-known SMART scheme [Gaskell and Lau, 1988], one of the earliest bounded high-order schemes, is based. The ULTRA-SHARP limiter is best defined in the *normalized variable diagram* (NVD). This diagram, shown in Fig. 5.4(a), depicts the value of the interpolated CV face variable in terms of three adjacent node values, an upstream ('U'), a central ('C') and a downstream ('D') node (Fig. 5.2(c)). The normalized variable $\tilde{\phi}$ is defined as

$$\tilde{\phi} = \frac{\phi - \phi_{\mathrm{U}}}{\phi_{\mathrm{D}} - \phi_{\mathrm{U}}} \tag{5.27}$$

Thus the normalized variable value at the upstream node is

$$\tilde{\phi_{\mathrm{U}}} = 0. \tag{5.28}$$

The normalized variable value at the downstream node is

$$\tilde{\phi_{\mathrm{D}}} = 1. \tag{5.29}$$

The normalized variable value at the east ('e') CV face is

$$\tilde{\phi}_{\mathrm{e}} = \frac{\phi_{\mathrm{e}} - \phi_{\mathrm{U}}}{\phi_{\mathrm{D}} - \phi_{\mathrm{U}}} \tag{5.30}$$

The ULTRA-SHARP limiter is designed based on the following criteria, expressed in terms of normalized variables.

- If the local field function over the three CV nodes ('U', 'C' and 'D') adjacent to CV face 'e' is monotonous, the CV face value has to preserve the monotonicity.

$$0 \leq \tilde{\phi}_{\mathrm{C}} \leq 1 \quad \Rightarrow \quad \tilde{\phi}_{\mathrm{C}} \leq \tilde{\phi}_{\mathrm{e}} \leq 1 \tag{5.31}$$

- If the values in 'U' and 'C' are equal with a steep gradient close to 'D', as in strong advection, ϕ_{e} has to approach ϕ_{C}.

$$\tilde{\phi}_{\mathrm{C}} \to 0_{+} \quad \Rightarrow \quad \tilde{\phi}_{\mathrm{e}} \to 0_{+} \tag{5.32}$$

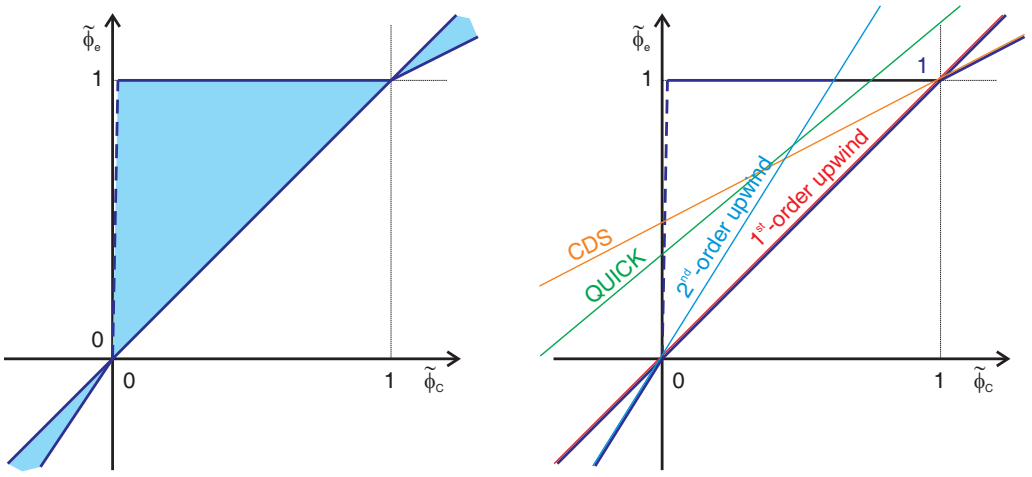

(a) ULTRA-SHARP flux limiter

(b) Common linear discretization schemes in the NVD

Figure 5.4: Normalized variable diagram (NVD).

- For nonmonotonous situations ($\tilde{\phi}_C < 0$ or $\tilde{\phi}_C > 1$) the criterion is based on maintaining a monotonically rising condition, approximated with the CDS interpolation for

$$\tilde{\phi}_C > 1 \quad \Rightarrow \quad \tilde{\phi}_e = 1 + \frac{1}{2}(\tilde{\phi}_C - 1), \tag{5.33}$$

  and second-order upwind for

$$\tilde{\phi}_C < 0 \quad \Rightarrow \quad \frac{3}{2}\tilde{\phi}_C. \tag{5.34}$$

The stable range defined by the ULTRA-SHARP limiter is shown in the NVD in Fig. 5.4(a).

We apply the ULTRA-SHARP limiter to the QUICK interpolation scheme, which is expressed in terms of normalized variables as

$$\tilde{\phi}_e = Q_D + Q_C\tilde{\phi}_C. \tag{5.35}$$

QUICK in conjunction with the ULTRA-SHARP limiter defines the so-called ULTRA-QUICK scheme. According to this scheme the normalized face value is defined as

$$\tilde{\phi}_e = \begin{cases} \tilde{\phi}_C & \tilde{\phi}_C \le 0 \\ S\tilde{\phi}_C & 0 < \tilde{\phi}_C \le \frac{Q_D}{S-Q_C} \\ Q_D + Q_C\tilde{\phi}_C & \frac{Q_D}{S-Q_C} < \tilde{\phi}_C \le \frac{1-Q_D}{Q_C} \\ 1 & \frac{1-Q_D}{Q_C} < \tilde{\phi}_C \le 1 \\ \tilde{\phi}_C & 1 < \tilde{\phi}_C \end{cases}, \tag{5.36}$$

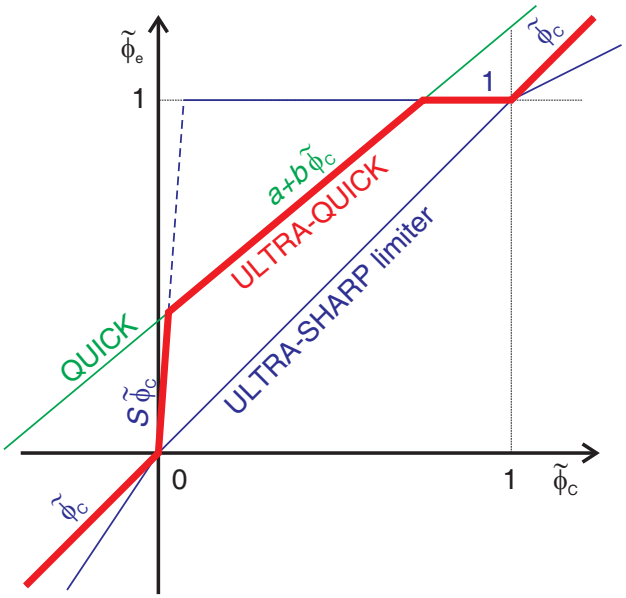

Figure 5.5: The ULTRA-QUICK scheme in the normalized variable diagram (NVD).

where Q_C and Q_D are the QUICK interpolation factors from Eq. (5.21). The ULTRA-QUICK scheme is shown in the NVD in Fig. 5.5.

In the developed code the ULTRA-QUICK interpolation is implemented via interpolation factors, such that

$$\phi_e = k_U \phi_U + k_C \phi_C + k_D \phi_D. \tag{5.37}$$

The interpolation factors are defined

$$k_U = \begin{cases} 0 & \tilde{\phi}_C \leq 0 \\ 1 - S & 0 < \tilde{\phi}_C \leq \frac{Q_D}{S - Q_C} \\ 1 - Q_D - Q_C & \frac{Q_D}{S - Q_C} < \tilde{\phi}_C \leq \frac{1 - Q_D}{Q_C} \\ 0 & \frac{1 - Q_D}{Q_C} < \tilde{\phi}_C \leq 1 \\ 0 & 1 < \tilde{\phi}_C \end{cases} \tag{5.38}$$

$$k_D = \begin{cases} 0 & \tilde{\phi}_C \leq 0 \\ 0 & 0 < \tilde{\phi}_C \leq \frac{Q_D}{S - Q_C} \\ Q_D & \frac{Q_D}{S - Q_C} < \tilde{\phi}_C \leq \frac{1 - Q_D}{Q_C} \\ 1 & \frac{1 - Q_D}{Q_C} < \tilde{\phi}_C \leq 1 \\ 0 & 1 < \tilde{\phi}_C \end{cases} \tag{5.39}$$

$$k_{\mathrm{C}} = \begin{cases} 1 & \tilde{\phi}_{\mathrm{C}} \leq 0 \\ S & 0 < \tilde{\phi}_{\mathrm{C}} \leq \frac{Q_{\mathrm{D}}}{S - Q_{\mathrm{C}}} \\ Q_{\mathrm{C}} & \frac{Q_{\mathrm{D}}}{S - Q_{\mathrm{C}}} < \tilde{\phi}_{\mathrm{C}} \leq \frac{1 - Q_{\mathrm{D}}}{Q_{\mathrm{C}}} \\ 0 & \frac{1 - Q_{\mathrm{D}}}{Q_{\mathrm{C}}} < \tilde{\phi}_{\mathrm{C}} \leq 1 \\ 1 & 1 < \tilde{\phi}_{\mathrm{C}} \end{cases} \tag{5.40}$$

The direction of the flow across CV face 'e' is taken into account in the same fashion as in the original QUICK scheme (Fig. 5.2(c)).

5.3.2 Viscous Term

The nonstandard part of the Newtonian viscous term $\nabla \cdot \left(\mu_{\mathrm{m}} (\nabla \vec{v}_{\mathrm{m}})^T\right)$ appears in Eq. (4.109) for the slurry flow regime. It was taken into account, although it finally appeared to be significantly smaller than $\nabla \cdot (\mu_{\mathrm{eff}} (\nabla \vec{v}_{\mathrm{m}}))$. The integration over the CV gives

$$\begin{aligned} \overline{\oint_S \mu_{\mathrm{m}} (\nabla \vec{v}_{\mathrm{m}})^T \cdot d\vec{S}} \approx \mu_{\mathrm{e}} A_{\mathrm{e}} \begin{pmatrix} \overline{\frac{\partial u}{\partial x}} \\ \overline{\frac{\partial u}{\partial y}} \end{pmatrix}_{\mathrm{e}} - \mu_{\mathrm{w}} A_{\mathrm{w}} \begin{pmatrix} \overline{\frac{\partial u}{\partial x}} \\ \overline{\frac{\partial u}{\partial y}} \end{pmatrix}_{\mathrm{w}} \\ + \mu_{\mathrm{n}} A_{\mathrm{n}} \begin{pmatrix} \overline{\frac{\partial v}{\partial x}} \\ \overline{\frac{\partial v}{\partial y}} \end{pmatrix}_{\mathrm{n}} - \mu_{\mathrm{s}} A_{\mathrm{s}} \begin{pmatrix} \overline{\frac{\partial v}{\partial x}} \\ \overline{\frac{\partial v}{\partial y}} \end{pmatrix}_{\mathrm{s}} \end{aligned} \tag{5.41}$$

The discretization involves the evaluation of partial derivatives $\partial u/\partial y$ at the vertical ('e' and 'w') faces of the CV and $\partial v/\partial x$ at the horizontal ('n' and 's') faces of the CV. The discretization is performed by linear interpolations in two dimensions between the six nodes adjacent to the CV face.

$$\begin{aligned} \left(\frac{\partial v}{\partial x}\right)_{\mathrm{n}} &\approx I_{\mathrm{n}} \left(\frac{\partial v}{\partial x}\right)_{\mathrm{N}} + (1 - I_{\mathrm{n}}) \left(\frac{\partial v}{\partial x}\right)_{\mathrm{P}} \\ &\approx \frac{I_{\mathrm{n}}}{2} \left[\left(\frac{\partial v}{\partial x}\right)_{\mathrm{nne}} + \left(\frac{\partial v}{\partial x}\right)_{\mathrm{nnw}}\right] + \frac{(1 - I_{\mathrm{n}})}{2} \left[\left(\frac{\partial v}{\partial x}\right)_{\mathrm{e}} + \left(\frac{\partial v}{\partial x}\right)_{\mathrm{w}}\right] \\ &\approx \frac{I_{\mathrm{n}}}{2} \left[\frac{v_{\mathrm{NE}} - v_{\mathrm{N}}}{x_{\mathrm{NE}} - x_{\mathrm{N}}} + \frac{v_{\mathrm{N}} - v_{\mathrm{NW}}}{x_{\mathrm{N}} - x_{\mathrm{NW}}}\right] + \frac{(1 - I_{\mathrm{n}})}{2} \left[\frac{v_{\mathrm{E}} - v_{\mathrm{P}}}{x_{\mathrm{E}} - x_{\mathrm{P}}} + \frac{v_{\mathrm{P}} - v_{\mathrm{W}}}{x_{\mathrm{P}} - x_{\mathrm{W}}}\right] \end{aligned} \tag{5.42}$$

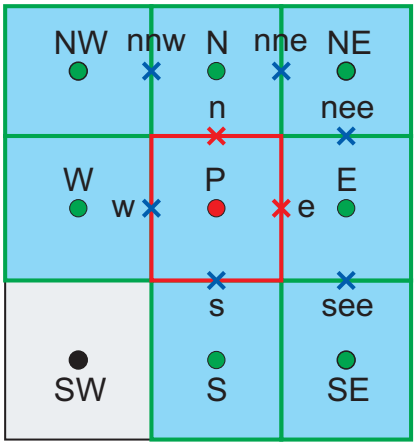

Figure 5.6: Stencil for the discretization of $(\nabla \vec{v}_\mathrm{m})^T$ in the viscous term.

$$\begin{aligned}\left(\frac{\partial u}{\partial y}\right)_\mathrm{e} &\approx I_\mathrm{e}\left(\frac{\partial u}{\partial y}\right)_\mathrm{E} + (1-I_\mathrm{e})\left(\frac{\partial u}{\partial y}\right)_\mathrm{P} \\ &\approx \frac{I_\mathrm{e}}{2}\left[\left(\frac{\partial u}{\partial y}\right)_\mathrm{nee} + \left(\frac{\partial u}{\partial y}\right)_\mathrm{see}\right] + \frac{(1-I_\mathrm{e})}{2}\left[\left(\frac{\partial u}{\partial y}\right)_\mathrm{n} + \left(\frac{\partial u}{\partial y}\right)_\mathrm{s}\right] \\ &\approx \frac{I_\mathrm{e}}{2}\left[\frac{u_\mathrm{NE}-u_\mathrm{E}}{y_\mathrm{NE}-y_\mathrm{E}} + \frac{u_\mathrm{E}-u_\mathrm{SE}}{y_\mathrm{E}-y_\mathrm{SE}}\right] + \frac{(1-I_\mathrm{e})}{2}\left[\frac{u_\mathrm{N}-u_\mathrm{P}}{y_\mathrm{N}-y_\mathrm{P}} + \frac{u_\mathrm{P}-u_\mathrm{S}}{y_\mathrm{P}-y_\mathrm{S}}\right]\end{aligned} \tag{5.43}$$

This part of the viscous term is small compared to the other equation terms and can be computed from the known preceding-iteration values of u and v and combined with the source terms.

5.3.3 Phase Mass Fluxes

The advection terms in the transport equations involve phase quantities for the solid and liquid phases: velocity, enthalpy, and concentration. They are determined from the mixture quantities by the respective constitutive laws. In addition, the phase advection terms involve mass fluxes of the solid and liquid phases across the CV faces, $\vec{F}_\mathrm{s}$ and $\vec{F}_\mathrm{l}$. Basically, their determination from the mixture velocity or mass flux has to be based on the constitutive law for the velocity of solid

$$\vec{v}_\mathrm{s} = \mathcal{R}\vec{v}_\mathrm{cast} + (1-\mathcal{R})\left(\vec{v}_\mathrm{m} - \frac{f_\mathrm{l}^2 \rho_\mathrm{m}(\rho_\mathrm{l}-\rho_\mathrm{s}) d_\mathrm{g}^2 \vec{g}}{18\rho_\mathrm{l}\mu_\mathrm{m}},\right) \tag{4.129}$$

and the definition of the mixture velocity

$$\vec{v}_\mathrm{m} = f_\mathrm{s}\vec{v}_\mathrm{s} + f_\mathrm{l}\vec{v}_\mathrm{l} \tag{4.87}$$

All the involved quantities have to be evaluated at the CV faces so the interpolation of some of them will have to be used. The conservation of mass, which is inherent in the mixture mass fluxes, is also required for the phase mass fluxes. The solid phase mass flux across CV face 'n' is defined

$$F_{\mathrm{s,n}} = \rho_{\mathrm{s}} \overline{(g_{\mathrm{s}})}_{\mathrm{n}} \overline{(v_{\mathrm{s}})}_{\mathrm{n}} A_{\mathrm{n}}. \tag{5.44}$$

The solid face velocity is given by Eq. (4.129), evaluated at face 'n', and depends on f_{l}, ρ_{m}, d_{g}, μ_{m}, and finally $\vec{v}_{\mathrm{m}}$. Expressing the relations between mass and volume phase fractions

$$g_{\mathrm{k}} = \frac{\rho_{\mathrm{m}}}{\rho_{\mathrm{k}}} f_{\mathrm{k}}\,, \tag{4.88}$$

the definition of the mixture density

$$\rho_{\mathrm{m}} = g_{\mathrm{s}}\rho_{\mathrm{s}} + g_{\mathrm{l}}\rho_{\mathrm{l}}\,, \tag{4.87}$$

the constitutive law for the grain diameter

$$d_{\mathrm{g}} = \sqrt[3]{\frac{6\rho_{\mathrm{m}} f_{\mathrm{s}}}{\pi \rho_{\mathrm{s}} n_{\mathrm{s}}}} = \sqrt[3]{\frac{6 g_{\mathrm{s}}}{\pi n_{\mathrm{s}}}}\,, \tag{4.127}$$

the constitutive law for the slurry viscosity

$$\mu_{\mathrm{m}} = \mu_{\mathrm{l}} \left[1 + 2.5 g_{\mathrm{s}} + 10.05 g_{\mathrm{s}}^2 + 0.00273 \exp(16.6 g_{\mathrm{s}})\right]\,, \tag{4.30}$$

and the mixture mass flux

$$F_{\mathrm{m,n}} = \left(\rho_{\mathrm{m}} v_{\mathrm{m}}\right)_{\mathrm{n}} A_{\mathrm{n}} \approx \rho_{\mathrm{m,n}} v_{\mathrm{m,n}} A_{\mathrm{n}} \tag{5.45}$$

we can see that we can reduce the problem of the determination of phase fluxes to the interpolation of g_{s} and n_{s}. The evaluation of the solid flux follows the sequence

$$g_{\mathrm{s,n}} \approx \overline{(g_{\mathrm{s}})}_{\mathrm{n}} \tag{5.46}$$

$$n_{\mathrm{s,n}} \approx \overline{(n_{\mathrm{s}})}_{\mathrm{n}} \tag{5.47}$$

$$\rho_{\mathrm{m,n}} = \overline{(g_{\mathrm{s}})}_{\mathrm{n}} \rho_{\mathrm{s}} + (1 - \overline{(g_{\mathrm{s}})}_{\mathrm{n}}) \rho_{\mathrm{l}} \tag{5.48}$$

$$\mu_{\mathrm{m,n}} = \mu_{\mathrm{l}} \left[1 + 2.5 \overline{(g_{\mathrm{s}})}_{\mathrm{n}} + 10.05 \overline{(g_{\mathrm{s}})}_{\mathrm{n}}^2 + 0.00273 \exp(16.6 \overline{(g_{\mathrm{s}})}_{\mathrm{n}})\right] \tag{5.49}$$

$$d_{\mathrm{g,n}} = \sqrt[3]{\frac{6\overline{(g_{\mathrm{s}})}_{\mathrm{n}}}{\pi \overline{(n_{\mathrm{s}})}_{\mathrm{n}}}} \tag{5.50}$$

$$F_{\mathrm{s,n}} = \mathcal{R}\left[\rho_{\mathrm{s}}\overline{(g_{\mathrm{s}})}_{\mathrm{n}}\vec{v}_{\mathrm{cast}}A_{\mathrm{n}}\right] + (1-\mathcal{R})\left[\frac{\rho_{\mathrm{s}}\overline{(g_{\mathrm{s}})}_{\mathrm{n}}}{\rho_{\mathrm{m,n}}}F_{\mathrm{m,n}} - \frac{\overline{(g_{\mathrm{s}})}_{\mathrm{n}}(1-\overline{(g_{\mathrm{s}})}_{\mathrm{n}})^2\rho_{\mathrm{l}}\rho_{\mathrm{s}}(\rho_{\mathrm{l}}-\rho_{\mathrm{s}})d_{\mathrm{g,n}}^2\|\vec{g}\|}{18\rho_{\mathrm{m,n}}\mu_{\mathrm{m,n}}}A_{\mathrm{n}}\right]. \quad (5.51)$$

The liquid mass flux is then simply

$$F_{\mathrm{l,n}} = F_{\mathrm{m,n}} - F_{\mathrm{s,n}}. \quad (5.52)$$

For the horizontal direction the phase velocities are $u_{\mathrm{s}} = u_{\mathrm{m}} = u_{\mathrm{m}}$ and consequently the fluxes are

$$F_{\mathrm{s,e}} = u_{\mathrm{m}}\rho_{\mathrm{s}}\overline{(g_{\mathrm{s}})}_{\mathrm{e}} \quad (5.53)$$

$$F_{\mathrm{l,e}} = F_{\mathrm{m,e}} - F_{\mathrm{s,e}}. \quad (5.54)$$

5.3.4 Flow Regime Function

The momentum equation includes some terms that are only valid in one of the two modeled flow regimes. To switch between these terms the flow regime function $\mathcal{R}$ was introduced in Section 4.4.2.

$$\mathcal{R}(\vec{x},t) = \begin{cases} 1 & g_{\mathrm{s}}(\vec{x},t) > g_{\mathrm{s}}^{\mathrm{c}} \\ 0 & g_{\mathrm{s}}(\vec{x},t) \leq g_{\mathrm{s}}^{\mathrm{c}} \end{cases} \quad (4.108)$$

A discontinuous step function could cause difficulties during the numerical solution, e.g. step cycling during the iterations. To preclude such problems, we use a smooth but sharp transition function for the flow regime function. It is shown in Fig. 5.7.

$$\mathcal{R}(g_{\mathrm{s}}) = \frac{1}{2}\left(1 - \tanh\left[c_{\mathcal{R}}(g_{\mathrm{s}}^{\mathrm{c}} - g_{\mathrm{s}})\right]\right), \qquad c_{\mathcal{R}} = 100 \quad (5.55)$$

The parameter $c_{\mathcal{R}}$ sets the slope of the tanh function at the trigger value $g_{\mathrm{s}}^{\mathrm{c}}$.

5.3.5 Darcy Function

As the solid fraction g_{s} approaches and finally reaches unity, all its terms approach zero and the one-domain momentum equation, Eq. (4.109), degenerates. At $g_{\mathrm{l}} = 0$, the buoyancy, pressure, and Darcy terms, which are multiplied by g_{l}, become zero. The slurry-regime terms are zero, turned off by the regime function multiplier $(1-\mathcal{R})$. Further, all velocity gradients and derivatives are zero in the solid phase, turning off the advective, viscous and

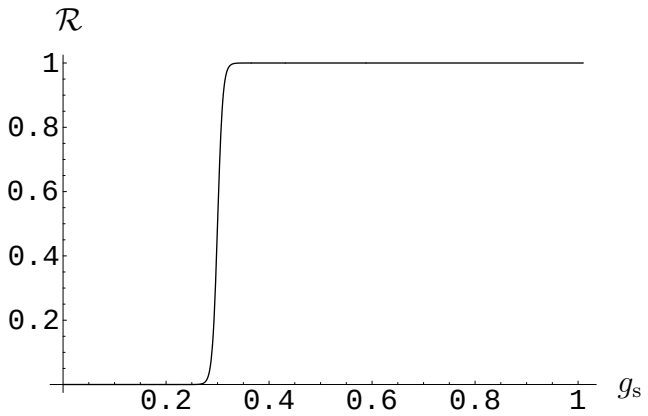

Figure 5.7: Regime function for $g_s^c = 0.3$ and $c_{\mathcal{R}} = 100$.

transient terms. In a one-domain model, which has to be valid in all phases, this behavior is not allowable. In previous one-phase models [Prescott *et al.*, 1991] this situation did not occur since the momentum equation was artificially modified by multiplying the Darcy equation (Eq.(5.56)) with g_s and adding it to the mixture momentum equation.

$$\nabla \langle P_l \rangle^l + \vec{g}\rho_l^{ref} \left[\beta_l^T \left(T - T_{ref} \right) + \beta_l^C \left(\langle C_l \rangle^l - C_{ref} \right) \right] + \left(\frac{\rho_m}{\rho_l} \right) \frac{\mu_l}{K} \cdot (\vec{v}_m - \vec{v}_{cast}) = 0 \tag{5.56}$$

This manipulation was done mainly to prevent the scaling of the pressure term by g_l, and to thereby enable the simple use of standard existing numerical algorithms. The rationale behind this manipulation is that the Darcy equation is a legitimate approximation of the momentum equation in the porous mushy structure and that all terms, apart from the Darcy-equation terms, become small. The augmentation of the Darcy-equation terms should thus not significantly change the solution. From the deduction of the porous-regime model in Chapter 4 we can see that this is not strictly true, certainly not at low g_s. Nevertheless, it is a good approximation at high g_s, when the Darcy and pressure terms indeed become very large with decreasing permeability and other terms become negligibly small. We can thus multiply the Darcy equation with a penalization function that will turn it on only above some high g_s, and add it to the momentum equation. This enables us to both prevent the degeneration of the momentum equation at $g_s \simeq 1$ *and* retain the full momentum equation in the low-g_s part of the porous mushy zone. we introduce the Darcy penalization function, which performs similarly to the

regime function.

$$\mathcal{D}(\vec{x},t) = \begin{cases} g_\mathrm{s} & g_\mathrm{s}(\vec{x},t) > g_\mathrm{s}^\mathrm{D} \\ 0 & g_\mathrm{s}(\vec{x},t) \leq g_\mathrm{s}^\mathrm{D} \end{cases} \tag{5.57}$$

We again smoothen it by using the tanh function, using parameter g_s^D to define the threshold g_s, and $c_\mathcal{D}$ to set the slope at $g_\mathrm{s} = g_\mathrm{s}^\mathrm{D}$. The function is shown in Fig. 5.8.

$$\mathcal{D}(g_\mathrm{s}) = \frac{1}{2}\left(1 - \tanh\left[c_\mathcal{D}(g_\mathrm{s}^\mathrm{D} - g_\mathrm{s})\right]\right) g_\mathrm{s}, \qquad g_\mathrm{s}^\mathrm{D} = 0.95, \quad c_\mathcal{D} = 500 \tag{5.58}$$

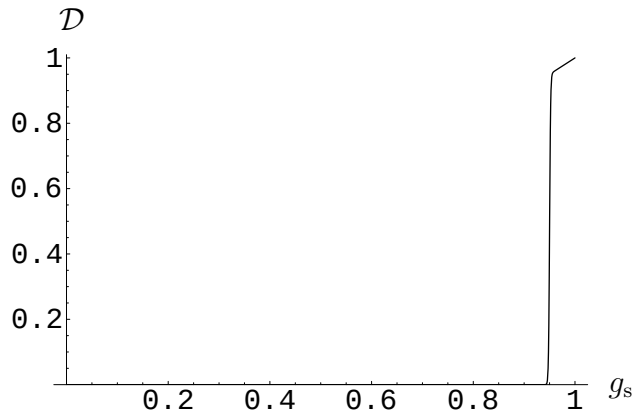

Figure 5.8: Darcy function for $g_\mathrm{s}^\mathrm{D} = 0.95$.

We can now write the one-phase momentum equation as it is numerically implemented in the model. The multiplier functions for the individual terms are shown in Fig. 5.9.

$$\begin{aligned} \frac{\partial}{\partial t}\left(\rho_\mathrm{m}\vec{v}_\mathrm{m}\right) + \nabla\cdot\left(\rho_\mathrm{m}\vec{v}_\mathrm{m}\vec{v}_\mathrm{m}\right) &= -(1 - \mathcal{R}g_\mathrm{s} + \mathcal{D})\nabla\left\langle P_\mathrm{l}\right\rangle^\mathrm{l} + \nabla\cdot\left(\mu_\mathrm{eff}\nabla\vec{v}_\mathrm{m}\right) \\ &\quad - (g_\mathrm{l} + \mathcal{D})\vec{g}\rho_\mathrm{l}^\mathrm{ref}\left[\beta_\mathrm{l}^T\left(T - T_\mathrm{ref}\right) + \beta_\mathrm{l}^C\left(\left\langle C_\mathrm{l}\right\rangle^\mathrm{l} - C_\mathrm{ref}\right)\right] \\ &\quad + \left[\nabla\cdot\left(\rho_\mathrm{m}\vec{v}_\mathrm{m}\vec{v}_\mathrm{m}\right) - \nabla\cdot\left(g_\mathrm{s}\left\langle\rho_\mathrm{s}\right\rangle^\mathrm{s}\left\langle\vec{v}_\mathrm{s}\right\rangle^\mathrm{s}\left\langle\vec{v}_\mathrm{s}\right\rangle^\mathrm{s}\right) - \nabla\cdot\left(g_\mathrm{l}\left\langle\rho_\mathrm{l}\right\rangle^\mathrm{l}\left\langle\vec{v}_\mathrm{l}\right\rangle^\mathrm{l}\left\langle\vec{v}_\mathrm{l}\right\rangle^\mathrm{l}\right)\right] \\ &\quad + (\mathcal{R}g_\mathrm{l} + \mathcal{D})\left(\frac{\rho_\mathrm{m}}{\rho_\mathrm{l}}\right)\frac{\mu_\mathrm{l}}{K}\cdot\left(\vec{v}_\mathrm{m} - \vec{v}_\mathrm{cast}\right) \\ &\quad + (1 - \mathcal{R})\left[\nabla\cdot\left(\mu_\mathrm{m}(\nabla\vec{v}_\mathrm{m})^T\right) + g_\mathrm{s}\vec{g}\left(\rho_\mathrm{s}^\mathrm{ref} - \rho_\mathrm{l}^\mathrm{ref}\right)\right. \\ &\quad \left. - g_\mathrm{s}\vec{g}\rho_\mathrm{s}^\mathrm{ref}\left[\beta_\mathrm{s}^T\left(T - T_\mathrm{ref}\right) + \beta_\mathrm{s}^C\left(\left\langle C_\mathrm{s}\right\rangle^\mathrm{s} - C_\mathrm{ref}\right)\right]\right] \end{aligned} \tag{5.59}$$

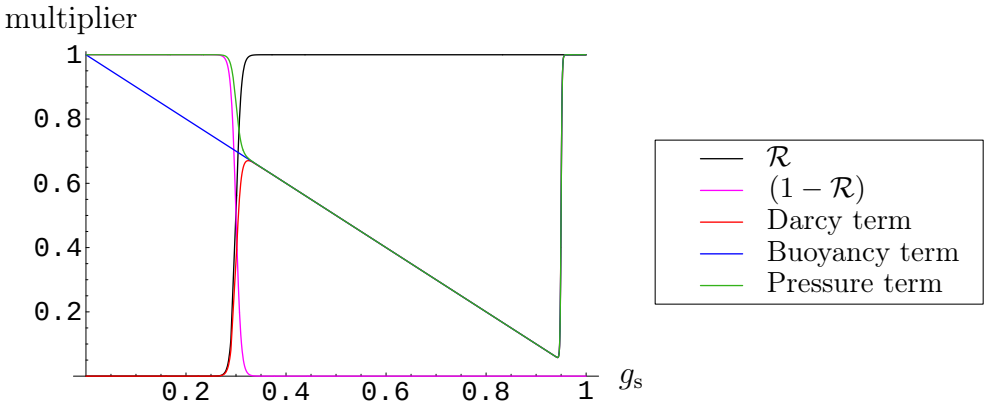

Figure 5.9: Penalization functions for individual terms in the momentum equation, Eq. (5.59), assembled of the regime and Darcy functions.

5.3.6 Pressure-Velocity Linkage With Collocated Variable Arrangement and Pressure Term Scaling

The momentum equation, an extension of the Navier-Stokes equation, involves a pressure gradient term that is not known in advance, but depends on the velocity field. For incompressible flows there is no separate equation directly describing the pressure field. Nevertheless, the whole system of model equations involves the same number of equations and unknowns. This enables us to calculate the pressure field indirectly, from the requirement of mass conservation expressed by the continuity equation.

A standard way of doing this is by inserting the discretized expression for the velocity from the momentum equation with the velocity field from the momentum equation solution into the continuity equation. The pressure term is kept separate. In this way a pressure correction equation is obtained giving the correction of the pressure that is necessary to adapt the velocities to fulfill the continuity requirement. The solutions of the momentum and pressure correction equation are iterated until the convergence of both equations, when the velocity and pressure together fulfill both the momentum and continuity equations. In the development of the pressure correction equation I had to take into account that the pressure gradient term in the momentum equation (4.109) is multiplied by $(1 - \mathcal{R}g_s + \mathcal{D})$ and to keep the scaling accordingly.

In the developed numerical code this kind of pressure-velocity coupling is done with the SIMPLE method for a collocated arrangement of velocity and pressure. Rhie-Chow momentum interpolation is used to cure potential stability problems appearing when using the collocated variable arrange-

ment [Ferziger and Perić, 1996]. The reason for using collocated grids is that the development of the numerical code was based on the DC casting code by Mencinger [Mencinger, 2002], which was developed as a simplified version of his adaptive-grid code [Mencinger, 2001]. The pressure-correction algorithm was already described in detail by Mencinger [Mencinger, 2001], generalized for r-adaptive curvilinear grids, and will not be repeated here.

5.3.7 Iterative Solution Scheme

The implicit iterative scheme for the solution of the coupled model equation is based on the SIMPLE scheme. The flowchart is shown in Fig. 5.10.

The iterative loop within each timestep is iterated until the convergence criterion is fulfilled.

$$\max_{ij}\left[\frac{\left|a_{\mathrm{P}}\phi_{\mathrm{P}}-\sum_{\mathrm{nb}}a_{\mathrm{nb}}\phi_{\mathrm{nb}}-b_{\mathrm{P}}\right|}{\left|a_{\mathrm{P}}\phi_{\mathrm{P}}\right|+\left|\sum_{\mathrm{nb}}a_{\mathrm{nb}}\phi_{\mathrm{nb}}+b_{\mathrm{P}}\right|}\right]<err_{\max} \tag{5.60}$$

5.4 The Linear Equation System and Its Solution

When we assemble all discretized terms from Eqs. (5.5), (5.8), (5.9), and (5.10) for CV centered in point 'P' and generalize the interpolation of CV-face values of ϕ in the advection term and the approximation of gradients of ϕ in the diffusion term as being expressed in terms of the neighboring CV node values (denoted 'nb'), according to the interpolation stencil, we obtain

$$a_{\mathrm{P}}\phi_{\mathrm{P}}-\sum_{\mathrm{nb}}a_{\mathrm{nb}}\phi_{\mathrm{nb}}-b_{\mathrm{P}}=0. \tag{5.61}$$

This is the general discretized form of the transport equation for the CV centered in point 'P'. It was obtained by integrating the transport equation over the CV and applying different approximations to express the volume and surface integrals. As mentioned before we use an implicit time integration. This is done to stabilize the time integration of the strongly coupled equation system within the model. The implicit formulation necessitates the solution of a system of linear Eqs. (5.61). When we assemble the linear discretized equations for all, say $m\times n$, CVs, we obtain a system of $m\cdot n$ linear equations

$$\boldsymbol{A}\cdot\boldsymbol{\phi}-\boldsymbol{b}=\boldsymbol{0}\qquad \boldsymbol{A}\in\mathbb{R}^{m\cdot n\times m\cdot n}\quad \boldsymbol{\phi}\in\mathbb{R}^{m\cdot n}\quad \boldsymbol{b}\in\mathbb{R}^{m\cdot n} \tag{5.62}$$

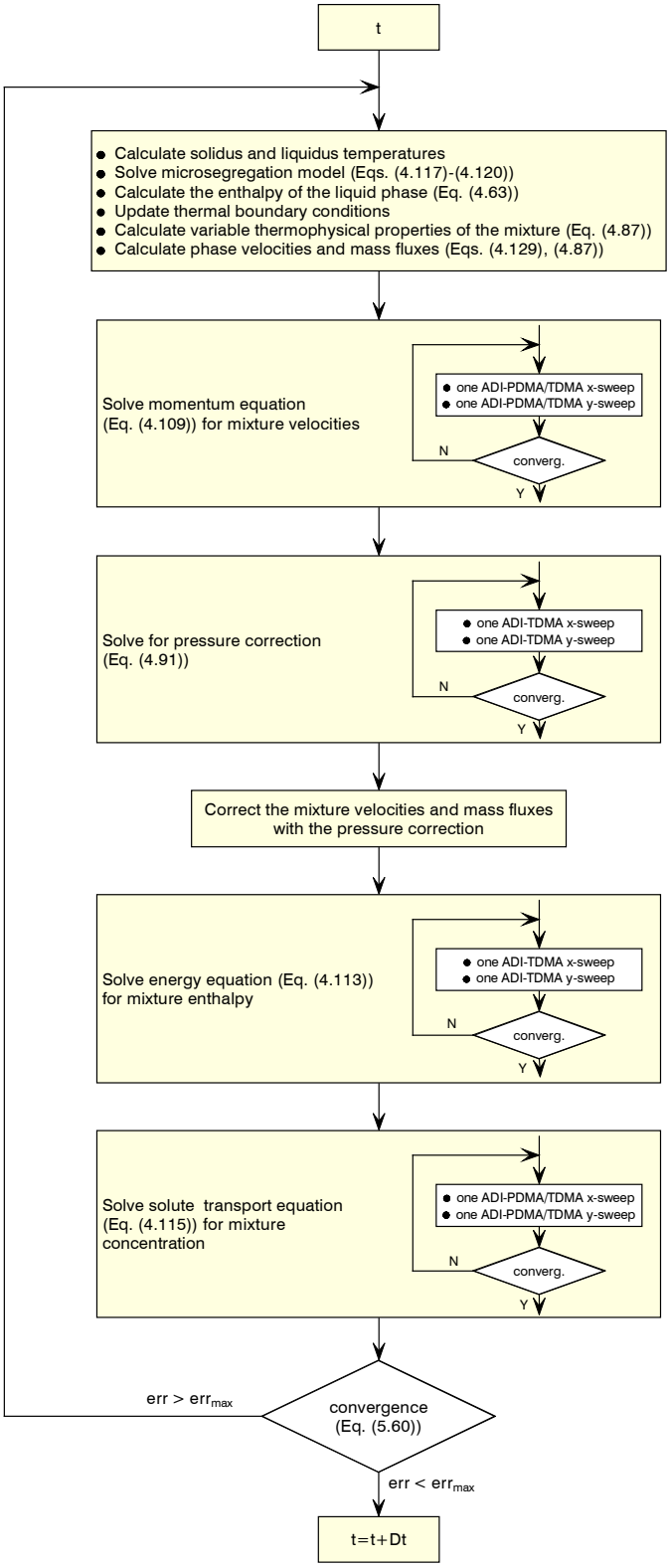

Figure 5.10: Flowchart of the iterative solution scheme.

Table 5.2: Interpolation schemes used for discretization of the advection term in the transport equations

Transport equation	Variable	Discretization scheme
Momentum (4.109)	u_m, v_m	QUICK
Energy (4.113)	h_m	CDS
Species (4.115)	C_m	QUICK
Continuity (Pressure) (4.109), (4.91)	p	CDS
Grain density (4.128)	n_s	ULTRA-QUICK

The best solution method depends on the structure of the matrix $\boldsymbol{A}$. The most effective methods often heavily rely on the known matrix structure. The matrix structure in turn depends on which 'nb' neighbors are included in the discretized equations. Within the developed FVM formulation this now depends exclusively on the interpolation functions used in the discretization of the advection terms.

With the central-difference scheme, which is used for the energy equation, we obtain linear equations of the form

$$a_\mathrm{P}^{i,j}\phi^{i,j} - a_\mathrm{W}^{i,j}\phi^{i-1,j} - a_\mathrm{E}^{i,j}\phi^{i+1,j} - a_\mathrm{S}^{i,j}\phi^{i,j-1} - a_\mathrm{N}^{i,j}\phi^{i,j+1} - b_\mathrm{P}^{i,j} = 0, \qquad (5.63)$$

where on the structured orthogonal grid the neighbors are denoted in index and compass notation $(i,j) \equiv \mathrm{P}$, $(i-1,j) \equiv \mathrm{W}$, $(i+1,j) \equiv \mathrm{E}$, $(i,j-1) \equiv \mathrm{S}$, $(i,j+1) \equiv \mathrm{N}$ (also shown in Fig. 5.3, where both compass and index notation are shown). This results in a five-band matrix with a nonzero central diagonal, one nonzero band directly above and below the diagonal and two off-diagonal nonzero bands one above and one below the diagonal.

With the QUICK scheme used for the momentum and species equations, eight neighbors are included in the discretized equation, as shown in Fig. 5.3.

$$a_\mathrm{P}^{i,j}\phi^{i,j} - a_\mathrm{WW}^{i,j}\phi^{i-2,j} - a_\mathrm{W}^{i,j}\phi^{i-1,j} - a_\mathrm{E}^{i,j}\phi^{i+1,j} - a_\mathrm{EE}^{i,j}\phi^{i+2,j} \qquad (5.64)$$

$$- a_\mathrm{SS}^{i,j}\phi^{i,j-2} - a_\mathrm{S}^{i,j}\phi^{i,j-1} - a_\mathrm{N}^{i,j}\phi^{i,j+1} - a_\mathrm{NN}^{i,j}\phi^{i,j+2} - b_\mathrm{P}^{i,j} = 0, \qquad (5.65)$$

This results in a nine-band matrix with four more off-diagonal nonzero bands, two above and two below the diagonal.

A standard and very effective method which exploits the matrix structure of the CDS matrix is to use the iterative alternating-direction-implicit tridiagonal-matrix-algorithm (ADI-TDMA). The basic TDMA (or Thomas algorithm) is a direct method, basically a Gaussian elimination, specialized for tridiagonal matrices, where it is very effective as it leaves out the operations involving the zero elements and makes a very compact scheme. The

TDMA is often used to directly solve the 1D diffusion problem (or convection-diffusion, provided that a 3-cell scheme is used). To solve the CDS matrix by TDMA the matrix has to be recast into tridiagonal form. This is done by transforming the 2D problem on the structured grid into a stack of 1D problems. If the 1D rows of CVs are running along, say, the x direction, the terms involving the 'N' and 'S' nodes are added to the source term.

$$\tilde{b}^{i,j}_{x,\,\mathrm{P}} = b^{i,j}_{\mathrm{P}} + a^{i,j}_{\mathrm{S}}\phi^{i,j-1} + a^{i,j}_{\mathrm{N}}\phi^{i,j+1} \tag{5.66}$$

and a modified matrix equation

$$\tilde{\boldsymbol{A}}_{\boldsymbol{x}} \cdot \boldsymbol{\phi} - \tilde{\boldsymbol{b}}_{\boldsymbol{x}} = \mathbf{0}, \tag{5.67}$$

involving a tridiagonal matrix $\tilde{\boldsymbol{A}}$ is solved by TDMA. After one TDMA sweep of the 2D domain in a line-by-line manner we change the direction of the 1D bands, compute

$$\tilde{b}^{i,j}_{y,\,\mathrm{P}} = b^{i,j}_{\mathrm{P}} + a^{i,j}_{\mathrm{W}}\phi^{i-1,j} + a^{i,j}_{\mathrm{E}}\phi^{i+1,j} \tag{5.68}$$

and again solve the stack of 1D problems

$$\tilde{\boldsymbol{A}}_{\boldsymbol{y}} \cdot \boldsymbol{\phi} - \tilde{\boldsymbol{b}}_{\boldsymbol{y}} = \mathbf{0} \tag{5.69}$$

in a line-by-line manner. This alternating-direction TDMA is iterated until the convergence criterion is met.

For the QUICK matrix a similar algorithm, ADI-PDMA, was used. The only difference is that it is based on the pentadiagonal matrix algorithm (PDMA), an extension of TDMA for pentadiagonal matrices; again essentially a specialized compact form of Gaussian elimination. The QUICK matrix is recast into pentadiagonal form by defining

$$\begin{aligned}
\tilde{b}^{i,j}_{\mathrm{P},\,x} &= b^{i,j}_{\mathrm{P}} + a^{i,j}_{\mathrm{SS}}\phi^{i,j-2} + a^{i,j}_{\mathrm{S}}\phi^{i,j-1} + a^{i,j}_{\mathrm{N}}\phi^{i,j+1} + a^{i,j}_{\mathrm{NN}}\phi^{i,j+2} \\
\tilde{b}^{i,j}_{\mathrm{P},\,y} &= b^{i,j}_{\mathrm{P}} + a^{i,j}_{\mathrm{WW}}\phi^{i-2,j} + a^{i,j}_{\mathrm{W}}\phi^{i-1,j} + a^{i,j}_{\mathrm{E}}\phi^{i+1,j} + a^{i,j}_{\mathrm{EE}}\phi^{i+2,j}
\end{aligned} \tag{5.70}$$

for the x- and y-direction sweeps, respectively. PDMA is less commonly encountered than TDMA; it is described for example in [Fletcher *et al.*, 1991], while a more optimized version was implemented in the DC casting code.

6 Natural Convection in the Casting: Physical Characteristics and Numerical Verification

> I can live with doubt and uncertainty and not knowing. I think it is much more interesting to live not knowing than to have answers that might be wrong.
>
> Richard P. Feynman

6.1 Introduction

The objective of the following part of the work is twofold. It aims to

- verify the numerical code and present a generalized verification of calculations of the thermosolutal buoyancy-driven flow, relevant for modeling of macrosegregation in DC casting.
- study the features of the flow occurring in the parameter range of thermosolutal natural convection found in the casting of binary aluminum alloys.

6.1.1 Verification

In the efforts to define guidelines to assess the credibility of computational fluid dynamics models, verification was defined as [AIAA, 1998, DoD, 2003] "The process of determining that a model implementation accurately represents the developer's conceptual description of the model and the solution to the model" and was distinguished from validation, "The process of determining the degree to which a model is an accurate representation of the

real world from the perspective of the intended uses of the model." Simply said, verification is a set of procedures which gives an answer to the question of whether the numerical solution of the model equations is appropriate. It is not proof in the mathematical sense. It is instead a method of increasing confidence in the numerical model implementation (code) by exercising it on, usually simplified, problems for which a reliable (exact analytical or approximative numerical) reference solution exists. In this way it helps to ensure that the code is free of mistakes and inconsistencies, and thus that all errors in the solutions stem from the finite accuracy of the discrete approximation, iterative convergence errors etc. Further, given a verified code, verification procedures are able to produce estimates of discretization error for specific solutions. The verification techniques which are to be employed in this work are described in detail in Section 6.2. In the present work, the verification focuses on the solution of flow and solute transport by natural convection in the liquid part of the casting. This is necessary because the accuracy of fluid flow solutions in previous model studies of DC casting is mostly lacking either due to insufficient grid resolution, the use of low-order numerical methods, or numerical instability [Flood *et al.*, 1991, Reddy and Beckermann, 1995, Reddy and Beckermann, 1997, Grün *et al.*, 2000, Vreeman and Incropera, 2000, Vreeman *et al.*, 2002, Venneker and Katgerman, 2002, Založnik *et al.*, 2004, Založnik and Šarler, 2005b]. No reference solution to a comparable problem is therefore available. To clearly investigate the effects of individual macrosegregation phenomena, accurate numerical solutions of the natural convection flow are required [Založnik and Šarler, 2006a], especially since the flow structure in the liquid pool was shown to have a significant influence on the macrosegregation patterns [Založnik and Šarler, 2005a]. The verification procedure, devised in Section 6.5, consists of a gradual increase of challenge to the numerical code and the systematic exercise of all equation terms decisive in the thermosolutal flow. With its results in Sections 6.6–6.10 I present and propose a generalized solution verification study that is valid for flow solutions in the physical parameter range of the natural convection flow in DC casting.

6.1.2 Natural Convection in Metal Mixtures

An understanding of the flow structures induced by thermal and solutal natural convection is an important piece of the puzzle of modeling macrosegregation in DC castings. It is all the more important within the present work as I hypothesize a significant impact of flow structure in the liquid sump on the macrosegregation patterns in DC castings (Ref. [Založnik and Šarler, 2005a] and Chapter 7). Thermosolutal natural convection flow and solute and heat

transport in liquid metal mixtures are complex physical phenomena as the flow is prone to several types of instability originating from thermal buoyancy, solutal buoyancy and the interaction of both forces. They are only poorly explored and the few published studies in this area [Shyy and Chen, 1991, Hyun *et al.*, 1995, Bergman and Hyun, 1996] do not cover the physical parameter range that is of interest in DC casting. The theoretical basis of the governing parameters and the parameter dependence of natural convection flow, as well as the interaction of thermal and solutal effects in the parameter range estimated to be of interest in DC casting, are discussed in Section 6.3. I argue that due to the physical complexity of the relevant thermosolutal flow problem it would not be reasonable to study the fully coupled problem straightaway. It is therefore subdivided into simplified convection subproblems where I study, by steps, the effects of thermal convection in liquid metals (low-Prandtl-number fluids), solutal convection in liquids at high solutal Rayleigh numbers, the relation between thermosolutal convection in high- and low-Prandtl-number fluids, and further the influence of geometry to relate thermal convection in a simplified rectangular geometry and in the realistic geometry of the liquid pool in a DC casting. All of this is done with the aim of better understanding the flow in the DC casting. This exploration is performed in Sections 6.6–6.10 on the same test cases and parallel to the verification procedure.

6.1.3 Numerical Methods

The numerical methods used to solve the governing macroscopic transport equations are an extremely important issue in the modeling of macrosegregation. A particular concern of solving natural convection flow and species transport in metals is the accuracy and stability of the method. Transport of momentum and species is predominantly advective, promoting the numerical instability of high-order accurate discretization schemes, as already discussed in Chapter 5. In the past, most DC casting models resorted from the threatening instability to stable but very inaccurate first-order discretization schemes. The discretization errors introduced by the low-order discretization were shown to be problematic [Vreeman and Incropera, 1999, Venneker and Katgerman, 2002]. It was shown that their inaccuracy can contaminate the solution with an error significant enough to obscure the qualitative structure of the flow [Hannoun *et al.*, 2003, Založnik and Šarler, 2005b, Založnik and Šarler, 2006a]. Proposing a solution to this problem is one of the objectives of the present work. The choice of the discretization method is therefore discussed in Section 6.4 in view of the (apparent) stability-accuracy dilemma.

6.2 Methods of Verification

6.2.1 Aims of Verification

There are two fundamental aspects of the verification of numerical models: code verification and solution (or calculation) verification [Roache, 1998b, Roy, 2005] and both are pursued here. In large part, the same or related methodological concepts [Lobe, 2006] and procedures are employed in both types of verification.

Code verification ensures that the numerical model implementation (computer code) is free of mistakes or inconsistencies in the solution algorithm. It thereby assures that the results will be physically sensible. In the quantitative sense it assures that the numerical errors are limited to discretization errors. These should be sufficiently small with respect to the reference (exact or benchmark) solution of the test problem, they should shrink towards zero as the discretization is refined, and should do so at the rate of the formal order of accuracy. Clearly, code verification has to exercise all equation terms; despite this, it only seems to be generally representative of the solution accuracy in the tested parameter range.

To verify the performance of the code in specific situations *solution verification* is employed. Solution verification deals with the estimation of numerical errors, particularly discretization errors for specific calculations (solutions). It provides quantitative error estimates for the solutions as error bands with some practical level of confidence [Roache, 1998b].

The main purpose of the verification analysis shown in this part of the present work is solution verification. Some separate cases of code verification are also shown since code verification in the parameter range that is of interest in the final calculations would be very difficult. A very careful approach to solution verification is taken. The performance of the code in the parameter range of the final problem of interest (DC casting) is first tested on partial model (prototypal) problems. Each of these prototypal problems represents a subset of the physics contained in the casting problem, however, most importantly, they retain the values of the relevant dimensionless parameters of the DC casting problem. The estimates of discretization errors of the prototypal problems are believed to give an idea of the general accuracy of the code in a certain relevant parameter range and its dependence on grid size and type. General estimates of accuracy for the solutions of thermosolutal natural convection flow in the liquid pool of the DC casting are obtained.

The verification methods used for both code and solution verification mostly belong to the class of extrapolation-based a posteriori error estimation methods. In addition, some benchmark and code-to-code comparisons

were also used. Only the methods used in the present work are described hereafter. More details and a more general and extensive overview of verification methods can be found in the two main references for verification methods used in this text, namely the book by Roache [Roache, 1998b] and the review paper by Roy [Roy, 2005].

6.2.2 Methods of Code Verification

Comparison to numerical benchmark solutions

Comparisons with numerical benchmark solutions [de Vahl Davis, 1983,Hortmann *et al.*, 1990, Wan *et al.*, 2001] are used to verify the code for natural convection problems. All quantities specified in the published benchmark solutions can be compared. The code is assessed based on its convergence towards the benchmark solution or, more appropriately, to the error band interval of the benchmark solution [de Vahl Davis, 1983].

Verification of the order of convergence

A good match of the observed (practical) and formal order of convergence ensures that the errors in the code are limited to discretization errors, which are ordered in the discretization size according to the order of accuracy of the discretization method. For a p-th order discretization method the (unknown) exact solution f^{exact} and the numerical solution f_i on a grid with grid distance h_i are related by

$$f_i = f^{\text{exact}} + \underbrace{C h_i^p}_{\text{leading error term}} + O(h_i^{p+1}) \tag{6.1}$$

If the solutions are in the asymptotic range of grid convergence (sufficiently close to f^{exact}) and grid convergence is monotonous (as it mostly is in the code verification cases used), the *leading error term* dominates and the factor C of the leading error term is approximately constant. For a constant grid refinement ratio r over three grids, the observed order of convergence (OOC) p is then

$$p = \frac{\ln\left(\frac{f_3 - f_2}{f_2 - f_1}\right)}{\ln r} \qquad r = \frac{h_3}{h_2} = \frac{h_2}{h_1}, \tag{6.2}$$

where h_3, h_2, and h_1 are the grid spacings from the coarsest to the finest, and f_3, f_2, and f_1 are the respective numerical solutions. Strictly speaking, the formal order of accuracy of the QUICK finite-volume discretization scheme, which is used for advection-diffusion of momentum and species, is second-order, due to some minor simplifications that were made by omitting

transverse-curvature terms in the advection interpolants, and thus not accounting for the two-dimensionality of the problem. It is also second-order for non-equidistant grids, which are used in some computations. Practically, these deviations from the otherwise third-order accuracy of QUICK [Leonard and Mokhtari, 1990,Leonard, 1997] are small however. The centered-difference scheme used in the energy equation is formally second-order accurate. We should thus expect the observed order of convergence to be at least second-order or slightly higher.

Error estimation

Different extrapolation-based error estimators are used, depending on the reference solution. When an exact solution is given, the actual relative discretization error (RDE) of solution f_i is simply

$$RDE_i = \frac{f_i - f_{\text{exact}}}{f_{\text{exact}}}. \tag{6.3}$$

In the absence of an exact solution a practical error band can be estimated from a grid convergence study. Roache [Roache, 1998b] recommends the GCI—grid convergence index—as an error band of solution f_i.

$$GCI_i = \frac{F_{\text{s}}}{r^p - 1}\left|\frac{f_{i+1} - f_i}{f_i}\right|, \qquad F_{\text{s}} = 3 \qquad r = \frac{h_{i+1}}{h_i}, \tag{6.4}$$

where f_i is the solution on the finer grid, f_{i+1} the solution on the coarser grid, r is the grid refinement factor from f_{i+1} to f_i and p is the observed order of convergence. $F_{\text{s}} = 3$ is a safety factor based on the convergence of a second-order method at a grid refinement factor of 2 as a reference. The GCI thus gives the relative error $|(f_{i+1} - f_i)/f_i|$ that would be obtained by a second-order method with $r = 2$ if the estimated error of the fine-grid solution (GCI_i) is the same. A third alternative of error estimation shows up when using a benchmark solution or an extrapolated solution as a reference. In this case f_{exact} in Eq. (6.3) can be replaced by the benchmark solution f_{bench} or the extrapolated solution f_{Rex}, but in this case an error band of f_{bench} or f_{Rex} has to be added to the error estimate. Using classical Richardson extrapolation the extrapolated solution is

$$f_{\text{Rex}} = f_i + \frac{f_i - f_{i+1}}{r^p - 1} \tag{6.5}$$

and, if the order of accuracy of f_i and f_{i+1} is p, its order of accuracy is $p + 1$ in general. Roache [Roache, 1998b] recommends estimating the error band of a fourth-order accurate

Richardson-extrapolated solution f_{Rex} by

$$GCI_{\mathrm{Rex}} = \frac{1}{r^p - 1}\left|\frac{f_i - f_{\mathrm{Rex}}}{f_{\mathrm{Rex}}}\right| \qquad r = \frac{h_{i+1}}{h_i}, \tag{6.6}$$

where r is the grid refinement factor between the coarse- and fine-grid solutions used in the Richardson extrapolation. Error bands of benchmark solutions are not always given but they can be estimated from the grid convergence data, according to Eqs. (6.2), (6.5) and (6.6).

Code-to-code comparison

A code-to-code comparison, which is performed for some cases, could also be classified as code verification. However, it should be used with much caution for this purpose [Trucano *et al.*, 2003] if none of the codes can be strictly defined as a reference and the "reference" code is not rigorously verified (as for example in [Vertnik *et al.*, 2006]). Thus, this step is regarded more as an initial confidence boost rather than a formal verification method.

6.2.3 Methods of Solution Verification

Extrapolation-based error estimators are used to verify the calculations. In the solutions of the investigated test cases and their evolution with grid refinement two situations were encountered and required different treatments. In the case of monotonous grid convergence, the classical Richardson extrapolation (Eq. (6.5)) can be used if we want to generate an extrapolated solution. Accordingly, we can use the observed order of convergence (Eq. (6.2)) to determine the GCI (Eq. (6.4)), based on the monotonous Richardson extrapolation (Eq. (6.5)). In many of the more demanding cases, however, the grid convergence was oscillatory even with very dense grids. While most literature sources argue that oscillatory convergence cannot occur in the asymptotic range and should thus be a sign of insufficient grid resolution or some other error, Celik et al. [Celik *et al.*, 2005] recently showed that oscillatory convergence can persist even when the discretization errors are already very small. They also proposed several alternative methods of extrapolation, which can be used in the case of oscillatory convergence. I employed the approximate error spline method which came out best in the tests of Celik and coworkers. Of course, the leading error term assumption of the Richardson extrapolation breaks down in the case of oscillatory convergence. An alternative way of determining a practical error band therefore had to be used.

Like with code verification before, the methods used for solution verification are now listed. They were adapted from references [Roache, 1998b]

and [Celik *et al.*, 2005].

Classical Richardson extrapolation

A Richardson extrapolation based on the observed order of convergence is used in cases of monotonous grid convergence and is given by Eqs. (6.2) and (6.5).

GCI as an error band

For monotonous grid convergence the GCI is determined as explained before and given by Eq. (6.6), taking into account the observed order of convergence.

Extrapolation with the approximate error spline method

The Approximate Error Spline (AES) method [Celik *et al.*, 2005] is used for extrapolation in cases of oscillatory grid convergence. In this method the approximate error $E_a = f_{i+1} - f_i$, which is the difference of solutions on two subsequent grids, as a function of grid distance h is interpolated by a cubic spline. Solutions on at least three different grids are needed to do this. This interpolation, explained in detail by Celik et al. [Celik *et al.*, 2005], finally allows us to determine a cubic polynomial interpolation function describing the evolution of the numerical solution on the grid spacing interval $0 \leq h \leq h_1$, where h_1, is the spacing of the finest grid.

$$f(h) = f(h{=}0) + a_2 h^2 + a_3 h^3 \qquad 0 \leq h \leq h_1 \tag{6.7}$$

The extrapolated solution $f_{\mathrm{AESex}} = f(h = 0)$ is then determined from the known finest-grid solution $f_1 = f(h_1)$ using Eq (6.7).

Extrapolation-based error band

The GCI (Eq. (6.4)) is actually based on a Richardson extrapolation but is formulated in a way that allows us to determine it without explicitly calculating the extrapolated solution. In the case of oscillatory convergence the oscillations are caused by competing error terms or nonconstant error term coefficients. The concept of a leading error term (Eq. (6.1)) is thus not applicable. Consequently, the Richardson-extrapolation based GCI (Eq. (6.4)) cannot be used. We can thus turn to the original expression for the extrapolation-based error band, which is based on simply approximating the exact solution f_{exact} in Eq. (6.3) by the extrapolated solution f_{AESex}. In addition we use a

safety factor $F_\mathrm{s} = 3$ as before and the *theoretical* order of convergence p. For solution f_i on grid h_i the error band is

$$RDE_i^{\mathrm{band}} = \frac{F_\mathrm{s}}{r^p - 1} \left| \frac{f_i - f_{i+1}}{f_{\mathrm{AESex}}} \right| . \tag{6.8}$$

For the AES-extrapolated solution f_{AESex} the error band is

$$RDE_{\mathrm{AESex}}^{\mathrm{band}} = \frac{1}{r^p - 1} \left| \frac{f_i - f_{\mathrm{AESex}}}{f_{\mathrm{AESex}}} \right| . \tag{6.9}$$

Roy [Roy, 2005] shows that the difference between the values of the GCI and a respective RDE^{band} are small and are also ordered in h. They can thus be compared consistently.

The leading error term in oscillatory convergence does not behave in accordance with Eq. (6.1) (C could change sign or the higher-order error terms are also significant) and Eq. (6.2) cannot be used to determine the OOC. Therefore, I tried to estimate the OOC using a *power-law approximation* where the dependence of the relative discretization error RDE_i (Eq. (6.3), approximating $f_{\mathrm{exact}} \approx f_{\mathrm{AESex}}$) on grid distance h is approximated by a power law.

$$RDE_i = Ch^p \tag{6.10}$$

The OOC is then estimated by the power p in the least-squares fit of the power-law function.

6.3 Natural Convection in Liquid Metal Mixtures During Casting

6.3.1 Governing Equations and Parameters

Fluid flow caused by natural convection in the molten part of the casting is a decisive phenomenon for macrosegregation. The solute transport by the flow determines the composition at the solidification front and in the mushy zone. The physics of the flow in DC casting is modeled by the equations derived in Section 4.4. In the purely liquid region and with additional simplifying assumptions of constant liquid density, viscosity, thermal conductivity, specific heat, and diffusion coefficient they reduce to the Boussinesq equations for thermal and solutal natural convection. The continuity, momentum, energy, and species equations thus reduce to

$$\nabla \cdot \vec{v} = 0 \tag{6.11}$$

$$\frac{\partial \vec{v}}{\partial t} + (\vec{v} \cdot \nabla)\, \vec{v} = -\frac{1}{\rho_0}\nabla p + \nu \nabla^2 \vec{v} - \vec{g}\left[\beta_T \left(T - T_0\right) + \beta_C \left(C - C_0\right)\right] \quad (6.12)$$

$$\frac{\partial T}{\partial t} + \vec{v}\nabla T = \kappa \nabla^2 T \quad (6.13)$$

$$\frac{\partial C}{\partial t} + \vec{v}\nabla C = D \nabla^2 C, \quad (6.14)$$

where the subscripts 'l', denoting the liquid phase are dropped for simplicity, ν is the kinematic viscosity and $\kappa = k/(\rho_0 c_p)$ is the thermal diffusivity. Equations (6.11)–(6.14) can be expressed in a dimensionless form in terms of nondimensional velocity, temperature, concentration, time, and coordinates $\vec{v}^* = (u^*, v^*)$, θ, ϕ, t^*, x^*, and y^* respectively, and in terms of four dimensionless numbers. These are the thermal Rayleigh and Prandtl numbers

$$Ra_T = \frac{g\beta_T \Delta T H^3}{\nu\kappa} \qquad Pr = \frac{\nu}{\kappa}, \quad (6.15)$$

and the solutal Rayleigh and Schmidt numbers

$$Ra_C = \frac{g\beta_C \Delta C H^3}{\nu D} \qquad Sc = \frac{\nu}{D}, \quad (6.16)$$

where g is the gravity acceleration, H is the characteristic height of the flow domain, and ΔT and ΔC are the characteristic temperature and concentration differences driving the flow. An additional parameter is the aspect ratio of the flow geometry

$$A = \frac{H}{L}. \quad (6.17)$$

The characteristic length, temperature and concentration scales are shown schematically in Fig. 6.1.

The dimensionless form of the equations reveals that the parameter dependence of the relations among different terms in the equations is reduced to the dependence on the five dimensionless parameters. The flow is thus studied in the $[Pr, Sc, Ra_T, Ra_C, A]$ space. The scales for the normalization of the leading quantities needed to transform the problem into the dimensionless space are based on scale estimates within the boundary layer approximation. This approximation is based on the notion that the region close to the wall (the boundary layer) can be considered as distinct from the rest of the flow domain. All mechanical, thermal and solutal effects introduced by the wall are confined to the boundary layer, while the free stream is not directly affected. The heat and species transfer can be thus characterized by analyzing the transport in the boundary layer. A prototypal situation for natural convection flow in a closed domain is the natural convection in a differentially

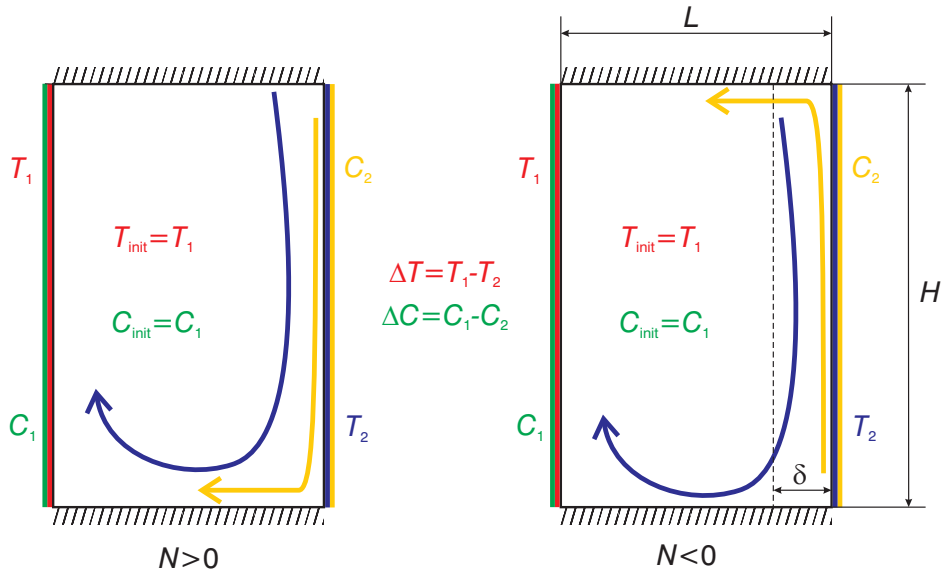

Figure 6.1: Rectangular enclosure with imposed temperatures and concentrations at the vertical side walls, a prototypal case of natural convection in a closed domain.

heated (and spiced) rectangular cavity with insulated top and bottom walls (Fig. 6.1). The scaling analysis within the domain of the boundary layer and horizontal discharge jet, shown in Fig. 6.1 relies on the basic scales

$$x \sim \delta_T \qquad y \sim H \qquad T \sim \Delta T \qquad C \sim \Delta C. \tag{6.18}$$

The scales of velocity and time then stem from estimates of velocity and boundary layer growth time and are deduced by scaling analysis. They are different for different heat transfer regimes, i.e. conductive or convective, and Prandtl number ranges, i.e. $Pr \ll 1$ or $Pr \gg 1$ [1]. The fact that in the literature they are not always used consistently with the parameter range of interest is marginal but it somewhat obscures the relations of the terms in the equations. The scales of velocity V, time τ and thermal boundary layer thickness δ_T in the different regimes are the following. In the conduction regime

$$\begin{aligned} V &\sim A^2 \frac{\kappa}{H} & U &\sim A \frac{\kappa}{H} \\ \delta_T &\sim \frac{H}{2A} & \tau &\sim \frac{H^2}{4A^2\kappa} \end{aligned} \qquad \begin{bmatrix} Pr \gg 1 \\ Ra_T^{-\frac{1}{4}} \ll 1 \end{bmatrix} \qquad \begin{bmatrix} Pr \ll 1 \\ (Ra_T Pr)^{-\frac{1}{4}} \ll 1 \end{bmatrix} \tag{6.19}$$

[1] Note, that the discussion of the velocity and time scales here is confined to the purely thermal situation. Its scales remain valid if the heat transfer is controlled by the thermal buoyancy flow. The scales found in thermosolutal flows are elaborated, for example, in reference [Bennacer and Gobin, 1996] for $Pr \gg 1$.

In the convection regime

$$\begin{aligned} V &\sim \frac{\kappa}{H} Ra_T^{\frac{1}{2}} \qquad U \sim \frac{\kappa}{H} Ra_T^{\frac{1}{4}} \\ \delta_T &\sim H Ra_T^{-\frac{1}{4}} \qquad \tau \sim \frac{H^2}{\kappa} Ra_T^{-\frac{1}{2}} \end{aligned} \qquad \begin{bmatrix} Pr \gg 1 \\ Ra_T^{-\frac{1}{4}} \gg 1 \end{bmatrix} \tag{6.20}$$

$$\begin{aligned} V &\sim \frac{\kappa}{H} (Ra_T Pr)^{\frac{1}{2}} \qquad U \sim \frac{\kappa}{H} (Ra_T Pr)^{\frac{1}{4}} \\ \delta_T &\sim H (Ra_T Pr)^{-\frac{1}{4}} \qquad \tau \sim \frac{H^2}{\kappa} (Ra_T Pr)^{-\frac{1}{2}} \end{aligned} \qquad \begin{bmatrix} Pr \ll 1 \\ (Ra_T Pr)^{-\frac{1}{4}} \gg 1 \end{bmatrix} \tag{6.21}$$

In the convection regime with $Pr \ll 1$, which is the relevant range for natural convection of metals, and with the assumption that the heat transfer is controlled by the thermal buoyancy force—both will be shown subsequently—we should use the scales in Eqs. (6.18) and (6.21) for nondimensionalization and obtain the following dimensionless equations, formulated in terms of dimensionless coordinates (x^*, y^*) velocity $\vec{v}^* = (u^*, v^*)^T$, temperature θ and concentration ϕ. Continuity equation

$$\overset{*}{\nabla} \cdot \vec{v}^* = 0, \tag{6.22}$$

momentum equations

$$\frac{\partial u^*}{\partial t^*} + u^* \frac{\partial u^*}{\partial x^*} + v^* \frac{\partial u^*}{\partial y^*} = -(Ra_T Pr)^{\frac{1}{2}} \frac{\partial p^*}{\partial x^*} + Pr \left(\frac{\partial^2 u^*}{\partial x^{*2}} + (Ra_T Pr)^{-\frac{1}{2}} \frac{\partial^2 u^*}{\partial y^{*2}} \right) \tag{6.23}$$

$$\frac{\partial v^*}{\partial t^*} + u^* \frac{\partial v^*}{\partial x^*} + v^* \frac{\partial v^*}{\partial y^*} = -\frac{\partial p^*}{\partial y^*} + Pr \left(\frac{\partial^2 v^*}{\partial x^{*2}} + (Ra_T Pr)^{-\frac{1}{2}} \frac{\partial^2 v^*}{\partial y^{*2}} \right) - (\theta + N\phi) \tag{6.24}$$

energy equation

$$\frac{\partial \theta}{\partial t^*} + u^* \frac{\partial \theta}{\partial x^*} + v^* \frac{\partial \theta}{\partial y^*} = \frac{\partial^2 \theta}{\partial x^{*2}} + (Ra_T Pr)^{-\frac{1}{2}} \frac{\partial^2 \theta}{\partial y^{*2}}, \tag{6.25}$$

and species equation

$$\frac{\partial \phi}{\partial t^*} + u^* \frac{\partial \phi}{\partial x^*} + v^* \frac{\partial \phi}{\partial y^*} = \frac{Pr}{Sc} \left[\frac{\partial^2 \phi}{\partial x^{*2}} + (Ra_T Pr)^{-\frac{1}{2}} \frac{\partial^2 \phi}{\partial y^{*2}} \right], \tag{6.26}$$

where the buoyancy ratio is $N = \frac{Ra_C}{Sc} \frac{Pr}{Ra_T}$. As the scaling is consistent with the heat and mass transfer regime, all dimensionless quantities in the above equations are of the order of magnitude of unity. The relations between the

various transport terms can thus be inferred from Pr, Ra_T, Sc, and Ra_C alone, which will be used in Section 6.3.2. An exception, although unimportant here, is the species equation, where the pertinent diffusion length is much smaller $\delta_C \ll \delta_T$ and the scales of the dimensionless term thus deviate from unity. The general relation with very small diffusion terms remains clear however.

Although the problems of main interest in this work fall in the convective regime with $Pr \ll 1$, the scale estimates of Eq. (6.20) will be used for the nondimensionalization of variables. Further, all dimensions are normalized by the same length—H. This is done simply to conform to the scales often used in the literature and to retain the same scales throughout the text. Thus, the dimensionless variables will be defined

$$(x^*, y^*) = \frac{(x,y)}{H} \qquad t^* = \frac{\kappa}{H^2}(Ra_T)^{\frac{1}{2}}\, t \qquad \vec{v}^* = \frac{H}{\kappa}(Ra_T)^{-\frac{1}{2}}\, \vec{v}$$
$$\psi^* = \frac{1}{\kappa}(Ra_T)^{-\frac{1}{2}}\, \psi \qquad \theta = \frac{T - T_0}{\Delta T} \qquad \phi = \frac{C - C_0}{\Delta C}. \tag{6.27}$$

6.3.2 Parameters of Natural Convection in DC Casting

From estimates of known parameters of the DC casting problem and properties of metal melts an evaluation of the parameter range of Ra_T, Ra_C, Pr, and Sc, that is of interest in investigating the flow in DC casting, can be made. The evaluation is based on the estimates given below, which were taken for an Al-Cu alloy (at around 5 wt.%Cu). The thermophysical properties of Al-Cu alloys give the most "severe" and thus the most conservative estimates of Ra_T and Ra_C since they combine high alloying element concentrations (up to 5 wt.%Cu) with strong solute partitioning and the largest solutal expansion coefficient of all prominent alloying elements. On the other hand, the estimates of Pr and Sc can be considered safe for all Al-alloys as they depend on properties that do not vary substantially for different alloys. Also, considering the geometry and boundary conditions of the relevant liquid pool in the DC casting the estimates of Ra_T and Ra_C given hereafter are safe [2]. In the liquid pool, the high temperature is imposed at the top and the low temperature at the inclined liquidus front (Fig. 6.2). This arrangement represents a configuration that should be considerably more stable than the prototypal enclosure heated at the side walls, similarly to the effect caused by inclining an enclosure as lucidly explained by Bejan [Bejan, 2004].

[2] To refer to parameter estimates as *safe* or *conservative* in this context means that they define *an equally or more complex* physical situation than the realistic parameters. These cannot always be determined exactly or they float within a range, depending on the casting parameters.

- The characteristic enclosure width is half of the diameter resp. width of the casting: $L = \frac{d}{2} \sim 0.2\,\mathrm{m}$
- Liquid pool depth: $H \sim 0.2\,\mathrm{m}$
- Characteristic temperature difference: $\Delta T = T_{\mathrm{cast}} - T_{\mathrm{L}} \sim 30\,\mathrm{K}$
- Characteristic concentration difference: $\Delta C \sim 2 \cdot 10^{-2}$ [Založnik and Šarler, 2006b]
- Volumetric thermal expansion coefficient: $\beta_T \sim 10^{-4}\,\mathrm{K}^{-1}$ [JMatPro, 2004]
- Volumetric solutal expansion coefficient: $\beta_C \sim 1$ [JMatPro, 2004]
- Dynamic viscosity: $\mu \sim 10^{-3}\,\mathrm{Pa\,s}$ [JMatPro, 2004, Iida and Guthrie, 1993, Dinsdale and Quested, 2004]
- Thermal conductivity: $k \sim 10^{2}\,\mathrm{W/m\,K}$ [JMatPro, 2004]
- Specific heat: $c_p \sim 10^{3}\,\mathrm{J/kg\,K}$ [JMatPro, 2004]
- Density: $\rho \sim 3 \cdot 10^{3}\,\mathrm{kg/m^3}$ [JMatPro, 2004]
- Diffusion coefficient: $D \sim 5 \cdot 10^{-9}\,\mathrm{m^2/s}$ [JMatPro, 2004]

The estimates of the orders of magnitude of the parameters are

$$Pr \sim 10^{-2} \qquad Ra_T \sim 2.7 \cdot 10^{9} H^3 \sim 7 \cdot 10^{6} \tag{6.28}$$

$$Sc \sim 10^{2} \qquad Ra_C \sim 10^{14} H^3 \sim 10^{12} \tag{6.29}$$

The implications of the low Prandtl number can be seen from the relations of the terms in Eq. (6.24), which is properly scaled for $Pr \ll 1$. The buoyancy forces driving the flow are balanced by the inertial forces. The viscous effect of the wall is confined to a very thin momentum boundary layer. This situation, occurring in low-Pr metals, is fundamentally different from the relations in high-Pr fluids, which is shown in Fig. 6.3. In high-Pr fluids the driving buoyant force is confined inside the viscous layer and the friction-inertia force balance outside the driving heated layer causes a transition into a stagnant zone. Contrarily, in low-Pr fluids the influence of the driving force extends with the heated layer beyond the near-wall region where the influence of viscous friction is still important. This means that most regions of the flow are governed by a balance of buoyancy and inertia. Intuitively, we

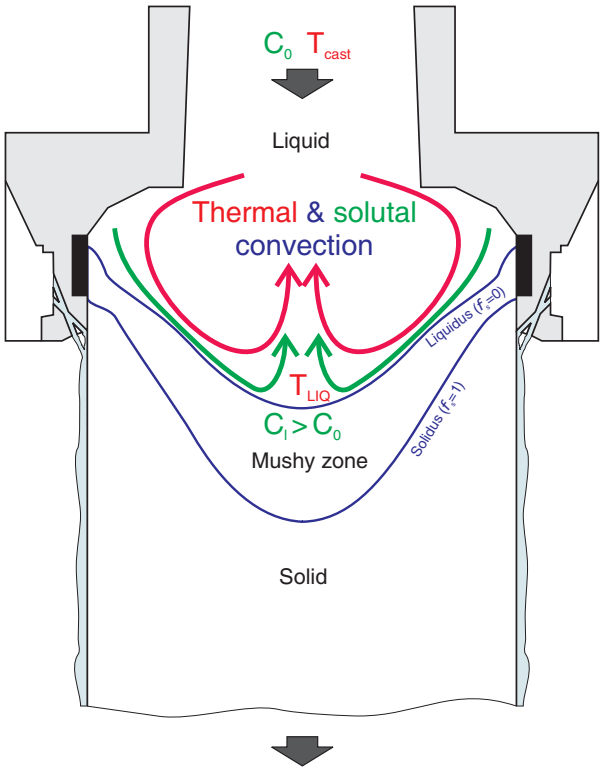

Figure 6.2: Thermosolutal convection in the liquid pool of a DC casting.

can understand that such a flow is less stable than a high-Pr flow. Mathematically, this means that the non-linearity of the governing equation system becomes stronger with the relative amplification of the non-linear advection term in the momentum equation.

The high thermal Rayleigh number implies a predominantly convective heat transfer. Special attention is given since the inherent instability of low-Pr flows amplifies with larger Ra_T. Instabilities, triggering flow structures with multiple flow cells and an oscillatory flow are known from experimental and numerical studies to already occur at moderate Ra_T at low Pr [Mohamad and Viskanta, 1991, Janssen and Henkes, 1993, Cless and Prescott, 1996a, Cless and Prescott, 1996b, Kamakura and Ozoe, 1996, Le Quéré and Gobin, 1999, Hannoun *et al.*, 2003]. In their numerical study and review of experimental results, Lage and Bejan [Lage and Bejan, 1991] recommend the relation $Ra_T \approx 10^9 Pr$ as an empirical threshold for the transition of laminar to turbulent flows in natural convection. From their numerical results and theoretical analysis a lower threshold-Ra_T for the onset of the transition would actually follow. But these lower values apparently (clearly in the case

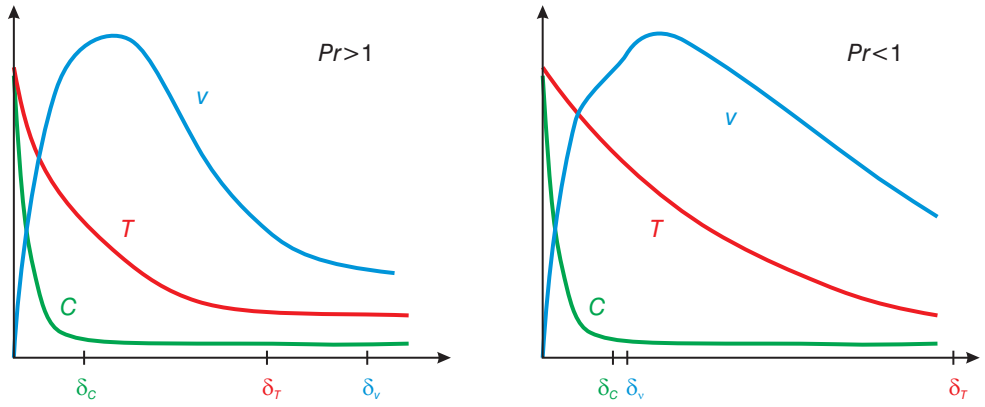

(a) High Prandtl number.

(b) Low Prandtl number.

Figure 6.3: Illustration of relative sizes of thermal, solutal and velocity boundary layers in thermosolutal natural convection in liquids.

of numerical results) only indicate a transition from a steady state flow to an unsteady oscillatory flow. In the parameter range of interest here (Eq. (6.28)) we can clearly expect an unstable and unsteady flow.

The high Schmidt number together with the very high Ra_C implies that the solutal buoyancy effect is confined to extremely thin solutal boundary layers inside the velocity boundary layers as shown in Fig. 6.3. The magnitude of Ra_C is again at the threshold of steady solutions as $Ra_C \approx 10^9 Sc$. The mechanisms of steady and unsteady instabilities in high-Pr fluids [Bergholz, 1977, Le Quéré and Gobin, 1999] are, however, different than in the low-Pr case. They occur in the boundary layer as observed in the results presented later. On the whole, it is not clear in advance whether the solutal effect will by itself cause a flow structure that is more complex than the boundary layer recirculation with a stagnant core. It is also unclear if such a solutal flow would be steady or unsteady.

The flow structures that could occur in combined thermosolutal convection in the range of Pr and Sc estimated above are not clear. The thermosolutal flow patterns in this parameter range are not well explored and presently no such results are known to exist in the literature. Clearly, flow structures in low-Pr, high-Sc liquid metals may be very complex already at low Ra numbers, which is shown in the few existing numerical studies published by Hyun, Bergman and coworkers [Hyun *et al.*, 1995, Bergman and Hyun, 1996] and Shyy and Chen [Shyy and Chen, 1991]. While Hyun and coworkers worked with liquid Al-Cu and Pb-Sn alloys, i.e. relevant Pr and Sc, their studies are

limited to low Rayleigh numbers of only up to $Ra_T = 5000$. The study of Shyy and Chen, on the other hand, reaches the interesting range of Rayleigh numbers $Ra_T \sim 2 \cdot 10^6$, however it keeps a relatively low Schmidt ($Sc \sim 10$) and a relatively high Prandtl number ($Pr \sim 10^{-1}$ in most cases). In summary, there is no known investigation of thermosolutal flow in the parameter range relevant for solidification during casting.

The complexity of the physical phenomena in the buoyancy-driven flow during casting, as is suggested by the foregoing scaling analysis, discussion and literature review, shows that it could be difficult to analyze the thermosolutal flow in the parameter range of interest (Eqs. (6.28)–(6.29)). It seems more reasonable to break up the convection problem with respect to thermal and solutal effects and the range of the physical dimensionless parameters into simplified subproblems and to study the effects of the individual transport phenomena on these simplified cases before exploring the thermosolutal convection problem for the final relevant parameters. This approach might help us understand more deeply the flow structures in the final parameter range and the final DC casting problem. At the same time, it is believed to clarify the code and calculation verification procedure. The stepwise approach of simultaneous flow studies and code/solution verification is defined in detail in Section 6.5.

6.4 Numerical Issues in Modeling the Fluid Flow in Liquid Metal Mixtures

The numerical solution of the model equation system of Eqs. (6.11)–(6.14) for high Ra_T and Ra_C, low Pr, and high Sc can pose serious difficulties. For dominating advection, i.e. a high Péclet number, the numerical solution of transport equations in the predominantly advective transport range by the finite-volume method is prone to numerical

instability when using second- or higher-order interpolation schemes for advection. This problem appears in the transport of momentum and species. On the other hand, caution must be exercised when using stabilized or inherently more stable lower order schemes as they induce low-order numerical errors which manifest themselves similarly to an augmented diffusion term (i.e. numerical diffusion). They might prevent us from achieving sufficiently grid-converged results at acceptable grid sizes.

During the work on this project this numerical problem was soon recognized. The solution did not seem trivial at first and the stabilized ULTRA-QUICK advection scheme was implemented for momentum transport, giving

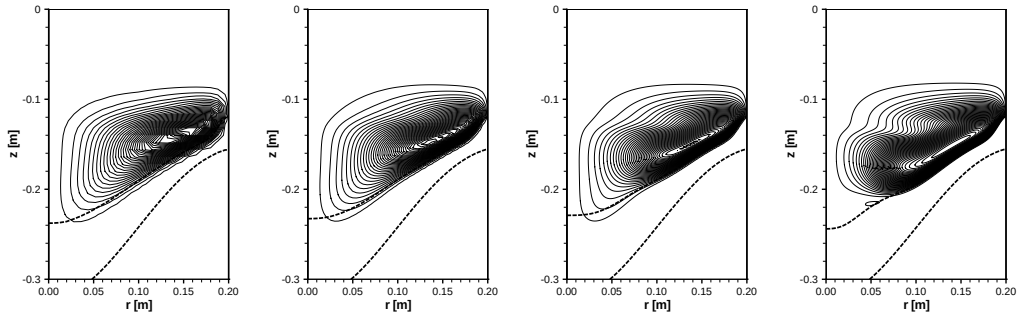

(a) First-order upwind scheme (mesh sizes, from left to right: 27×77, 52×152, 102×302, 270×502).

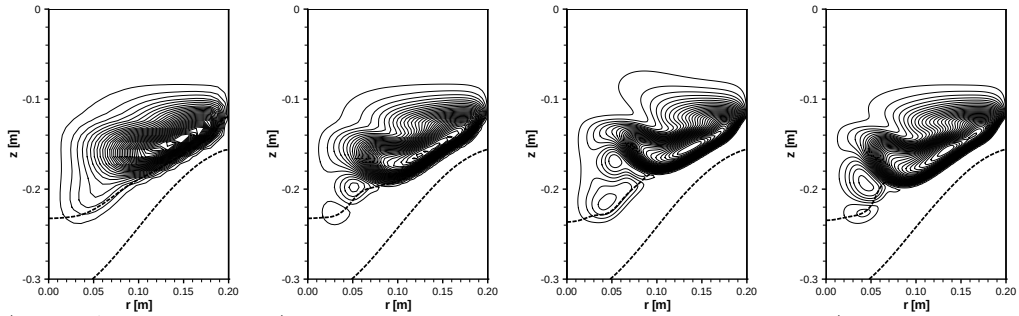

(b) ULTRA-QUICK scheme (mesh sizes, from left to right: 27×77, 52×152, 102×302 (periodic flow at two different times)).

Figure 6.4: Computation of flow in DC casting with two discretization schemes. Streamlines of relative velocity ($\vec{v} - \vec{v}_{\text{cast}}$) are shown.

excellent results [Založnik and Šarler, 2005b]. The scheme is based on the QUICK scheme and stabilized by the ULTRA-SHARP limiter [Leonard and Mokhtari, 1990], uniting higher-order accuracy and stability. After some exploration it was later found that the original QUICK scheme remains stable at moderately dense grids. The mistaken belief that a linear higher-order scheme (QUICK) would not be stable at grid Péclet numbers far beyond the stability limit [Založnik *et al.*, 2004] was based on the case of a one-dimensional convection-diffusion with Dirichlet boundary conditions [Patankar, 1980]. It was later corrected by the observation that the two-dimensionality of the problem and the presence of source terms stabilizes the numerical method. As the QUICK scheme was found to be more effective (faster and easier to code) than the nonlinear-limiter ULTRA-QUICK scheme, it was used afterwards for the discretization of the momentum and species equations.

6.5 Devising a Verification Procedure

We want to devise a testing procedure that will satisfy two aims, which were pointed out before:

- a systematic and thorough code and solution verification
- a comprehensive study of flow structures and heat and solute transport in thermosolutal natural convection in casting-relevant situations.

Both aims are pursued in parallel on the same test cases. The cases consider thermal, solutal and thermosolutal natural convection in rectangular cavities with imposed temperatures and concentrations at both vertical walls. The test cases are specified below and are arranged by increasing the complexity of the flow physics and demands to the numerical code. The findings gained in the tests can be used on the way as we approach the final parameters of thermosolutal flow. All explored cases, their parameters and verification objectives are summarized in tables 6.1 and 6.2.

case	Pr	Sc	Ra_T	Ra_C	A	steady flow/ transient flow
1a	-	0.71	-	10^5	1	steady
1b	-	1	-	10^8	1	steady
2	7	700	$7 \cdot 10^5$	$7 \cdot 10^8$	1	steady
3	0.0137	-	$2.81 \cdot 10^5$	-	4	transient
4		100	-	10^{10}	4	transient
5a	0.0137	100	$2.81 \cdot 10^5$	10^{11}	4	transient
5b	0.0154	187	$2.92 \cdot 10^5$	$2.85 \cdot 10^{10}$	4	transient
6	0.0184	-	$\sim 2.5 \cdot 10^5$	-	$\sim \frac{1}{2}$	steady

Table 6.1: Summary of test cases for natural convection flow: Physical parameters.

To achieve a solution of better quality (smaller discretization errors) on a grid with a given number of CVs it turns out to be effective to refine the grid locally in regions of large gradients and to coarsen it in low-gradient regions [Mencinger, 2001]. Therefore, two types of grids are used in the tests. In addition to the uniform grids, wall-refined grids are tested in situations where particularly thin solutal boundary layers were expected. The wall-refined grids are defined by the Chebyshev-Gauss-Lobatto points

$$x_i = x_1 + \frac{L}{2}\left[1 - \cos\left(\frac{(i-1)\pi}{m-1}\right)\right], \tag{6.30}$$

case	verification type	verification methods†
1a	code verification	Bench, OOC, ErrEst
1b	code verification	Bench, OOC, ErrEst, CtCC
2	code verification	OOC, ErrEst, CtCC (limited)
3	solution & code verification	OOC, ErrEst, CtCC
4	solution verification	OGC
5a	solution verification	OGC
5b	solution verification	-
6	solution verification	OGC

†**Bench**: comparison to benchmark solution, **CtCC**: code-to-code comparison, **ErrEst**: error band estimation, **OGC**: observation of grid convergence, **OOC**: verification of the observed order of convergence

Table 6.2: Summary of test cases for natural convection flow: Verification methods and objectives.

where x_i is the position of the i-th node and m is the total number of nodes in the x direction along length L. An analogous formula applies to the vertical (y) direction. Both the uniform and wall-refined grids are shown in Fig. 6.5. In the subsequent figures and tables the uniform and wall-refined grids are denoted by 'u' and 'c' respectively.

Case 1: Basic code verification for thermal or solutal buoyancy-driven flow

With the aim of code verification two benchmark cases, namely the original study of de Vahl Davis [de Vahl Davis, 1983] and the later extension of Wan, Patnaik and Wei [Wan *et al.*, 2001] which correspond to thermal natural convection of air and a similar fluid in a square cavity, were considered. The code was tested for cases of purely thermal and purely solutal convection by assessing the discretization error and observed order of grid convergence. Only the results of the solutal convection tests are shown here since Case 3 is later presented as a much more discriminative initial test for thermal natural convection. In any case, the parameter range of the benchmark cases ($Pr \sim 1$) is not relevant to thermal natural convection and the test was used merely as a first check. The parameters of the two benchmark cases are $Sc = 0.71$, $Ra_C = 10^5$, $A = 1$ [de Vahl Davis, 1983] and $Sc = 1.0$, $Ra_C = 10^8$, $A = 1$ [Wan *et al.*, 2001]. [3] In the purely solutal convection

[3]The results in ref. [Wan *et al.*, 2001] should be used with caution because the paper does not explicitly state the Prandtl number that was used ($Pr = 1.0$), while the comparison with de Vahl Davis' results for $Pr = 0.71$ gives the misleading impression that the

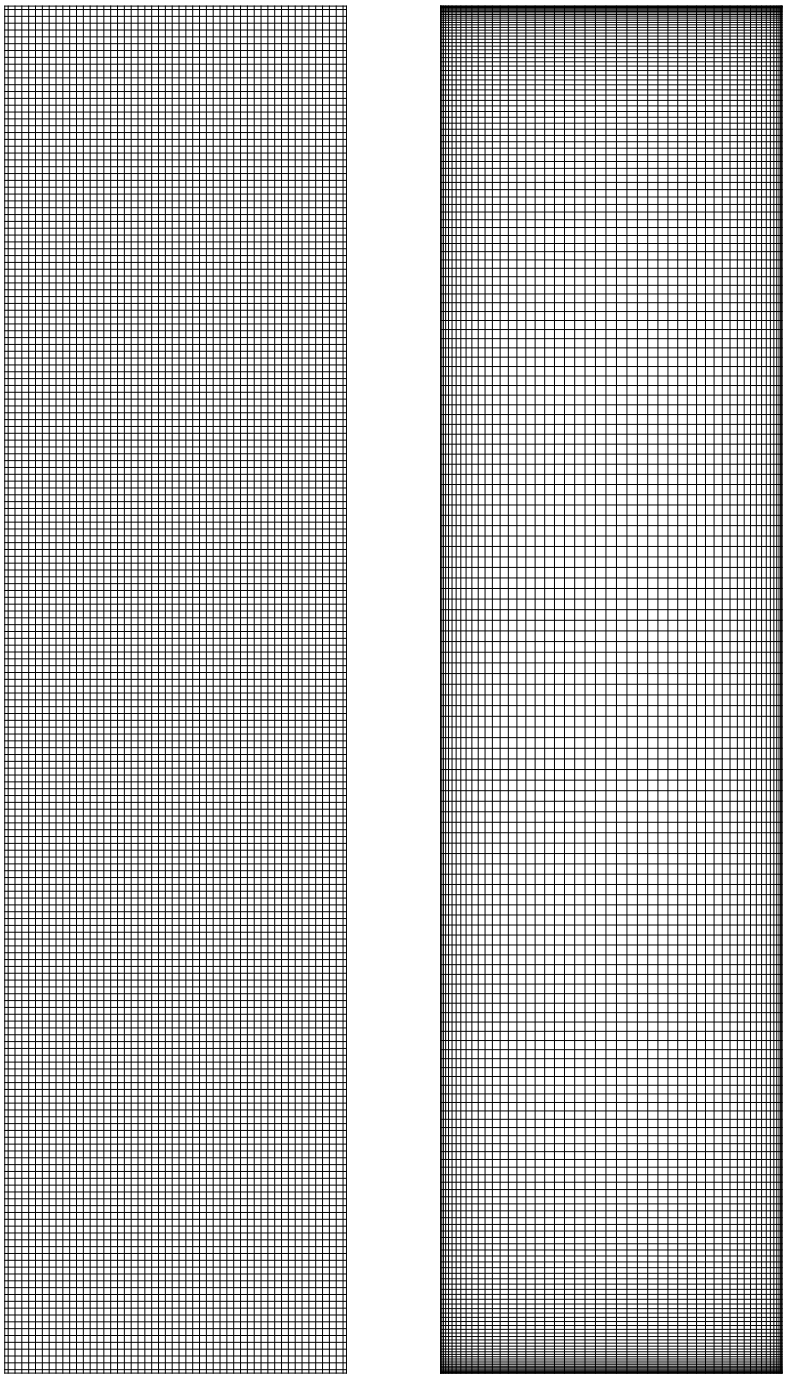

(a) Uniform grid (b) Wall-fitted Gauss-Lobatto grid

Figure 6.5: Grid types for the natural convection computations, shown for a grid of 50×100 CVs on a $A = 4$ domain.

case, the parameters of the benchmark are somewhat closer to the realistic parameter range, the essential similarity lying in the fact that the solutal boundary layer is not thicker than the velocity boundary layer. Also, like in the realistic parameter range, the parameters are close to the threshold of steady solutions $Ra_C < 10^9 Sc$ [Lage and Bejan, 1991].

Case 2: Thermosolutal natural convection of a high-Pr, high-sc liquid in a cavity

This case serves as a basic test case for double-diffusive natural convection to check the coupling of continuity, momentum, energy, and species conservation equations. The well-documented solutions by Bennacer and Gobin [Gobin and Bennacer, 1996] can be used for comparison and an initial check.

Case 3: Thermal natural convection of a pure liquid metal in a cavity

In this case a numerically more demanding and physically more relevant prototypal thermal-buoyancy driven flow of a metal is studied as a step in the gradual generalized calculation verification. The parameters $Pr = 0.0137$, $Ra_T = 2.81 \cdot 10^5$, $A = H/L = 4$ are relevant for casting situations and were extracted to be conservative for a case of solidification in a cavity. The results have been extensively studied. An extrapolated solution is calculated and discretization errors of the solutions as well as the extrapolated solution are estimated. Further, a comparison with the results obtained independently by a code based on the spectral Chebyshev-collocation method [Xin and Le Quéré, 2002] is shown.

Case 4: Solutal natural convection of an isothermal liquid metal in a cavity

The hypothetical situation, relevant to solutal natural convection with $Sc = 10^2$ and $Ra_C = 10^{10}$ is again tested on a case of natural convection in a cavity. This case does not represent a physically realistic situation but is tackled to explore the stability of the solutal boundary layer and the existence of steady solutions at high Ra_C (the threshold of steady solutions is estimated at $Ra_C < 10^9 Sc$ [Lage and Bejan, 1991]), as well as the dependence of the numerical solution of the solutal convection problem on the grid size and type. In the case of extremely thin solutal boundary layers sufficient grid refinement should be required at the cavity walls.

---

same Pr was used.

Case 5: Thermosolutal natural convection of a liquid metal in a cavity

The last two test cases on a simplified cavity geometry finally approach the parameters of double-diffusive natural convection relevant to the DC casting problem. They are used primarily to explore the arising flow structures. Concerning the quantitative accuracy of the results, I mainly rely on the verification by the previous test cases. Only a qualitative check of the sensitivity of the results to grid coarsening is performed. The relations with some previous research are hard to establish since there are no known studies of double-diffusive natural convection in this parameter range. The only known studies of natural convection in low-Pr, high-Sc fluids are the already mentioned works of Hyun, Bergman and coworkers [Hyun *et al.*, 1995, Bergman and Hyun, 1996], however they are limited to $Ra_T = 10^3$ for cooperating ($N = 23.7$) and to $Ra_T = 5 \cdot 10^3$ for counteracting ($N = -10$) buoyancy. They give a hint about the fine-scale structures that are to be expected in the flow.

Case 6: Thermal DC casting problem

In the first test case on the realistic geometry, the DC casting problem is approximated by the thermal part of the problem where the concentration C, solidus T_S, and liquidus T_L temperatures are fixed. It is used to test the code on realistic geometry, observe the interaction of the flow with the porous mushy zone, and test the requirements for grid density on a realistic problem, together with possible pitfalls, absent in the simplified prototypal cases.

6.6 Case 1: Basic Verification for Buoyancy-Driven Flow

Two numerical benchmark cases are considered for a basic verification of the code. The first is the classical benchmark defined by de Vahl Davis [de Vahl Davis, 1983] and later refined by Hortmann, Perić, and Scheurer [Hortmann *et al.*, 1990], which is used to check the solute transport model with $Sc = 0.71$ and $Ra_C = 10^5$. Three uniform grids were calculated, with 50×50, 100×100, and 200×200 CV. The grid convergence is monotonous and achieves an observed order of convergence slightly above 2, uniformly distributed across the whole domain for all relevant variables (u, v, ψ, and C). The maximum error in the field values of these variables is estimated as $GCI_\mathrm{Rex} \leq 0.2\%$ and the function values agree with the benchmark results and estimated error

bands given in refs. [de Vahl Davis, 1983] and [Hortmann *et al.*, 1990].

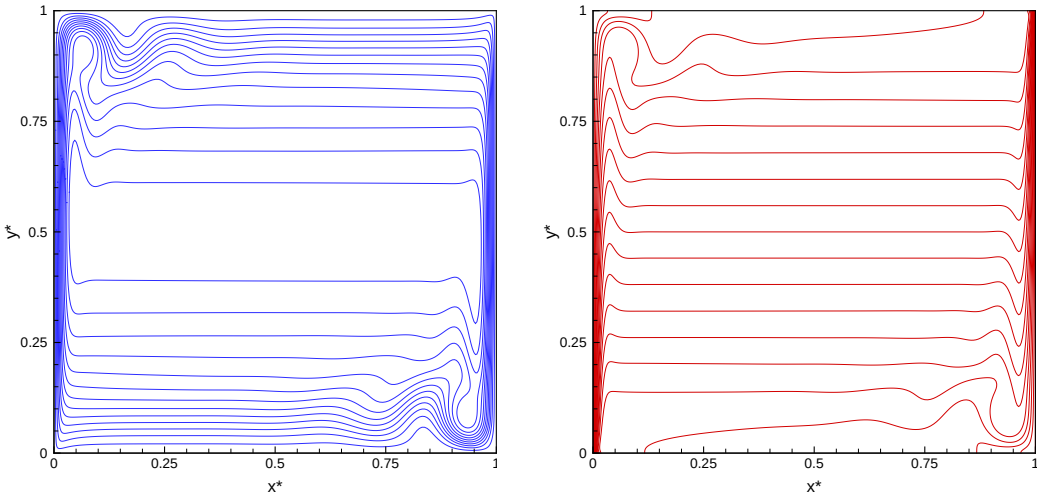

(a) Concentration field ($\Delta\phi = 0.05$). (b) Streamlines ($\Delta\psi^* = 0.005$).

Figure 6.6: Case 1b: Concentration and flow fields at $Sc = 1.0$, and $Ra_C = 10^8$. Solution by the FVM DC casting code on a 200×200 Gauss-Lobatto grid.

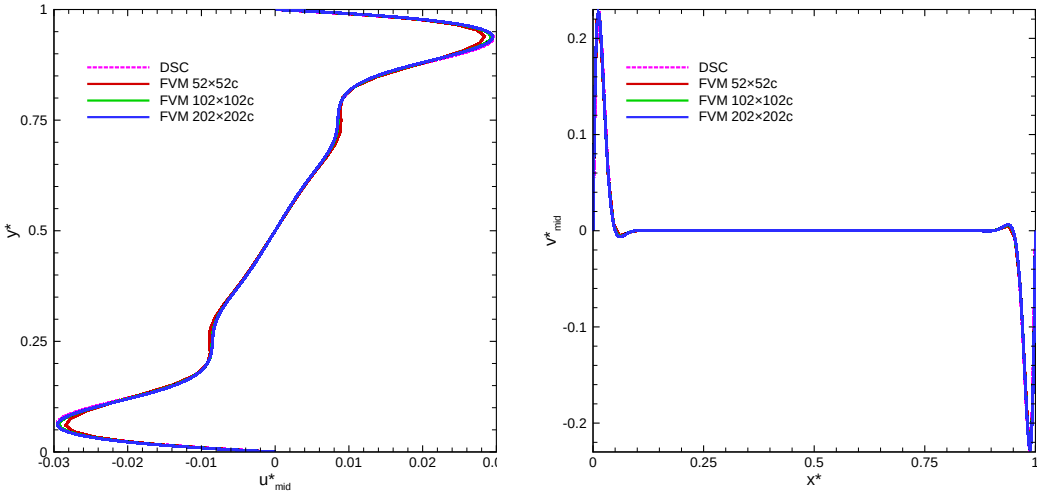

(a) Horizontal velocity component u^* at cavity mid-width ($x^* = 0.5$). (b) Vertical velocity component v^* at cavity mid-height ($y^* = 0.5$).

Figure 6.7: Case 1b: Grid convergence of velocity profiles and comparison with the DSC solution by Wan, Patnaik and Wei [Wan *et al.*, 2001].

The second case is a little more demanding and reaches $Ra_C = 10^8$, with $Pr = 1.0$. Some more exploration of the numerical results was undertaken since the benchmark results claimed by Wan, Patnaik and Wei [Wan *et al.*, 2001] are less clear and do not explicitly specify error estimates. The problem was calculated on uniform and Gauss-Lobatto grids with 50×50, 100×100, and 200×200 CV to find out the difference in the performance of the two grid types in the case of relatively high Ra_C and moderate Sc (i.e. thin boundary layers). The results might give some useful conclusions on the best meshing of the subsequent cases, which move toward the final parameter range of interest, $Sc = 10^2$ and $Ra_C = 10^{10} \ldots 10^{11}$. The convergence over the three uniform grids was found to be oscillatory and the approximate error spline (AES) method had to be used to extrapolate the results and compute the errors based on the extrapolated solution. The observed order of convergence (OOC) could not be clearly determined by the power-law approximation of p, the convergence field values nor from the functionals $u_{\max}$, $v_{\max}$, and $\psi_{\max}$. Based on some exploration it is felt, however, that the OOC can be assumed to be $p \approx 2$ for uniform grids. Based on $p = 2$ the error band of the AES-extrapolated solution on a uniform grid is estimated as $GCI_{\text{AESex}} \approx 3\%$. On the Gauss-Lobatto grids the convergence was found to be oscillatory as well. The OOC however, determined by the power-law approximation, is clear and mostly $p \geq 2$ across all fields. The error band of the extrapolated solution on the Gauss-Lobatto grid is $GCI_{\text{AESex}} \approx 1\%$.

From these first tests we can conclude the very good performance of the code at moderate Pr and Ra_T and respectively Sc and Ra_C, and the clearly better performance of locally refined grids in cases with local sharp gradients as they occur in thin boundary layers at high Ra.

6.7 Case 2: Thermosolutal Natural Convection of a High-Pr Liquid

The problem that was tackled next corresponds to the case characterized by $A = 1$, $Pr = 7$, $Le = 100$, $Gr_T = 10^5$, and $N = 10$ in the detailed study of Gobin and Bennacer [Gobin and Bennacer, 1996]. This problem represents the steady multicellular regime of thermosolutal flow in an aqueous solution. Gobin and Bennacer found out that this regime occurs in the transition between the extremes of thermally and solutally dominated monocellular flow regimes. If the solutal buoyancy dominates over the thermal buoyancy force, stratified zones appear at the top and bottom of the cavity, while the core is solutally homogeneous, thermally stratified and driven by the thermal buoy-

ancy. If, in turn, the lateral thermal gradient in the solutally stratified layers is large enough to induce a lateral density gradient that is strong enough to destabilize the solutal stratification, new thermal cells will appear inside the initially solutally stratified layers. This kind of multicellular regime occurs at moderate buoyancy ratios $N = \frac{Ra_C Pr}{Ra_T Sc}$ as the solutal buoyancy has to be dominant on the solutal boundary layer scale to cause the primary solutal stratification, but the thermal buoyancy has to be large enough to trigger the destabilization. The destabilization to a multicellular regime is also promoted by the larger aspect ratio of the cavity as it augments the destabilizing lateral thermal gradient. The understanding of these mechanisms will help us understand the flow patterns in the studies of thermosolutal convection in low-Pr metals later on.

variable	$\max(GCI_{\mathrm{Rex}})$
u, v	$3\,\%$
T	$10^{-4}\,\%$
ψ	$0.1\,\%$
C	$0.1\,\%$

Table 6.3: Case 2: Field maxima of the error band estimate for the Richardson-extrapolated solution (GCI_{Rex}).

Grid	$u^*_{\max}$	$v^*_{\max}$	$\lvert\psi^*\rvert_{\max}$	Nu	Sh
100×100 c	$9.7569\cdot10^{-2}$	$1.7781\cdot10^{-1}$	$1.4283\cdot10^{-2}$	5.4507	57.461
200×200 c	$9.4965\cdot10^{-2}$	$1.7690\cdot10^{-1}$	$1.4178\cdot10^{-2}$	5.4107	57.449
400×400 c	$9.4482\cdot10^{-2}$	$1.7681\cdot10^{-1}$	$1.4173\cdot10^{-2}$	5.4053	57.445
p_{Rex}	2.4	3.4	4.2	3.0	1.7
$f_{\mathrm{Rex}}(p)$	$9.4372\cdot10^{-2}$	$1.7680\cdot10^{-1}$	$1.4172\cdot10^{-2}$	5.4045	57.444
$f_{\mathrm{Rex}}(p=2)$	$9.4321\cdot10^{-2}$	$1.7678\cdot10^{-1}$	$1.4171\cdot10^{-2}$	5.4035	57.444
$GCI_{\mathrm{Rex}}(p)$	$0.03\,\%$	$5\cdot10^{-4}\,\%$	$10^{-4}\,\%$	$2\cdot10^{-3}\,\%$	$1\cdot10^{-3}\,\%$
$GCI_{\mathrm{Rex}}(p=2)$	$0.04\,\%$	$2\cdot10^{-3}\,\%$	$10^{-3}\,\%$	$5\cdot10^{-3}\,\%$	$1\cdot10^{-3}\,\%$

Table 6.4: Case 2: Observed order of convergence p_{Rex}, extrapolated solution f_{Rex} and error band estimates GCI_{Rex} based on functionals.

The numerical tests were all performed on Gauss-Lobatto grids since the preceding case showed that they perform better in terms of grid convergence. The solution is again studied on three grids, 100×100, 200×200, and 400×400 CV. Finer grids as before were chosen since finer solutal field structures are expected to occur at the high $Sc = 700$ and sharper boundary layers are anticipated at the $Ra_C = 7\cdot10^8$. The convergence of all variables of interest (u, v, ψ, T, and C) is monotonous across most of the domain, thus the classical Richardson extrapolation can be used. The OOC is clearly $p = 2$

(except in some limited regions of oscillatory convergence, and in regions of very small GCI errors, where the determination of OOC is very sensitive). The more conservative error estimates based on field values give the error bands shown in table 6.3. The error estimates based on the functionals give an extremely small general error band of 0.05 % as shown in Table 6.4.

In this basic test for double-diffusive convection the numerical code suc-

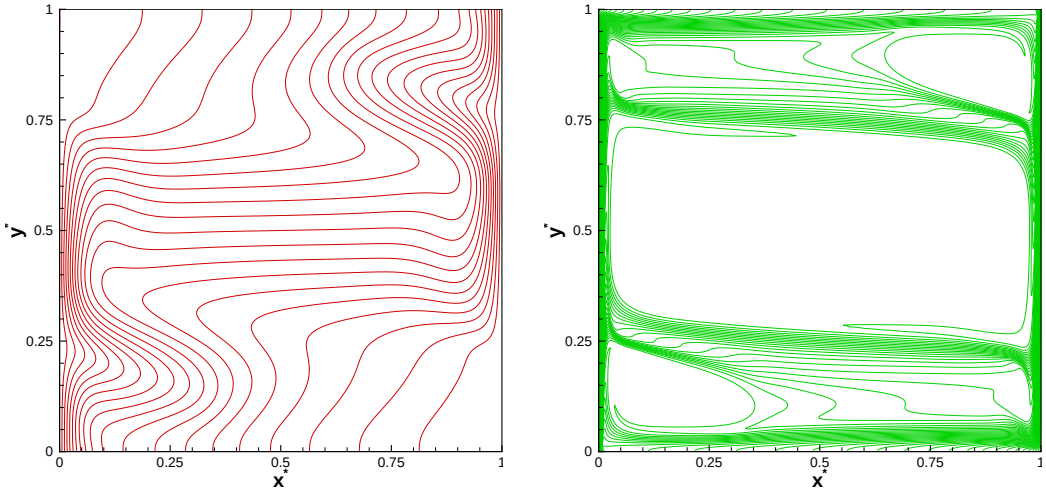

(a) Temperature field ($\Delta\theta = 0.05$).

(b) Concentration field ($\Delta\phi = 0.05$).

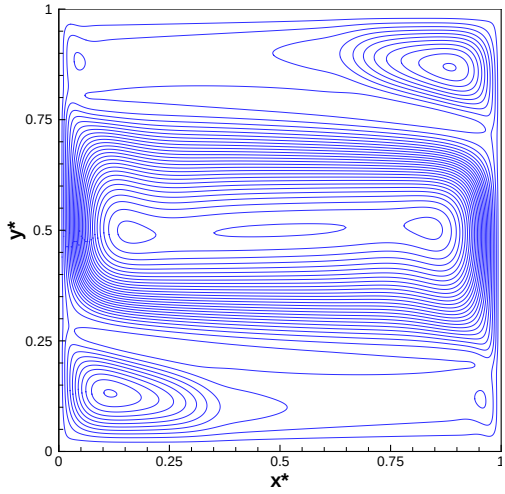

(c) Streamlines ($\Delta\psi^* = 5 \cdot 10^{-4}$).

Figure 6.8: Case 2: Temperature, concentration and flow fields. Solution by the FVM DC casting code on a 400×400 Gauss-Lobatto grid.

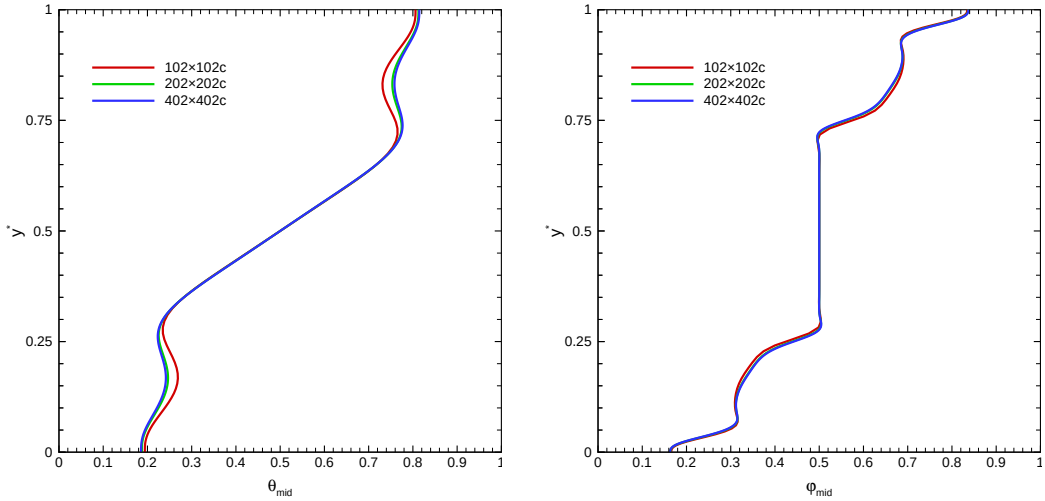

(a) Temperature θ. (b) Concentration ϕ.

Figure 6.9: Case 2: Grid convergence of temperature and concentration profiles at cavity mid-width ($x^* = 0.5$).

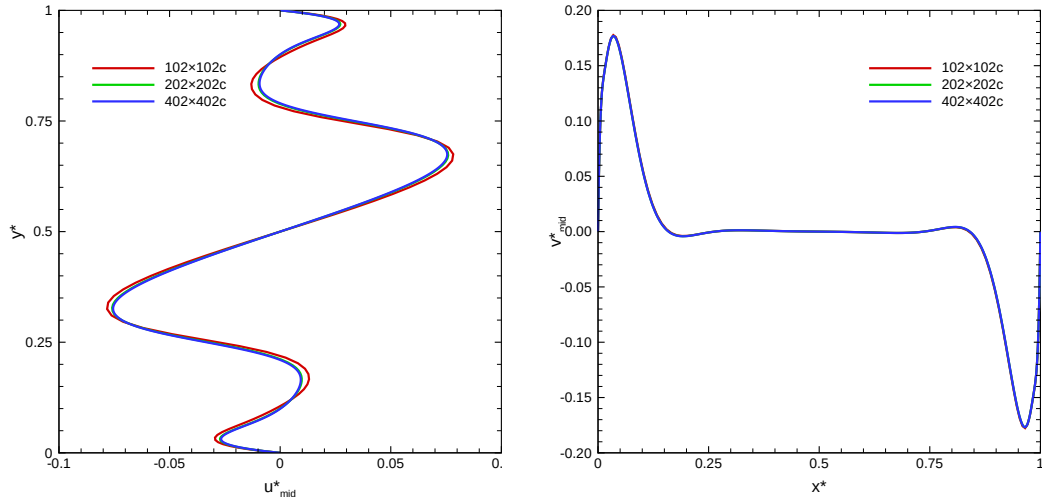

(a) Horizontal velocity component u^* at cavity mid-width ($x^* = 0.5$).

(b) Vertical velocity component v^* at cavity mid-height ($y^* = 0.5$).

Figure 6.10: Case 2: Grid convergence of velocity profiles.

cessfully reproduced the known multicellular flow structure [Gobin and Bennacer, 1996]. Excellent accuracy of the results was shown and was particularly remarkable with respect to the concentration field. The high accuracy is at-

tributed to the dense, wall-refined grids used in conjunction with 2nd- to 3rd-order accurate discretization schemes.

6.8 Case 3: Thermal Natural Convection of a Pure Liquid Metal

The DC casting code is further tested on the problem of transient thermal natural convection in a rectangular cavity, which was devised to be prototypal for the flow during the initial stages of solidification in a cavity. The fluid in the cavity, initially at the temperature of the left wall, is cooled at the right wall which is maintained at a constant temperature. After the onset of cooling the thermal conductive layer quickly spreads into the interior of the cavity and reaches the left wall by conduction. The instability of the conduction layer induces a convection flow cell spreading across the whole height of the cavity (Fig. 6.11(a)). Contrary to high-Pr fluids, where the relations between thermal and momentum diffusivity (Pr) confine the buoyancy driving force to a thin thermal boundary layer and the larger thickness of the momentum boundary layer helps to maintain a stagnant core with a stable stratification, the large thermal diffusivity in the low-Pr metal prevents a stable stratification of the core while the mechanical wall-shear effect is confined to a very thin momentum boundary layer. The thermal instability of the cavity core thus accelerates the flow circulation in the core without much viscous friction. The central flow cell is augmented and shrinks, which creates unstable conduction layers at the top and bottom of the cavity, additionally destabilized by the advective heat transfer caused by the core flow cells (Fig. 6.11(b)). These instabilities generate two additional flow cells (Fig. 6.11(c)). The center and bottom cells finally merge (Fig. 6.11(d)) and two strong cells remain pulsating in the final oscillatory state (Figs. 6.11(e), 6.11(f)). In addition, weak cells periodically appear in the top and bottom corners of the cavity. The influence of the two primary cells destabilizes the conductive zones at the top and bottom of the cavity, which induces the weak corner flow cells. As they are generated, these stabilize the thermal field in their region and increase the instability of the thermal field in the primary cells. The secondary cells diminish and the primary cells are made stronger again. This process is cyclic and generates the periodic oscillations. In the cavity center between the two corotating primary cells a shear layer with a thermally unstable configuration evolves. The unstable configuration is maintained by the weak shear flow, apparently a result of balancing buoyancy and shear forces.

In a verification attempt the numerical results were initially compared

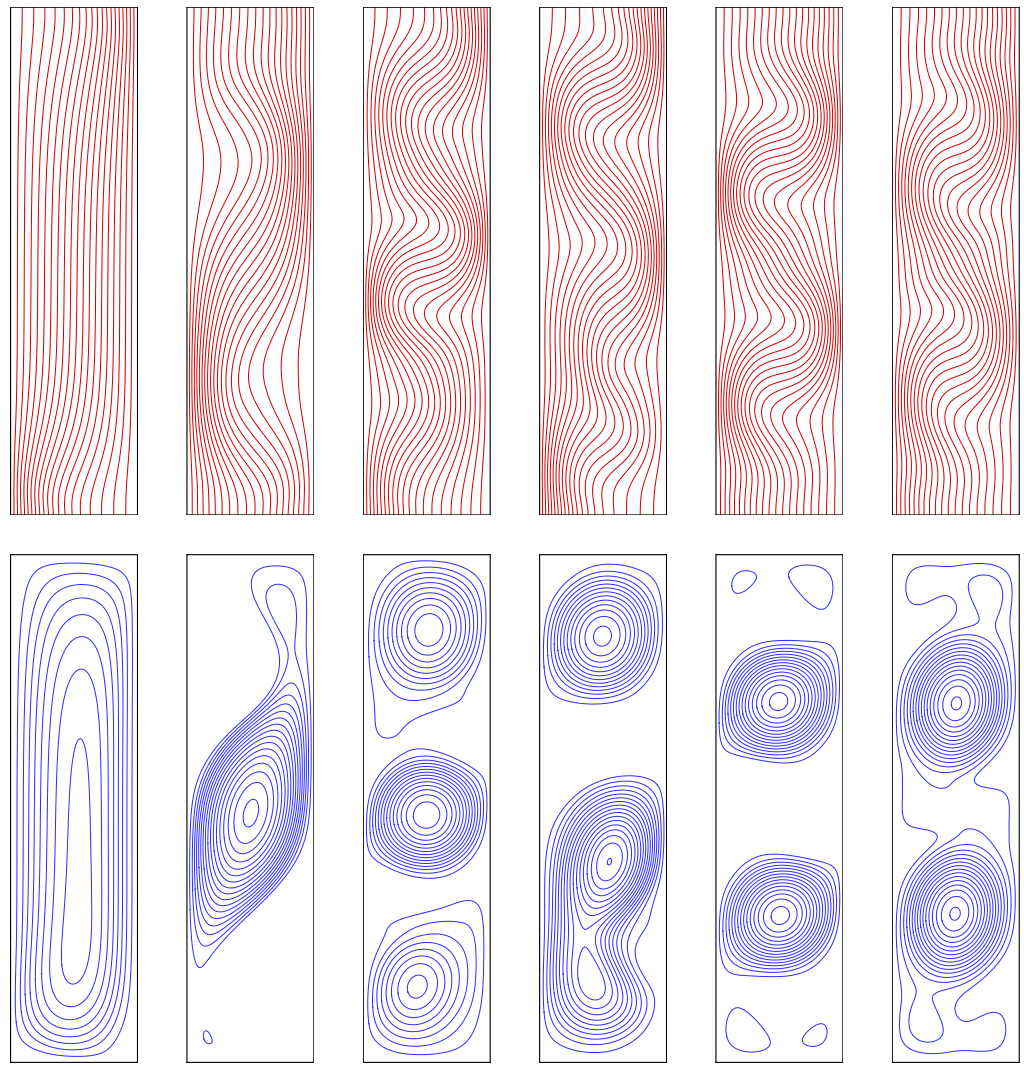

(a) $t^* = 12.29$ (b) $t^* = 32.77$ (c) $t^* = 53.24$ (d) $t^* = 73.72$ (e) $t^* = 821.61$ (f) $t^* = 827.34$

Figure 6.11: Case 3: Evolution of temperature and flow fields in the cavity. The first four times are from the initial transient, the last two correspond to oscillation extrema in the final oscillatory state. Solution by the FVM DC casting code on a 100×400 uniform grid. ($\Delta\theta = 0.05$, $\Delta\psi^* = 5 \cdot 10^{-4}$)

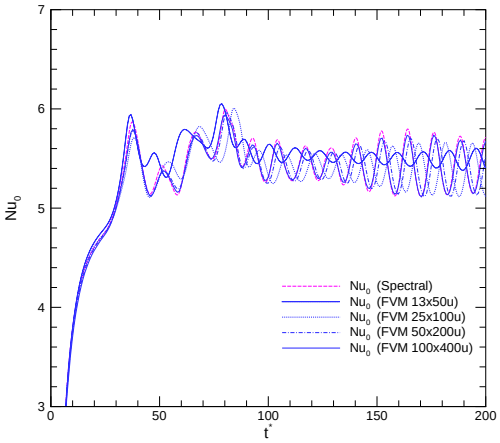

(a) Left wall—Nu_0

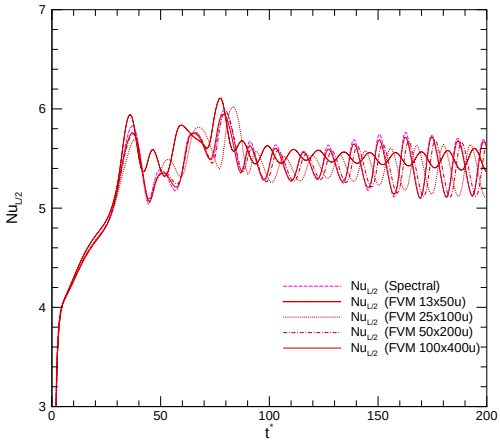

(b) Vertical mid-plane—$Nu_{L/2}$

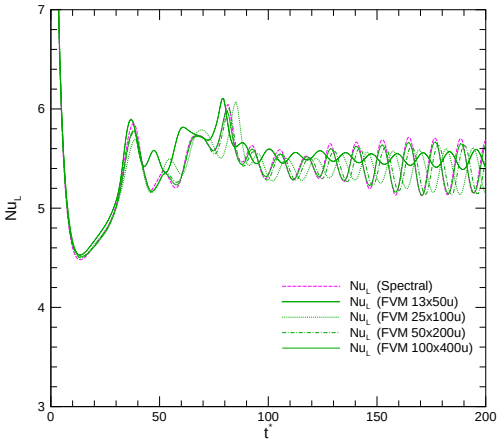

(c) Right wall—Nu_L

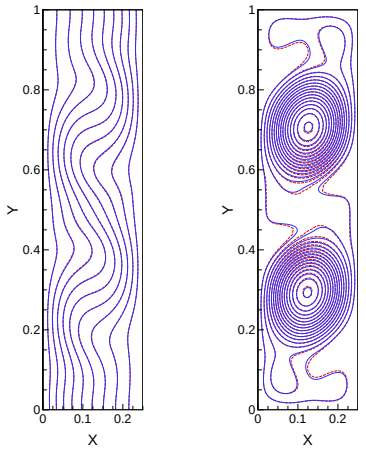

(d) Temperature and flow fields in the cavity: comparison of the 100×400 grid FVM solution with the SM solution ($\Delta\theta = 0.1$, $\Delta\psi^* = 5 \cdot 10^{-4}$)

Figure 6.12: Case 3: Grid convergence of the FVM solution and comparison with the SM solution. Time evolution of the Nusselt number.

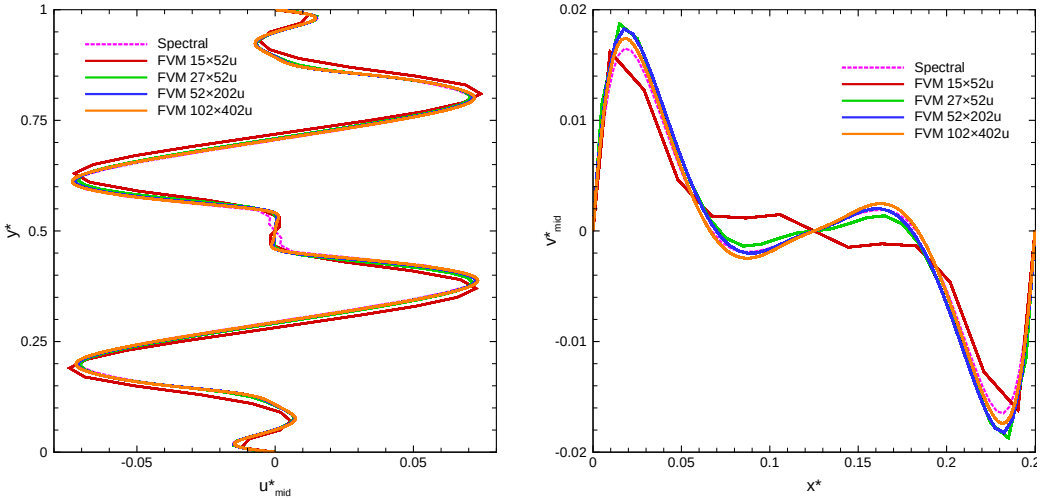

(a) Horizontal velocity component u^* at cavity mid-width ($x^* = 0.5$).

(b) Vertical velocity component v^* at cavity mid-height ($y^* = 0.5$).

Figure 6.13: Case 3: Grid convergence of the FVM solution and comparison with the SM solution. Velocity profiles.

in detail [Založnik *et al.*, 2005] to the solution obtained by Shihe Xin, using the spectral Chebyshev-collocation method (SM) [Xin and Le Quéré, 2002]. The SM solution is verified to be grid independent, however, error estimates are not specified. This comparison could be regarded as a code-verification activity, but not in a very rigorous manner. Despite this, the belief in the good accuracy of the SM solution gives substantial confidence in a correct result of the FVM code. An additional comparison was attempted with a local meshless method [Divo and Kassab, 2006]. While the latter comparison gave a very good qualitative match, and thus some additional confidence, the quantitative comparison is lacking and is not shown here in detail.

The time evolution of the Nusselt numbers at both walls of the cavity and at the vertical mid-plane is shown in Fig. 6.12 for the FVM solutions on the four grids and for the SM solution. The differences in the evolution between the FVM on the densest (100×400) grid and the SM solution are very small. Also, the final oscillation periods match to within 1 % and the oscillation amplitudes are close. The SM solution should have a much better time accuracy as it employs a second-order time-stepping scheme and uses a much smaller timestep. This should have some impact on the small discrepancies. The numerical parameters used in both codes are given in Table 6.5. A comparison of the instantaneous temperature field and streamlines in the final oscillatory state is shown in Fig. 6.12(d). The results in Fig. 6.12(d)

Code	Grid type	Spatial resolution	Timestepping	Timestep Δt^*
FVM	uniform	100×400 CV	implicit Euler	$8.91 \cdot 10^{-2}$
SM	Gauss-Lobatto	59×101 nodes	second order	$1.00 \cdot 10^{-2}$

Table 6.5: Case 3: Numerical parameters of the Spectral (SM) and FVM computations.

are compared at a time corresponding to 0.7366 of the oscillation period, the beginning of the period taken at the point where Nu_0 is equal to the period median and $\partial Nu_0/\partial t > 0$. This choice is based on the results available from the SM computation and the phase angle corresponds the one achieved at $t^* = 1000$ in the SM computation, which is long after the final oscillatory state settles down.

A detailed convergence analysis and error estimation of the FVM solution is performed on results at the aforementioned phase angle in the final oscillatory state. The analysis is based on four solutions on uniform grids with 13×50, 25×100, 50×200, and 100×400 CV. The grid convergence was found to be oscillatory, therefore the AES method was used for extrapolation. The OOC was estimated using the power-law approximation method. In analyzing the whole domain the OOC was found to be $p \geq 1.5$ for u, v, and ψ in all regions of steep gradients. The GCI_{AESex} error bands were estimated to be 1 % for u and v and 2 % for ψ using the respective *average* field values as normalizing values. The same methods were used to analyze the convergence of the functionals $u^*_{\max}$, $v^*_{\max}$, and $|\psi^*|_{\max}$, which gave slightly different results for the OOC and drastically smaller error bands (Table 6.6). The grid convergence of the temperature field is monotonous across most of the domain with an OOC $p \geq 2$ and the Richardson-extrapolation-based error band is estimated as $GCI_{\mathrm{Rex}} < 0.1\,\%$. Tests on Gauss-Lobatto grids, which are not shown here, gave comparable results (with the exception of the very coarse 13×50 grid, which was found to be too coarse in the central region to correctly capture the oscillations).

In the present test case we observed the oscillatory instability of the thermal natural convection in a liquid metal and analyzed its origin in the unstable buoyancy-inertia force balance. By an error analysis and comparison to an independent solution remarkable accuracy of the code was shown in the relevant parameter range of thermal convection.

Grid	$u^*_{\max}$	$v^*_{\max}$	$\lvert\psi^*\rvert_{\max}$
13×50 u	1.060	$3.051\cdot10^{-2}$	$3.93017\cdot10^{-2}$
25×100 u	1.019	$2.940\cdot10^{-2}$	$3.91031\cdot10^{-2}$
50×200 u	1.032	$2.989\cdot10^{-2}$	$3.99413\cdot10^{-2}$
100×400 u	1.038	$3.023\cdot10^{-2}$	$4.00588\cdot10^{-2}$
AESex	1.040	$3.039\cdot10^{-2}$	$4.00448\cdot10^{-2}$
p_{AESex}	1.7	1.3	3.0
GCI_{AESex}	0.1 %	0.3 %	0.005 %

Table 6.6: Case 3: Observed order of convergence p_{AESex}, extrapolated solution AESex, and error band estimates GCI_{AESex} based on functionals.

6.9 Case 4: Solutal Natural Convection of an Isothermal Liquid Metal

The high-Ra_C flow of a high-Sc fluid in this case is close to the limit of the steady flow given by Lage and Bejan for fluids with $Sc \gg 1$ and cavities of an aspect ratio $A < 50$ as $Ra_C \sim 10^8 Sc^2$. An objective of this test case is to determine the possible occurrence of instabilities in the solutal convection flow. It was found out that the small oscillatory flow structures are confined to regions close to the vertical walls (Fig. 6.14). They form small near-wall flow cells which appear due to instabilities of the boundary layer. It was shown before [Bergholz, 1977, Le Quéré and Gobin, 1999] that large-Sc fluids in slender enclosures or slots are prone to different kinds of instabilities at high enough Ra_C, however, a detailed discussion of the exact mechanism exceeds the scope of this work.

Looking at the most accurate numerical solution, obtained on a 100×400 Gauss-Lobatto grid, the oscillation amplitude of $\psi_{\max}$ reaches about 15 % of its value while the vertical velocity fluctuations ($v_{\max}$) are only about 3 %. The horizontal velocity ($u_{\max}$) and Sh fluctuations are even much smaller. We can conclude that the solution of the problem with $Ra_C = 10^{10}$ is oscillatory, but with relatively small oscillation amplitudes and long oscillation periods (of the order of 10^3 s). Also, the periodicity of oscillations could not be clearly determined as there are several lower-frequency oscillations superimposed onto the base frequency. The boundary layer instability occurring in this flow does not necessarily present implications for the double-diffusive flow representative for solidification since there we can expect a dominant effect of the thermal buoyancy in those regions where the solutal boundary layer instability occurs in the solutal flow.

The numerical solution of the solutal-buoyancy driven flow at $Sc = 100$

No. of CV	uniform grid solution	Gauss-Lobatto grid solution
27×100	numerically unstable	steady state
50×200	steady state	non-periodic oscillatory
100×400	non-periodic oscillatory	non-periodic oscillatory

Table 6.7: Case 4: Characteristics of solutions on the tested grids.

and $Ra_C = 10^{10}$ is strongly dependent on the right choice of grid type and density. As shown in Table 6.7, a steady solution is obtained with coarse grids, apparently due to a damping effect of the discretization error. With very coarse grids the solution of the high-Péclet flow quickly becomes numerically unstable. Based on the fine-grid solutions I concluded that the flow is oscillatory. We can also confirm that the Gauss-Lobatto grid, refined at the walls, is better suitable in this case for the numerical approximation to capture the effects triggering the instabilities. Obviously, however, the influence of the instabilities on the overall species transport at the wall (Sh) is not important here and the effect is minor even locally.

6.10 Case 5: Thermosolutal Natural Convection of a Liquid Metal

6.10.1 Cooperating Thermal and Solutal Buoyancy

After the onset of cooling and imposed concentration gradient the thermally induced convection builds up quickly and is not affected by the solutal effect. The latter remains confined to the very thin solutal boundary layer at the right wall and a shallow accumulation of virtually stagnant solute rich liquid at the bottom of the enclosure (Fig. 6.16(a)). The thermal convection results in a multicellular flow pattern, qualitatively similar to the one found with identical parameters for pure thermal convection in section 6.8. With time the density of the upper of the two main thermal flow cells is increased by the advective solute transport from the solutal boundary layer. The cell moves downwards and merges with the lower cell. At the same time, a new thermal cell is generated at the top of the enclosure. This phenomenon is observed repeatedly. The lower cell interacts with the solutal layer and attempts to carry solute into the center of the enclosure. Due to the vigorous thermally-induced flow and consequently effective mixing this does not establish a closed solutal loop between the thermal cells. Later, the stagnant stratified layer continues to grow and the concentration in the top part slowly increases (Fig. 6.16(b)). A solute-lean stratified layer starts to grow at the top of the cavity, while

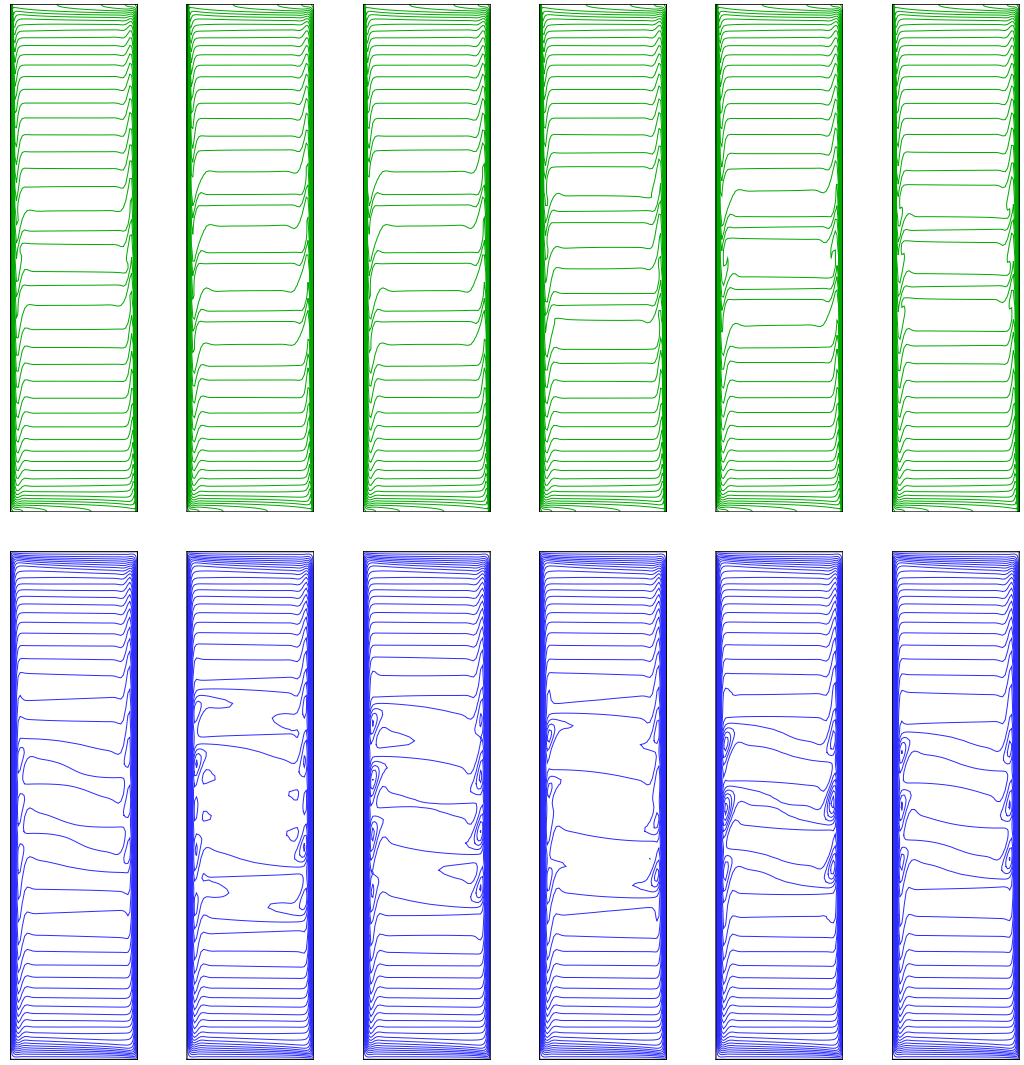

(a) $t^* = 5629.0$ (b) $t^* = 5807.3$ (c) $t^* = 5946.6$ (d) $t^* = 6154.1$ (e) $t^* = 6268.0$ (f) $t^* = 6599.8$

Figure 6.14: Case 4: Concentration fields and streamlines in the enclosure at local minima, maxima and inflection points of a representative oscillation period (oscillations shown in Fig. 6.15) Solution by the FVM DC casting code on the 50×200 Gauss-Lobatto grid. ($\Delta\phi = 0.02$, $\Delta\psi^* = 10^{-4}$).

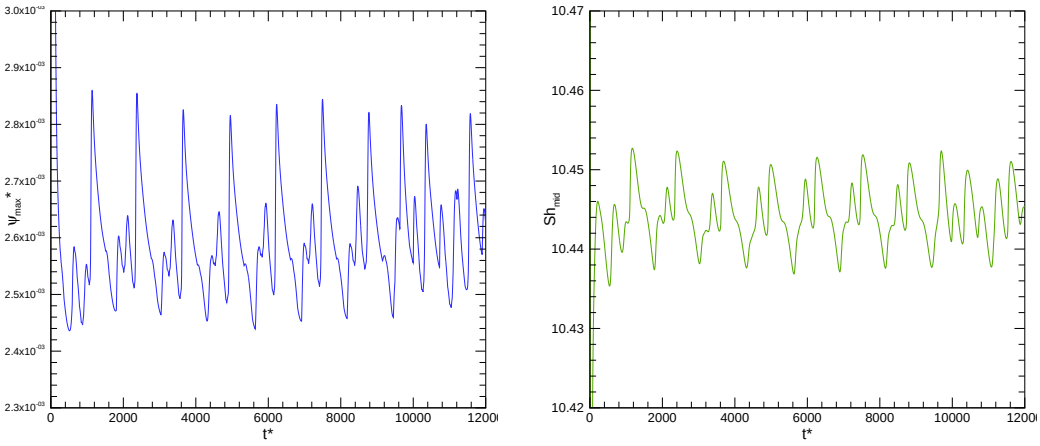

(a) Streamfunction maximum.

(b) Sherwood number at the cavity midplane.

Figure 6.15: Case 4: Time evolution of the flow obtained on the 50×200 Gauss-Lobatto grid.

the bottom layer is somewhat reduced in height (Fig. 6.16(c)). The stratification of the top layer is slightly weaker than that of the bottom layer, which remained stable at its maximum height (Fig. 6.16(b)). Consequently, the lateral temperature gradient finally destabilizes the stratification at the top (Fig. 6.16(d)). A pulsating flow continues to evolve with transitions changing from a structure with two solutally uniform thermal cells confined by a sharp solutal gradient (Fig. 6.16(e)) to monocellular flow between two solutally stratified layers (Fig. 6.16(f)).

The evolution of the flow seems to depend on the buoyancy ratio ($N = 31$ in this case) and on the stability of the thermally-induced flow. The thermal force resulting from the lateral temperature gradient inside the solutally stratified layer is strong enough to destabilize the stable solutal stratification as the layer grows; a pulsating multicellular thermosolutal flow structure evolves. Such structures are also shown in Section 6.7. They were studied by Bennacer and Gobin [Gobin and Bennacer, 1996] in high-Pr fluids, where at moderate N several thermal flow cells, internally of uniform concentration, were observed which were contained in the outer solutal cells, with the solutal effect confined to the wall boundary layers and the high-concentration-gradient layers between the thermal cells. Bennacer and Gobin showed that the multicellular regime is promoted by higher Rayleigh numbers and higher geometry aspect ratios $A = H/L$. The buoyancy ratio N, where a similar transition should occur at lower Pr, is not obvious. Although not very extensive in this respect, the results of Shyy and Chen [Shyy and Chen, 1991]

for cooperating double diffusive convection in low-Pr fluids suggest that with lower Pr the transition to multicellular regimes occurs at higher N. Above all, however, the nature of the instability that triggers the splitting up into cells is different. In case of high-Pr fluids the destabilizing thermal force is confined to the interior of the momentum boundary layer and a stagnant zone remains in the core of the cells at all times. In low-Pr fluids, on the other hand, the thermal effect reaches well beyond the momentum boundary layer, establishing a zone of balancing buoyancy and inertia, which presents a much more unstable flow configuration. Keeping the focus on the flow problem in the DC casting of aluminum alloys, we are interested in buoyancy ratios N defined by the most important alloying elements, Cu, Mn, Si, Zn, Fe and Ni. These are equal (for Cu) or lower (for the other elements) than that of the presented case. A lower N should decrease the height of the solutally stratified layers and, at even smaller N, reduce the solutal effect in the core and confine it to the near-wall regions.

A rigorous error analysis of the numerical solution was not performed in this case as it would be extremely difficult due to the complexity of the flow. This was already indicated by the case of pure solutal convection; a grid-independent solution in the range of $Sc \sim 10^2$ and $Ra_C \sim 10^{10} \ldots 10^{11}$ is not feasible on reasonable grid sizes. In any case, this is not the objective here. The requirement is to correctly capture the flow structure and trends of solute transport in the flow. The quality of the solution is judged by investigating the sensitivity to grid size by comparing computations on 50×200 and 100×400 Gauss-Lobatto grids, the two grids that showed reasonable accuracy performance in the solutal convection case (case 4). The evolutions of wall and mid-plane Nusselt and Sherwood numbers are compared in Fig. 6.17. Apart from the mid-plane Sh, shown in Fig. 6.17(e), which is very difficult to analyze, all trends of evolution and magnitudes match. We also observe similar oscillation patterns. Based on this comparison we can estimate that the wall solutal fluxes (Sh), which are relevant for macrosegregation, are accurate to within a few percent. The solution on the coarser 50×200 is thus deemed sufficiently accurate to study the evolution of the thermosolutal flow in this case. Consequently, the initial computation on a 100×400 grid was continued on the 50×200 grid to enable a longer time of simulation. The latter grid was also used for the calculation of the counteracting case 5b.

6.10.2 Counteracting Thermal and Solutal Buoyancy

In the case of counteracting thermal and solutal buoyancy, with parameters otherwise similar to the cooperating case (Table 6.1), the picture is completely different from the cooperating case. Already at the onset of cooling

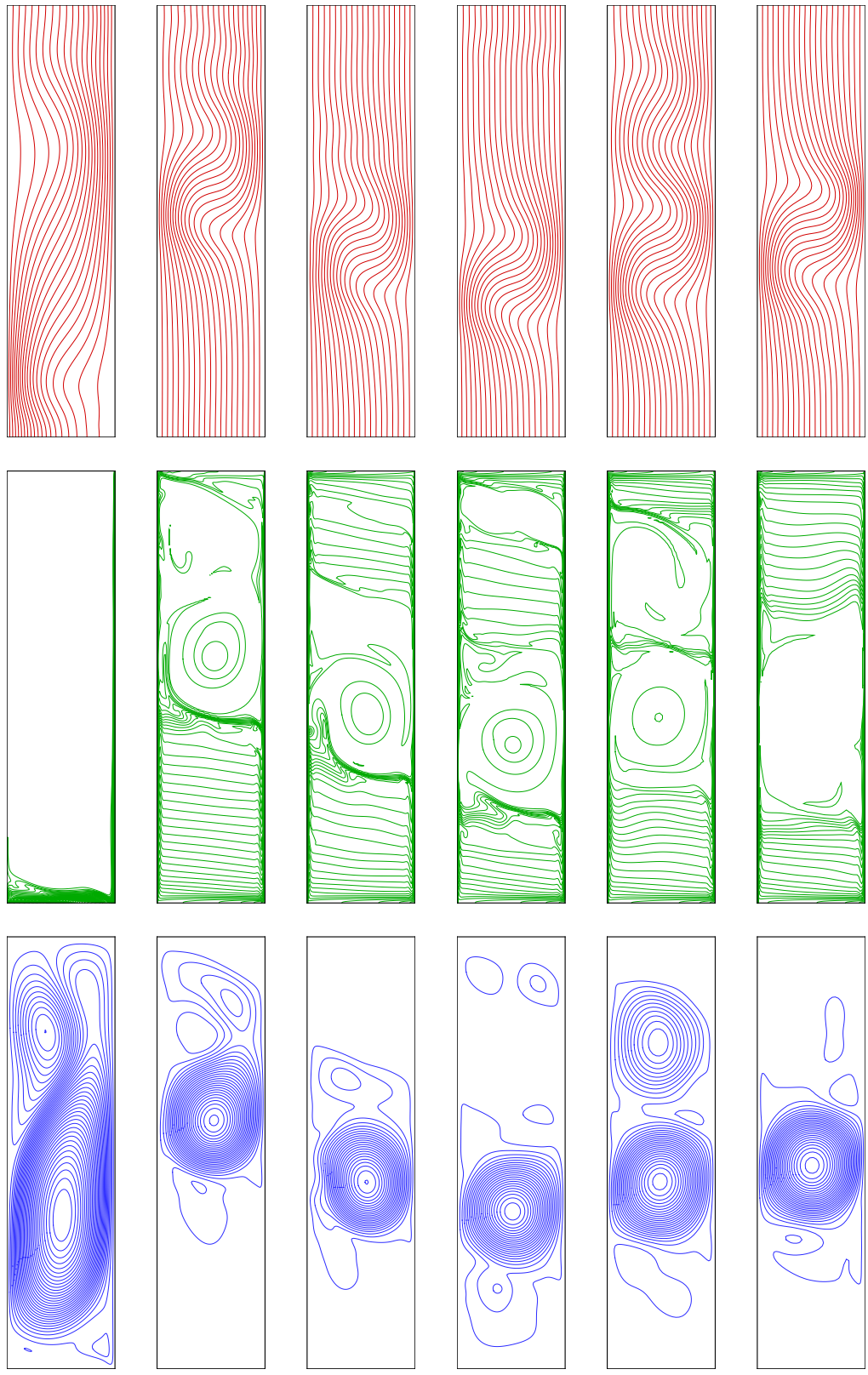

(a) $t^* = 32.77$ (b) $t^* = 1555.56$ (c) $t^* = 3305.26$ (d) $t^* = 4047.41$ (e) $t^* = 7618.90$ (f) $t^* = 11533.61$

Figure 6.16: Case 5a: Temperature, concentration and streamlines in the enclosure for the case of cooperating thermal and solutal forces (Al-Cu). Solution obtained on the 50×200 Gauss-Lobatto grid. ($\Delta\theta = 0.05$, $\Delta\phi = 0.02$, $\Delta\psi^* = 3 \cdot 10^{-4}$)

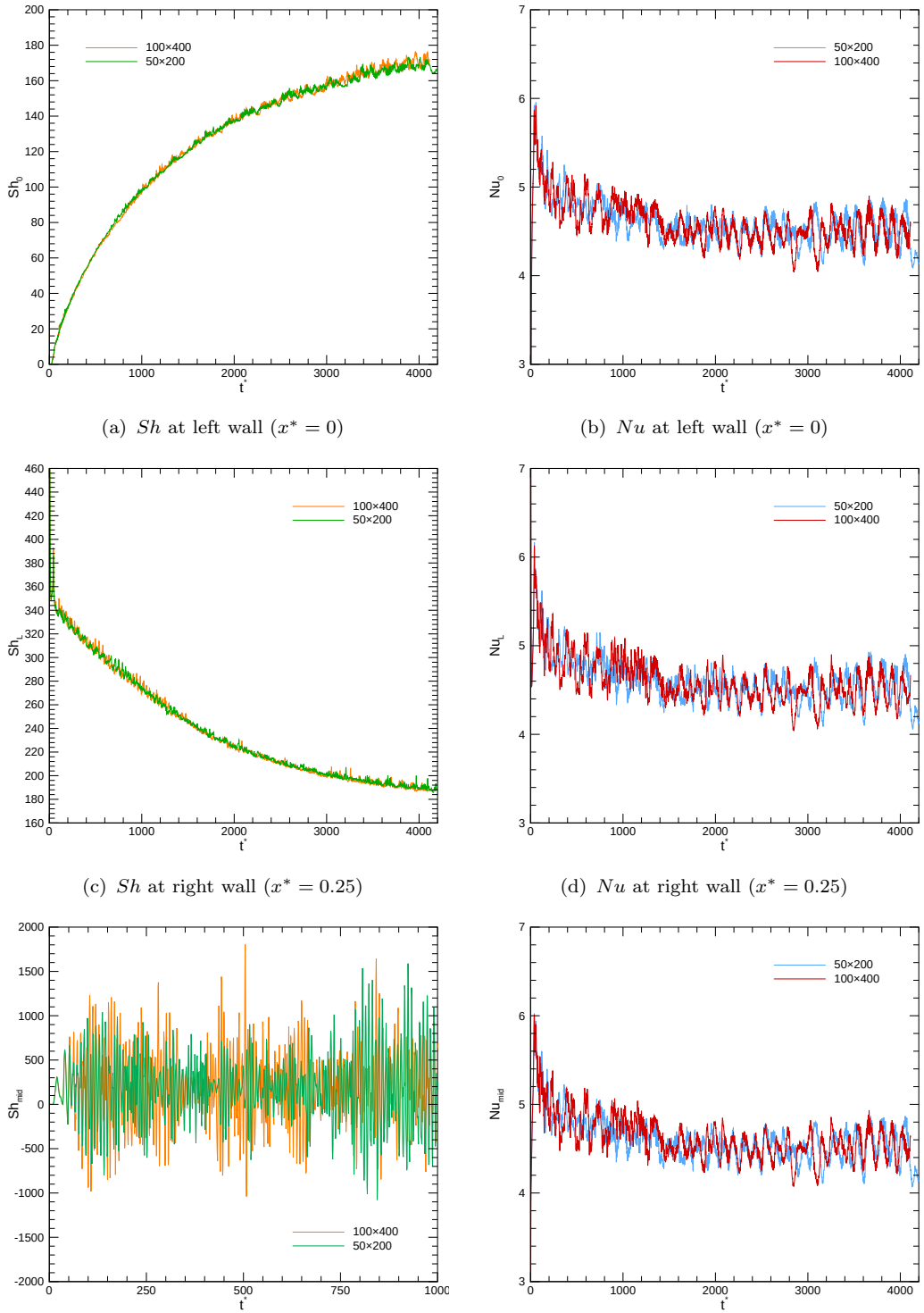

(a) Sh at left wall ($x^* = 0$)

(b) Nu at left wall ($x^* = 0$)

(c) Sh at right wall ($x^* = 0.25$)

(d) Nu at right wall ($x^* = 0.25$)

(e) Sh at mid-plane ($x^* = 0$)

(f) Nu at mid-plane ($x^* = 0$)

Figure 6.17: Case 5a: Evolution of Sherwood and Nusselt numbers calculated on Gauss-Lobatto grids with 50×200 and 100×400 CV.

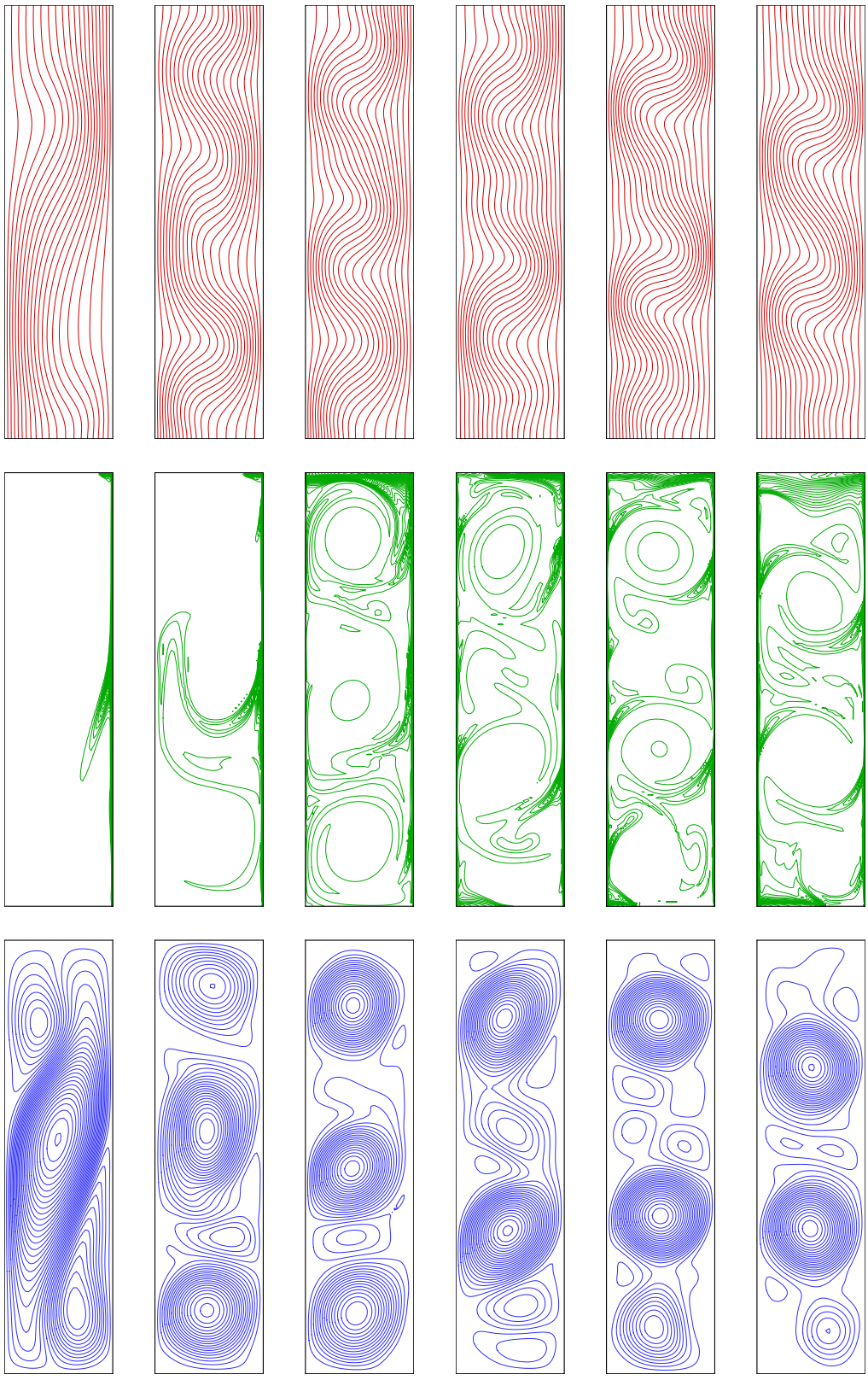

(a) $t^* = 29.17$ (b) $t^* = 41.00$ (c) $t^* = 406.07$ (d) $t^* = 2539.69$ (e) $t^* = 6205.33$ (f) $t^* = 12237.19$

Figure 6.18: Case 5b: Temperature, concentration and streamlines in the enclosure for the case of counteracting thermal and solutal forces (Al-Mg). Solution obtained on the 50×200 Gauss-Lobatto grid. ($\Delta\theta = 0.05$, $\Delta\phi = 0.02$, $\Delta\psi^* = 3 \cdot 10^{-4}$)

and imposed concentration gradient the thermally induced flow in the cavity core peels the thin upward-flowing solutal boundary layer away from the wall (Fig. 6.18(a)). The thermal instability keeps generating flow cells which carry light solute into the core. With their increased concentration the cells in the core become lighter, move upward, merge, and new thermal cells are generated. As this process keeps up, the transport of solute into the core and mixing are very effective. The concentration in the cavity core is practically uniform at all times and its solute content is slowly increasing (Figs. 6.18(b)–6.18(e)). No significant solutal stratification is generated at the top of the cavity. Finally a concentration of $\phi = 0.5$ is built up in the cavity and a pulsating thermal convection remains, without significant changes of the concentration field (Fig. 6.18(f)).

6.11 Case 6: Thermal DC Casting Problem

The test is mostly numerical since a purely thermal flow is not really relevant for alloy casting and the flow in pure aluminum castings is not of interest in this work. The properties of the metal are defined with fixed solidus and liquidus temperatures approximating the solidification range of an Al-5.25 %Cu alloy ($T_\mathrm{S} = 827\,\mathrm{K}$, $T_\mathrm{L} = 920\,\mathrm{K}$). The liquid fraction in the mushy zone is assumed to vary as

$$f_\mathrm{l} = \frac{T - T_\mathrm{S}}{T_\mathrm{L} - T_\mathrm{S}}. \tag{6.31}$$

The results of a grid convergence study are presented in Figs. 6.19 and 6.20. Note that the whole computational domain extended vertically to $-1.0\,\mathrm{m}$ and the discretizations across the liquid pool are 25×73, 50×146, 100×109, and 200×219 CV, respectively. The flow field shows an evolution of the solution into a multicellular flow with grid refinement. The flow structure is practically grid independent at the final grid density and the velocity profiles, shown in Fig. 6.20, clearly converge with only small differences left. The accuracy of the results for the two finest grids can thus be regarded as satisfactory, being cognizant of the fast grid convergence of the numerical code. The result lives up to the expectations given by the results of the thermal convection case as the grid extending over the liquid pool is of a comparable size at very similar parameters (Pr and Ra_T).

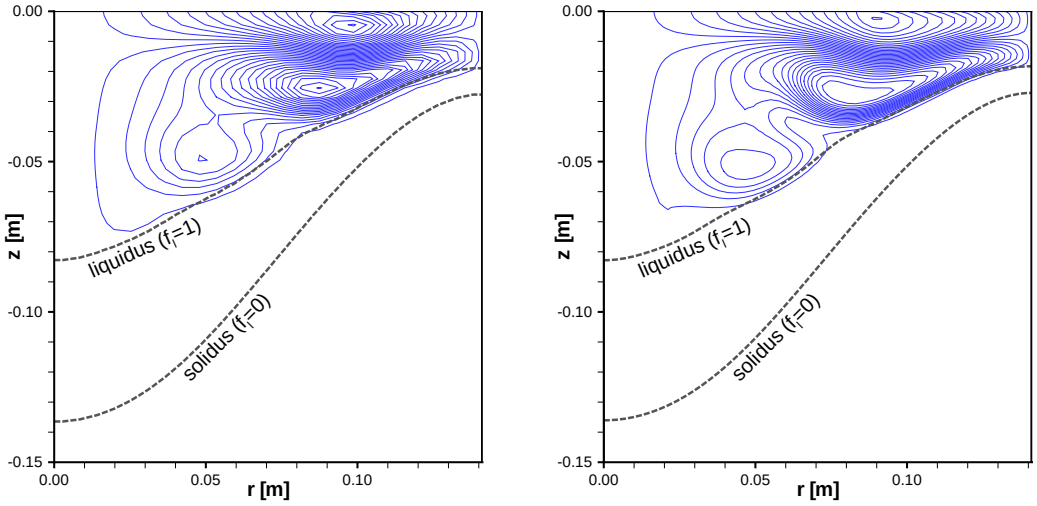

(a) 25×100 (b) 50×200

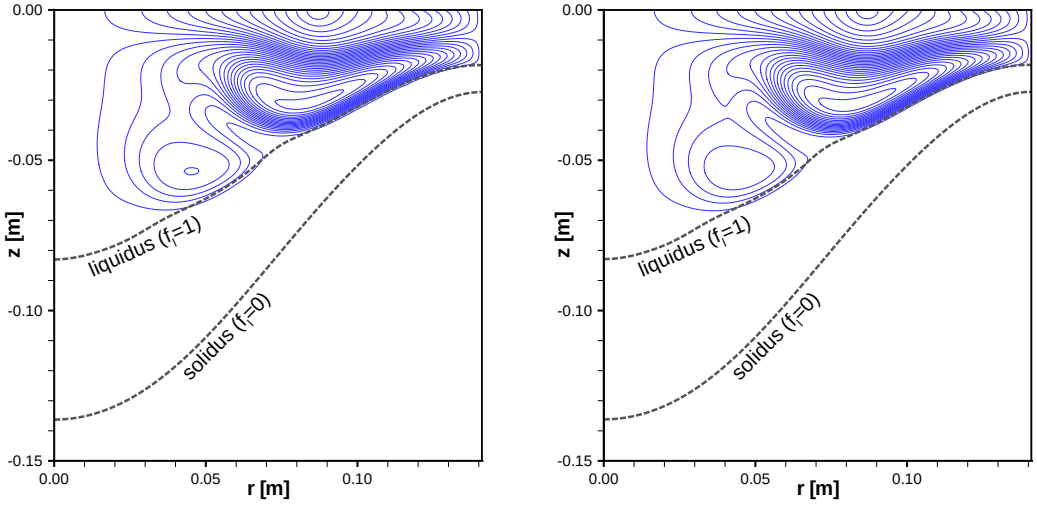

(c) 100×400 (d) 200×800

Figure 6.19: Case 6: Grid convergence of the flow field. Streamlines of relative velocity $(\vec{v} - \vec{v}_{\text{cast}})$ are shown as obtained on four grids.

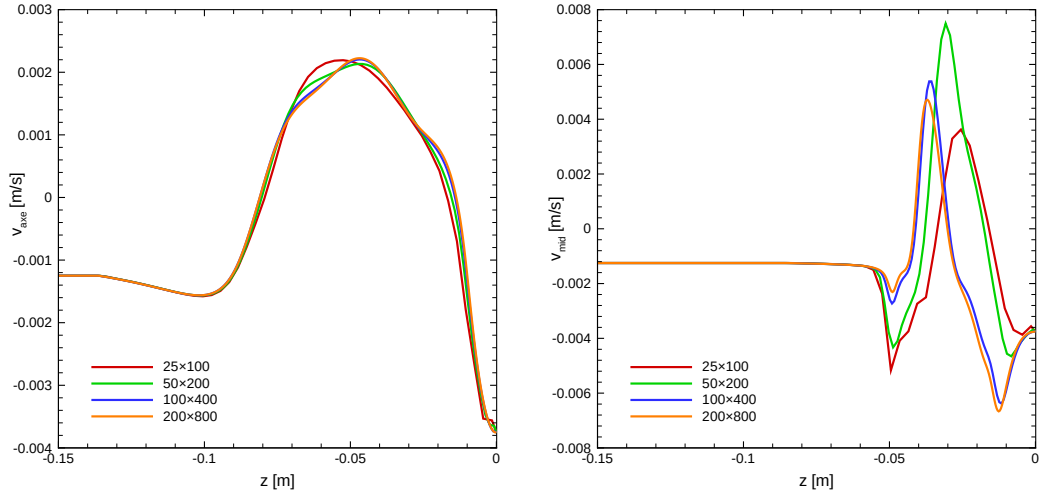

(a) Vertical velocity component v at the billet centerline ($r = 0$)

(b) Vertical velocity component v at the billet mid-radius ($r = R/2$)

Figure 6.20: Case 6: Grid convergence of velocity profiles.

6.12 Summary

Physical aspects

The range of parameters of thermosolutal natural convection relevant for the flow in the liquid pool of a DC casting was estimated. The flow in the pertinent parameter range was studied on test cases of natural convection in a rectangular cavity. Instabilities of the thermal convection in low-Pr liquid metals were found to be decisive for the flow structure and consequently the mass transfer along the walls. We could use the good understanding of flow structures in thermosolutal convection in high-Pr fluids to partly explain the occurrence of thermal flow cells, solutally stratified layers, and the destabilization of the stratification. Further, we could explain the implications of the fundamental difference in the mechanisms of thermal convection between high- and low-Pr fluids for the thermosolutal flow structures. The main conclusions are the following.

- With cooperating thermal and solutal buoyancy thermally-driven flow cells and solutally-stratified layers are generated. The flow structure is important for macrosegregation during solidification because mass transfer from the wall (representative of the liquid-mush interface) is enhanced in the regions of thermal flow and smaller at the stratified layers. The flow is very unstable primarily due to the instability of the

thermally-driven flow. The local flow pattern changes as the solutal stratifications are destabilized and regenerated again. Being further interested in flows with smaller buoyancy ratios (pertaining to the most important alloying additions to aluminum), I speculated that stratification at smaller N will be less pronounced and the effect of thermal flow will be stronger.

- Counteracting buoyancy forces result in very effective transport of solute into the thermally driven core. A solutally well mixed core without significant stratification is built up and the mass transfer along the walls is almost uniform. The thermal instability maintains an unstable pulsating flow.

Numerical aspects

The numerical code was verified for the simulation of natural convection flows. Further, a general solution verification valid for solutions of natural-convection flows in DC casting was proposed. The high accuracy of thermal convection flow solutions in the relevant parameter range was demonstrated by using extrapolation-based error estimators. The demands of the species-transport and solutal-convection components of the flow problem to the numerical method are much higher than for purely thermal convection. It was therefore not possible to achieve equally high accuracy. Despite this obstacle, preventing an equally rigorous verification of the solutal and thermosolutal flow solutions, it was shown that the solution of the thermosolutal problem is of reasonable accuracy. The uncertainty of the solute flux at the cooled wall can be expected to be within a few percent. This should be related to the solute flux at the liquid-mush interface in casting and is thus a relevant criterion for the quality of the thermosolutal convection solution within the macrosegregation problem. The accuracy of the code should thus be sufficient to enable a reliable prediction of trends of the impact of the natural convection flow in the liquid pool on macrosegregation in DC casting. We should, however, remain aware that the good numerical accuracy was achieved using adapted (i.e. wall-refined) grids. This will not be possible in solidification computations as the code presently does not support any type of grid adaptivity which would allow local refinement along a solidification front.

7 Simulation of the DC Casting of Binary Aluminum Alloys

7.1 Introduction

In Chapter 6 the structures of flow and solute transport in thermosolutal natural convection in binary liquid metals were explored. It was shown that complex and unstable flow structures arise in the parameter range of thermosolutal convection relevant for the flow in DC casting. The flow and transport structures were explained, building on knowledge of the characteristics of thermosolutal convection in high-Pr liquids and the instabilities of thermal natural convection in low-Pr liquid metals. Further, I speculated that the natural convection parameters (Ra_T, Ra_C and A; while Pr and Sc are approximately fixed for liquid metals) are in a range where their variations within the range defined by the DC casting process could cause qualitative changes in the flow structure and species transport. While a more extensive study would be required to explore the parameter dependence of the test Cases 5a and 5b and to get a deeper understanding of the general parameter dependence of the flow structure and species transport in liquid alloys, I remain clearly focused on the application investigated in the present work—DC casting. Within an extended study I thus sharpen and limit the focus on the flow in the liquid pool and at the solidification front within the realistic DC casting problem and its impact on macrosegregation.

The rationale of this study is that numerical simulation should give an insight into the impact of thermosolutal flow on macrosegregation in DC casting. Here, the thermosolutal flow is investigated within the limits of variations of realistic casting parameters. The direct effect of casting parameters on the flow and species transport structures and the impact of the flow structure on the final macrosegregation pattern are observed.

Table 7.1: Choice of casting parameters expected to affect macrosegregation, based on their impact on the characteristic parameters of thermosolutal natural convection.

Casting parameter	Direct effect	Affected parameters
casting size	sump size (H, L)	Ra_T, Ra_C, A
casting velocity	sump depth (H)	Ra_T, Ra_C, A
casting temperature	char. temp. difference (ΔT)	Ra_T
mold cooling	sump depth (H)	Ra_T, Ra_C, A

7.2 Influence of DC Casting Parameters on Macrosegregation

The casting parameters to investigate are those we expect would most strongly impact on the macrosegregation. One way is to determine them based on experimental evidence or industrial experience. Another way is to identify the most relevant casting parameters based on the impact they have on the solute transport phenomena (Fig. 1.8). The shrinkage-induced flow depends on the shape of the mushy zone. A deeper sump (larger slope of the sump) promotes the impact of shrinkage. The thermosolutal flow is best characterized by the natural convection parameters (Ra_T, Ra_C and A) as this helps to see where a significant change in the flow structure could be triggered. The anticipated effects are summarized in Table 7.1. In this way, I identified the size of the casting, the casting velocity, as well as the mold cooling (mold type) having the strongest impact on macrosegregation. Another, generally important casting parameter, the water flow rate, should only have a very small effect on the thermal field in the liquid sump, which is inferred from experience [Volšak *et al.*, 2005]. Consequently, it should not impact on the flow and thus should have only a negligible effect on macrosegregation. The latter was also shown experimentally [Dorward and Beerntsen, 1990, Eskin *et al.*, 2004]. The impact of parameters on the effect of grain transport is less clear; it should be affected by the sump depth and the mushy zone thickness. A more detailed investigation of the grain transport is presented in Section 8.2.

7.2.1 System Specifications and Boundary Conditions

The model equations presented in Section 4.5 are solved for an entirely porous mushy zone, i.e. equations deduced from $\mathcal{R} = 1$ (or $g_\mathrm{s}^\mathrm{c} = 0$). A minor difference with the original equations is in the momentum equation, where the Darcy equation terms are reshaped as previously by Prescott, Incropera and Bennon [Prescott *et al.*, 1991], being equivalent to setting $\mathcal{D} = g_\mathrm{s}$ (or $g_\mathrm{s}^\mathrm{D} = 0$).

This transforms the momentum equation, Eq. (4.109) into

$$\begin{aligned}
&\frac{\partial}{\partial t}\left(\rho_{\mathrm{m}}\vec{v}_{\mathrm{m}}\right)+\nabla\cdot\left(\rho_{\mathrm{m}}\vec{v}_{\mathrm{m}}\vec{v}_{\mathrm{m}}\right)=-g_{\mathrm{l}}\nabla\left\langle P_{\mathrm{l}}\right\rangle^{\mathrm{l}}+\nabla\cdot\left(\mu_{\mathrm{l}}\nabla\vec{v}_{\mathrm{m}}\right)\\
&+g_{\mathrm{l}}\left(\frac{\rho_{\mathrm{m}}}{\rho_{\mathrm{l}}}\right)\frac{\mu_{\mathrm{l}}}{K}\cdot\left(\vec{v}_{\mathrm{m}}-\vec{v}_{\mathrm{cast}}\right)-g_{\mathrm{l}}\vec{g}\rho_{\mathrm{l}}^{\mathrm{ref}}\left[\beta_{\mathrm{l}}^{T}\left(T-T^{\mathrm{ref}}\right)+\beta_{\mathrm{l}}^{C}\left(\left\langle C_{\mathrm{l}}\right\rangle^{\mathrm{l}}-C^{\mathrm{ref}}\right)\right]\\
&+\left[\nabla\cdot\left(\rho_{\mathrm{m}}\vec{v}_{\mathrm{m}}\vec{v}_{\mathrm{m}}\right)-\nabla\cdot\left(g_{\mathrm{s}}\left\langle\rho_{\mathrm{s}}\right\rangle^{\mathrm{s}}\left\langle\vec{v}_{\mathrm{s}}\right\rangle^{\mathrm{s}}\left\langle\vec{v}_{\mathrm{s}}\right\rangle^{\mathrm{s}}\right)-\nabla\cdot\left(g_{\mathrm{l}}\left\langle\rho_{\mathrm{l}}\right\rangle^{\mathrm{l}}\left\langle\vec{v}_{\mathrm{l}}\right\rangle^{\mathrm{l}}\left\langle\vec{v}_{\mathrm{l}}\right\rangle^{\mathrm{l}}\right)\right]. \quad (7.1)
\end{aligned}$$

The reason for this is that the computations were performed before the derivation and code implementation of the full model were finalized, and that this formulation does not cause a significant difference in the results. Further, the grain transport equation (Eq. (4.128)) and constitutional equations needed in the slurry regime (Eqs. (4.129), (4.127), and (4.30)) are omitted in the porous-regime model.

Billets of two different sizes are simulated, with diameters of 218 mm and 282 mm. Axisymmetry is assumed. Two different molds are investigated for the smaller dimension. The first one is a Wagstaff$^{\mathrm{TM}}$AirSlip$^{\mathrm{TM}}$hot-top mold, which is 4 cm high and incorporates an insulation ring on the upper 3 cm of height. The second one is a conventional water-cooled mold of 7 cm height. In both cases the metal entry is only through part of the mold opening; the exact inlet diameters are given in Table 7.2. The melt enters with the nominal composition of 5.25 %Cu, the prescribed casting temperature T_{cast} and a uniform velocity v_{in}, determined by the casting velocity v_{cast} (the withdrawal velocity of the bottom block), the inlet cross-section area A_{in}, and by the solidification shrinkage; i.e. the inflow mass flux must be the same as the outflow from the domain at the bottom.

$$v_{\mathrm{in}}=\frac{\pi d^2}{4A_{\mathrm{in}}}\frac{\rho_{\mathrm{s}}}{\rho_{\mathrm{l}}}v_{\mathrm{cast}} \quad (7.2)$$

Slip boundary conditions are prescribed at the right boundary for the contact of the liquid and the mold. The heat transfer to the mold in the non-insulated part was modeled by a heat transfer coefficient, varying between 400 W/m^{2}K and 5000 W/m^{2}K, depending on the liquid fraction at the contact surface. At the insulation ring the heat transfer coefficient is approximated to be zero. The secondary cooling is modeled using the Weckman-Niessen correlation [Weckman and Niessen, 1982] for the heat transfer coefficient at a vertical surface cooled by a subcooled-nucleate-boiling falling-water film. The heat transfer coefficient is thus

$$h_{\text{chill}} = \begin{cases} h_{\text{graphite}} = 0\,\text{W/m}^2\text{K} & z > z_{\text{graphite}} \\ h_{\text{mold}} = h_{\text{high}}^{f_l}\, h_{\text{low}}^{(1-f_l)} & z_{\text{graphite}} > z > z_{\text{mold}} \\ h_{\text{DC}} = \left[-1.67 \cdot 10^5 + 352(T + T_{\text{w}})\,[\text{K}]\right] & \\ \quad \cdot \left(\dfrac{Q_{\text{w}}\,[\text{m}^3/\text{s}]}{\pi D\,[\text{m}]}\right)^{1/3} & z_{\text{mold}} > z \\ \quad + 20.8(T\,[\text{K}] - T_{\text{sat}}\,[\text{K}])^3 \quad [\text{W/m}^2\text{K}] & \end{cases} \tag{7.3}$$

$$h_{\text{high}} = 400\,\text{W/m}^2\text{K}$$

$$h_{\text{low}} = 5000\,\text{W/m}^2\text{K}.$$

The water entry temperature is 300 K and a heat balance is used to calculate the increase of the water temperature T_{w} along the billet surface. The bottom of the computational domain is assumed to be adiabatic. While this assumption is not exact due to the short domain length of 0.6 m, it should not significantly affect the flow nor the macrosegregation. All boundaries, except the inflow boundary, are impermeable for species transport. The left boundary (billet centerline) is a symmetry boundary. These boundary conditions are shown schematically in Fig. 7.1. The thermophysical properties of Al-5.25 wt%Cu used in the simulations are given in Table B.1 in Appendix B together with their sources. They were obtained from the materials properties modeling software JMatPro [Saunders *et al.*, 2001] and from reference [Vreeman and Incropera, 2000]. All process parameters, which vary from case to case and are not explicitly given here, are summarized in Table 7.2.

7.3 Numerical Solution Procedure

7.3.1 Specifics of the Numerical Method

The numerical method is described in detail in Chapter 5. Only some features, specific to the computations performed in this part of the work, are given here. The set of macroscopic transport equations (Eqs. (4.91), (7.1), (4.113), and (4.115)) was solved in axisymmetric geometry and on an orthogonal structured grid. A grid of 100×356 control volumes (CVs) with additional nodes at the domain boundaries (thus a total of 102×358 nodes) was used in all cases and it was strongly biased in the top part (the height of the liquid and mushy regions). The top part (0.15 m in the large billet and 0.12 m in the small billet) was discretized into 100×200 equal CVs and the remaining bottom part into 100×256 CVs with a grid expansion factor of 1.0175. The

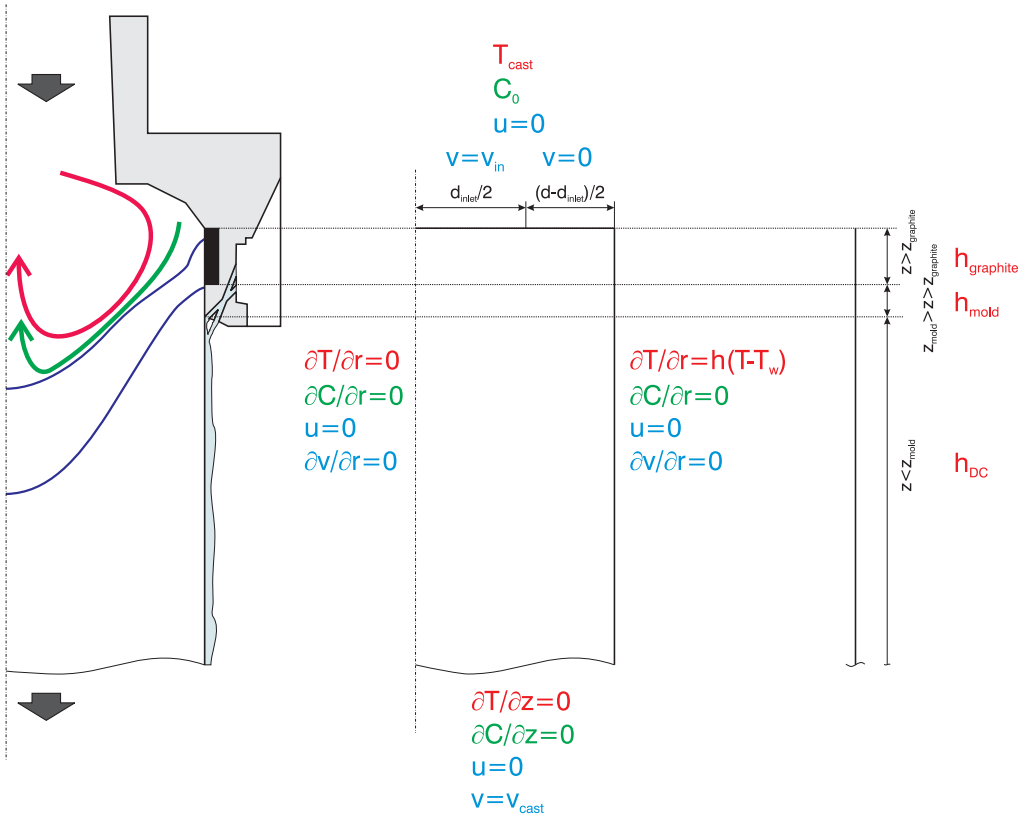

Figure 7.1: Schematics of the boundary conditions of the DC casting model.

grid is shown in Fig 7.2. For the discretization of advective fluxes the central difference scheme was used in the energy equation and the first-order upwind scheme in the species and momentum equations. The upwind scheme was used to cure the severe problems with the iterative convergence of the coupled equation system which were encountered upon the use of higher-order schemes for momentum and species advection. One should note that this is only a preliminary computational framework that works efficiently. It is used before the stable full implementation of more accurate numerical schemes, which have been shown to be necessary [Založnik and Šarler, 2005b], is completed.

7.3.2 Solution Procedure

The implicit iterative solution of the strongly coupled equations can be relatively unstable at the beginning of the calculation. The development of a strong thermosolutal convective flow in the liquid pool and its interaction with the mushy zone can severely slow down the convergence if the solution

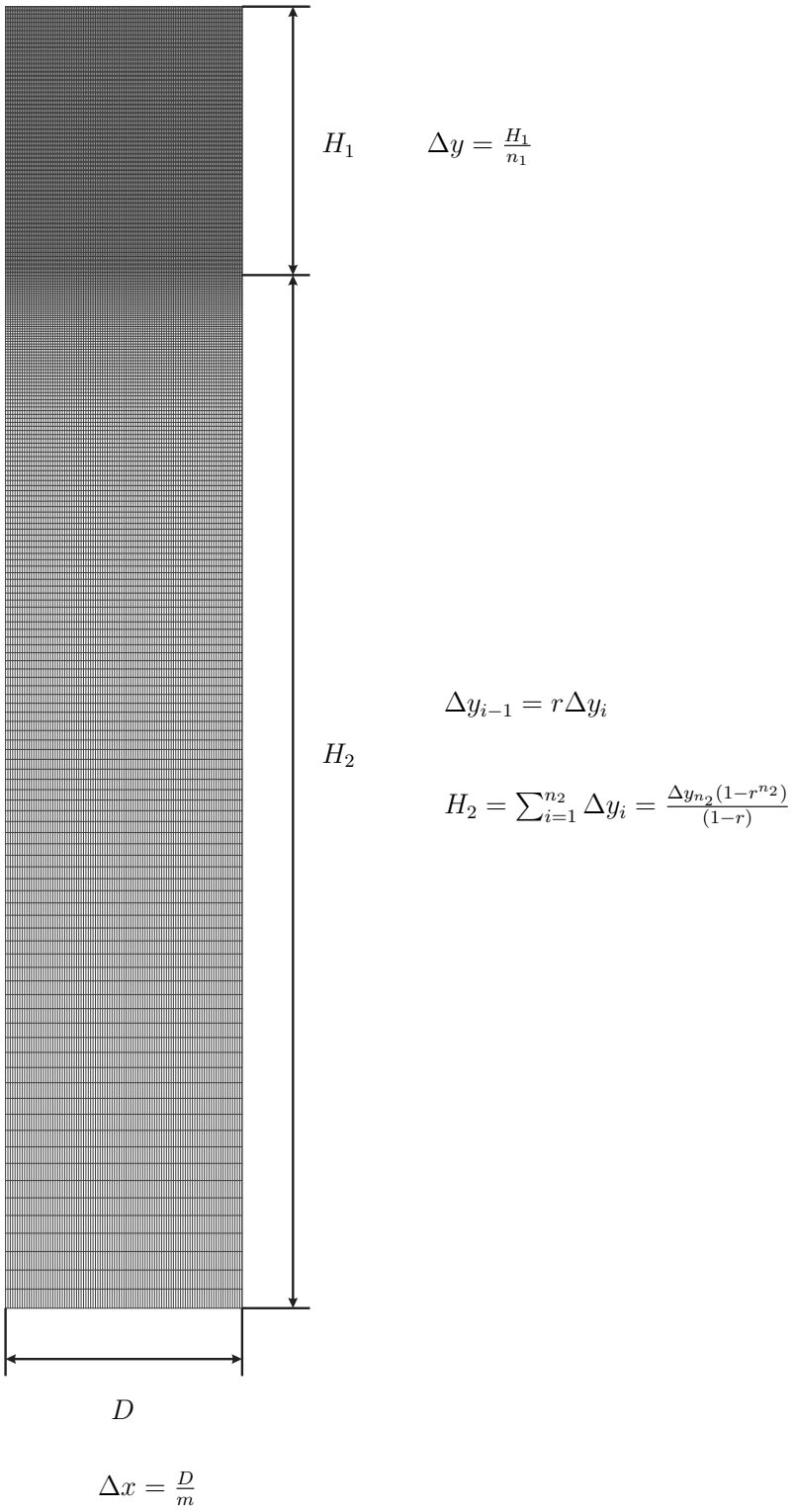

Figure 7.2: A biased 102×358-node finite volume grid for DC casting calculations.

of the full problem is started right from the beginning with an unfavorable initial state. Therefore, a special procedure was used to speed up the computations.

1. First, only an approximation of the temperature, liquid fraction and flow fields was obtained by solving the energy and momentum equations with both thermal and solutal expansion coefficients (β_T, β_C) set to zero.

2. Then the realistic expansion coefficients and the solute conservation equation were invoked, with species diffusion coefficients initially increased by 100 times. The latter was done to somewhat relax the gradients of the solutal buoyancy body force driving the flow, thus easing convergence during the initial redistribution of copper in the mushy and liquid zones.

3. After a calmed down flow was obtained, the diffusion coefficients were set to their realistic values and the computations were continued until a quasi-steady radial macrosegregation profile was obtained.

A steady state of the system was not found since slight oscillations of the flow persisted even long after the quasi-steady segregation profile was reached. This is not surprising; strong instabilities of the thermosolutal natural convection flow were already observed in Chapter 6. Also, a physically oscillatory flow was reported before in computations of thermal convection in DC casting [Založnik and Šarler, 2005b]. However, it is important to note that in the cases treated here the flow oscillations were weak and had only a negligible effect on the flow structure and the macrosegregation pattern. Previously, Vreeman and Incropera [Vreeman and Incropera, 2000], who reported an unsteady flow in some of their macrosegregation computations, presumed a numerical problem. Even though some unphysical oscillations are present in the concentration field it is believed that they are not an important source of the flow oscillations in the present computations, and their origin is physical.

Severe oscillations are present in the subsurface part of the segregation profile (Figs. 7.10–7.10). Their origin is numerical and was analyzed before in detail [Venneker and Katgerman, 2000]. The effect is stronger with a small mushy zone thickness (larger f_l-gradient). A remedy is the alignment of the grid with the liquid-mush interface and local grid refinement.

Table 7.2: Process parameters for the simulated cases

Case	Diameter [mm]	v_{cast} [mm/s]	T_{cast} [K]	Mold type	Q_{cool} [m^3/s]	Inlet [mm]
1	282	1.25	973.15	hot-top	$1.75 \cdot 10^{-3}$	172
2	218	1.43	973.15	hot-top	$1.56 \cdot 10^{-3}$	140
3	218	1.14	973.15	hot-top	$1.56 \cdot 10^{-3}$	140
4	218	1.43	953.15	hot-top	$1.56 \cdot 10^{-3}$	140
5	218	1.43	973.15	water cooled	$1.56 \cdot 10^{-3}$	140

7.4 Results and Discussion

7.4.1 Simulated Cases

Five different cases are studied. They represent variations of the billet diameter, casting velocity (v_{cast}), casting temperature (T_{cast}), and mold type. As reasoned in Section 7.2, these casting parameters are expected to have the strongest influence on macrosegregation. The specifications of the five cases are given in Table 7.2. Case 2 represents the basic case, also used to study the impact of billet size, when compared to Case 1. The casting velocity is decreased by 20 % in Case 3 and the casting temperature by 20 K in Case 4. In Case 5 a change of mold type causing a significant change of heat transfer in the mold is simulated. Case 1 is observed in more detail to explain the flow structures and species transport in the sump and on the way they result in the final macrosegregation pattern. The other cases are discussed afterwards, focusing on the mechanism of the effect of the different parameters on the macrosegregation profile. The main distinguishing features of the flow and species transport are explained.

7.4.2 Sump Flow and Formation of Macrosegregation

To make a clear presentation of the origins of the thermosolutal buoyancy-driven flow in the liquid sump, Fig. 7.5 shows the flow field together with the liquid-density field (calculated according to the Boussinesq approximation used in the momentum equation—Eq. (7.1)). As can be seen in the plot, the liquid is relatively quiescent at the bottom and in the center of the liquid sump, which is caused by the counteracting effect of thermal buoyancy and the stratification tendency of the heavy solute-rich liquid. Next to the liquid-mush interface a complex flow structure consisting of small vortices forms. Five vertically arranged flow cells can be identified, delimited by sharp density gradients. Each cell contains one or two vortices of thermoso-

lutal origin. The solutal buoyancy effect also causes a slight vertical density bump inside each thermosolutal cell and raises the splitting of the flow into two vortices. As explained in Section 6.10.1, such a multicellular structure occurs in thermosolutal flows when a stable solutal stratification is destabilized by a large enough lateral temperature gradient. In contrast to test Case 5a in Section 6.10.1, however, the flow in the liquid pool of the casting is relatively stable. Despite the small oscillations that persist which prevent the development of a steady state, the structure and arrangement of the flow cells are retained throughout. In the solidification zone ($0 < f_\mathrm{l} < 1$) the liquid is enriched due to segregation of the solute ($C_\mathrm{l} > C_\mathrm{m}$; $C_\mathrm{s} < C_\mathrm{m}$). Since copper has a larger density than aluminum, a solutal downward flow of enriched liquid can be observed in the high-f_l portion of the mushy zone (along the liquidus front). This flow carries enriched liquid away from the top-outer part (top right in Fig. 7.4) of the mushy zone, replacing it with solute-lean liquid, which penetrates into the mush from the bulk liquid region. Solute is carried into the bulk liquid and the heavy, enriched liquid flows down the slope of the mushy zone front, accumulating at the bottom of the sump. Along the liquidus front the thermosolutal circulations additionally carry high-concentration liquid out of the mushy zone into the bulk-liquid sump. In the low-f_l regions of the mushy zone, the permeability of the porous mush rapidly decreases; consequently, drag forces dominate over buoyancy and inertia. The flow is driven mostly by solidification shrinkage, as the liquid fills up the space left by the shrunken solidified metal. The liquid in the low-f_l mushy zone is highly segregated, thus even the small shrinkage-induced relative velocities can result in considerable net solute transport. This can be clearly seen along the whole mushy zone. The direction of the shrinkage-induced flow is opposite to the liquid fraction gradient (Fig. 7.5). As the enriched liquid flows towards the solidus front it is replaced by the leaner liquid from regions of the mushy zone with higher f_l. The enriched liquid accumulates at the front and the concentration rapidly increases in the direction opposite to the f_l-gradient. Because of the characteristic sump shape and the direction of the shrinkage-induced solute transport, this flow tends to decrease the concentration in the billet center and increase the concentration in the outer part of the billet. This is also the mechanism causing typical positive subsurface segregation.

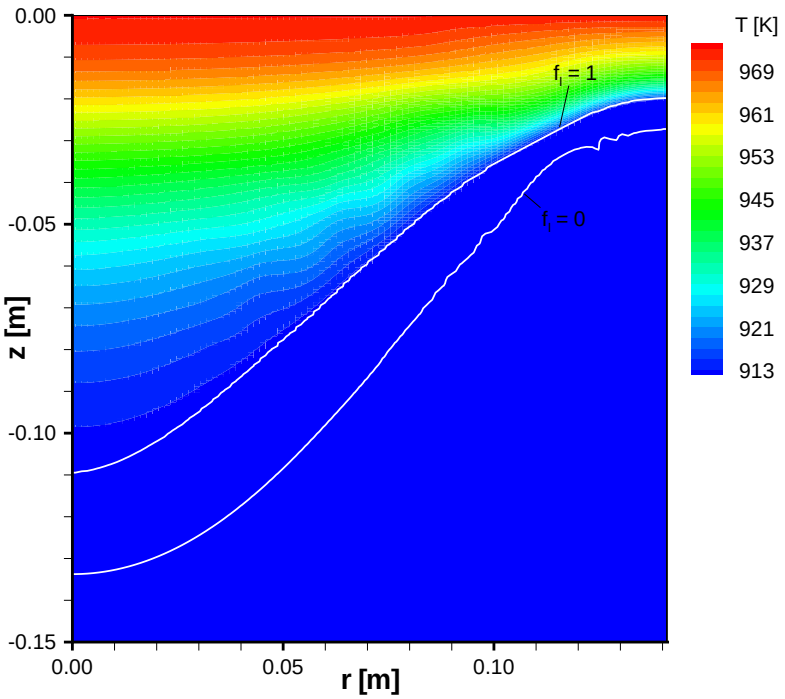

Figure 7.3: Temperature field in the billet for Case 1.

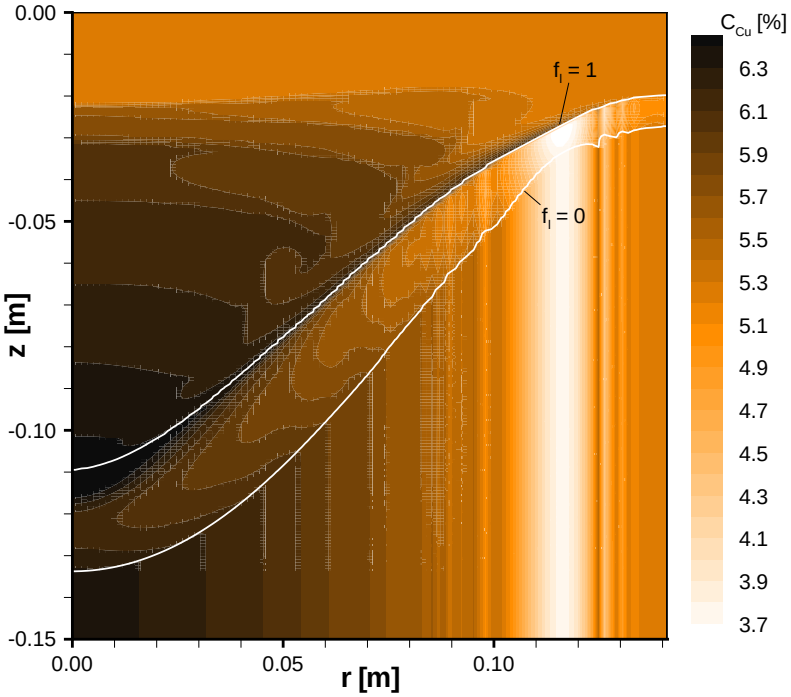

Figure 7.4: Mixture Cu concentration (C_{m}) field in the billet for Case 1.

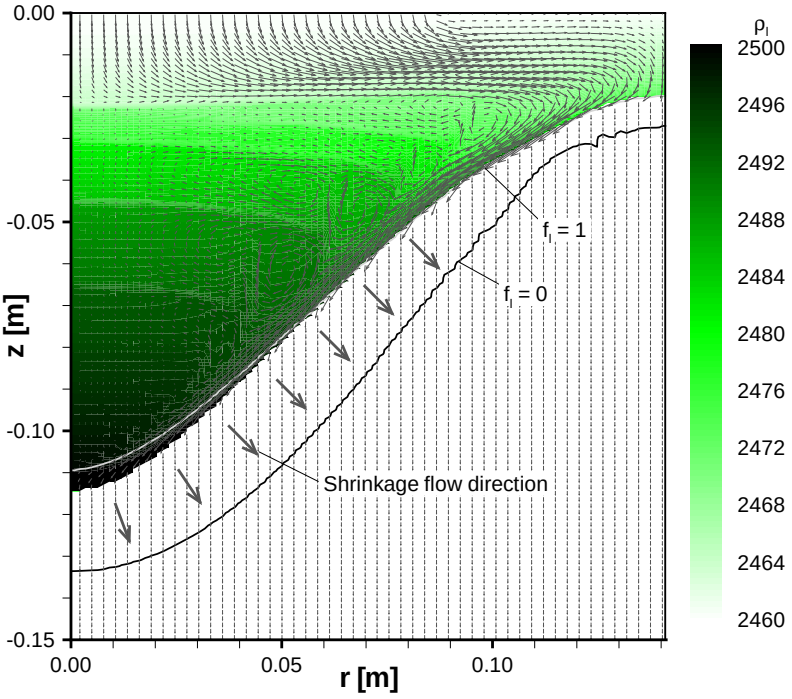

Figure 7.5: Liquid density (ρ_l) and relative velocity ($\vec{v}$) fields in the billet for Case 1. The density field is shown only in the liquid and part of the mushy zone ($f_\mathrm{l} > 0.1$).

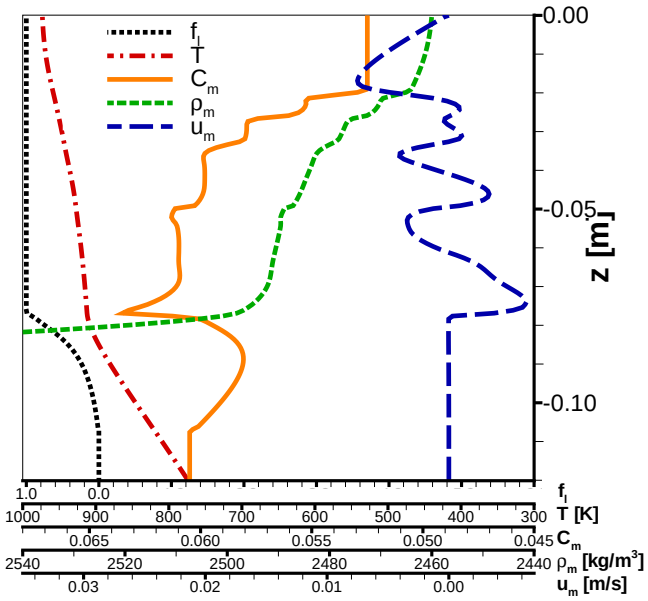

Figure 7.6: Vertical profiles of liquid mass fraction (f_l), temperature (T), mixture concentration (C_m), mixture density (ρ_m), and horizontal mixture velocity component (u_m) at ($r = 0.051465\,\mathrm{m}$).

7.4.3 Simulation of Parameter Influence

Case 2: Billet Size

The thermosolutal flow structure driving the species transport in the basic Case 2 (Figs. 7.7–7.9) is similar to the structure described for Case 1. In both cases there is positive segregation in the center and a smooth negative segregation minimum, which is shown in Fig. 7.10. Its position coincides with the outer (right) boundary of the top flow cell. As expected, the segregation is more pronounced in the larger billet due to the more intensive solute transport from the high-f_l mushy zone caused by stronger convection currents.

Case 3: Casting Velocity

In Case 3, where the casting velocity was decreased, the sump is much shallower than in Case 2, as shown in Fig. 7.23(a). In the language of dimensionless parameters of natural convection, this decreases the characteristic height H and consequently the effective Rayleigh numbers (Ra_T, $Ra_C \sim H^3$) and the aspect ratio (A=H/L). The flow is restricted, resulting in a simpler flow structure with one dominant main circulation and three hardly discernible smaller circulation cells (Fig. 7.13). In the absence of small circulations at the liquid-mush interface, less solute is advected from the mushy zone into the bulk liquid (Fig. 7.12), somewhat decreasing the effective buoyancy ratio N. As we would expect from the knowledge of thermosolutal convection, this causes the stratification of enriched liquid at the sump bottom to be less pronounced. The smooth, slightly negatively segregated part of the profile around the 0.06 m radius, shown in Fig. 7.14, coincides with the region where the flow of the main circulation is aligned with the liquid-mush interface (i.e. no flow deflections of smaller cells are present) and the interface has a constant slope (Fig. 7.23(a)). A relatively sharp transition to positive segregation then appears in the direction towards the centerline, at the place where the interface slope changes and the flow penetrates into the mush under a low angle, causing an effect of solute pileup, as in inverse segregation. As expected, at lower casting velocity the overall segregation is weaker, which can be seen in Fig. 7.14.

Case 4: Casting Temperature

A decrease of casting temperature in Case 4 causes only a slight shift of the shape of the mushy zone as is shown in Fig. 7.23(b). The key to the explanation of the lower segregation is the flow in the liquid region. The

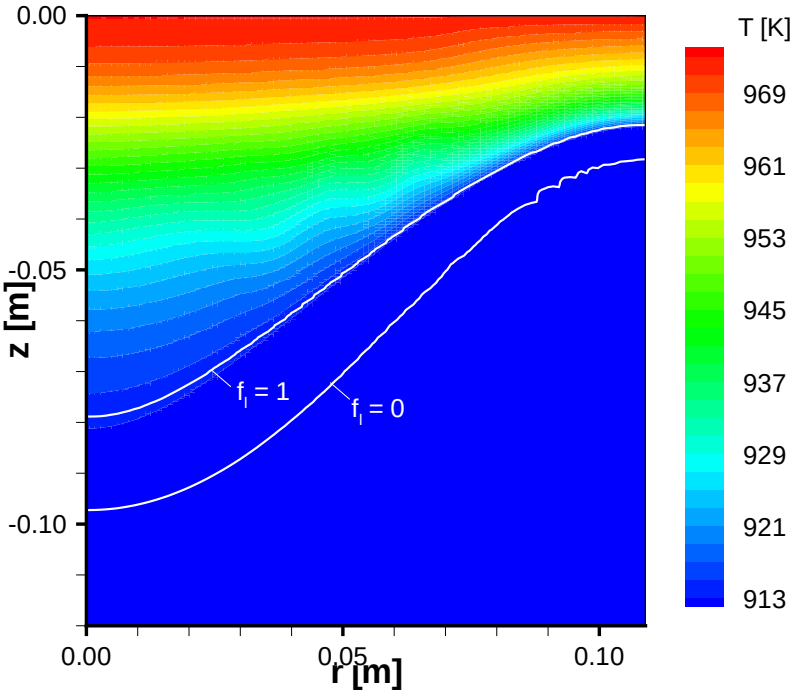

Figure 7.7: Temperature field in the billet for Case 2.

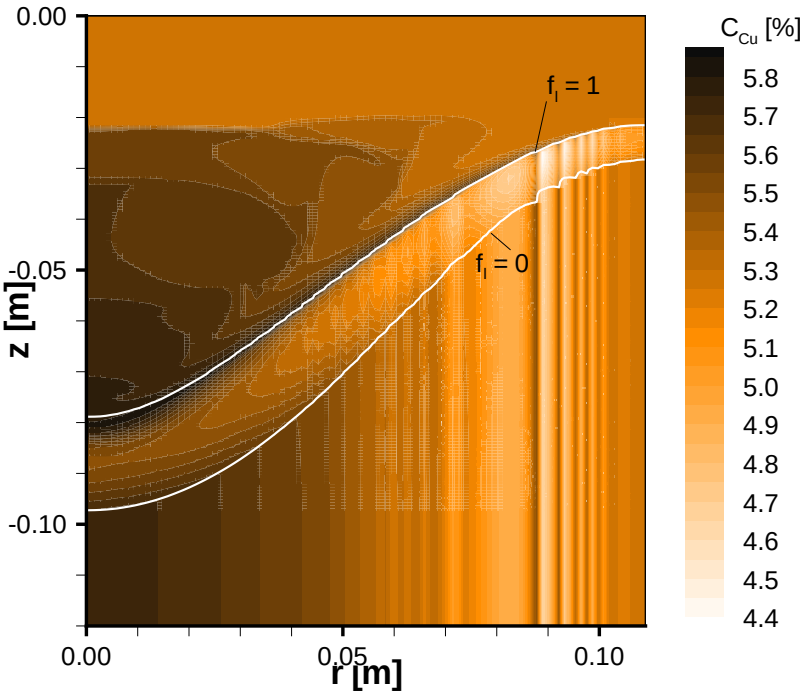

Figure 7.8: Mixture Cu concentration (C_{m}) field in the billet for Case 2.

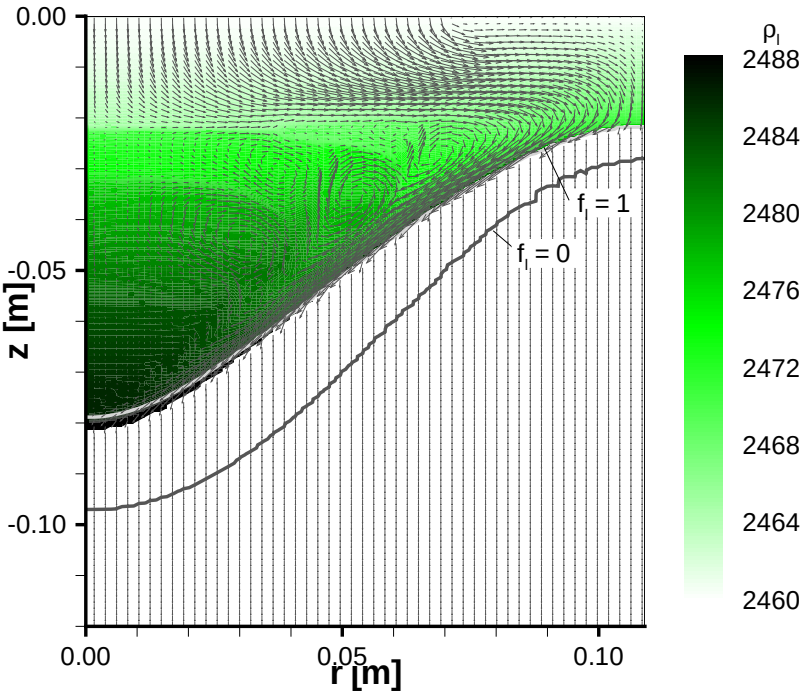

Figure 7.9: Liquid density (ρ_l) and relative velocity ($\vec{v}$) fields in the billet for Case 2. The density field is shown only in the liquid and part of the mushy zone ($f_l > 0.1$).

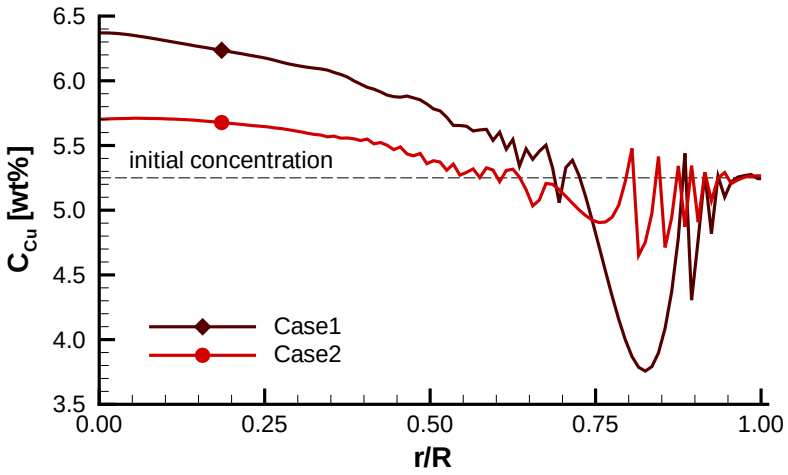

Figure 7.10: Comparison of macrosegregation profiles as a function of the normalized radius for different billet sizes.

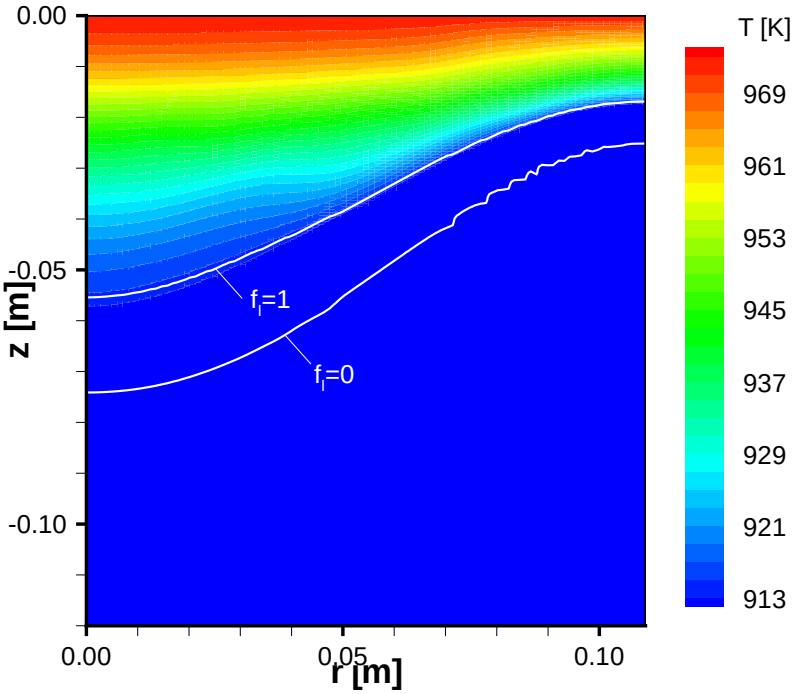

Figure 7.11: Temperature field in the billet for Case 3.

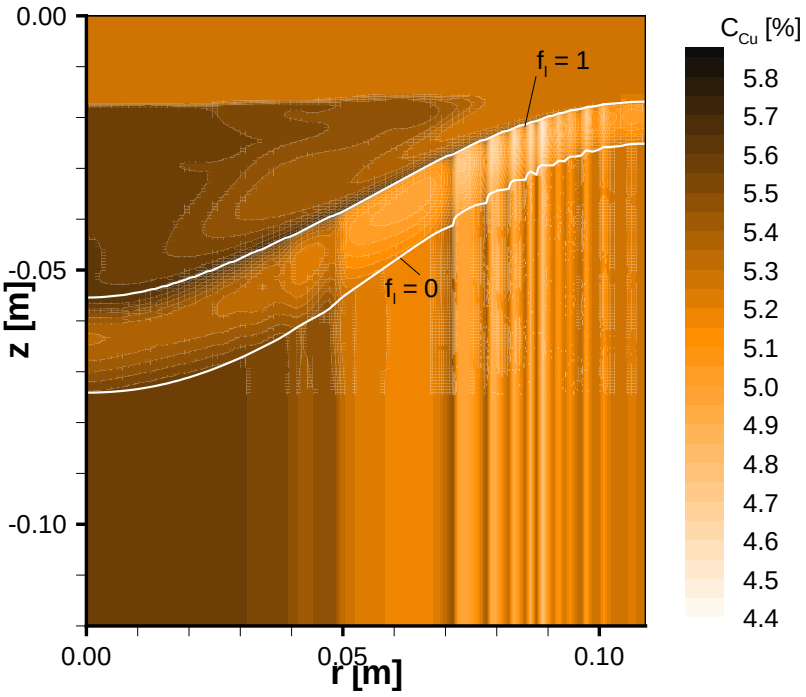

Figure 7.12: Mixture Cu concentration (C_{m}) field in the billet for Case 3.

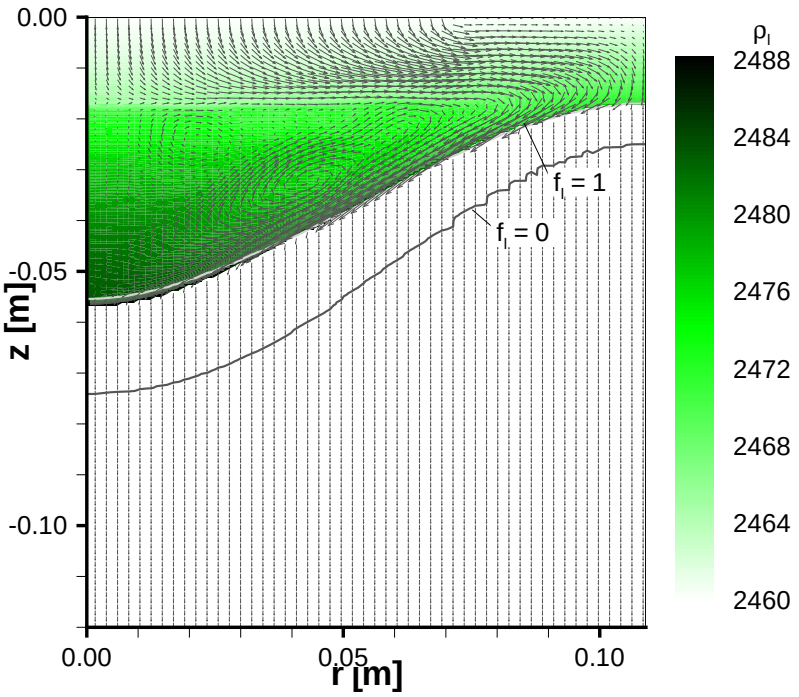

Figure 7.13: Liquid density (ρ_l) and relative velocity ($\vec{v}$) fields in the billet for Case 3. The density field is shown only in the liquid and part of the mushy zone ($f_l > 0.1$).

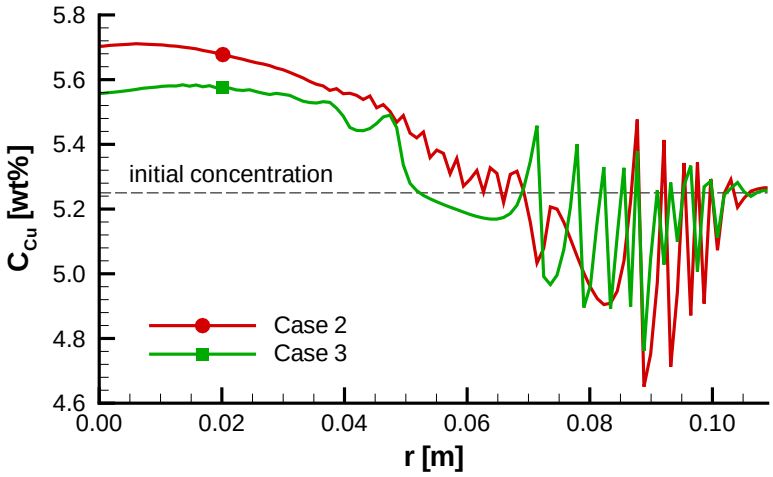

Figure 7.14: Prediction of the influence of casting velocity on macrosegregation.

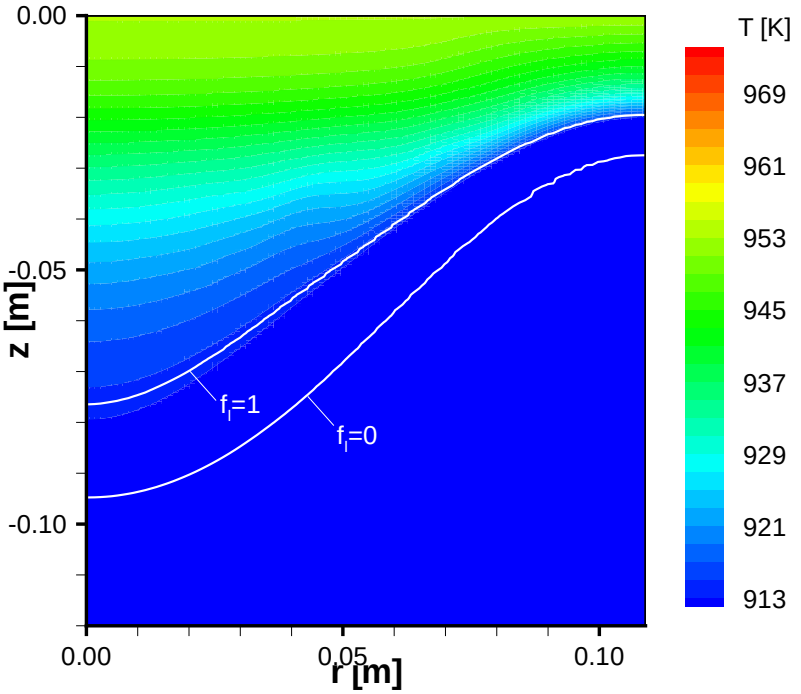

Figure 7.15: Temperature field in the billet for Case 4.

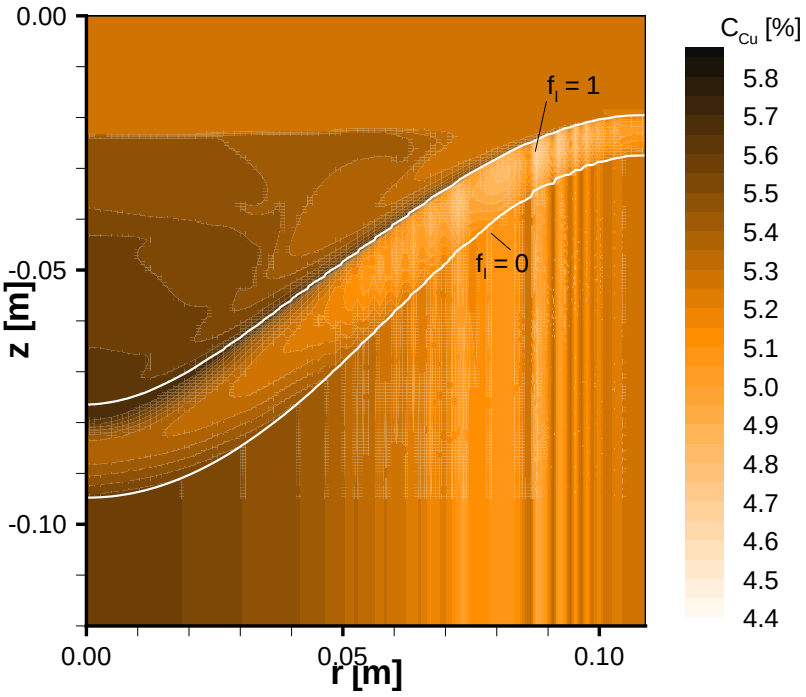

Figure 7.16: Mixture Cu concentration (C_{m}) field in the billet for Case 4.

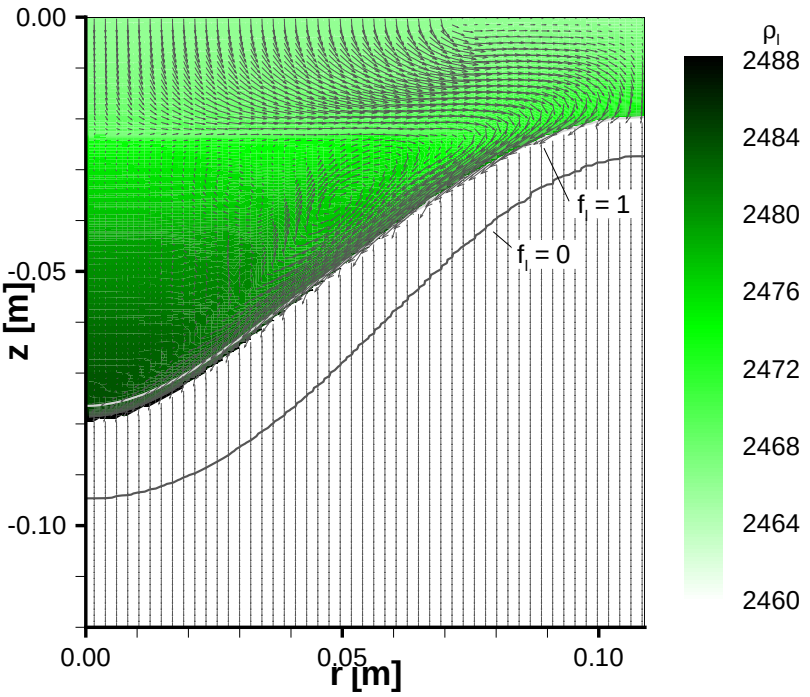

Figure 7.17: Liquid density (ρ_l) and relative velocity ($\vec{v}$) fields in the billet for Case 4. The density field is shown only in the liquid and part of the mushy zone ($f_l > 0.1$).

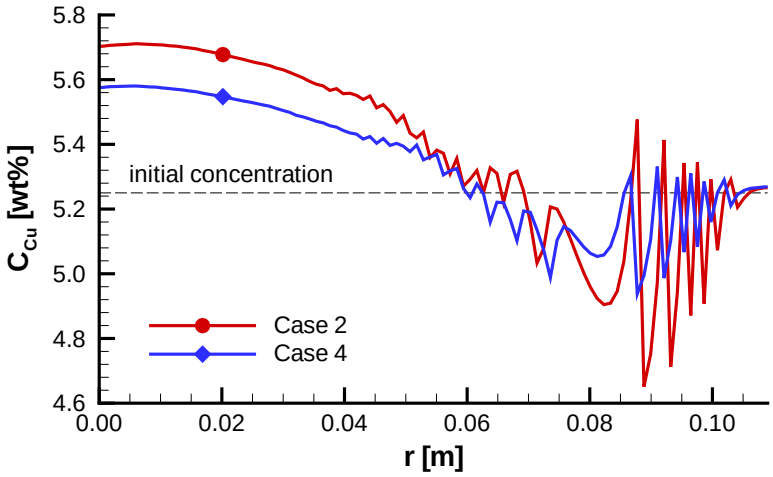

Figure 7.18: Prediction of the influence of casting temperature on macrosegregation.

primary effect of a smaller temperature difference in an otherwise preserved sump is a smaller driving force for thermal natural convection (a smaller effective Ra_T). The consequence is a less intensive main circulation (Fig. 7.17) resulting in less transport of the enriched liquid from the mush into the bulk liquid and along the liquid-mush interface towards the centerline (Fig. 7.16). This also lowers the "initial" concentration of the shrinkage induced solute transport towards the solid front in the billet center. The tendency of the shrinkage-induced solute transport, driving solute in the direction away from the centerline remains the same, on the other hand, due to the preserved shape of the mushy zone.

Case 5: Mold Type

Case 5, shown in Fig. 7.22, simulates a variation in mold cooling. The conventional water-cooled mold causes the earlier formation of a solid shell and a lower heat flux in the direct-chill zone (as a consequence of lower surface temperatures the secondary direct-chill cooling zone below the mold also starts with a lower heat flux). Consequently, the thickness of the mushy zone is significantly increased. The decrease of the liquid fraction next to the liquid-mush interface is more gradual compared to Case 2. This allows a deeper penetration of the downward flowing current into the mushy zone. The throughout concave shape of the liquid-mush interface on the outer half of the billet radius also appears to favor less discharge of solute-rich liquid from the mushy zone into the liquid pool, which explains the steep transition from negative subsurface macrosegregation to positive macrosegregation at the mid-radius. The flow of the enriched liquid stays in the mushy zone and transports solute towards the center. In the central part this effect is less pronounced and the compensation by the solute-transport by shrinkage flow causes the plateau of relatively constant positive macrosegregation in the center (Fig. 7.22).

7.5 Summary

The effects of casting velocity, casting temperature, and mold cooling on macrosegregation during the DC casting of an Al-5.25 wt%Cu alloy were numerically simulated and analyzed. The results show that these parameters influence the macrosegregation pattern through their direct impact on the thermosolutal natural convection flow in the liquid pool and on the shape and thickness of the mushy zone. The thermosolutal flow has the tendency to increase macrosegregation in the billet center due to solute transport by the

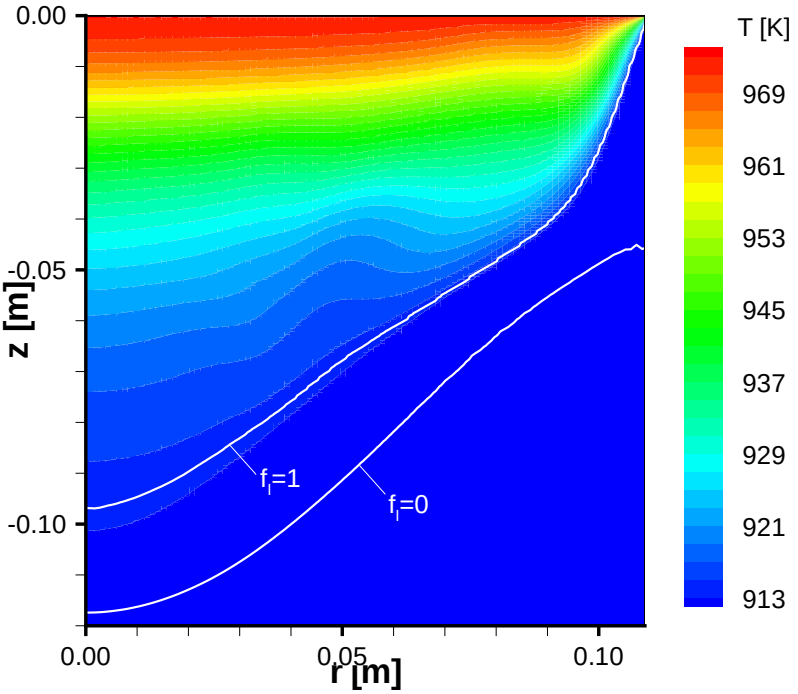

Figure 7.19: Temperature field in the billet for Case 5.

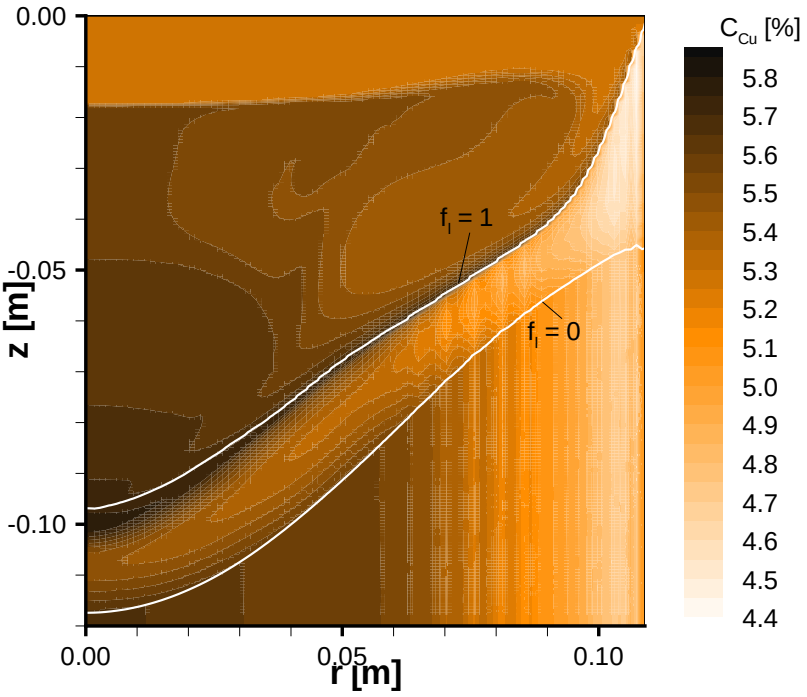

Figure 7.20: Mixture Cu concentration (C_{m}) field in the billet for Case 5.

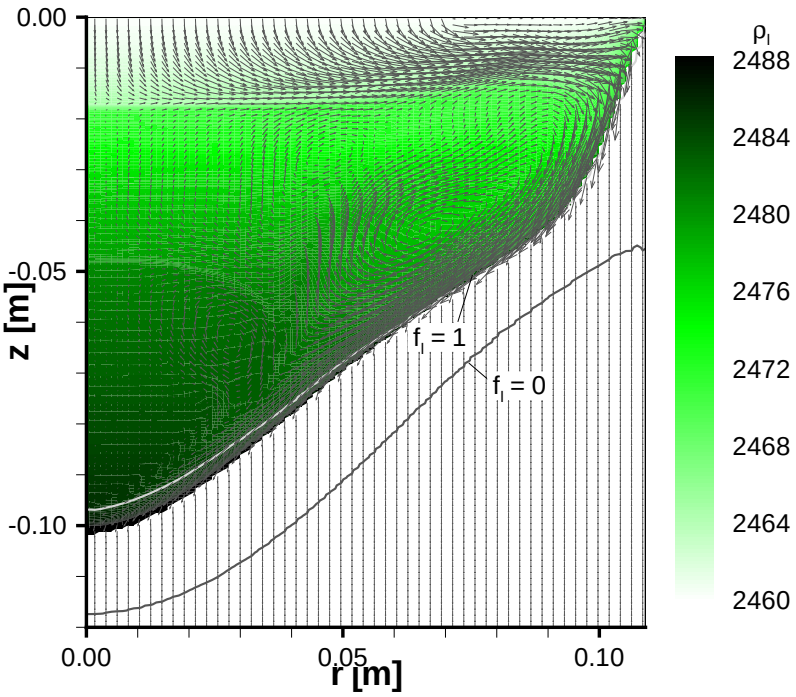

Figure 7.21: Liquid density (ρ_l) and relative velocity ($\vec{v}$) fields in the billet for Case 5. The density field is shown only in the liquid and part of the mushy zone ($f_l > 0.1$).

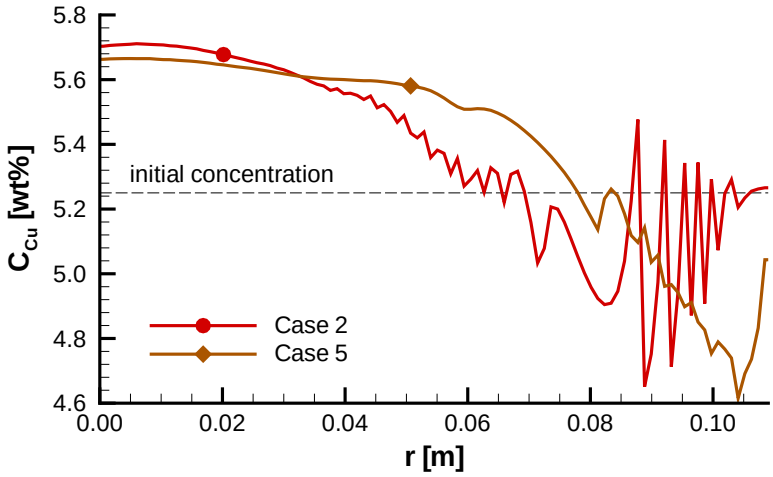

Figure 7.22: Prediction of the influence of mold cooling on macrosegregation.

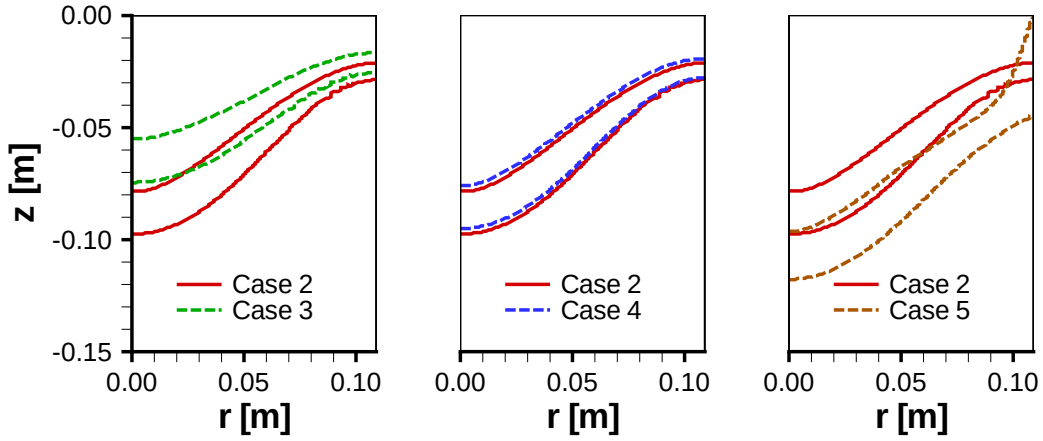

(a) casting velocity (b) casting temperature (c) mold cooling

Figure 7.23: Impact of process parameters on the sump shape. The solidus ($f_l = 0$) and liquidus ($f_l = 1$) fronts are shown.

thermal flow along the liquidus front and due to solutal stratification, particularly pronounced in the Al-Cu alloy. The solute transport is intensified when instability causes the emergence of smaller flow cells which make the transport of solute-rich liquid from the mushy zone even more effective. It is generally intensified by a deeper liquid pool and by a higher casting temperature. The opposite, or better said, alleviating effect is that of the shrinkage flow which transports solute-rich interdendritic liquid away from the centerline. Its magnitude depends primarily on the shape of the mushy zone, i.e. locally on its slope and globally on its depth. A more detailed investigation of the interaction of convection and shrinkage flow is necessary to estimate the interaction of both solute transport modes and is made in Chapter 8. Higher casting velocity and higher casting temperature both promote macrosegregation through their effect on the natural convection in the sump. The first occurs through an increase of the liquid pool depth and the latter by an increase of the temperature difference driving the thermal natural convection in the liquid pool.

The estimations of the effects of the casting parameters show that, although the porous flow regime model is incapable of properly predicting macrosegregation patterns, it can be used to predict trends caused by variations of the parameters. Most importantly, the effect on the thermosolutal flow is shown. The results indicate that the flow structure plays an important role in macrosegregation formation. These trends, in the sense of changes of the global degree of macrosegregation, show some relation to experimentally and industrially observed trends. Macrosegregation is generally observed to

increase with casting velocity [Dorward and Beerntsen, 1990, Eskin *et al.*, 2004]. The AirSlip^{TM}mold cooling is known from industrial practice to produce less macrosegregation than conventional water-cooled molds, especially in the subsurface layer. The effect of casting temperature seems to be more complex since different effects were observed: a reversal from negative to positive centerline segregation with a temperature increase [Dorward and Beerntsen, 1990], and no significant influence of the casting temperature except close to the surface [Eskin *et al.*, 2005]. It remains clear that an extension of the model to account for grain transport is necessary to move closer to the correct prediction of local macrosegregation deviations.

8 Interaction of Flow Phenomena Causing Macrosegregation in DC Casting

This chapter is dedicated to investigations of the effects of flow phenomena leading to macrosegregation in DC castings (recall Section 1.2.3, Fig. 1.8).

- thermosolutal convection in the bulk liquid
- shrinkage-induced flow
- motion of solid grains

The exact mechanism of macrosegregation formation in DC casting is still unexplained and this short study presents a contribution to the discussion on the subject. The effects of shrinkage-induced flow and, in a simplified way, the impact of free-floating solid grains on the macrosegregation are analyzed. This is investigated by the following.

- Comparisons of macrosegregation tendency in the porous mushy zone caused by shrinkage flow only and by combined thermosolutal convection and shrinkage flow are made. Segregation patterns are compared and the impact of the flow in the porous mushy zone is estimated by a simplified macrosegregation criterion.
- Computations of solid and liquid flow in the casting in the presence of a slurry zone with free-floating grains are performed using a simplified model (at constant concentration and constant grain size).

Difficulties with convergence of the iterative numerical solution scheme prevented use of the full model (Chapter 4). A modification of the present

iterative solution strategy 5.10 could possibly alleviate these problems, but such developments were out of scope of the present work. Facing these problems, the decision was taken to try to extract some conclusions on the effect of the presence of a slurry flow regime in part of the mushy zone on macrosegregation from a simplified model, assuming a constant concentration (i.e. no solute transport) and presuming a fixed-grain diameter. Constant concentration implies that the liquid mass fraction depends solely on temperature according to the inverse-lever rule.

$$f_\mathrm{l} = \left(\frac{k_\mathrm{p}}{1-k_\mathrm{p}}\right)\left(\frac{T_\mathrm{S}(C_0)-T}{T-T_f}\right) \tag{8.1}$$

By presuming a constant grain diameter the grain density becomes an unnecessary parameter, making the grain transport equation (Eq. 4.128) redundant.

8.1 The Effects of Shrinkage and Thermosolutal Convection

Shrinkage-induced flow was argued to be the determining factor resulting in the common macrosegregation pattern in DC castings [Jalanti, 2000, Jalanti *et al.*, 2001], a finding somewhat disputed by other investigations [Reddy and Beckermann, 1997, Gruber-Pretzler *et al.*, 2006], which imply an important but not decisive role of shrinkage flow in macrosegregation formation and show important impacts of thermosolutal natural convection and mold feeding. Previous investigations focused on the one alloy and casting format. Here, the effects of alloying element and casting geometry (sheet ingot or extrusion billet) are also included. Further, previous studies only compared profiles from computations featuring shrinkage and thermosolutal convection with hypothetical cases of shrinkage only. Following from a different flow, observed in the high-f_l regions of the mushy zone, the macrosegregation tendencies following from the flow inside the mushy zone on macrosegregation are investigated.

8.1.1 System Specifications and Numerical Solution Procedure

Six cases are studied by comparing computations of macrosegregation, accounting for shrinkage only with computations taking into account both thermosolutal convection and shrinkage, for three different castings.

- An Al-5.25 wt%Cu billet identical to Case 5 of the study in Chapter 7, representing cooperating thermal and solutal buoyancy ($N > 0$), strong partitioning pertinent to the Al-Cu system ($k_\mathrm{p} = 0.17$), and a cylindrical geometry (billet).

- An Al-5.0 wt%Mg billet of the same size and with the same casting parameters and cooling conditions, representing counteracting thermal and solutal buoyancy forces ($N < 0$), and less pronounced partitioning ($k_\mathrm{p} = 0.44$).

- An Al-5.25 wt%Cu ingot of the same width and with the same casting parameters and cooling conditions as in Case 5, representing a rectangular geometry (ingot).

Table 8.1: Summary of cases: Effect of shrinkage and thermosolutal convection

Case	Alloy composition	k_p	Geometry	Flow[†]	N
5	Al-5.25 wt%Cu	0.17	billet	TSC + Sh	>0
5_sh	Al-5.25 wt%Cu	0.17	billet	Sh	-
6	Al-5.00 wt%Mg	0.44	billet	TSC + Sh	<0
6_sh	Al-5.00 wt%Mg	0.44	billet	Sh	-
7	Al-5.25 wt%Cu	0.17	ingot	TSC + Sh	>0
7_sh	Al-5.25 wt%Cu	0.17	ingot	Sh	-

[†]**TSC**: thermosolutal convection, **Sh**: shrinkage

Table 8.2: Process parameters for the simulated cases

Case	Diameter/ Width [mm]	v_cast [mm/s]	T_cast [K]	Mold type	Q_cool [m^3/s]	Inlet [mm]
5, 5_sh	218	1.43	973.15	water cooled	$1.56 \cdot 10^{-3}$	140
6, 6_sh	218	1.43	963.15	water cooled	$1.56 \cdot 10^{-3}$	140
7, 7_sh	218	1.25	973.15	water cooled	$1.56 \cdot 10^{-3}$	140

The boundary conditions, computational grids and numerical solution procedure are the same as those used in Chapter 7. The casting parameters are summarized in Table 8.1.1. The thermophysical properties of Al-5.25 wt%Cu and Al-5.0 wt%Mg are given in Appendix B in tables B.1 and B.2, respectively.

8.1.2 Results and Discussion

The velocity field and its impact on macrosegregation for Case 5 (Fig. 8.1) was discussed in more detail in Section 7.4.2. Recall that the thermally-driven flow extracts some solute (Cu) from the mushy zone. The solute is transported with a strong current (additional effect of solutal buoyancy) to the bottom of the sump. The stratification tendency of the solute-rich liquid creates an enriched region in the center, causing strong positive centerline segregation.

The result for Case 5_{sh} is shown in Fig. 8.2. The velocity field is set up by the mold feeding geometry and the shrinkage-induced flow. The flow enters the mold and expands into an outward radial direction. The cooperation of the inflow geometry and the shrinkage feeding generates a flow component, flowing outward-parallel to the isotherms in the high-f_{l} part of the mushy zone. This is shown for Case 7_{sh} in a close up of the flow field near the liquidus front in Figs. 8.11(b) and 8.10(b). While it is true that the shrinkage flow is driven by the increase of density, which is directed opposite to the f_{l} gradient, this demonstrates that the flow in the porous region is determined by the flow in the bulk liquid and the pressure relations in the porous mush, as the flow in the high-f_{l} part of the porous mush is governed by the momentum equation which can in the low-f_{l} regions be approximated by the Darcy equation.

$$\langle \vec{v}_{\mathrm{l}} \rangle^{\mathrm{l}} - \vec{v}_{\mathrm{cast}} = -\frac{1}{g_{\mathrm{l}}} \frac{K}{\mu_{\mathrm{l}}} \nabla \langle P_{\mathrm{l}} \rangle^{\mathrm{l}} \tag{8.2}$$

Comparing the situation for Al-Mg, the picture in the case of the shrinkage-driven flow (Case 6_{sh}, shown in Fig. 8.4) is very similar to the Al-Cu Case 5_{sh}. Case 6 with thermosolutal flow and shrinkage, on the other hand, shows a picture very different from that of the Al-Cu Case 5. In a similar way, driven by thermal convection and the inlet flow, solute (Mg) is transported into the bulk liquid. Unlike in the Al-Cu case, however, where the heavy copper flows downwards and stratifies at the sump bottom, magnesium creates a solutal buoyancy force, cooperating with the thermal buoyancy effect and driving the flow of enriched liquid upwards. Part of the horizontal flow deflects downwards to the sump bottom, carrying enriched liquid to the liquidus front. This is the cause of the positive segregation in the central region. At the centerline a downward flowing current, originating from the inflow, remains unaffected by the solutal effect. It carries solute-lean liquid to the sump bottom and creates the relatively sharp negative segregation in the center. The smaller overall Mg-segregation in Al-Mg is attributed to two factors: less pronounced partitioning (larger k_{p}) and the absence of solutal stratification, which causes a more uniform composition in the liquid sump.

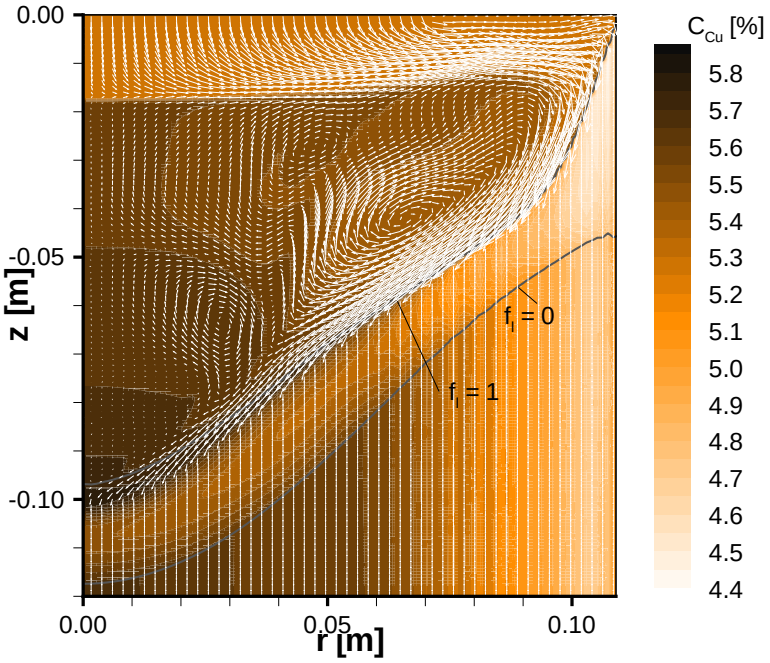

Figure 8.1: Mixture Cu concentration (C_m) and velocity ($\vec{v}_\mathrm{m}$) fields in the billet for Case 5.

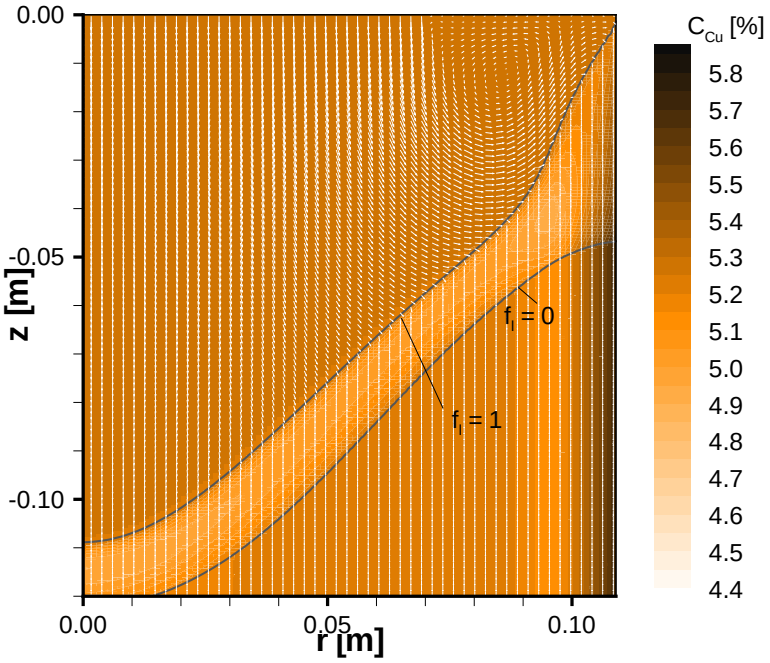

Figure 8.2: Mixture Cu concentration (C_m) and velocity ($\vec{v}_\mathrm{m}$) fields in the billet for Case 5_sh.

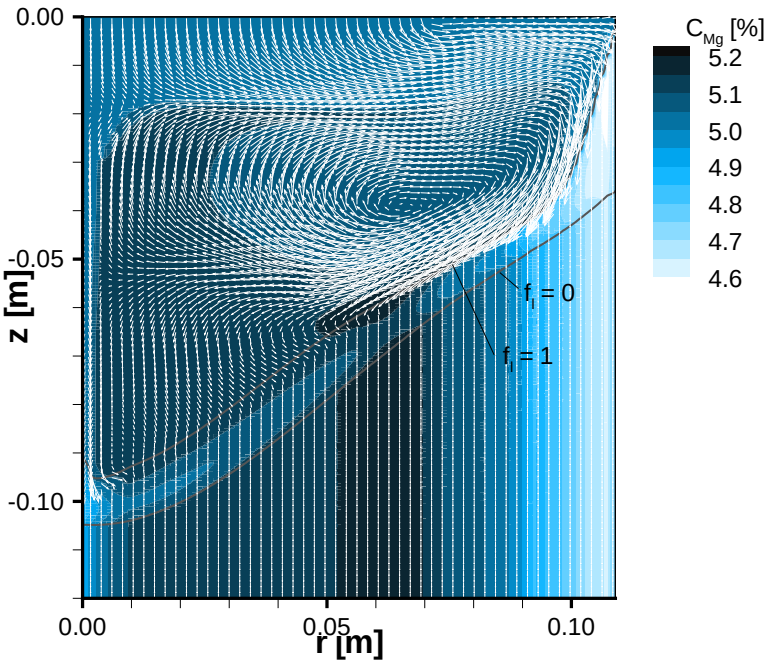

Figure 8.3: Mixture Mg concentration (C_m) and velocity ($\vec{v}_\mathrm{m}$) fields in the billet for Case 6.

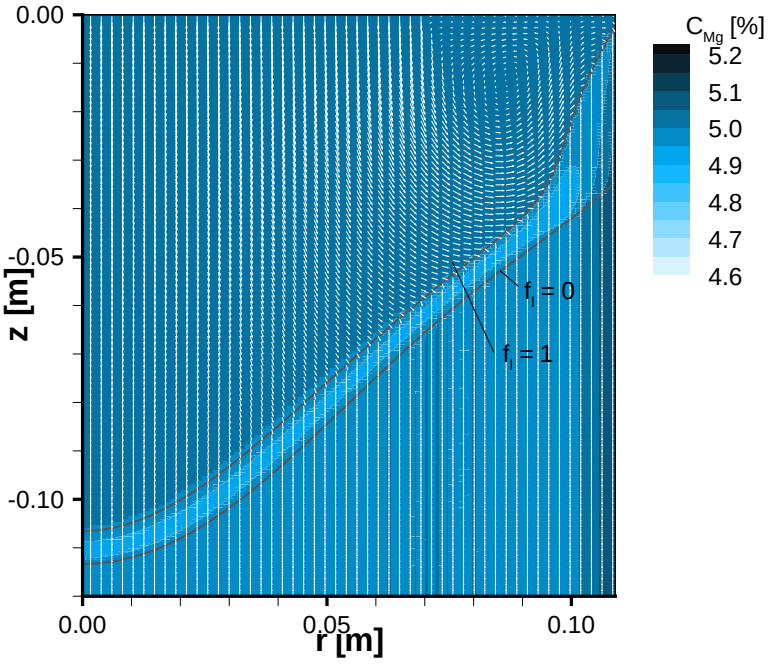

Figure 8.4: Mixture Mg concentration (C_m) and velocity ($\vec{v}_\mathrm{m}$) fields in the billet for Case 6_sh.

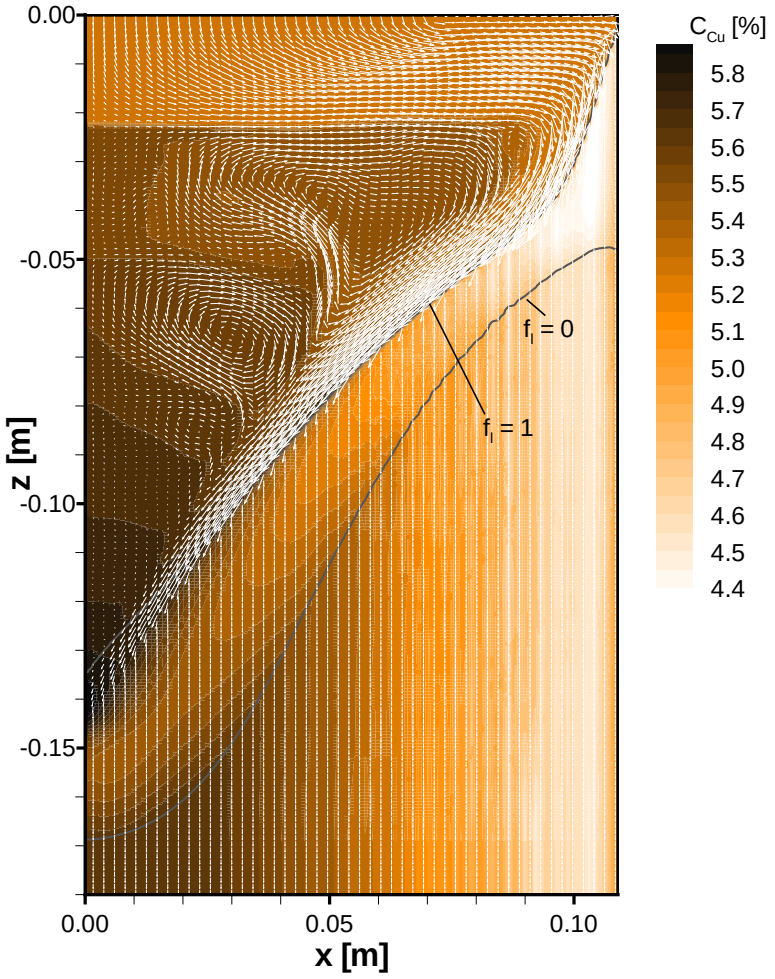

Figure 8.5: Mixture Cu concentration (C_{m}) and velocity ($\vec{v}_{\mathrm{m}}$) fields in the ingot for Case 7.

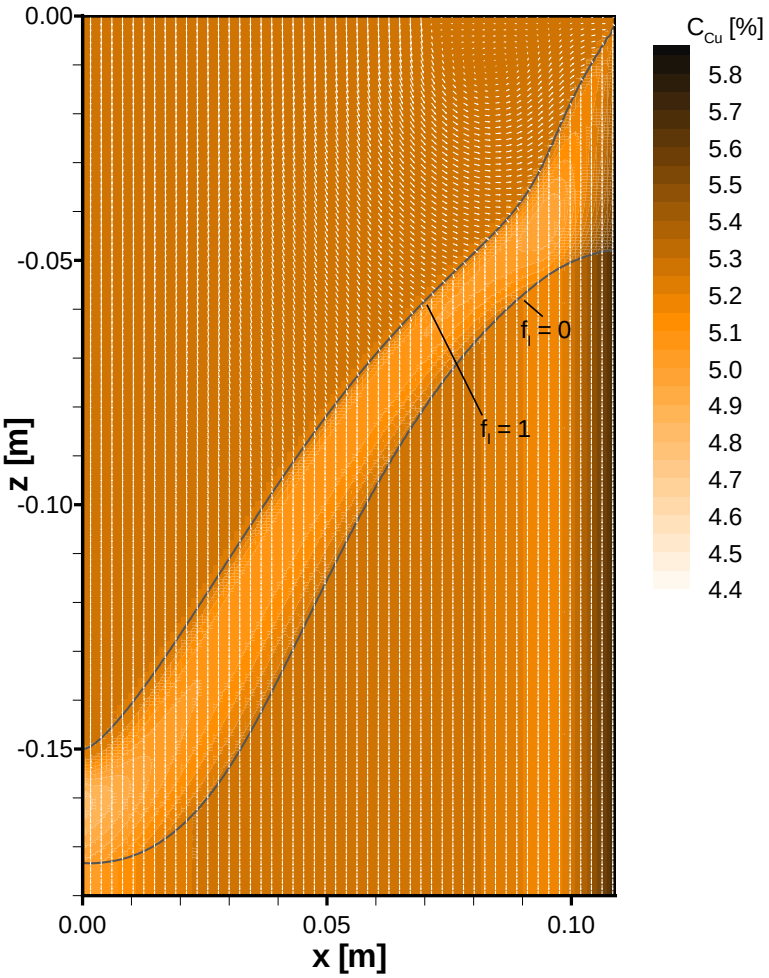

Figure 8.6: Mixture Cu concentration (C_m) and velocity ($\vec{v}_\mathrm{m}$) fields in the ingot for Case 7_sh.

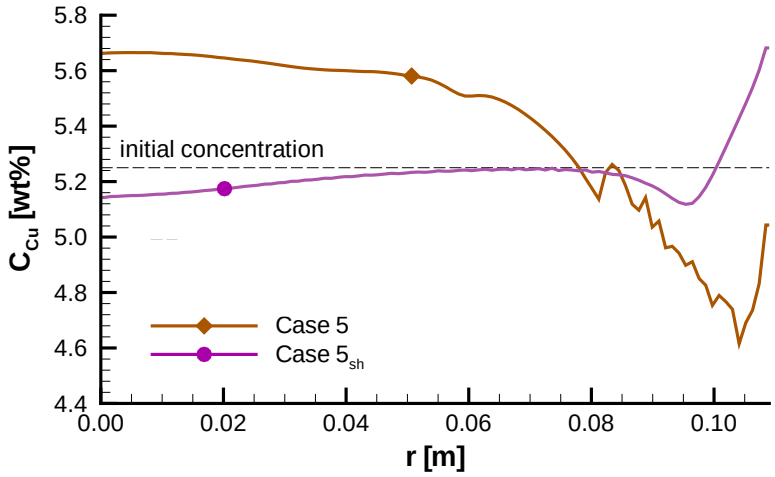

Figure 8.7: Radial Cu macrosegregation profiles for Cases 5 and 5_{sh}.

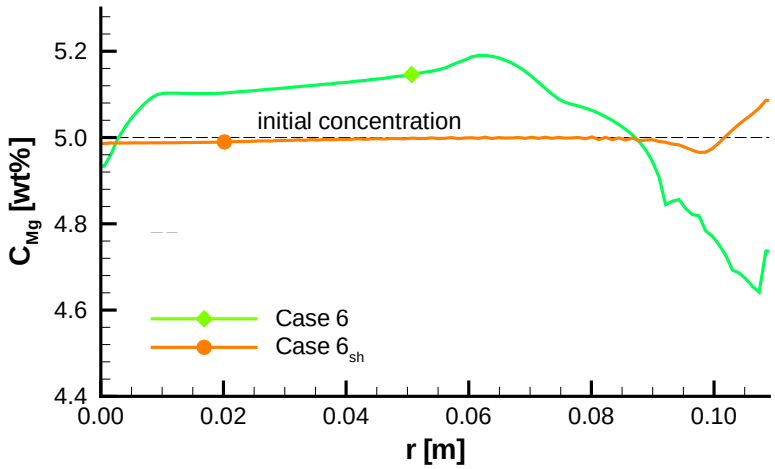

Figure 8.8: Radial Mg macrosegregation profiles for Cases 6 and 6_{sh}.

To explain the typical shrinkage-induced composition profile originating from the 2D flow in the porous mushy zone, we employ Jalanti's macrosegregation criterion [Jalanti, 2000] which is based on the simplified analysis by Flemings' local solute redistribution equation (LSRE) [Flemings and Nereo, 1967a]. The LSRE follows from the continuity and solute conservation equations, the Scheil model for microsegregation, and a linearized equilibrium phase diagram. Knowing the temperature field and the velocities of solid and liquid phases, it gives the evolution of the local concentration of liquid $\langle C_{\mathrm{l}} \rangle^{\mathrm{l}}$ surrounding a solidifying Lagrangian particle as the function of liquid volume

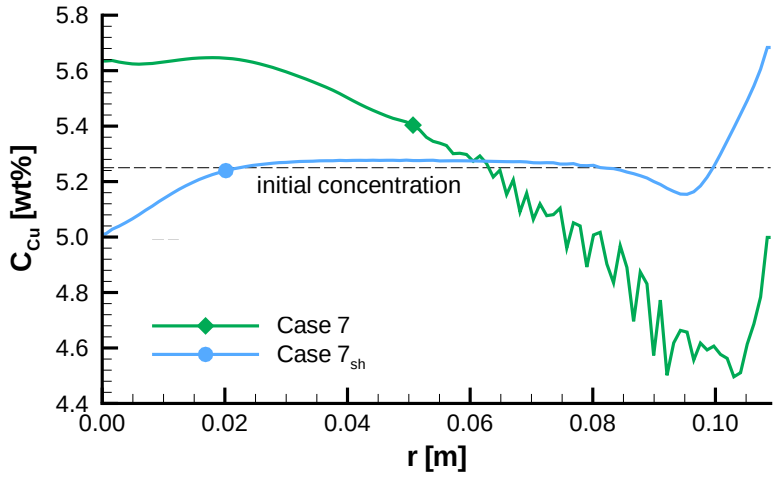

Figure 8.9: Radial Cu macrosegregation profiles for Cases 7 and 7_{sh}.

fraction g_{l}

$$\frac{\partial g_{\mathrm{l}}}{\partial \langle C_{\mathrm{l}} \rangle^{\mathrm{l}}} = -\left(\frac{1-\beta}{1-k_{\mathrm{p}}}\right)\left(1+\frac{(\langle \vec{v}_{\mathrm{l}} \rangle^{\mathrm{l}} - \langle \vec{v}_{\mathrm{s}} \rangle^{\mathrm{s}}) \cdot \nabla T}{DT/Dt}\right)\frac{g_{\mathrm{l}}}{\langle C_{\mathrm{l}} \rangle^{\mathrm{l}}} \tag{8.3}$$

$$\beta = \frac{\rho_{\mathrm{s}} - \rho_{\mathrm{l}}}{\rho_{\mathrm{s}}} \tag{8.4}$$

Its integration in the absence of an eutectic reaction gives

$$g_{\mathrm{s}} \langle C_{\mathrm{s}} \rangle^{\mathrm{s}} = -kC_0 \int_1^{g_{\mathrm{l}}} \exp\left[-\left(\frac{1-k_{\mathrm{p}}}{1-\beta}\right)\int_1^{g_{\mathrm{l}}}\left(\frac{1}{1+\Phi}\right)\frac{dg_{\mathrm{l}}}{g_{\mathrm{l}}}\right] dg_{\mathrm{l}} \tag{8.5}$$

$$\Phi = \frac{(\vec{v}_{\mathrm{l}} - \vec{v}_{\mathrm{s}}) \cdot \nabla T}{DT/Dt} \tag{8.6}$$

Jalanti [Jalanti, 2000] proposed approximating the integration by assuming a constant Φ and proposed a simplified segregation criterion. He demonstrated its legitimacy by comparing the prediction of the simplified criterion with macrosegregation computations in DC casting with a rigid, porous solid model. The criterion is based on a parameter Ψ

$$\Psi = (1-\beta)(1+\Phi) \tag{8.7}$$

and states

$$\Psi < 1 \quad \Rightarrow \quad \text{positive macrosegregation} \tag{8.8}$$

$$\Psi > 1 \quad \Rightarrow \quad \text{negative macrosegregation,} \tag{8.9}$$

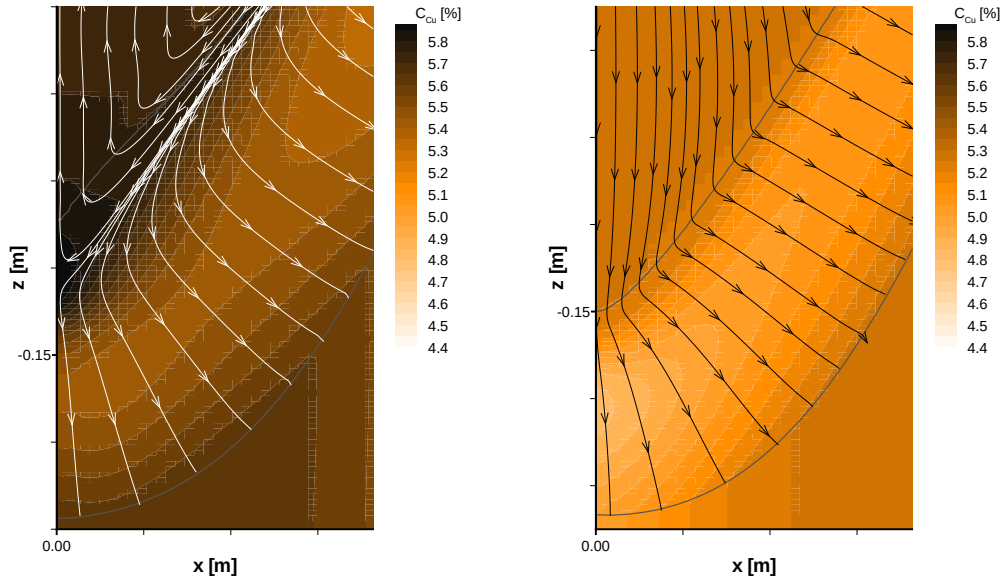

(a) Case 7: Shrinkage and thermosolutal flow

(b) Case 7_{sh}: Shrinkage only

Figure 8.10: Mixture Cu concentration (C_{m}) field and relative velocity ($\vec{v}_{\mathrm{l}} - \vec{v}_{\mathrm{s}}$) streamlines in the mushy zone at the ingot center.

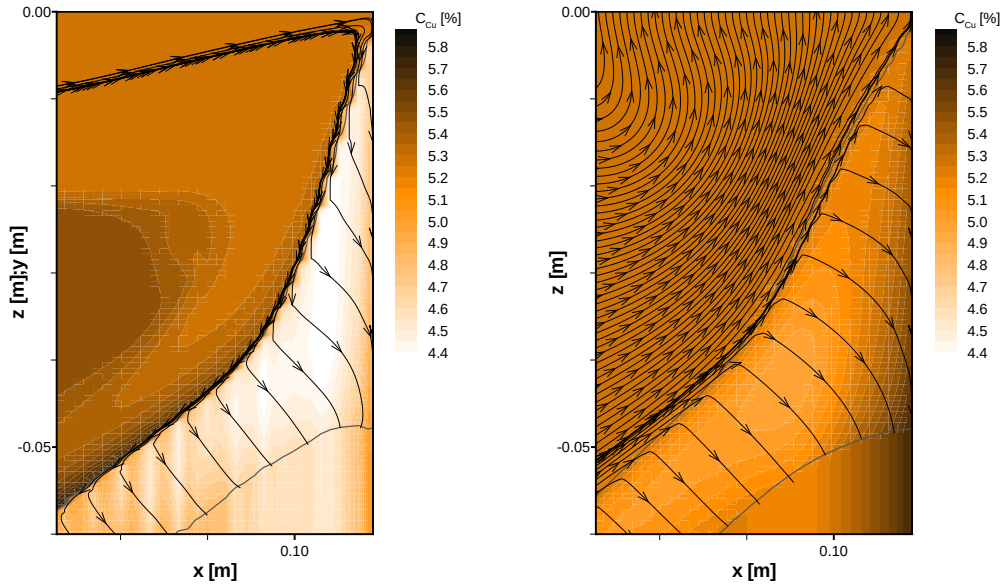

(a) Case 7: Shrinkage and thermosolutal flow

(b) Case 7_{sh}: Shrinkage only

Figure 8.11: Mixture Cu concentration (C_{m}) field and relative velocity ($\vec{v}_{\mathrm{l}} - \vec{v}_{\mathrm{s}}$) streamlines in the mushy zone at the ingot surface.

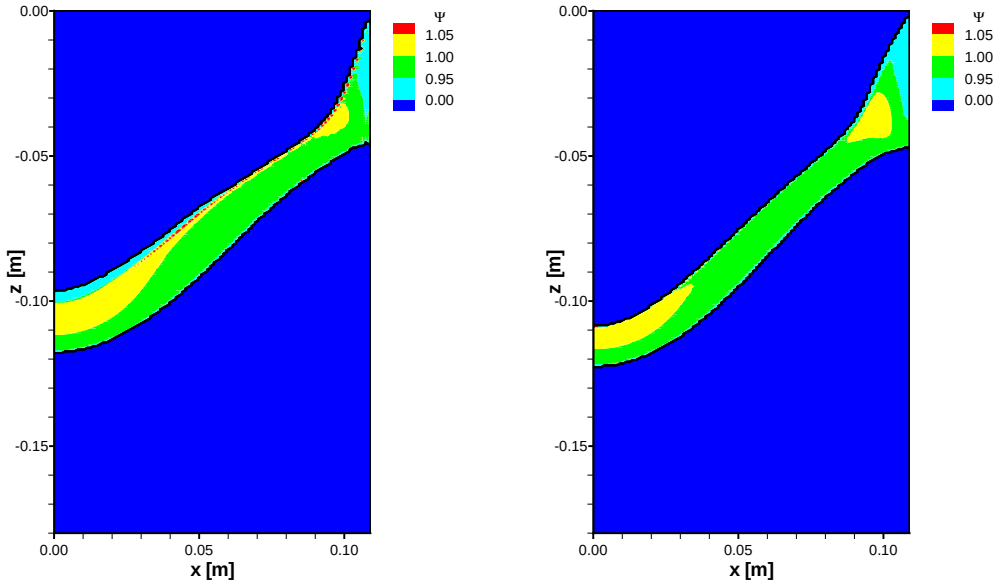

(a) Case 5: Shrinkage and thermosolutal flow (b) Case 5_{sh}: Shrinkage only

Figure 8.12: Macrosegregation criterion Ψ in the mushy zone of the Al-Cu billet.

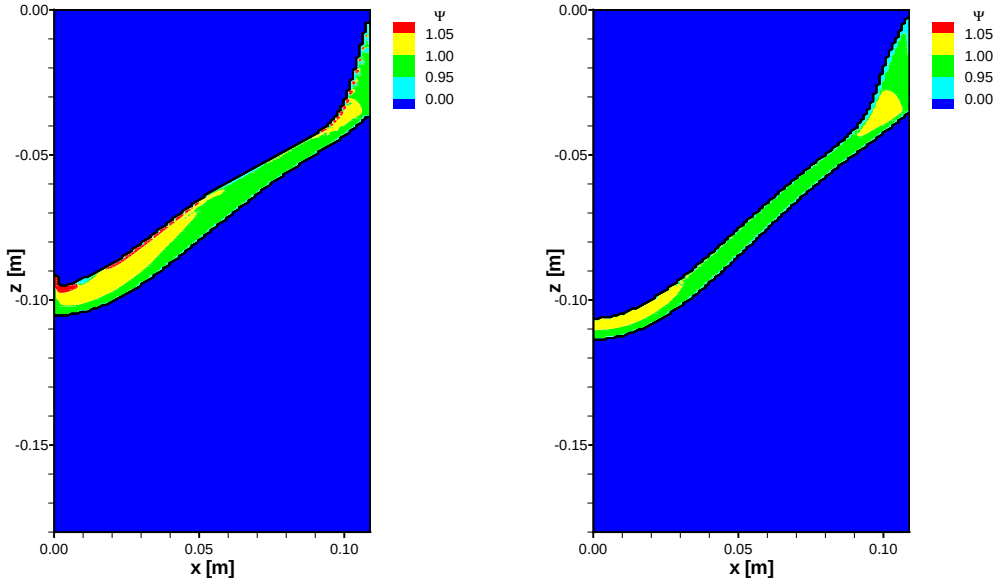

(a) Case 6: Shrinkage and thermosolutal flow (b) Case 6_{sh}: Shrinkage only

Figure 8.13: Macrosegregation criterion Ψ in the mushy zone of the Al-Mg billet.

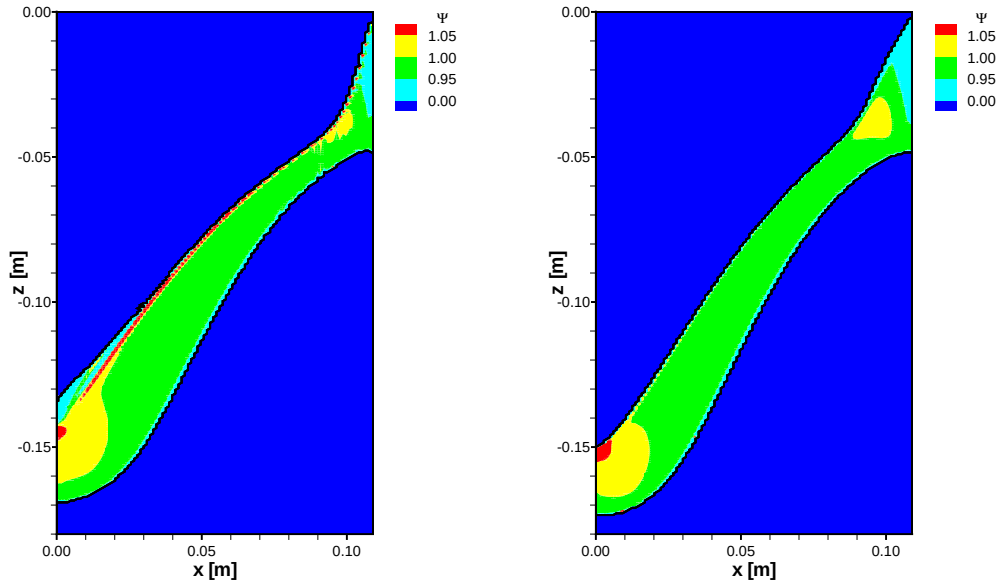

(a) Case 7: Shrinkage and thermosolutal flow

(b) Case 7_{sh}: Shrinkage only

Figure 8.14: Macrosegregation criterion Ψ in the mushy zone of the Al-Cu ingot.

where 'positive' and 'negative' refers to increased and decreased final concentration with respect to the initial concentration C_0.

The criterion is applied for all six cases investigated in this chapter. The Ψ maps are shown in Figs. 8.12-8.14. We can see that for all cases with shrinkage-driven flow only (Figs. 8.12(b), 8.13(b) and 8.14(b)), the criterion clearly predicts positive segregation at the surface and negative segregation in the center and in the region next to the surface. What is interesting is the comparison to the corresponding cases with both thermosolutal flow and shrinkage, shown in Figs. 8.12(a), 8.13(a) and 8.14(a). As we would expect, the general situation in the deeper (i.e. low-f_l) region of the porous mushy zone is retained. We can even observe a more pronounced tendency to negative segregation in the center. In the center, in the high-f_l part of the mushy zone, just below the liquidus front, the situation changes drastically due to the changed path of liquid flow. In Cases 5 and 7, the path of relative liquid motion out of the mushy zone (see Figs. 8.10(a) and 8.11(a) for Case 7) creates a tendency to positive segregation in the center (Figs. 8.12 and 8.14). In Case 6 these effects are less pronounced (Fig.8.13), but they clearly create zones with a tendency to negative segregation at points of flow penetrating the mushy zone and a tendency to positive segregation at around $r = 0.06\,\mathrm{m}$, where the flow detaches from the liquidus front (Fig.8.13(a)). In all three cases (5, 6 and 7), we observe a thin region of negative segregation tendency

just below the liquidus front. It starts close to the surface and extends towards the center. Correlating it with the segregation profiles, it becomes clear that these zones must be causing the strong reversal of segregation, predicted at the surface. At the surface the concentration of the liquid at the liquidus front (the jet coming from the inlet) is close to the nominal concentration in both cases (shrinkage only and combined thermosolutal convection and shrinkage) so the difference cannot originate in different initial melt concentrations but must be exclusively due to the relative motion of liquid and solid in the mushy zone. Moving on to the center with the analysis, at around mid-radius/mid-width the Ψ-map still shows a more pronounced negative-segregation tendency for cases 5 and 7 than for cases 5_{sh} and 7_{sh}, respectively. Despite this, we observe a clear reversal to positive segregation in cases 5 and 7 (Figs. 8.7 and 8.9). This implies that the enrichment of the melt in the liquid region next to the liquidus front competes with the segregation tendency in the mushy zone and outweighs the negative-segregation tendency of the relative solid-liquid motion. A similar effect is observed in Case 6 at around $r = 0.02 \ldots 0.05\,\mathrm{m}$, where segregation is strongly positive despite the clearly more negative segregation tendency in the mushy zone; clearly an impact of the *enriched* melt penetrating the porous mush (the composition actually decreases across the mushy zone but remains above the nominal due to the high melt concentration at the onset of solidification at the liquidus front—Fig. 8.3). In the center, the effects of melt-concentration (stratification of heavy solute-rich liquid in the Al-Cu cases and the solute-lean jet in the Al-Mg case) and segregation tendency in the high-f_{l} part of the mushy-zone mostly cooperate. Thus it is not easy to say which effect is stronger, but already from the discussion of mid-radius/mid-width segregation it is clear that the bulk-melt composition at the liquidus plays an important role.

To summarize, the thermosolutal flow affects both the transport of solute in the bulk liquid pool *and* the flow in the porous mushy zone (alas, only in the high-f_{l} part). The impact of thermosolutal convection on macrosegregation is a combined effect of both the altered segregation tendencies due to the changed relative liquid-solid motion *and* the solute transport in the bulk liquid region caused by natural (thermosolutal) and forced convection. The effect of the mushy-zone flow is most obvious in the subsurface region where a thin region with changed flow conditions drastically reverses the relative segregation. The effect of bulk liquid concentration is most pronounced in the region between the center and surface, where the effects of bulk-liquid concentration and mush flow compete and the situation is quite delicate (Ψ is close to unity). At the centerline we have seen (in the studied cases) that both effects cooperate to some degree.

8.2 The Effect of Moving Solid Grains

In this section I study

- the impact of the presence of a slurry zone with moving grains on the melt flow, on the motion and path of the solid grains, and on the distribution of solid phase in the mushy zone.
- the impact of the consolidation fraction (g_s^c) and average grain size (d_g) on these phenomena
- discuss the implications for macrosegregation in DC castings

8.2.1 System Specifications and Numerical Solution Procedure

The ranges of of g_s^c and d_g were chosen based on values used in previous model studies [Vreeman and Incropera, 2000, Wu *et al.*, 2003, Vreeman *et al.*, 2002], and those determined in experimental investigations [Daloz *et al.*, 2002, Eskin *et al.*, 2004]. The model studies use grain diameters between 25 and 100 μm. The experiments show grain sizes in the solidified cast structure of around 150 to 250 μm in billets [Eskin *et al.*, 2004] and between 300 and 500 μm for non-grain refined [Daloz *et al.*, 2002] and between 120 and 270 μm for grain refined ingots [Daloz *et al.*, 2002]. The grains in the slurry zone will be considerably smaller than in the cast structure. As we do not expect the nucleation of new grains but only further growth (recall the discussion on grain initiation and growth in Section 4.4.6), we can roughly estimate the grain size by $d_g \sim dg_\mathrm{s}^\mathrm{c}/2 \sim 25 \ldots 150\,\mu$m. In laboratory experiments the consolidation solid fraction is usually observed at around 30 % of solid and should not vary a lot. Vreeman, Schloz and Krane [Vreeman *et al.*, 2002] surmised from comparisons of numerical and experimental results that g_s^c could be somewhere around 20 % to 25 % in grain-refined DC cast billets. These estimations remain relatively speculative, however, and I decided to study the variation between 15 % and 45 % solid volume fraction. In short, to study the impact of the consolidation fraction g_s^c and the grain size d_g, six calculations with varying g_s^c and d_g are compared. Their parameters are summarized in Table 8.3.

The casting parameters, thermophysical properties, boundary conditions and computational grids are identical to Case 1 in Chapter 7. For the solution of the momentum equation the QUICK discretization scheme was used, ensuring high (second-order) accuracy (also see Section 6.11).

8.2.2 Results and Discussion

The results of the simulations are presented in Figs. 8.15-8.20, showing the solid fraction in the sump and the streamlines of the solid phase, and additionally in Figs. 8.21-8.26, showing the mixture velocity field. In all cases we observe a strong flow of free-floating grains down along the liquidus front. Once they reach the grain accumulation at the bottom of the sump their path depends primarily on the grain size, which more strongly affects the relative velocity of grains. Smaller grains are carried by the liquid, driven by thermal convection in the bulk liquid region and in the slurry zone an important portion is transported upwards, where they remelt. With a large grain size, on the other hand, the settling tendency is more pronounced as is also evident from Fig. 8.27 where the profiles of g_s along the centerline are shown. Despite the effect of fluid flow, most solid grains end up attached to the porous matrix. In Case G30D150 (Fig. 8.18) the solid that forms in the slurry region is observed to settle to the bottom, an effect caused by the large grain size. This is probably not realistic since the grains in the high-f_l part of the slurry should be much smaller than average in reality. It is also interesting to see that larger grains effectively "coalesce" at a lower solid fraction, their further path, once g_s gets close to g_s^c, being drastically shorter than for smaller grains (compare figs. 8.17 and 8.18).

The variation in the consolidation solid fraction does not fundamentally change the path of the solid in the slurry region but does strongly affect the extent and shape of the mushy zone. A higher g_s^c enhances the transport of the solid to the bottom of the sump and thus the adverse transport of latent heat, resulting in a "colder" sump. At higher g_s^c a larger fraction of the solid in the center of the solidified casting will originate from free-floating grains and this zone will be wider.

The solid streamlines show that the solid in the center forms from solid grains transported from the outer regions of the billet. The grains slide down with the flow along the liquidus front and reach deep into the center of the

Table 8.3: Summary of cases: Effect of moving solid grains

Case	g_s^c	d_g
G00	0	-
G30D075	0.30	75 μm
G30D025	0.30	25 μm
G30D150	0.31	150 μm
G15D075	0.15	75 μm
G45D075	0.45	75 μm

casting. The grains higher in the mostly isothermal slurry region are partly a result of the portion of grains originating from the periphery being deflected by the flow upwards, partly remelting completely and partly traveling downwards and attaching to the porous solid region.

It becomes evident that the solid in the center originates in most part from the solid grains that start to grow at the periphery and grow isothermally in a thin layer close to the liquidus before accumulating at the bottom. Due to the settling tendency of the solute-lean solid and adverse flow of liquid upwards in the slurry zone this should cause a solutal stratification tendency, with a positive (upward) gradient of concentration (in terms of the mixture—C_{m}). This should also cause a more isothermal slurry region, with the solid fraction gradients being more affected by the compositional stratification than by temperature. In the Al-Cu case this implies that the solid phase, which ends up in the center of the solidified casting, does not start growth from a strongly enriched liquid (accumulated at the bottom due to stratification) but from a solute lean solid and lower-concentration liquid.

In the Al-Mg case we have seen that the solutal buoyancy force can drive enriched interdendritic liquid extracted from the mushy zone away from the liquidus front. There is no solutal stratification and liquid enrichment in the high-f_{l} regions at the sump bottom is thus less pronounced. In the presence of moving grains the grains should grow at a low concentration, with the solutal buoyancy being weaker than the sedimentation tendency, which should cause the downward flow of the lean solid and additional drainage of solute-rich liquid into the bulk liquid region. The effect in the billet center will be the same as for Al-Cu, although the difference from the prediction of the porous model should be smaller as there is no solutal stratification effect in Al-Mg and the overall segregation is smaller also due to the less severe solute partitioning.

In summary, as a consequence of solid transport we expect the formation of a negative or lower concentration region at the centerline. A larger grain size should cause a narrower centerline segregation band. A larger consolidation fraction should cause more segregation with a wider distribution. The region close to the surface should not be significantly affected. Conservation of the solute dictates a positive segregation zone between the surface and center, but any more detailed speculation on the patterns in this zone is impossible as the interplay of the governing phenomena is very delicate.

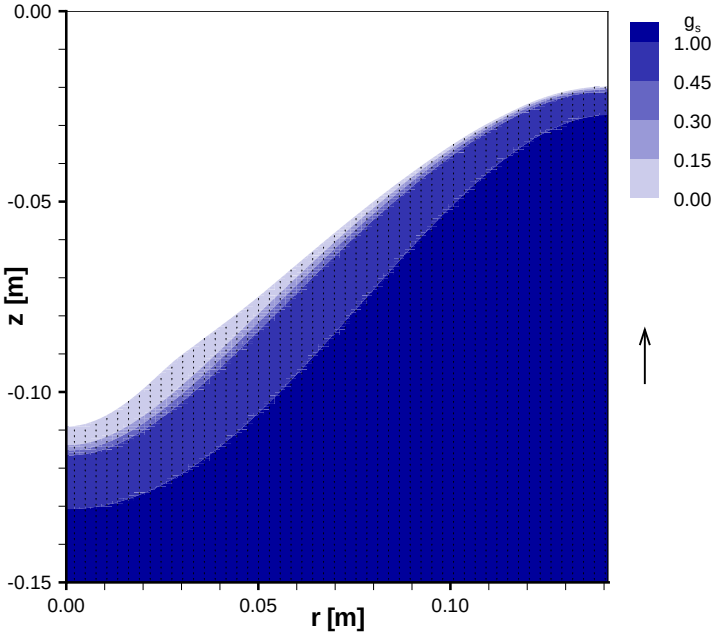

Figure 8.15: Influence of moving solid grains: Streamlines of solid and solid volume fraction in the billet at $g_s^c = 0$ (rigid solid phase, Case G00).

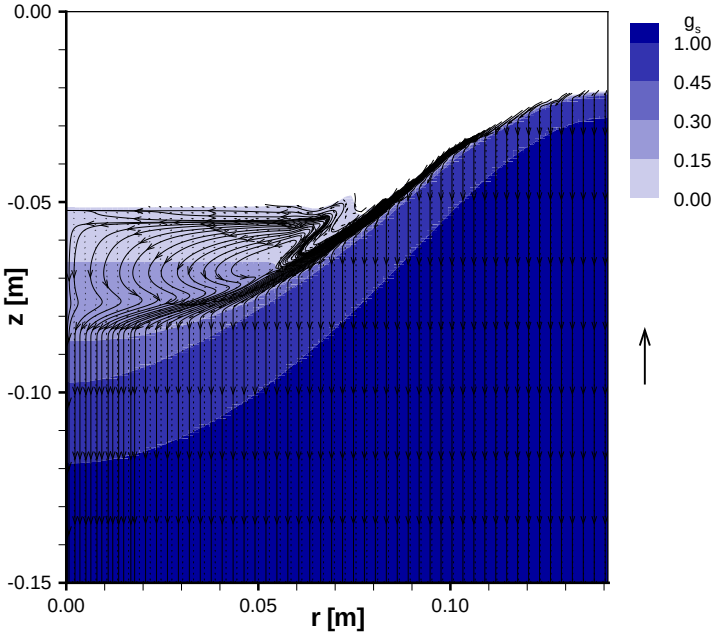

Figure 8.16: Influence of moving solid grains: Streamlines of solid and solid volume fraction in the billet at $g_s^c = 0.30$, $d_g = 75\,\mu$m (Case G30D075).

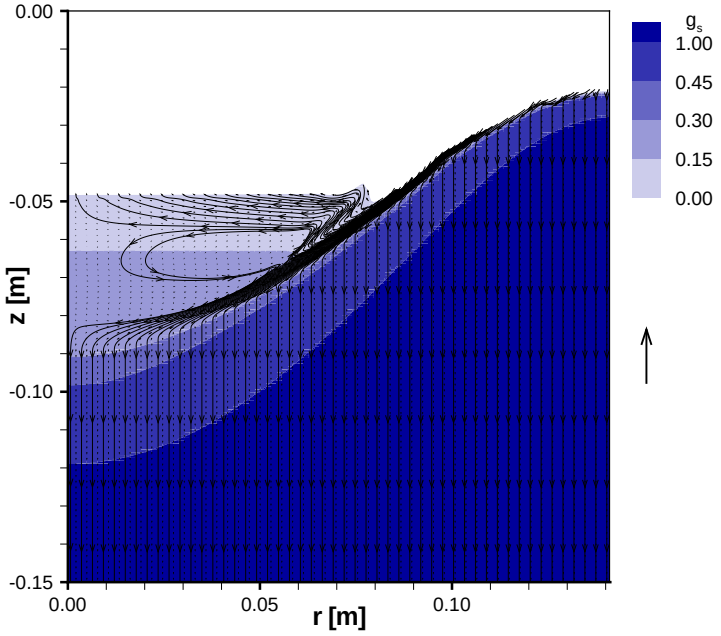

Figure 8.17: Influence of grain size: Streamlines of solid and solid volume fraction in the billet at $g_{\mathrm{s}}^{\mathrm{c}} = 0.30$, $d_g = 25\,\mu\mathrm{m}$ (Case G30D025).

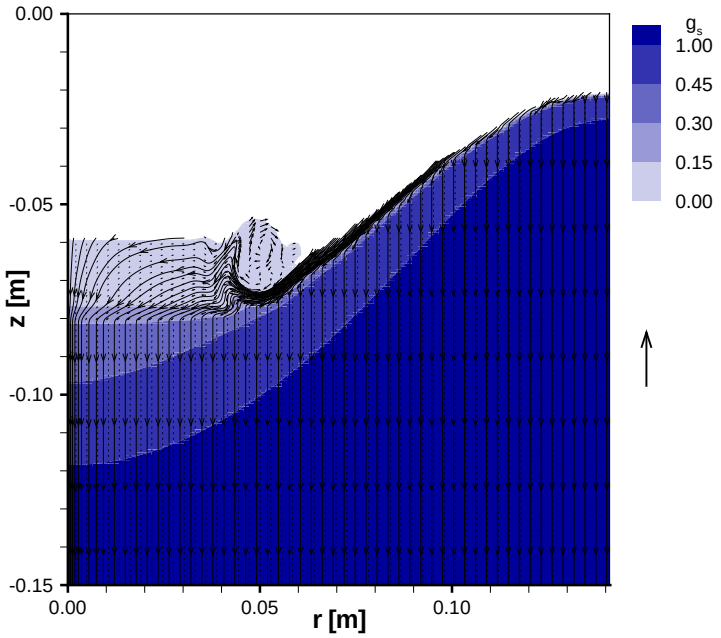

Figure 8.18: Influence of grain size: Streamlines of solid and solid volume fraction in the billet at $g_{\mathrm{s}}^{\mathrm{c}} = 0.30$, $d_g = 150\,\mu\mathrm{m}$ (Case G30D150).

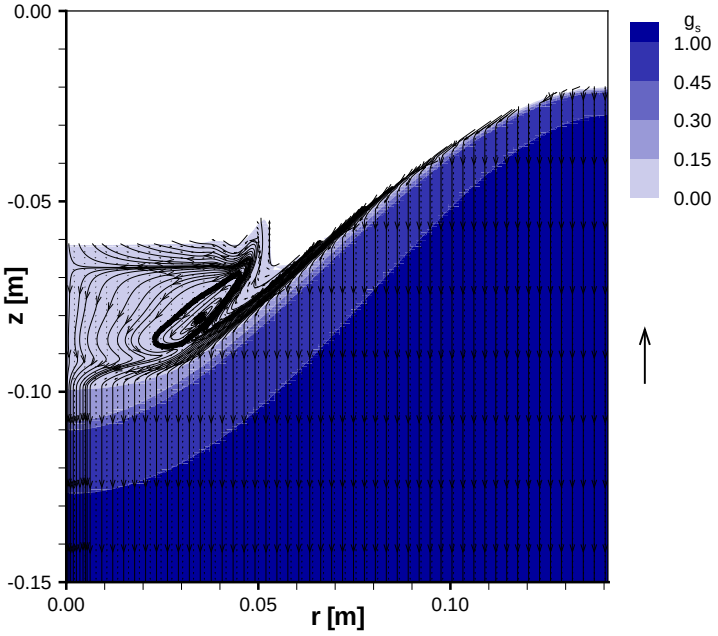

Figure 8.19: Influence of consolidation solid fraction: Streamlines of solid and solid volume fraction in the billet at $g_s^c = 0.15$, $d_g = 75\,\mu$m (Case G15D075).

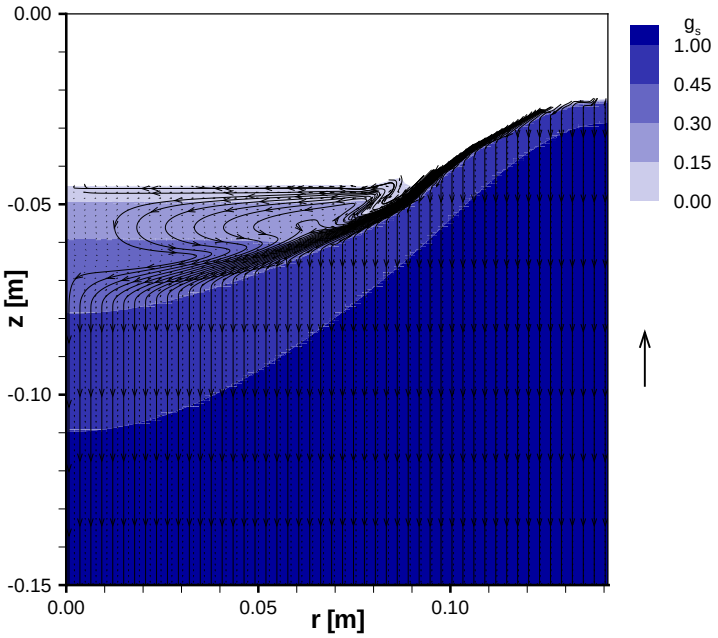

Figure 8.20: Influence of consolidation solid fraction: Streamlines of solid and solid volume fraction in the billet at $g_s^c = 0.45$, $d_g = 75\,\mu$m (Case G45D075).

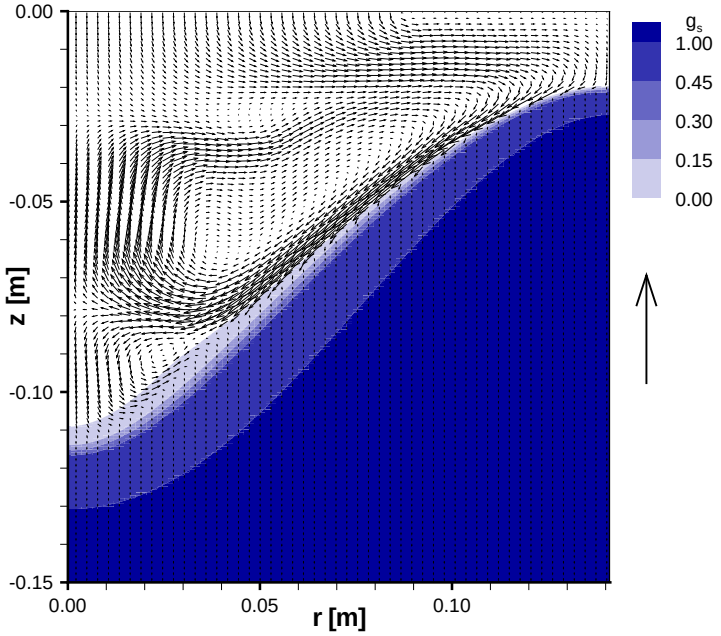

Figure 8.21: Influence of moving solid grains: Mixture velocity ($\vec{v}_\mathrm{m}$) field and solid volume fraction in the billet at $g_\mathrm{s}^\mathrm{c} = 0$ (rigid solid phase, Case G00).

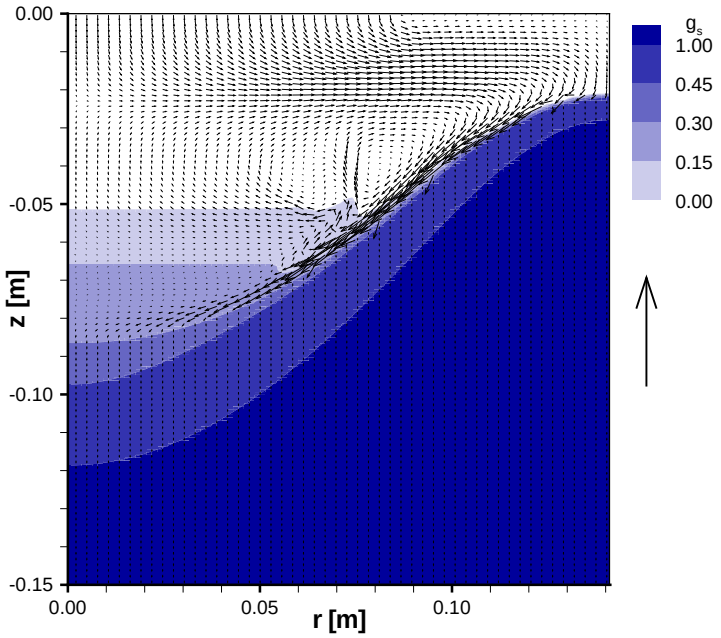

Figure 8.22: Influence of moving solid grains: Mixture velocity ($\vec{v}_\mathrm{m}$) field and solid volume fraction in the billet at $g_\mathrm{s}^\mathrm{c} = 0.30$, $d_g = 75\,\mu$m (Case G30D075).

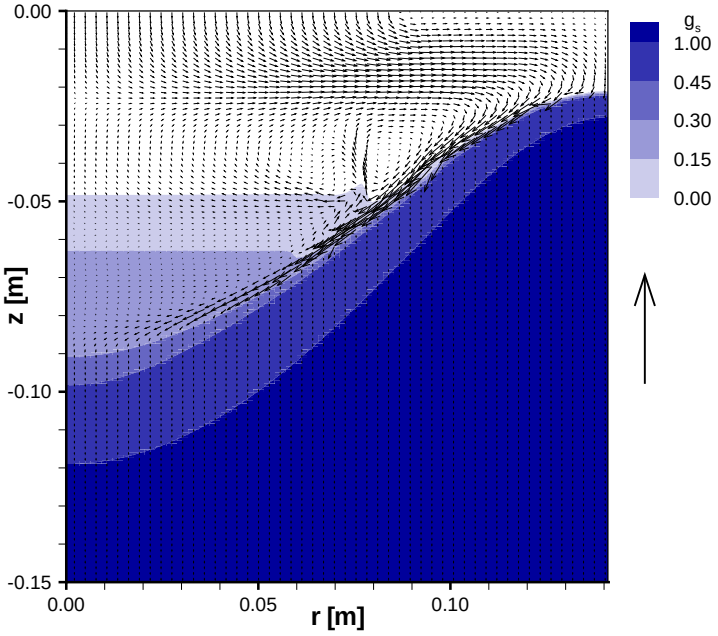

Figure 8.23: Influence of grain size: Mixture velocity ($\vec{v}_\mathrm{m}$) field and solid volume fraction in the billet at $g_\mathrm{s}^\mathrm{c} = 0.30$, $d_g = 25\,\mu$m (Case G30D025).

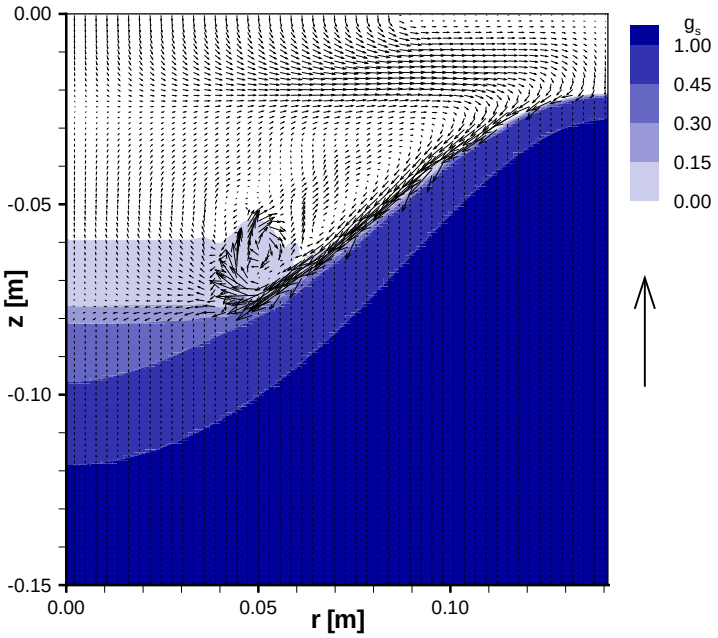

Figure 8.24: Influence of grain size: Mixture velocity ($\vec{v}_\mathrm{m}$) field and solid volume fraction in the billet at $g_\mathrm{s}^\mathrm{c} = 0.30$, $d_g = 150\,\mu$m (Case G30D150).

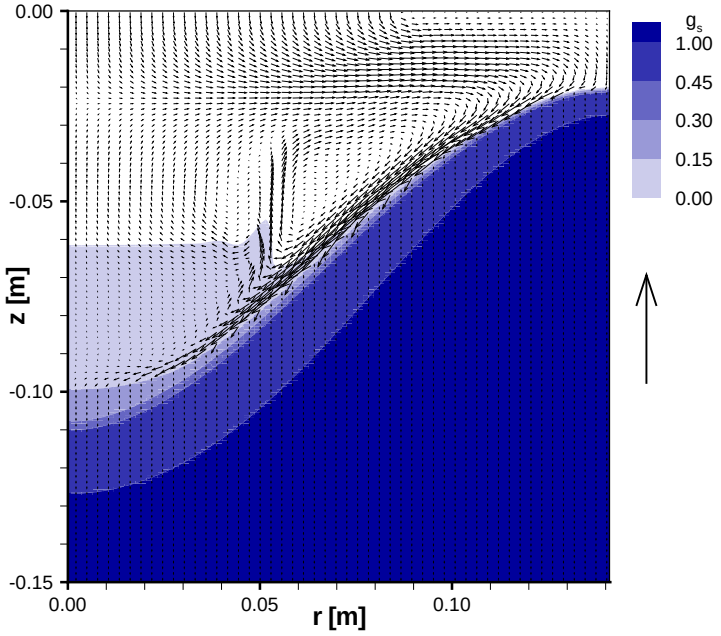

Figure 8.25: Influence of consolidation solid fraction: Mixture velocity ($\vec{v}_\mathrm{m}$) field and solid volume fraction in the billet at $g_\mathrm{s}^\mathrm{c} = 0.15$, $d_g = 75\,\mu$m (Case G15D075).

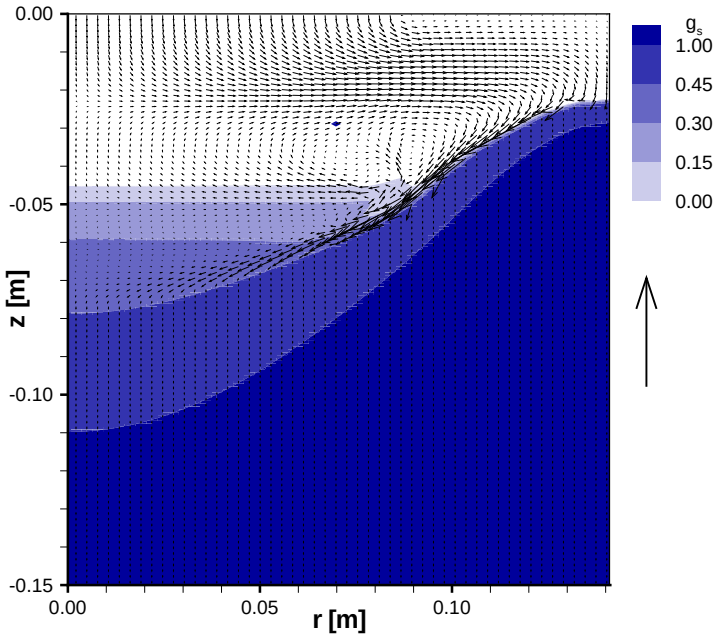

Figure 8.26: Influence of consolidation solid fraction: Mixture velocity ($\vec{v}_\mathrm{m}$) field and solid volume fraction in the billet at $g_\mathrm{s}^\mathrm{c} = 0.45$, $d_g = 75\,\mu$m (Case G45D075).

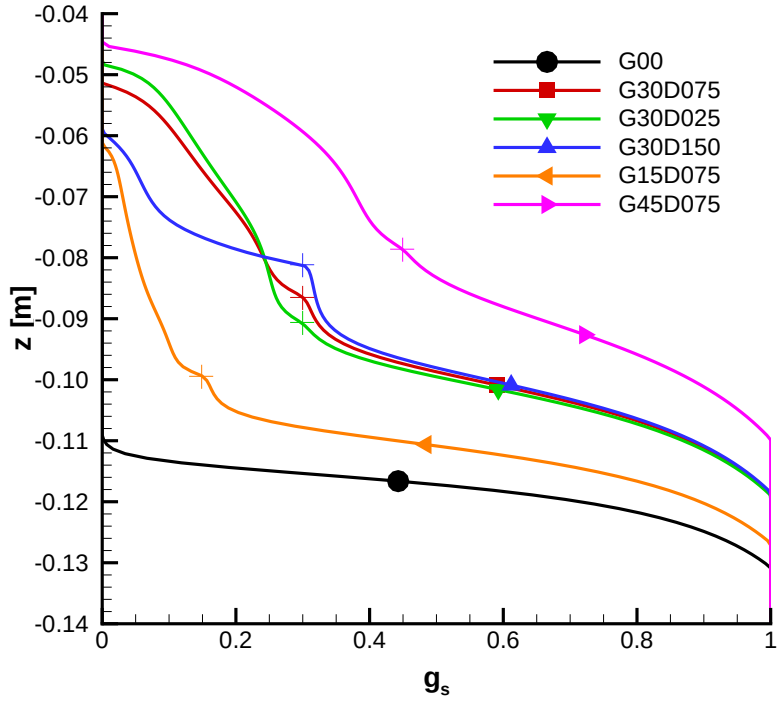

Figure 8.27: Longitudinal profiles of solid volume fraction (g_s) along the centerline. The respective consolidation solid fraction (g_s^c) is marked by a cross.

9 Summary and Conclusions

> The purpose of a fish trap is to catch fish and when the fish are caught, the trap is forgotten. The purpose of a rabbit snare is to catch rabbits. When the rabbits are caught, the snare is forgotten. The purpose of the word is to convey ideas. When the ideas are grasped, the words are forgotten. Where can I find a man who has forgotten words? He is the one I would like to talk to.
>
> Laozi

The major building blocks of macrosegregation simulation in DC casting had been arranged prior to this PhD dissertation: namely, the determination of transport phenomena affecting macrosegregation (shrinkage flow, bulk liquid flow, grain transport and exudation), the development of single-domain solidification models taking these phenomena into account, and several numerical and scaling studies of the interplay of these transport phenomena. However, a number of details of these building blocks showed some rough initial workmanship. This thesis presents several refinements of the numerical framework and the physical understanding that contribute to the finish of the building blocks and help to strengthen the future final construction of the clearly challenging task of simulating DC casting.

9.1 Summary of the Main Contributions

A single-domain mixture model was developed to describe the solidification of a binary alloy, accounting for two distinct flow regimes in the mushy zone. In the slurry regime the solid phase is in the form of free-floating grains and behaves rheologically as a slurry. Above a threshold solid volume fraction—the consolidation limit—the solid grains coalesce and form a porous skeleton, behaving as a saturated porous medium. The initiation and growth of the free-floating grains are modeled by a simplified treatment that is justified by the recent free-growth model of grain initiation on inoculant particles. The model was partly implemented in a numerical code, with persisting numerical

difficulties preventing the exploitation of its full features. Suggestions for the further refinement of the numerical construction should help resolve the remaining issues.

Being aware of the complexity of flow structures of thermosolutal natural convection in liquid metal mixtures and of the difficulties of their accurate numerical solution, a numerical study of thermal, solutal and thermosolutal natural convection was performed to fill in the gaps in our understanding of the physics and to dispel concerns over the accuracy performance of the numerical code. The physical exploration of natural convection flow patterns, heat and mass transfer was accompanied by an extensive error analysis of the simulated solutions; here it was of prime importance being that both were done at the parameters pertaining to natural convection in the liquid pool of the DC casting.

The numerical model was used to study the impact of the main DC casting parameters (casting velocity, casting temperature, mold cooling and billet diameter) on the macrosegregation pattern in DC cast billets. It was found that, assuming an entirely porous mushy zone, variations of the casting parameters modify the structure of the natural convection flow in the liquid pool, which influences the species transport at the liquidus front and consequently macrosegregation.

The cooperation of transport phenomena leading to macrosegregation was studied by simulating the effects of shrinkage flow, natural convection and grain transport.

The principal contributions of the present work are the following.

- The single-domain mixture model of solidification was rigorously derived by volume averaging, clearly identifying all simplifying assumptions and justifying them by results from previous detailed investigations drawn from the literature. The grain initiation model included is suited for the modeling of grain-refined melts, unlike previous models which incorporate stochastic nucleation models. A simplified treatment of grain nucleation and growth is proposed.

- The description of momentum transport for a dual slurry-porous flow regime in the mushy zone was cast into one single-domain equation, contrary to previous treatments of mixture models which used switching between distinct equations [Vreeman *et al.*, 2000]. It was shown that the momentum equations for the slurry and porous regimes are not easily compatible. They were merged into one by penalization of the distinct equation terms, using a smooth but sharp penalization function $\mathcal{R}$, based on the hyperbolic tangent function.

- Thermosolutal natural convection in low-Pr fluids was studied for the first time in a parameter range relevant for the casting (DC casting in particular) of metal alloys: $Pr \sim 10^{-2}$, $Sc \sim 10^2$, $Ra_T \sim 10^5 \ldots 10^6$, $Ra_C \sim 10^{10}$. Although the scope of the study had to be limited, explanations of the unsteady flow structure were proposed based on two numerical experiments and on more profound knowledge of thermosolutal convection in high-Pr fluids and unstable thermal convection in low-Pr fluids. Further, the fundamental difference of the flow in cooperating ($N > 0$) and counteracting ($N < 0$) thermal and solutal buoyancy was explained. The parameter dependence in the vicinity of the simulated parameters was surmised and discussed in view of possible implications for DC casting.

- The developed numerical code was rigorously verified for cases of thermal natural convection in the ($Pr \sim 10^{-2}$, $Ra_T \sim 10^5 \ldots 10^6$) parameter range of DC casting using a posteriori error estimation. Confidence was further reinforced by a code-to-code comparison. The verification procedure was a difficult task since no verified reference results presently exist in this parameter range. The extrapolated solution with error estimates (Case 3, Chapter 6) could serve as a benchmark quality solution for natural convection in low-Pr fluids. Attempts at a comparably rigorous verification of solutal and thermosolutal convection in the $Sc \sim 10^2$, $Ra_C \sim 10^{11}$ range showed that this task is severely complicated by the fine-scale features in the concentration field and the unsteady nature of the flow. A nearing of a grid independent solution was not evident even on reasonably dense grids, where the flow structure was inferred to be qualitatively correct by comparing solutions on two grid sizes.

- A model study of the impact of the main DC casting parameters on the macrosegregation pattern in DC cast billets was performed for the first time. The investigation was done for a porous-mush model not accounting for the impact of grain transport on macrosegregation, which precluded realistic results. The impact of casting parameters on macrosegregation was linked to their direct impact on the structure of the natural convection flow in the liquid pool of the casting and explanations in terms of the impact on effective natural convection parameters (Ra_T, Ra_C) were proposed.

- The impact of the three species transport modes (natural convection flow, shrinkage flow and grain transport) on macrosegregation in a DC casting was investigated by numerical experiments. The discussion of

the relative prominence of thermosolutal flow and shrinkage was complemented by an investigation of the origins of the effect of thermosolutal flow on local macrosegregation tendencies in the mushy zone. This investigation, performed for an industrial-size casting, shows that the thermosolutal flow affects macrosegregation both through the impact on melt flow in the porous mushy zone and through the transport of solute in the bulk liquid pool. It further shows that the interaction of shrinkage flow and thermosolutal flow varies locally and that it is primarily affected by the flow at the liquidus front. The transport of free-floating solid grains in a slurry zone was demonstrated in simplified casting computations and inferred to cause negative centerline macrosegregation. It was indicated how the negative segregation tendency should vary with grain size and consolidation fraction.

9.2 Conclusions

The conclusions of the present work can be summarized in the following points.

- The formulation of a dual slurry-porous flow regime model by a single momentum equation using The penalization of distinct terms is feasible. The numerical implementation was performed using a smooth but sharp regime penalization function $\mathcal{R}$ to transition between the slurry and porous flow regimes, and a similar Darcy penalization function $\mathcal{D}$ was employed to prevent the degeneration of the momentum equation. This technique was shown to be robust and to work well in the simplified purely-thermal solidification cases. Unlike in previous two-equation momentum transport models [Vreeman and Incropera, 2000], where switching between two distinct momentum equations was used, no problems related to the switching of terms were identified.

- Thermosolutal flow in liquid metals in the (Pr, Sc, Ra_T, Ra_C) parameter range of casting is highly unstable and results in complex flow structures and fine-scale features of the concentration field. The flow and species transport patterns of cooperating and counteracting thermal and solutal buoyancy are fundamentally different in this parameter range. In cooperating convection an unsteady, pulsating structure consisting of stagnant solutally stratified layers and solutally uniform thermal flow cells is generated, destabilized by the unstable thermal convection. In the counteracting case a solutally well-mixed flow is built

up, driven by unstable thermal convection and additionally destabilized by the interaction with the solutal buoyancy forces.

- The accurate simulation of thermal and thermosolutal natural convection in liquid metals was shown to be a difficult task, requiring much care in the numerical implementation if accurate results are desired. The use of stable second- or higher-order discretization methods is required to accurately simulate these flows. Rigorous verification of thermal convection flows in the ($Pr \sim 10^{-2}$, $Ra_T \sim 10^5 \ldots 10^6$) parameter range showed that the developed code gives an excellent performance in terms of accuracy even at relatively coarse grids. The solutal and thermosolutal convection solutions present much more complex verification problems, possibly preventing truly grid-converged solutions at reasonable grid sizes. Simple grid-sensitivity tests showed, however, that the grids used for the solutal and thermosolutal computations reproduce the qualitative flow structure, species and heat flows within acceptable margins.

- The DC casting parameters affect the flow structure in the liquid pool. The flow is affected by parameters that alter the characteristic pool height—the sump depth (casting velocity, mold cooling, casting size), the characteristic temperature difference driving the flow (casting temperature), the characteristic concentration difference (alloy system—partition coefficient, flow intensity), and liquid pool aspect ratio (casting size). The manner in which these parameters act can be inferred from the prototypal thermosolutal flow in the rectangular enclosures. The same applies to the observed patterns of solutal stratification, thermal destabilization and formation of multicellular flow and, to some extent, to the difference between the cooperating and counteracting thermal and solutal effects. The limitation of these conclusions is that they were obtained for a porous mushy zone. The prominence and mechanism of the effects might change in the presence of a slurry region due to a decreased liquid pool depth, the settling tendency of grains and an increase of viscosity in the slurry.

- The thermosolutal flow affects macrosegregation *both* through the impact on melt flow in the porous mushy zone and through the transport of solute in the bulk liquid pool. The interaction of the influences of shrinkage flow and thermosolutal flow on macrosegregation varies locally and can be either competing or cooperating. In the studied cases the thermosolutal flow has a stronger impact but it seems that this observation cannot be generalized.

9.3 Recommendations for Further Work

A lot of work remains to be done to arrive at a reasonably predictive DC casting model. The following recommendations for further research and development in the modeling of macrosegregation in DC casting emanate from the experience of conducting the present work and the findings that evolved and were presented above.

Numerical Development

Further simulation studies of macrosegregation with the developed DC casting model would ideally be preceded by some additional improvements to the numerical implementation of the model. The origin of the persisting problems with the solution of the coupled solute, and heat transfer and slurry flow in the slurry regime should be investigated and a remedy developed, most probably consisting of a modification of the iterative solution strategy. The more accurate QUICK discretization should be used in the DC casting model.

An excellent step towards the solution of many of the numerical problems encountered would be to use a self-adaptive grid [Mencinger, 2001] to refine the grid resolution in the mushy zone. This would present an elegant remedy for the aforementioned oscillations and, at the same time, improve the efficiency (in terms of computation time) and robustness of the code. Attempts at manual grid refinement have already been made, for example by Jalanti [Jalanti, 2000], and an adaptive domain decomposition method has been developed by Kaempfer [Kaempfer, 2002]. A self-adaptive grid would presumably present a more effective solution while simultaneously introducing grid refinement and alignment.

Model Development

A microsegregation model approximating the constitutional subcooling of equiaxed grains should capture the dynamics of grain growth and release some simplifying assumptions in the present simplification of the free-growth model.

Given improvements in the numerical implementation, investigations of parameter dependence with a slurry-porous flow should be conducted. Confrontations with more elaborate experiments should be performed to check the predictive capabilities of the model. The experimental program could present a problem since a relatively extensive experiment would be required to thoroughly test the model and provide some calibration of the parameters.

Industrial Relevance

In a broader context the present work relates to the development of integrated process modeling. This idea was previously propagated, e.g. by the VIR[*] projects (VIR[CAST], VIR[FAB] and VIR[FORM]) [VIR[*], 2004], aimed at modeling an aluminum production chain from casting operations through to finished products. The model developed by the author fits into the similar, alas much smaller-scale, context of aluminum production modeling initiated at the Laboratory for Multiphase Processes, University of Nova Gorica [Šarler *et al.*, 2006]. The idea is to couple models of casting (macrosegregation), microsegregation, and homogenization. The local solidification path of solid determined by the casting model should be used as an input for a decoupled microsegregation model [Vušanović, 2004, Vušanović *et al.*, 2005] using thermodynamic model data [JMatPro, 2004] which can estimate the microscopic solute distribution in primary Al dendrites and the quantities and compositions of other solid phases in the cast structure. This information is to be used as input data for the homogenization model of solid-solid phase transformations [Kovačević *et al.*, 2005b, Kovačević *et al.*, 2005a, Kovačević and Šarler, 2005]. Given properly defined requirements for the homogenized microstructure this model chain should help optimize the production chain for extruded products.

Further relevance of this work for industry lies in its exploitation of the understanding of the formation of macrosegregation to develop technical measures for macrosegregation optimization. Details of such developments lie beyond the scope of the present work as they require a prior definition of requirements for macrosegregation tolerances and a survey of the possibilities to redesign or supplement the installed casting equipment, both of which must be defined in close cooperation with process engineers.

A Volume Averaging

Volume averaging is a formal procedure used to derive macroscopic continuum equations for individual phases in a multiphase system. The procedure is performed by averaging the governing equations over the pertinent phase inside a volume element, significantly larger than the scale of the phase structures. This volume element is usually called the representative elementary volume (REV) or the averaging volume. The volume averaging concept relies upon scale separation among the microscopic continuum scale ℓ_m, the scale of the primary solid phase structures ℓ_α, and the macroscopic continuum scale L ($\ell_m \ll \ell_\alpha \ll L$). The main advantage of volume averaging over alternative theories used to derive macroscopic equations is that volume averaging clearly defines the relations between the microscopic and the volume-averaged macroscopic variables and thus also elucidates the origins of the individual volume-averaged terms in the macroscopic equations [Drew, 1983]. The procedures of volume averaging employed here are extracted mainly from the review paper by Drew [Drew, 1983].

The volume average of a quantity ϕ is defined as

$$\langle \phi \rangle = \frac{1}{V_0} \int_{V_0} \phi \, dV, \tag{A.1}$$

where V_0 is the volume of the averaging volume (REV). Accordingly, the local value of a variable is

$$\phi = \langle \phi \rangle + \hat{\phi}, \tag{A.2}$$

where $\langle \phi \rangle$ is the average over an averaging volume centered in the point of interest and $\hat{\phi}$ is the local deviation from the average in the point of interest. Accordingly

$$\left\langle \hat{\phi} \right\rangle = 0 \tag{A.3}$$

The averaging process is assumed to satisfy the following properties

$$\langle \phi + \psi \rangle = \langle \phi \rangle + \langle \psi \rangle \tag{A.4}$$

$$\langle \langle \phi \rangle \, \psi \rangle = \langle \phi \rangle \, \langle \psi \rangle \tag{A.5}$$

$$\langle \text{const} \rangle = \text{const} \tag{A.6}$$

$$\left\langle \frac{\partial \phi}{\partial t} \right\rangle = \frac{\partial \, \langle \phi \rangle}{\partial t} \tag{A.7}$$

$$\left\langle \frac{\partial \phi}{\partial x_i} \right\rangle = \frac{\partial \, \langle \phi \rangle}{\partial x_i} \tag{A.8}$$

To be able to average the equations over each of the interspersed phases the phase function X_k is introduced, which is defined as

$$X_\mathrm{k}(\vec{x}, t) = \begin{cases} 1 & \text{where } \vec{x} \text{ is in phase } k \text{ at time } t \\ 0 & \text{elsewhere} \end{cases} \tag{A.9}$$

It picks out the phase k, so the quantity ϕ in phase k is expressed as $\phi_\mathrm{k} = X_\mathrm{k}\phi$ The phase function X_k is a generalized function and the properties of averaging of derivatives, given above in Eqs. (A.7) and (A.8), do not apply for it. The volume average of the phase function is equal to the phase volume fraction

$$\langle X_\mathrm{k} \rangle = \frac{1}{V_0} \int\limits_{V_0} X_\mathrm{k} \, dV = \frac{V_\mathrm{k}}{V_0} = g_\mathrm{k} \tag{A.10}$$

The gradient of X_k is zero everywhere, except at the phase interface. There, its magnitude is equivalent to the normal derivative of the phase function and thus to the three- (or two-) dimensional Dirac's delta function and its direction is defined to point in the direction into phase k.

$$\nabla X_\mathrm{k} = \vec{n}_\mathrm{k} \frac{\partial X_\mathrm{k}}{\partial n} = \vec{n}_\mathrm{k} \delta(\vec{x} - \vec{x}_\mathrm{i}) \tag{A.11}$$

The properties of the generalized function $(\partial X_\mathrm{k}/\partial n)$ are

$$\int\limits_{V_0} \frac{\partial X_\mathrm{k}}{\partial n} \phi \, dV = \int\limits_{A_\mathrm{k}} \phi \, dA \tag{A.12}$$

$$\left\langle \frac{\partial X_\mathrm{k}}{\partial n} \right\rangle = \frac{1}{V_0} \int\limits_{V_0} \frac{\partial X_\mathrm{k}}{\partial n} \, dV = \frac{1}{V_0} \int\limits_{A_\mathrm{k}} dA = \frac{A_\mathrm{i}}{V_0} = S_\mathrm{i}, \tag{A.13}$$

where A_i is the phase interface area and S_i the volumetric interface density. The volume integral of the field quantity ϕ multiplied by $(\partial X_\mathrm{k}/\partial n)$ thus picks out the interface and equals the integral of ϕ over the phase interface. The volume average of $(\partial X_\mathrm{k}/\partial n)$ is equal to the interfacial area per unit

volume S_i. Further, Drew [Drew, 1983] shows that the phase function obeys the relationship

$$\frac{\partial X_\mathrm{k}}{\partial t} + \vec{w}_\mathrm{i} \cdot \nabla X_\mathrm{k} = 0, \tag{A.14}$$

where $\vec{w}_\mathrm{i}$ is the velocity of the phase interface.

For use in the derivation that follow, we here further define the phase quantity averages and the properties of their product and derivatives. The volume average of quantity ϕ in phase k over the volume V_0 is

$$\langle \phi_\mathrm{k} \rangle = \langle X_\mathrm{k} \phi \rangle = \frac{1}{V_0} \int\limits_{V_0} X_\mathrm{k} \phi \, dV \tag{A.15}$$

The intrinsic volume average, i.e. the average value of the quantity *inside* phase k is

$$\langle \phi_\mathrm{k} \rangle^\mathrm{k} = \langle X_\mathrm{k} \phi \rangle^\mathrm{k} = \frac{1}{V_k} \int\limits_{V_0} X_\mathrm{k} \phi \, dV = g_\mathrm{k} \langle \phi_\mathrm{k} \rangle \tag{A.16}$$

The local deviation of the phase quantity is defined via the definition

$$\phi_\mathrm{k} = \langle \phi_\mathrm{k} \rangle^\mathrm{k} + \hat{\phi}_\mathrm{k} \tag{A.17}$$

The average of the product is thus

$$\begin{aligned}
\langle \phi_\mathrm{k} \psi_\mathrm{k} \rangle = \langle X_\mathrm{k} \phi \psi \rangle &= \left\langle (\langle \phi_\mathrm{k} \rangle^\mathrm{k} + \hat{\phi}_\mathrm{k})(\langle \psi_\mathrm{k} \rangle^\mathrm{k} + \hat{\psi}_\mathrm{k}) \right\rangle \\
&= \left\langle \langle \phi_\mathrm{k} \rangle^\mathrm{k} \langle \psi_\mathrm{k} \rangle^\mathrm{k} \right\rangle + \left\langle \langle \psi_\mathrm{k} \rangle^\mathrm{k} \hat{\phi}_\mathrm{k} \right\rangle + \left\langle \langle \phi_\mathrm{k} \rangle^\mathrm{k} \hat{\psi}_\mathrm{k} \right\rangle + \left\langle \hat{\phi}_\mathrm{k} \hat{\psi}_\mathrm{k} \right\rangle \\
&= \langle \phi_\mathrm{k} \rangle \langle \psi_\mathrm{k} \rangle^\mathrm{k} + \langle \psi \rangle \left\langle \hat{\phi}_\mathrm{k} \right\rangle^\mathrm{k} + \langle \phi \rangle \left\langle \hat{\psi}_\mathrm{k} \right\rangle^\mathrm{k} + \left\langle \hat{\phi}_\mathrm{k} \hat{\psi}_\mathrm{k} \right\rangle \\
&= \langle \phi_\mathrm{k} \rangle \langle \psi_\mathrm{k} \rangle^\mathrm{k} + \left\langle \hat{\phi}_\mathrm{k} \hat{\psi}_\mathrm{k} \right\rangle
\end{aligned} \tag{A.18}$$

The average of the time derivative is

$$\begin{aligned}
\left\langle \left(\frac{\partial \phi}{\partial t} \right)_{\mathrm{k}} \right\rangle = \left\langle \frac{\partial \phi}{\partial t} X_{\mathrm{k}} \right\rangle &= \left\langle \frac{\partial}{\partial t}(X_{\mathrm{k}} \phi) \right\rangle - \left\langle \phi \frac{\partial X_{\mathrm{k}}}{\partial t} \right\rangle \\
&= \left\langle \frac{\partial}{\partial t}(X_{\mathrm{k}} \phi) \right\rangle + \langle \phi \, \vec{w}_{\mathrm{i}} \cdot \nabla X_{\mathrm{k}} \rangle \\
&= \frac{\partial \langle \phi_{\mathrm{k}} \rangle}{\partial t} + \left\langle \phi \, \vec{w}_{\mathrm{i}} \cdot \vec{n}_{\mathrm{k}} \frac{\partial X_{\mathrm{k}}}{\partial n} \right\rangle \\
&= \frac{\partial \langle \phi_{\mathrm{k}} \rangle}{\partial t} + \frac{1}{V_0} \int_{A_{\mathrm{k}}} \phi_{\mathrm{k}} \, \vec{w}_{\mathrm{i}} \cdot \vec{n}_{\mathrm{k}} \, dA \\
&= \frac{\partial}{\partial t} \left(g_{\mathrm{k}} \langle \phi_{\mathrm{k}} \rangle^{\mathrm{k}} \right) + \frac{1}{V_0} \int_{A_{\mathrm{k}}} \phi_{\mathrm{k}} \, \vec{w}_{\mathrm{i}} \cdot \vec{n}_{\mathrm{k}} \, dA
\end{aligned} \tag{A.19}$$

The average of the gradient is

$$\begin{aligned}
\langle (\nabla \phi)_{\mathrm{k}} \rangle = \langle X_{\mathrm{k}} \nabla \phi \rangle &= \langle \nabla (X_{\mathrm{k}} \phi) \rangle - \langle \phi \nabla X_{\mathrm{k}} \rangle \\
&= \nabla \langle X_{\mathrm{k}} \phi \rangle - \left\langle \phi_{\mathrm{k}} \, \vec{n}_{\mathrm{k}} \frac{\partial X_{\mathrm{k}}}{\partial n} \right\rangle \\
&= \nabla \langle \phi_{\mathrm{k}} \rangle - \frac{1}{V_0} \int_{A_{\mathrm{k}}} \phi \vec{n}_{\mathrm{k}} \, dA \\
&= \nabla \left(g_{\mathrm{k}} \langle \phi_{\mathrm{k}} \rangle^{\mathrm{k}} \right) - \frac{1}{V_0} \int_{A_{\mathrm{k}}} \phi_{\mathrm{k}} \vec{n}_{\mathrm{k}} \, dA
\end{aligned} \tag{A.20}$$

This is also equal to

$$\begin{aligned}
\langle (\nabla \phi)_{\mathrm{k}} \rangle &= \nabla \langle \phi_{\mathrm{k}} \rangle - \frac{1}{V_0} \int_{A_{\mathrm{k}}} \phi \vec{n}_{\mathrm{k}} \, dA \\
&= \nabla \left(g_{\mathrm{k}} \langle \phi_{\mathrm{k}} \rangle^{\mathrm{k}} \right) - \frac{1}{V_0} \int_{A_{\mathrm{k}}} \left(\langle \phi_{\mathrm{k}} \rangle^{\mathrm{k}} + \hat{\phi}_{\mathrm{k}} \right) \vec{n}_{\mathrm{k}} \, dA \\
&= g_{\mathrm{k}} \nabla \langle \phi_{\mathrm{k}} \rangle^{\mathrm{k}} + \langle \phi_{\mathrm{k}} \rangle^{\mathrm{k}} \nabla g_{\mathrm{k}} - \langle \phi_{\mathrm{k}} \rangle^{\mathrm{k}} \left\langle \vec{n}_{\mathrm{k}} \frac{\partial X_{\mathrm{k}}}{\partial n} \right\rangle - \frac{1}{V_0} \int_{A_{\mathrm{k}}} \hat{\phi}_{\mathrm{k}} \vec{n}_{\mathrm{k}} \, dA \\
&= g_{\mathrm{k}} \nabla \langle \phi_{\mathrm{k}} \rangle^{\mathrm{k}} + \langle \phi_{\mathrm{k}} \rangle^{\mathrm{k}} \nabla g_{\mathrm{k}} - \langle \phi_{\mathrm{k}} \rangle^{\mathrm{k}} \nabla g_{\mathrm{k}} - \frac{1}{V_0} \int_{A_{\mathrm{k}}} \hat{\phi}_{\mathrm{k}} \vec{n}_{\mathrm{k}} \, dA \\
&= g_{\mathrm{k}} \nabla \langle \phi_{\mathrm{k}} \rangle^{\mathrm{k}} - \frac{1}{V_0} \int_{A_{\mathrm{k}}} \hat{\phi}_{\mathrm{k}} \vec{n}_{\mathrm{k}} \, dA
\end{aligned} \tag{A.21}$$

Finally, to summarize we write

$$\langle \nabla \phi_{\mathrm{k}} \rangle = \nabla \langle \phi_{\mathrm{k}} \rangle - \frac{1}{V_0} \int\limits_{A_{\mathrm{k}}} \phi_{\mathrm{k}} \vec{n}_{\mathrm{k}} \, dA = g_{\mathrm{k}} \nabla \langle \phi_{\mathrm{k}} \rangle^{\mathrm{k}} - \frac{1}{V_0} \int\limits_{A_{\mathrm{k}}} \hat{\phi}_{\mathrm{k}} \vec{n}_{\mathrm{k}} \, dA \tag{A.22}$$

The average of the divergence is

$$\begin{aligned} \left\langle \left(\nabla \cdot \vec{\phi} \right)_{\mathrm{k}} \right\rangle = \left\langle X_{\mathrm{k}} \nabla \cdot \vec{\phi} \right\rangle &= \nabla \cdot \left\langle X_{\mathrm{k}} \vec{\phi} \right\rangle - \left\langle \vec{\phi} \cdot \nabla X_{\mathrm{k}} \right\rangle \\ &= \nabla \cdot \left\langle \vec{\phi}_{\mathrm{k}} \right\rangle - \frac{1}{V_0} \int\limits_{A_{\mathrm{k}}} \vec{\phi}_{\mathrm{k}} \cdot \vec{n}_{\mathrm{k}} \, dA \\ &= \nabla \cdot \left(g_{\mathrm{k}} \left\langle \vec{\phi}_{\mathrm{k}} \right\rangle^{\mathrm{k}} \right) - \frac{1}{V_0} \int\limits_{A_{\mathrm{k}}} \vec{\phi}_{\mathrm{k}} \cdot \vec{n}_{\mathrm{k}} \, dA \\ &= g_{\mathrm{k}} \nabla \cdot \left\langle \vec{\phi}_{\mathrm{k}} \right\rangle^{\mathrm{k}} + \left\langle \vec{\phi}_{\mathrm{k}} \right\rangle^{\mathrm{k}} \cdot \nabla g_{\mathrm{k}} - \frac{1}{V_0} \int\limits_{A_{\mathrm{k}}} \vec{\phi}_{\mathrm{k}} \cdot \vec{n}_{\mathrm{k}} \, dA \end{aligned} \tag{A.23}$$

B Thermophysical Properties

Table B.1: Thermophysical properties of Al-5.25 wt%Cu.

Solid density	ρ_s	$[\mathrm{kg/m^3}]$	2750	*
Liquid density	ρ_l	$[\mathrm{kg/m^3}]$	2460	*
Solid specific heat	$c_{p\mathrm{s}}$	[J/kgK]	1030	*
Liquid specific heat	$c_{p\mathrm{l}}$	[J/kgK]	1130	*
Solid thermal conductivity	k_s	[W/mK]	180	*
Liquid thermal conductivity	k_l	[W/mK]	80	*
Solid diffusivity	D_s	$[\mathrm{m^2/s}]$	$5 \cdot 10^{-12}$	†
Liquid diffusivity	D_l	$[\mathrm{m^2/s}]$	$5 \cdot 10^{-9}$	*
Latent heat at eutectic	L_eut	[J/kg]	$3.77 \cdot 10^{5}$	*
Liquid viscosity	μ	[Pa s]	$1.3 \cdot 10^{-3}$	*
Thermal expansion coefficient	β_T	$[\mathrm{K^{-1}}]$	$1.17 \cdot 10^{-4}$	†
Solutal expansion coefficient	β_C	[−]	−0.73	†
Reference temperature	T_0	[K]	973.15	
Reference concentration	C_0	[−]	0.0525	
Reference density	ρ_0	$[\mathrm{kg/m^3}]$	2460	
Permeability constant	K_0	$[\mathrm{m^2}]$	$6.67 \cdot 10^{-11}$	†
Pure Al melting temperature	T_f	[K]	933.6	*
Al-Cu eutectic temperature	T_eut	[K]	821.2	*
Eutectic solidification interval	ΔT_eut	[K]	1	
Eutectic concentration	C_eut	[wt% Cu]	33.21	*
Cu solubility in Al at T_eut	$C_{\alpha,\mathrm{eut}}$	[wt% Cu]	5.74	*
(Partition coefficient)	(k_p)	[−]	(0.173)	

* [JMatPro, 2004], † [Vreeman and Incropera, 2000]

Table B.2: Thermophysical properties of Al-5.00 wt%Mg.

Solid density	ρ_s	$[\mathrm{kg/m^3}]$	2510	*
Liquid density	ρ_l	$[\mathrm{kg/m^3}]$	2340	*
Solid specific heat	$c_{p\mathrm{s}}$	[J/kgK]	1080	*
Liquid specific heat	$c_{p\mathrm{l}}$	[J/kgK]	1180	*
Solid thermal conductivity	k_s	[W/mK]	165	*
Liquid thermal conductivity	k_l	[W/mK]	85	*
Solid diffusivity	D_s	$[\mathrm{m^2/s}]$	$1 \cdot 10^{-12}$	†
Liquid diffusivity	D_l	$[\mathrm{m^2/s}]$	$3 \cdot 10^{-9}$	*
Latent heat at eutectic	L_eut	[J/kg]	$3.30 \cdot 10^{5}$	*
Liquid viscosity	μ	[Pa s]	$1.3 \cdot 10^{-3}$	*
Thermal expansion coefficient	β_T	$[\mathrm{K^{-1}}]$	$1.22 \cdot 10^{-4}$	†
Solutal expansion coefficient	β_C	[−]	0.49	†
Reference temperature	T_0	[K]	963.15	
Reference concentration	C_0	[−]	0.0500	
Reference density	ρ_0	$[\mathrm{kg/m^3}]$	2340	
Permeability constant	K_0	$[\mathrm{m^2}]$	$6.67 \cdot 10^{-11}$	†
Pure Al melting temperature	T_f	[K]	933.6	*
Al-Mg eutectic temperature	T_eut	[K]	723.44	*
Eutectic solidification interval	ΔT_eut	[K]	1	
Eutectic concentration	C_eut	[wt% Mg]	34.15	*
Mg solubility in Al at T_eut	$C_{\alpha,\mathrm{eut}}$	[wt% Mg]	16.19	*
(Partition coefficient)	(k_p)	[−]	(0.474)	

* [JMatPro, 2004], † [Vreeman and Incropera, 2000]

C Experimental Measurements

This section presents an attempt of confrontation of model results with industrial experimental data. While it is not within the scope of the present work to perform an extensive experimental program or to calibrate the developed numerical model, it is indeed desirable to show and discuss the relation of model results to measured data.

Macrosegregation was measured in a DC cast non-grain-refined binary Al-4.6 wt%Cu billet, cast by the Wagstaff^{TM}AirSlip^{TM}system, presenting practically identical process conditions as Case 1 in Chapter 7, with exception of the alloy composition (Al-5.25 wt%Cu in Case 1). Two transversal sections of the billet were made and in each section the chemical composition was measured with optical emission spectrometry (OES) in a line across the diameter (sample shown in Fig. C.1). The number of measurement points was 26 on the first section (Profile 1 in Fig. C.2) and 22 on the second section (Profile 2 in Fig. C.2). The results are shown in Fig. C.2.

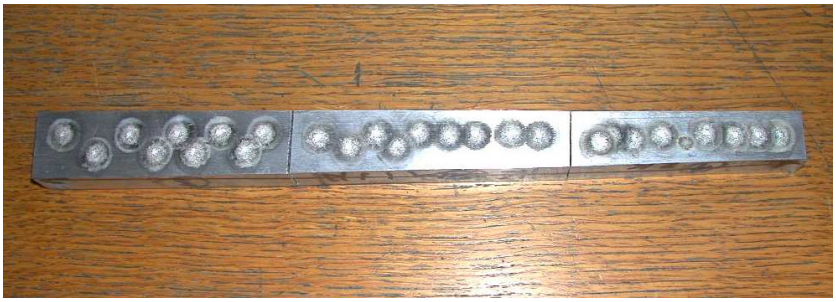

Figure C.1: Optical emission spectrometry sample of the first billet section (Profile 1 in Fig. C.2).

Observing the two measured segregation profiles we note that there is no clearly consistent pattern. While Profile 1 could be interpreted as a somewhat symmetric profile with negative centerline segregation, positive segregation at the periphery, and an indication of negative segregation close to the surface (note that a substantial positively segregated subsurface layer does not

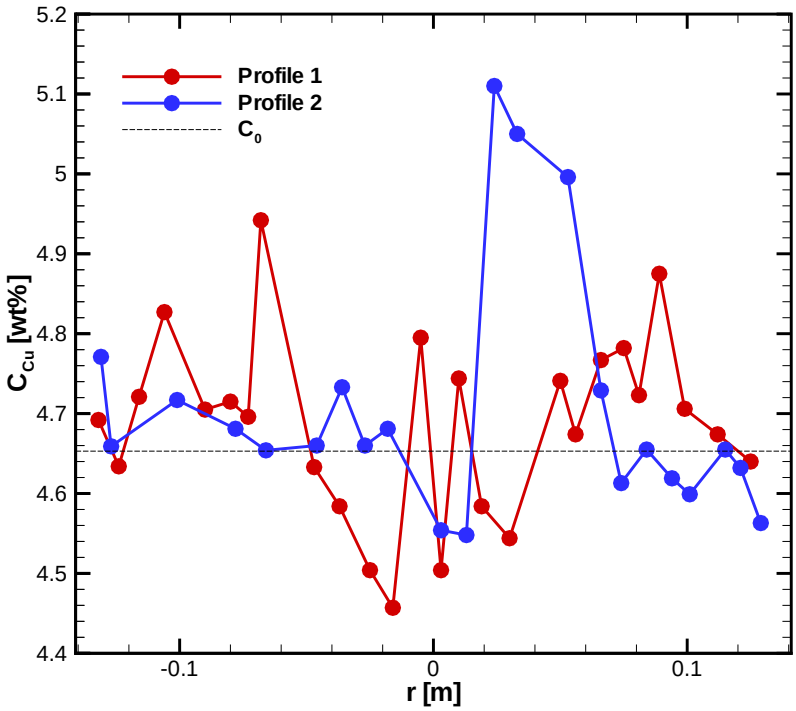

Figure C.2: Measured concentration of copper over two transversal sections of a 282 mm-diameter Al-4.6 wt%Cu billet.

develop with the AirSlip mold technology), this interpretation seems somewhat preconceived in light of the results of Profile 2. The latter shows smaller deviations, which are mostly of opposite sign. Further, it shows a very clear (over three measurement points) strong peak at $r = 0.02 \ldots 0.06$ m, clearly distorting the expected symmetry of the profile.

Due to the unclear repeatability, these experimental results cannot be directly used to validate the numerical model. More samples should be taken at several billet cross sections before we can affirm the experimental observation. An attempt to get more detailed experimental data was made at Impol Aluminium Industry, by taking OES samples at transversal planes of a bar cut across the diameter of the transversal billet section. By gradually grinding away layers of the bar in the transversal direction this technique allows to take samples at smaller distances (i.e. more samples across the diameter). The results showed good resolution and repeatability (the measurements were made before and after homogenizing heat treatment and showed identical trends). However, due to an unidentified systematic error in the measurements [Dragojević, 2006], they could not be used. The employed measurement technique was thus recognized as efficient, but the problems

arisen during the measurements should be identified and the experiments should be repeated to gather reliable data. Unfortunately, this experimental program was not completed before the finalization of the present work.

Despite that, the results of the first experiment can be used to define the total deviation of composition. We see in Fig. C.2 that it can be estimated at 0.7 wt%, which is a maximum relative deviation of $(C^{\mathrm{Cu}} - C_0^{\mathrm{Cu}})/C_0^{\mathrm{Cu}} \approx 15\,\%$. The numerical results of Case 1 in Chapter 7, which has comparable conditions, show a relative deviation of about 50 % on the other hand (Fig. 7.10). Given the uncertain interpretation and reliability of the gathered experimental data, the model results were further confronted with experimental results from the literature. A relevant source are the measurements by Eskin et al. [Eskin *et al.*, 2004]. They cast 200 mm-diameter Al-4.5 wt%Cu billets on a laboratory DC caster equipped with hot-top molds. These castings can be roughly compared with Case 2 in Chapter 7. We see that the measured maximum relative deviation is around 10 % [Eskin *et al.*, 2004], while the model predicts around 20 % (Fig. 7.10).

The large discrepancies between numerical predictions and experimental results in terms of estimated maximum macrosegregation deviations cannot be completely clarified at this point. It was clear already at the beginning, however, that a quantitatively correct segregation map can hardly be expected from the porous-mush model (Chapter 7) as even the qualitative segregation profiles are not realistic. All discussions on DC casting macrosegregation mechanisms, made previously in this chapter, and those already presented in the Literature review (Chapter 2), point to the tentative conclusion that the transport of free-floating grains is a phenomenon that decisively changes the local and global segregation deviations. The porous-mush model is thus not directly applicable for segregation prediction but is a tool for studying the possible flow patterns in the liquid pool and the interaction of flow and mushy zone on the periphery of the solidification zone.

Bibliography

AIAA (1998). *AIAA Guide for the Verification and Validation of Computational Fluid Dynamics Simulations (G-077-1998).* AIAA Standards Series. AIAA, Reston (VA), USA.

Banaszek, J. and Furmański, P. (2005). Momentum equation in macroscopic modelling of interdendritic flow in the columnar mushy zone. In Białecki, R. A. and Węcel, G., editors, *Eurotherm Seminar 82: Numerical Heat Transfer 2005*, pages 397–404, Gliwice, Poland. Institute of Thermal Technology, Silesian University of Technology.

Barnes, H. A., Hutton, J. F., and Walters, K. (1998). *An Introduction to Rheology.* Elsevier, Amsterdam.

Beckermann, C. (1987). *Melting and Solidification of Binary Mixtures with Double-Diffusive Convection in the Melt.* PhD thesis, School of Mechanical Engineering, Purdue University, West Lafayette (IN), USA.

Beckermann, C. and Viskanta, R. (1988). Double-diffusive convection during dendritic solidification of a binary mixture. *Physico Chemical Hydrodynamics*, 10:195–213.

Beckermann, C. and Viskanta, R. (1993). Mathematical modeling of transport phenomena during alloy solidification. *Applied Mechanical Review*, 46:1–27.

Bejan, A. (2004). *Convection Heat Transfer.* John Wiley and Sons, Hoboken (NJ), USA, 3rd edition.

Bennacer, R. and Gobin, D. (1996). Cooperating thermosolutal convection in enclosures—I. scale analysis and mass transfer. *International Journal of Heat and Mass Transfer*, 39(13):2671–2681.

Bennon, W. D. and Incropera, F. P. (1987). A continuum model for momentum, heat and species transport in binary solid-liquid phase change

systems—I. model formulation. *International Journal of Heat and Mass Transfer*, 30(10):2161–2170.

Bennon, W. D. and Incropera, F. P. (1988). Numerical analysis of a binary solid-liquid phase change using a continuum model. *Numerical Heat Transfer*, 13(3):277–296.

Bergholz, R. F. (1977). Instability of steady natural convection in a vertical fluid layer. *Journal of Fluid Mechanics*, 84:743–768.

Bergman, T. L. and Hyun, M. T. (1996). Simulation of two-dimensional thermosolutal convection in liquid metals induced by horizontal temperature and species gradients. *International Journal of Heat and Mass Transfer*, 39(14):2883–2894.

Bertrand, O., Binet, B., Combeau, H., Couturier, S., Delannoy, Y., Gobin, D., Lacroix, M., Le Quéré, P., Médale, M., Mencinger, J., Sadat, H., and Vieira, G. (1999). Melting driven by natural convection. a comparison exercise : First results. *International Journal of Thermal Sciences*, 38:5–26.

Bousquet-Melou, P., Goyeau, B., Quintard, M., Fichot, F., and Gobin, D. (2002a). Average momentum equation for interdendritic flow in a solidifying columnar mushy zone. *International Journal of Heat and Mass Transfer*, 45:3651–3665.

Bousquet-Melou, P., Neculae, A., Goyeau, B., and Quintard, M. (2002b). Averaged solute transport during solidification of a binary mixture: Active dispersion in dendritic structures. *Metallurgical and Materials Transactions B*, 33B:365–376.

Celik, I., Li, J., Hu, G., and Shaffer, C. (2005). Limitations of Richardson extrapolation and some possible remedies. *Journal of Fluids Engineering ASME*, 127:795–805.

Chu, M. G. and Jacoby, J. E. (1990). Macrosegregation characteristics of commercial size aluminum alloy ingot cast by the direct chill method. *Light Metals 1990*, pages 925–930.

Cless, C. M. and Prescott, P. J. (1996a). Effect of time marching schemes on predictions of oscillatory natural convection in fluids of low Prandtl number. *Numerical Heat Transfer A*, 29:575–597.

Cless, C. M. and Prescott, P. J. (1996b). Effect of time varying thermal boundary conditions on oscillatory natural convection of a low-Prandtl-number fluid. *Numerical Heat Transfer A*, 29:645–669.

Combeau, H. and Mo, A. (1997). Eutectic reaction and nonconstant material parameters in micro-macrosegregation modeling. *Metallurgical and Materials Transactions A*, 28A(12):2705–2714.

Daloz, D., Combeau, H., Joly, A., Lesoult, G., Grün, G.-U., Jarry, P., and Commet, B. (2002). Étude sur l'origine de la macroségrégation centrale dans la coulée semi-continue d'aluminium. In *Materiaux 2002: De la conception à la mise en œuvre*, Tours, France.

de Vahl Davis, G. (1983). Natural convection of air in a square cavity: a bench mark numerical solution. *International Journal of Numerical Methods in Fluids*, 5:249–264.

Dhodapkar, S., Jacob, K., and Hu, S. (2006). *Multiphase Flow Handbook*, chapter 4. Fluid-Solid Transport in Ducts. CRC Press, Boca Raton (FL), USA.

Dinsdale, A. T. and Quested, P. N. (2004). The viscosity of aluminium and its alloys—a review of data and models. *Journal of Materials Science*, 39(24):7221–7228.

Divo, E. and Kassab, A. J. (2006). Fractional time step localized meshless method for forced and natural convective heat transfer. *AIAA Journal of Thermophysics*. (in review).

DoD (2003). DoD instruction 5000.61: Modeling and simulation (M&S) verification, validation, and accreditation (VV&A). Technical report, Defense Modeling and Simulation Office, Office of the Director of Defense Research and Engineering, US Department of Defense.

Dong, M. and Dullen, F. A. L. (2006). *Multiphase Flow Handbook*, chapter 10. Porous Media Flows. CRC Press, Boca Raton (FL), USA.

Dorward, R. C. and Beerntsen, D. J. (1990). Effects of casting practice on macrosegregation and microstructure of 2004 alloy billet. *Light Metals 1990*, pages 919–924.

Dragojević, V. (2006). personal communication.

Drew, D. A. (1983). Mathematical modeling of two-phase flow. *Annual Review of Fluid Mechanics*, 15:261–291.

Drikakis, D. and Rider, W. (2005). *High-Resolution Methods For Incompressible And Low-Speed Flows*. Computational Fluid and Solid Mechanics. Springer-Verlag, Berlin.

Du, Q., Eskin, D., and Katgerman, L. (2006). Modeling macrosegregation during DC casting of a binary aluminium alloy. In Gandin, C.-A. and Bellet, M., editors, *Modeling of Casting, Welding and Advanced Solidification Processes XI*, pages 235–242, Warrendale (PA), USA. TMS.

Eskin, D. G., Savran, V. I., and Katgerman, L. (2005). Effects of melt temperature and casting speed on the structure and defect formation during direct-chill casting of an Al-Cu alloy. *Metallurgical and Materials Transactions A*, 36A:1965–1976.

Eskin, D. G., Zuidema Jr., J., Savran, V. I., and Katgerman, L. (2004). Structure formation and macrosegregation under different process conditions during DC casting. *Materials Science and Engineering A*, 384:232–244.

Ferziger, J. H. and Perić, M. (1996). *Computational Methods for Fluid Dynamics*. Springer-Verlag, Berlin, 2nd edition.

Flemings, M. C., Mehrabian, R., and Nereo, G. E. (1967). Macrosegregation: Part II. *Transactions TMS-AIME*, 242:41–49.

Flemings, M. C. and Nereo, G. E. (1967a). Macrosegregation: Part I. *Transactions TMS-AIME*, 239:1449–1461.

Flemings, M. C. and Nereo, G. E. (1967b). Macrosegregation: Part III. *Transactions TMS-AIME*, 242:50–55.

Fletcher, C. A. J., Orszag, S. A., Holt, M., and Glowinski, R. (1991). *Computational Techniques for Fluid Dynamics 1: Fundamental and General Techniques*. Springer-Verlag, Berlin, Heidelberg, 1st edition.

Flood, S. C., Katgerman, L., and Voller, V. R. (1991). The calculation of macrosegregation and heat and fluid flows in the DC casting of aluminum alloys. In Rappaz, M., Ozgu, M. R., and Mahin, K. W., editors, *Modeling of Casting, Welding and Advanced Solidification Processes V*, pages 683–690, Warrendale (PA), USA. TMS.

Furmański, P. (1992). Effective macroscopic description for heat conduction in heterogeneous materials. *Interantional Journal of Heat and Mass Transfer*, 35(11):3047–3058.

Ganesan, S. and Poirier, D. (1990). Conservation of mass and momentum for the flow of interdendritic liquid during solidification. *Metallurgical and Materials Transactions B*, 21B:173–181.

Gariepy, B. and Caron, Y. (1991). Investigation in the effects of casting parameters on the extent centerline macrosegregation in DC cast sheet ingots. *Light Metals 1991*, pages 961–971.

Gaskell, P. H. and Lau, A. K. C. (1988). Curvature-compensated convective transport: SMART, a new boundedness-preserving transport algorithm. *International Journal for Numerical Methods in Fluids*, 8:617–641.

Gobin, D. and Bennacer, R. (1996). Cooperating thermosolutal convection in enclosures—II. heat transfer and flow structure. *International Journal of Heat and Mass Transfer*, 39(13):2683–2697.

Goyeau, B., Benihaddadene, T., Gobin, D., and Quintard, M. (1997). Averaged momentum equation for flow through a nonhomogeneous porous structure. *Transport in Porous Media*, 28:19–50.

Greer, A. L., Bunn, A. M., Tronche, A., Evans, P. V., and Bristow, D. J. (2000). Modelling of inoculation of metallic melts: Application to grain refinement of aluminium by Al-Ti-B. *Acta Materialia*, 48:2823–2835.

Gruber-Pretzler, M., Mayer, F., Wu, M., Ludwig, A., Kuhn, H.-A., and Riedle, J. (2006). Modeling of macrosegregations in DC casting of bronze. In Gandin, C.-A. and Bellet, M., editors, *Modeling of Casting, Welding and Advanced Solidification Processes XI*, pages 799–806, Warrendale (PA), USA. TMS.

Grün, G.-U., Buchholz, A., and Mortensen, D. (2000). 3-D modeling of fluid flow and heat transfer during the DC casting process—influence of flow modeling approach. In Peterson, R. D., editor, *Light Metals 2000*, pages 573–578, Warrendale (PA), USA. TMS.

Hannoun, N., Alexiades, V., and Mai, T. Z. (2003). Resolving the controversy over tin and gallium melting in a rectangular cavity heated from the side. *Numerical Heat Transfer B*, 44:253–276.

Hecht, U., Gránásy, L., Pusztai, T., Böttger, B., Apel, M., Witusiewicz, V., Ratke, L., Wilde, J. D., Froyen, L., Camel, D., Drevet, B., Faivre, G., Fries, S. G., Legendre, B., and Rex, S. (2004). Multiphase solidification in multicomponent alloys. *Materials Science and Engineering R*, 46:1–49.

Hortmann, M., Perić, M., and Scheuerer, G. (1990). Finite volume multigrid prediction of laminar natural convection: Bench-mark solutions. *International Journal for Numerical Methods in Fluids*, 11(2):189–207.

Huppert, H. E. and Worster, M. G. (1985). Dynamic solidification of a binary melt. *Nature*, 314:703–707.

Hyun, M. T., Kuo, D. C., Bergman, T. L., and Ball, K. S. (1995). Direct simulation of double diffusion in low Prandtl number liquids. *Numerical Heat Transfer A*, 27:639–650.

IAI (2006). Statistics of the International Aluminium Institute (IAI). http://www.world-aluminium.org.

Iida, T. and Guthrie, R. I. (1993). *The Physical Properties of Liquid Metals*. Clarendon Press, Oxford Science Publications, Oxford.

Ishii, M. (1975). *Thermo-Fluid Dynamic Theory of Two-Phase Flow*. Eyerolles, Paris.

Jalanti, T. (2000). *Étude et modélisation de la macroségrégation dans la coulée semi-continue des alliages d'aluminium*. PhD thesis, École polytechnique fédérale de Lausanne, Lausanne.

Jalanti, T., Swierkosz, M., Gremaud, M., and Rappaz, M. (2001). Modelling of macrosegregation in continuous casting of aluminium. In Ehrke, K. and Schneider, W., editors, *Continuous Casting*, pages 191–198, Weinheim, Germany. DGM Publ., Wiley VCH.

Janssen, R. J. A. and Henkes, R. A. W. M. (1993). Accuracy of finite-volume discretizations for the bifurcationg natural-convection flow in a square cavity. *Numerical Heat Transfer A*, 24:191–207.

JMatPro (2004). JMatPro the materials property simulation package, version 3.0, Sente Software Ltd., Guildford, UK. Computer program.

Joly, A., Grün, G.-U., Daloz, D., Combeau, H., and Lesoult, G. (2000). Effect of grain refinement on macrosegregation in direct chill semi-continous cast aluminium sheet ingot. *Materials Science Forum*, 329-330:111–120.

Kaempfer, T. U. (2002). *Modeling of Macrosegregation Using an Adaptive Domain Decomposition Method*. PhD thesis, École polytechnique fédérale de Lausanne, Lausanne.

Kamakura, K. and Ozoe, H. (1996). Oscillatory phenomena of low-Prandtl-number fluids in a rectangular cavity. *Numerical Heat Transfer A*, 30:427–437.

Kattner, U. R. (1997). The thermodynamic modeling of multicomponent phase equilibria. *JOM*, 49(12):14–19.

Kitanovski, A., Vuarnoz, D., Ata-Caesar, D., Egolf, P. W., Hansen, T. M., and Doetsch, C. (2005). The fluid dynamics of ice slurry. *International Journal of Refrigeration*, 28:37–50.

Kovačević, I. and Šarler, B. (2005). Solution of a phase-field model for dissolution of primary particles in binary aluminum alloys by an r-adaptive mesh-free method. *Materials Science and Engineering A*, 413-414:423–428.

Kovačević, I., Šarler, B., and Kores, S. (2005a). Numerično modeliranje procesa homogenizacije, drugi del: Mikroskopski model, zlitine: D50, D60, AC30, AC41, AC42. Technical report, Politehnika Nova Gorica, Nova Gorica, Slovenia.

Kovačević, I., Vertnik, R., and Šarler, B. (2005b). Numerično modeliranje procesa homogenizacije, prvi del: Makroskopski model, zlitine: D50, D60, AC30, AC41, AC42. Technical report, Politehnika Nova Gorica, Nova Gorica, Slovenia.

Krane, M. J. M. (2004). Macrosegregation development during solidification of a multicomponent alloy with free-floating solid particles. *Applied Mathematical Modelling*, 28:95–107.

Krane, M. J. M., Incropera, F. P., and Gaskell, D. R. (1997). Solidification of ternary metal alloys—I. model development. *International Journal of Heat and Mass Transfer*, 40(16):3827–3835.

Kurz, W. and Fisher, D. J. (1998). *Fundamentals of Solidification*. Trans Tech Publications, Aedermannsdorf, Switzerland, 4th edition.

Lage, J. L. and Bejan, A. (1991). The Ra-Pr domain of laminar natural convection in an enclosure heated from the side. *Numerical Heat Transfer A*, 19:21–41.

Larson, R. G. (1998). *The Structure and Rheology of Complex Fluids*. Oxford University Press, New York.

Le Quéré, P. and Gobin, D. (1999). A note on possible flow instabilities in melting from the side. *International Journal of Thermal Sciences*, 38:595–600.

Leonard, B. P. (1997). *Advances in Numerical Heat Transfer*, volume 1, chapter 1. Bounded Higher-Order Upwind Multidimensional Finite-Volume Convection-Diffusion Algorithms, pages 1–57. Taylor & Francis.

Leonard, B. P. and Drummond, J. E. (1995). Why you should not use hybrid, power-law or related exponential schemes for convective modeling - there are much better alternatives. *International Journal for Numerical Methods in Fluids*, 20(6):421–442.

Leonard, B. P. and Mokhtari, S. (1990). Beyond 1st-order upwinding—the ULTRA-SHARP alternative for nonoscillatory steady-state simulation of convection. *International Journal for Numerical Methods in Engineering*, 30(4):729–766.

Lesoult, G., Albert, V., Appolaire, B., Combeau, H., Daloz, D., Joly, A., Stomp, C., Grün, G.-U., and Jarry, P. (2001). Equi-axed growth and related segregations in cast metallic alloys. *Science and Technology of Advanced Materials*, 2:285–291.

Lobe, B. (2006). *Mixing qualitative and quantitative methods in the environment of new information-communication technologies*. PhD thesis, University of Ljubljana, Ljubljana.

Ludwig, A. and Wu, M. (2002). Modeling of globular equiaxed solidification with a two-phase approach. *Metallurgical and Materials Transactions A*, 33:3673–3683.

Mathiesen, R. H. and Arnberg, L. (2006). X-ray monitoring of solidification phenomena in Al-Cu alloys. *Materials Science Forum*, 508:69–74.

Mencinger, J. (2001). *Numerična simulacija taljenja in strjevanja z uporabo samoprilagodljive računske mreže* (in slovenian; *Numerical Simulation of Melting and Solidification Using Self-Adaptive Grid*). PhD thesis, Fakulteta za Strojništvo, Univerza v Ljubljani, Ljubljana.

Mencinger, J. (2002). Polkontinuirno ulivanje aluminijevih zlitin: izračun časovnega razvoja temperaturnega in hitrostnega polja. Technical report, Politehnika Nova Gorica, Nova Gorica, Slovenia.

Mohamad, A. A. and Viskanta, R. (1991). Transient natural convection of low-Prandtl-number fluids in a differentially heated cavity. *International Journal of Numerical Methods in Fluids*, 13:61–81.

Murthy, J. Y. (2002). ME 608, Numerical Methods in Heat, Mass, and Momentum Transfer. Lecture Notes, School of Mechanical Engineering, Purdue University.

Neculae, A., Goyeau, B., Quintard, M., and Gobin, D. (2002). Passive dispersion in dendritic structures. *Materials Science and Engineering A*, A323:367–376.

Ni, J. and Beckermann, C. (1991). A volume-averaged two-phase model for transport phenomena during solidification. *Metallurgical and Materials Transactions B*, 22B(6):349–361.

Ni, J. and Incropera, F. P. (1995a). Extension of the continuum model for transport phenomena occurring during metal alloy solidification—I. The conservation equations. *International Journal of Heat and Mass Transfer*, 38(7):1271–1284.

Ni, J. and Incropera, F. P. (1995b). Extension of the continuum model for transport phenomena occurring during metal alloy solidification—II. Microscopic considerations. *International Journal of Heat and Mass Transfer*, 38(7):1285–l296,.

Oberkampf, W. L., Trucano, T. G., and Hirsch, C. (2003). Verification, validation and predictive capability in computational engineering and physics. Technical Report SAND2003-3769, Sandia National Laboratories, Albuquerque (NM), USA.

Patankar, S. V. (1980). *Numerical Heat Transfer and Fluid Flow*. Hemisphere, New York.

Peyret, R., editor (2000). *Handbook of Computational Fluid Dynamics*. Academic Press, San Diego.

Prescott, P. J., Incropera, F. P., and Bennon, W. D. (1991). Modeling of dendritic solidification systems: Reassessment of the continuum momentum equation. *International Journal of Heat and Mass Transfer*, 34(9):2351–2359.

Quested, T. E. (2004). *Solidification of Inoculated Aluminium Alloys*. PhD thesis, Department of Materials Science and Metallurgy, University of Cambridge, Cambridge.

Reddy, A. V. and Beckermann, C. (1995). Simulation of the effects of thermosolutal convection, shrinkage induced flow and solid transport on macrosegregation and equiaxed grain size distribution in a DC continuous cast Al-Cu round ingot. In Voller, V. R., Marsh, S. P., and El-Kaddah, N., editors, *Materials Processing in the Computer Age II*, pages 89–102. TMS.

Reddy, A. V. and Beckermann, C. (1997). Modeling of macrosegregation due to thermosolutal convection and contraction-driven flow in direct chill continuous casting of an Al-Cu round ingot. *Metallurgical and Materials Transactions B*, 28B(3):479–489.

Ridder, S. D., Kou, S., and Mehrabian, R. (1981). Effect of fluid flow on macrosegregation in axi-symmetric ingots. *Metallurgical and Materials Transactions B*, 12B:435–447.

Roache, P. J. (1998a). *Fundamentals of Computational Fluid Dynamics*. Hermosa, Albuquerque (NM), USA.

Roache, P. J. (1998b). *Verification and Validation in Computational Science and Engineering*. Hermosa, Albuquerque (NM), USA.

Roy, C. J. (2005). Review of code and solution verification procedures for computational simulation. *Journal of Computational Physics*, 205:131–156.

Šarler, B., Kovačević, I., Vertnik, R., Hartman, S., Vušanović, I., Založnik, M., Šafhalter, R., Slaček, E., Dragojević, V., Jelen, M., Strnad, V., and Robič, A. (2006). Integrated numerical simulation aproach in Impol Aluminium Industry casthouse. In *International Conference on Aluminium, 21-22 September, 2006, Essen, Germany*. DGM.

Šarler, B. and Pepper, D. (2004). Momentum transport modeling including solid phase movement and nucleation for direct chill casting processes. In Bergles, A. E., Golobič, I., Amon, C. H., and Bejan, A., editors, *Thermal Sciences 2004: Proceedings of the ASME - ZSIS International Thermal Science Seminar ITSS II*, Ljubljana. ZSIS.

Šarler, B., Založnik, M., and Vertnik, R. (2003). Razvoj makroizcejnih modelov za polkontinuirno in tračno ulivanje aluminijevih zlitin (in slovenian: Development of models of macrosegregation in direct-chill and twin-roll strip casting of aluminum alloys). Technical Report PNG-DP-046, Politehnika Nova Gorica, Nova Gorica, Slovenia.

Saunders, N., Li, X., Miodownik, A. P., and Schillé, J.-P. (2001). Computer modeling of materials properties. In Zhao, J.-C., Fahrmann, M., and Pollock, T. M., editors, *Materials Design Approaches and Experiences*, Warrendale (PA), USA. TMS.

Scheil, E. (1942). *Zeitschrift für Metallkunde*, 34(70-72).

Shyy, W. and Chen, M.-H. (1991). Double-diffusive flow in enclosures. *Physics of Fluids A*, 3(11):2592–2607.

Suyitno, Eskin, D. G., Savran, V. I., and Katgerman, L. (2004). Effects of alloy composition and casting speed on structure formation and hot tearing during direct-chill casting of Al-Cu alloys. *Metallurgical and Materials Transactions A*, 35A:3551–3561.

Trucano, T. G., Pilch, M., and Oberkampf, W. L. (2003). On the role of code comparisons in verification and validation. Technical Report SAND2003-2752, Sandia National Laboratories, Albuquerque (NM), USA.

Venneker, B. C. H. (2001). A quest for the best discretisation scheme to prevent numerical diffusion and dispersion at high Péclet number flows. Technical Report p.01.4.023, Netherlands Institute for Metals Research, Delft, The Netherlands.

Venneker, B. C. H. and Katgerman, L. (2000). Macrosegregation during DC casting of aluminum alloys: Numerical issues and the effect of metal entry. In Sahm, P. R., Hansen, P. N., and Conley, J. G., editors, *Modeling of Casting, Welding and Advanced Solidification Processes IX*, pages 680–686, Aachen, Germany. Shaker Verlag.

Venneker, B. C. H. and Katgerman, L. (2002). Modelling issues in macrosegregation predictions in direct chill castings. *Journal of Light Metals*, 2(3):149–159.

Vertnik, R., Založnik, M., and Šarler, B. (2006). Solution of transient direct-chill aluminium billet casting problem with simultaneous material and interphase moving boundaries by a meshless method. *Engineering Analysis with Boundary Elements*, 30(10):847–855.

VIR[*] (2004). VIR[*] conference 2004. *Aluminium*, 80(6):550–752.

Volšak, D., Založnik, M., and Šarler, B. (2005). Izračun regulacijskaih koeficientov polkontinuirnega ulivanja drogov na livni napravi Wagstaff za spekter aluminijevih zlitin in spekter formatov. Technical report, Politehnika Nova Gorica, Nova Gorica, Slovenia.

Vreeman, C. J. and Incropera, F. P. (1999). Numerical discretization of species equation source terms in binary mixture models of solidification and their impact on macrosegregation in semicontinuous, direct chill casting systems. *Numerical Heat Transfer B*, 36:1–14,.

Vreeman, C. J. and Incropera, F. P. (2000). The effect of free-floating dendrites and convection on macrosegregation in direct chill cast aluminum alloys, part II: Predictions for Al-Cu and Al-Mg alloys. *International Journal of Heat and Mass Transfer*, 43(5):687–704.

Vreeman, C. J., Krane, M. J. M., and Incropera, F. P. (2000). The effect of free-floating dendrites and convection on macrosegregation in direct chill cast aluminum alloys, part I: Model development. *International Journal of Heat and Mass Transfer*, 43(5):677–686.

Vreeman, C. J., Schloz, J. D., and Krane, M. J. M. (2002). Direct chill casting of aluminum alloys: Modeling and experiments on industrial scale ingots. *Journal of Heat Transfer ASME*, 124(10):947–953.

Vušanović, I. (2001). *Analiza fenomena faznog prelaza u višekomponentnim sistemima sa aspektima tehničke primjene*. PhD thesis, Univerzitet Crne Gore, Mašinski fakultet u Podgorici, Podgorica.

Vušanović, I. (2004). Development of ternary microsegregation models for direct-chill casting and twin-roll strip casting of aluminum based alloys (D50, D60, AC30, AC41, AC42, AF11, AF40, AF61). Technical Report PDG-DP-073, Politehnika Nova Gorica, Nova Gorica, Slovenia.

Vušanović, I., Šarler, B., and Krane, M. J. M. (2005). Microsegregation during the solidification of an Al-Mg-Si alloy in the presence of back diffusion and macrosegregation. *Materials Science and Engineering A*, 413-414:217–222.

Wan, D. C., Patnaik, B. S. V., and Wei, G. W. (2001). A new benchmark quality solution for the buoyancy-driven cavity by discrete singular convolution. *Numerical Heat Transfer B*, 40:199–228.

Wang, C. Y. and Beckermann, C. (1993). A multiphase solute diffusion model for dendritic alloy solidification. *Metallurgical and Materials Transactions A*, 24A(12):2787–2802.

Wang, C. Y. and Beckermann, C. (1996a). Equiaxed dendritic solidification with convection: Part I. multiscale/multiphase modeling. *Metallurgical and Materials Transactions A*, 27A(9):2754–2764.

Wang, C. Y. and Beckermann, C. (1996b). Equiaxed dendritic solidification with convection: Part II. numerical simulations for an Al-4 wt pct Cu alloy. *Metallurgical and Materials Transactions A*, 27A(9):2765–2783.

Wang, C. Y. and Beckermann, C. (1996c). Equiaxed dendritic solidification with convection: Part III. comparison with NH_4Cl–H_2O experiments. *Metallurgical and Materials Transactions A*, 27A(9):2784–2795.

Weckman, D. C. and Niessen, P. (1982). A numerical simulation of the D.C. continuous casting process including nucleate boiling heat transfer. *Metallurgical Transactions B*, 13B:593–602.

Whitaker, S. (1986). Flow in porous media I: A theoretical derivation of Darcy's law. *Transport in Porous Media*, 1:3–25.

Whitaker, S. (1996). The Forchheimer equation: A theoretical development. *Transport in Porous Media*, 25:27–61.

Wu, M., Ludwig, A., Buhrig-Polaczek, A., Fehlbier, M., and Sahm, P. R. (2003). Influence of convection and grain movement on globular equiaxed solidification. *International Journal of Heat and Mass Transfer*, 46(15):2819–2832.

Xin, S. and Le Quéré, P. (2002). An extended Chebyshev pseudo–spectral benchmark for the 8:1 differentially–heated cavity. *International Journal of Numerical Methods in Fluids*, 40(8):981–998.

Yu, H. and Granger, D. A. (1986). Macrosegregation in aluminum alloy ingot cast by the semicontinuous direct chill (DC) method. In *Aluminum Alloys: Their Physical and Mechanical Properties*, pages 17–29, Sheffield, UK. EMAS.

Založnik, M. and Šarler, B. (2003). Razvoj mikroizcejnih modelov za polkontinuirno in tračno ulivanje aluminijevih zlitin. Technical Report PNG-DP-047, Politehnika Nova Gorica, Nova Gorica, Slovenia.

Založnik, M. and Šarler, B. (2005a). Modeling of macrosegregation in DC casting of aluminum alloys: Estimating the influence of casting parameters. *Materials Science and Engineering A*, 413-414:85–91.

Založnik, M. and Šarler, B. (2005b). New insights into flow structure in the DC casting of aluminum alloys. In Kvande, H., editor, *Light Metals 2005*, pages 1031–1036, Warrendale (PA), USA. TMS.

Založnik, M. and Šarler, B. (2006a). Melt flow and macrosegregation in DC casting of binary aluminum alloys. *Materials Science Forum*, 508:515–522.

Založnik, M. and Šarler, B. (2006b). Thermosolutal flow in metals and implications for DC casting. In Gandin, C.-A. and Bellet, M., editors, *Modeling of Casting, Welding and Advanced Solidification Processes XI*, pages 243–250, Warrendale (PA), USA. TMS.

Založnik, M., Šarler, B., and Gobin, D. (2004). Macrosegregation simulation in DC casting of binary aluminum alloys. *Materiali in tehnologije*, 38:249–255.

Založnik, M., Xin, S., and Šarler, B. (2005). Verification of a numerical model of macrosegregation in direct chill casting. In Białecki, R. A. and Węcel, G., editors, *Eurotherm Seminar 82: Numerical Heat Transfer 2005*, pages 345–355, Gliwice, Poland. Institute of Thermal Technology, Silesian University of Technology.